Quantification of biomolecular binding dynamics by Fluorescence Correlation Spectroscopy

Jonas Peter Mücksch

München 2018

Quantification of biomolecular binding dynamics by Fluorescence Correlation Spectroscopy

Jonas Peter Mücksch

Dissertation
an der Fakultät für Physik
der Ludwig-Maximilians-Universität
München

vorgelegt von
Jonas Peter Mücksch
aus Frankfurt (Oder)

München, den 04. April 2018

Dissertation eingereicht am:	04. April 2018
1. Gutachter:	Prof. Dr. Petra Schwille
2. Gutachter:	Prof. Dr. Ralf Jungmann
Tag der mündlichen Prüfung:	16. Mai 2018

Für meine Familie

KURZFASSUNG

Diffusion und molekulare Bindungsreaktionen sind elementare Prozesse in biologischen Systemen. Für das Verständnis solcher Dynamiken und deren Wechselwirkungen ist es letztlich unabdingbar die beteiligten Parameter exakt zu quantifizieren. Diesem Ziel folgend setzt sich diese Arbeit mit der Quantifizierung von Diffusions- und Bindungsdynamiken unter Nutzung der Fluoreszenzkorrelationsspektroskopie (FCS) auseinander.

Um die Assoziations- und Dissoziationsraten von reversiblen Bindungsreaktionen an Oberflächen zu messen, wurde im Rahmen dieser Arbeit eine neuartige Methode namens "surface-integrated FCS" (SI-FCS) entwickelt. Mittels dieser Methode können Bindungsraten zwischen Rezeptoren und fluoreszierenden Liganden in Zeitbereichen von Millisekunden bis über einer Minute gemessen werden. Die zu untersuchende Oberfläche, an der die Bindungsreaktionen stattfinden, wird mit einer Weitfeldausleuchtung beschienen und die daraufhin emittierte Fluoreszenz von den Liganden wird mit einer sehr empfindlichen Kamera (electron-multiplying charge-coupled device) detektiert. Diese Flächendetektion verfügt nicht nur über ausreichende Empfindlichkeit um einzelne Moleküle zu detektieren, sondern ermöglicht auch die parallele Messung mehrerer Autokorrelationskurven im Sichtfeld. Zur Validierung dieses neuartigen Ansatzes wird die reversible Hybridisierung von Desoxyribonukleinsäuren (DNS) mit einem im Rahmen dieser Arbeit konstruierten totalreflexionsbasiertem Fluoreszenzmikroskop (TIRF Mikroskop) quantifiziert. Die Anzahl der hybridisierenden Basenpaare wird in dieser Studie systematisch variiert und drückt sich in klaren Änderungen der gemessenen Bindungsraten aus. Damit wird die Sensitivität der Methode unterstrichen.

Darüber hinaus bedient sich diese Arbeit der konventionellen konfokalen FCS. Das Problem von Proben, die einen anderen Brechungsindex als den von Wasser aufweisen, wird intensiv im Kontext von FCS Messungen beleuchtet. Abschließend werden Messbedingungen aufgezeigt unter denen systematische Messfehler und Artefakte, die auf den Brechungsindex zurčkzuführen sind, vermieden werden können.

In einem Teil dieser Arbeit wird die konfokale FCS genutzt um die Polymerisation von FtsZ Proteinen (Filamenting Temperature-Sensitive Z), sowie deren Zerlegung durch das Protein MipZ, zu untersuchen. Potentielle Fehlerquellen solcher Messungen werden beleuchtet und ein neues Modell für die Analyse von konfokalen FCS Messungen an Filamenten wird hergeleitet. Die präsentierten Ergebnisse zeigen nicht nur, dass FCS eine

geeignete Methode ist um Wachstum und Zerfall von Filamenten im Allgemeinen zu charakterisieren, sondern liefern auch deutliche Hinweise, dass FtsZ aus dem Bakterium *Caulobacter crescentus* auch in Abwesenheit von Guanosintriphosphat (GTP) kurze Oligomere bildet. Letzteres ist insbesondere interessant, da typischerweise angenommen wird, dass FtsZ als monomeres Protein vorliegt und erst in Anwesenheit von GTP zu Filamenten polymerisiert.

Abschließend quantifiziert diese Arbeit die Diffusion von Biomolekülen in Lipidmonoschichten an der Grenzfläche zwischen Luft und Wasser. Unter Verwendung der konfokalen FCS werden Messungen in Miniaturkammern durchgeführt und validiert. Mithilfe dieser Methode werden Messungen an Biomolekülen ermöglicht, die nur in sehr geringen Mengen aufgereinigt werden können. Die hier präsentierten Diffusionsmessungen stellen einen wichtigen Schritt hin zur FCS basierten Charakterisierung der Bindungskinetiken von Biomolekülen zu Lipidmonoschichten dar.

ABSTRACT

Diffusion and molecular binding processes are indispensable for biological systems. A vital step towards the understanding of such dynamics and their interplay is a thorough quantification of all parameters involved. This work addresses the characterization of biomolecular diffusion and binding dynamics using fluorescence correlation spectroscopy (FCS).

To quantify the reversible surface attachment of fluorescently labeled molecules, a novel method termed surface-integrated FCS (SI-FCS) is developed. Using this technique, the association and dissociation rates of receptor-ligand pairs can be determined over a wide range of time scales, ranging from hundreds of milliseconds to tens of seconds. The surface of interest is exposed to a widefield illumination and a highly sensitive electron-multiplying charge-coupled device (EMCCD) camera is used for detection, not only providing single-molecule sensitivity, but also enabling a parallel detection of the signal, which facilitates multiplexed SI-FCS measurements across the field of view. To validate this approach, we quantify the reversible hybridization of single-stranded deoxyribonucleic acid (DNA) using a standard total internal reflection fluorescence (TIRF) microscope. The nucleotide overlap was systematically varied to demonstrate the sensitivity of SI-FCS.

Furthermore, this work extensively employs FCS in its more conventional form using a confocal microscope. The effect of refractive index mismatches on single-focus FCS measurements is thoroughly characterized and a regime in which unbiased experiments are possible is identified.

Confocal FCS is used to monitor the filament formation of FtsZ proteins (filamenting temperature-sensitive mutant Z) and their breakage by the protein MipZ *in vitro*. Potential artifacts are identified and a novel model to analyze diffusing filaments in FCS experiments is derived, applied, and validated. These findings not only demonstrate that filament formation can be efficiently studied using confocal FCS, but also indicate that FtsZ from *Caulobacter crescentus* may intrinsically form small oligomers.

Finally, this work characterizes the diffusion of biomolecules in lipid monolayers at the air-water interface using confocal FCS. A miniaturized fixed area-chamber, which requires only minute amounts of protein, is presented and validated. Using this design, monolayer experiments become accessible to studies where biomolecules can only be purified in small amounts. Moreover, the quantification of diffusion in monolayers using FCS is a major step towards the routine characterization of binding of biomolecules to lipid monolayers.

Contents

List of Figures

List of Tables

List of Abbreviations

aa	amino acid
AFM	atomic force microscopy
AOTF	acousto optical tunable filter
APD	avalanche photodiode
ATP	adenosine triphosphate
bfp	back-focal plane
BLI	bio-layer interferometry
BLM	black lipid membrane
BSA	bovine serum albumin
CMOS	complementary metal-oxide-semiconductor
cpp	counts per particle
Ctl	C-terminal linker
CtxB	pentameric β subunit of cholera toxin
cw	continuous wave
DiO	3,3'-Dilinoleyloxacarbocyanine Perchlorate
DLS	dynamic light scattering
DMPC	1,2-dimyristoyl-sn-glycero-3-phosphocholine
DNA	deoxyribonucleic acid
DOGS-NTA(Ni)	1,2-dioleoyl-sn-glycero-3-[(N-(5-amino-1-carboxypentyl)iminodiacetic-acid)succinyl] (nickel salt)
DOPC	1,2-dioleoyl-sn-glycero-3-phosphocholine
DOPE	1,2-dioleoyl-sn-glycero-3-phosphoethanolamine

DPSS	diode-pumped solid state
EDTA	ethylenediaminetetraacetic acid
eGFP	enhanced green fluorescent protein
EMCCD	electron-multiplying charge-coupled device
FA-model	free area model
FCCS	fluorescence cross-correlation spectroscopy
FCS	fluorescence correlation spectroscopy
FOV	field of view
FRAP	fluorescence recovery after photobleaching
FRET	Förster resonance energy transfer
FtsZ	filamenting temperature-sensitive mutant Z
G_{M1}	ovine brain ganglioside
GC	gas chromatography
GFP	green fluorescent protein
GTP	guanosine triphosphate
GUV	giant unilamellar vesicle
HEPES	4-(2-hydroxyethyl)-1-piperazineethanesulfonic acid
HPW-model	Hughes-Pailthorpe-White-model
ICS	image correlation spectroscopy
IgG	immunoglobulin G
ITC	isothermal titration calorimetry
ITO	indium tin oxide
LSM	laser scanning microscope
LUV	large unilamellar vesicle

MMA	mean molecular area
MPER	membrane proximal external region
MSD	mean squared displacement
MST	microscale thermophoresis
mts	membrane targeting sequence
NA	numerical aperture
NFP	nominal focus position
nt	nucleotide
PAINT	points accumulation for imaging in nanoscale topography
PMT	photomultiplier tube
PSF	point spread function
PTFE	polytetrafluoroethylene
QCM	quartz crystal microbalance
QCM-D	quartz crystal microbalance with dissipation
QPD	quadrant photodiode
RICS	raster image correlation spectroscopy
RNA	ribonucleic acid
ROI	region of interest
SAF	supercritical angle fluorescence
SD-model	Saffmann-Delbrück-model
SI-FCS	surface-integrated FCS
SLB	supported lipid bilayer
SPAD	single-photon avalanche diode
SPR	surface plasmon resonance

SPT	single particle tracking
ssDNA	single-stranded DNA
STED	stimulated emission depletion
SUV	small unilamellar vesicle
TCSPC	time correlated single photon counting
TEM	transmission electron microscopy
TICS	temporal image correlation spectroscopy
TIR	total internal reflection
TIR-FCS	total internal reflection fluorescence correlation spectroscopy
TIRF	total internal reflection fluorescence
Tris	tris(hydroxymethyl)aminomethane
TTL	transistor transistor logic
UV	ultraviolet

I

INTRODUCTION AND OUTLINE

Life is constantly governed by a plethora of interconnected dynamic processes. The nature of these dynamics can be very different, ranging from conformational transitions of biomolecules to large scale collective motions. The versatility and the finely tuned interplay of these processes has attracted the attention of researchers for many decades. Despite the immense research conducted on biologically relevant questions, the knowledge about underlying general laws and principles is still limited. Although many insights have been gained, the precise quantification of processes and the formulation of all-embracing descriptions, at least of partial aspects of life, require further attention.

Many biological functions involve multiple components which are not only interacting, but also constitute a nonlinear system; meaning that even small changes in the system may alter its functionality or cause its collapse [May, 1976]. Thus, an all-embracing understanding of such nonlinear systems requires the precise knowledge of all parameters and quantities that govern the process. Ultimately, such insights may lead not only to the full description of the system, but potentially pave the way towards directed man-made modifications, purposeful utilization, and synthetic replicas. In particular, depending on the system under investigation, this includes the development of new drugs and synthetic biology applications.

When it comes to life on the cellular level, the plasma membrane is one of the key players [Alberts, 2002]. In the simplest picture, it is a bilayer of amphiphilic molecules separating the inside from the outside of the cell [Mouritsen and Bagatolli, 2015], which in itself is a tremendously important feature, e.g. for establishing and maintaining concentration gradients. In reality, the plasma membrane is made up of a manifold of components and has a highly complex structure. Moreover, it is an integral constituent in a multitude of processes, including transport, signaling and cell division. The mechanisms by which all these purposes are met by the membrane rely on very different physical phenomena. This can be illustrated by considering three examples. First, the membrane is practically impermeable to ions due to its hydrophobic core. This allows for the existence of a proton (H^+) gradient that drives the generation of adenosine triphosphate (ATP) [Alberts, 2002]. Second, the binding of proteins to membranes significantly reduces their mobility compared to free diffusion. The resulting differences in diffusion coefficients, coupled with a finely tuned interplay of molecular interactions, can result in symmetry breaking pattern formation [Gierer and Meinhardt, 1972], which itself is key for the survival of organisms [Li et al., 2010]. Finally, in comparison to a 3D volume, the membrane has a reduced dimensionality. One of the key results is that membrane binding of a biomolecular species corresponds to a massive up-concentration of these molecules, which can in turn shift chemical equilibria and increase the rates of reactions [Vauquelin and Packeu, 2009].

The co-existence of these various functions highlights the complexity of biological systems. Consequently, when looking at a particular dynamic within a living organism, an overwhelming amount of processes, which are vital for the organism, are happening in parallel. Moreover, in many cases there may be a crosstalk between these processes, hampering the unbiased study of a specific molecular process. To circumvent these problems, and to have a clear, unobstructed view at the process of interest, *in vitro* approaches were established [Liu and Fletcher, 2009, Lagny and Bassereau, 2015]. This way, observations are made on fully controllable reconstituted systems that comprise only essential components. This approach was also pursued in this work, either by studying purified proteins in aqueous buffers, or by the use of model membrane systems.

In a typical approach to quantify dynamic processes in a thermodynamic ensemble, this system is perturbed and its relaxation back into equilibrium is followed. Alternatively, if the system is sufficiently small, the dynamic process of interest may cause fluctuations of an appropriate read-out signal. Following this idea, in this work the fluctuations of fluorescence signals are analyzed by means of autocorrelation functions [Magde et al., 1972], an approach commonly referred to as fluorescence correlation spectroscopy (FCS). Conceptually, FCS is accessible for many sizes and shapes of the detection volume from which the fluorescence is collected. Thus, the microscopy schemes can be optimized for the system under investigation [Eigen and Rigler, 1994, Singh and Wohland, 2014, Li et al., 2017].

This thesis contributes to the goal of precise quantifications of biological systems by establishing novel methods for the study of dynamic processes. In particular, chapter III presents a new technique to measure surface association and dissociation rates based on FCS together with a camera-based detection scheme. This approach combines the advantages of highly specific fluorescence imaging with multiplexed camera detection in many pixels at a time to measure binding rates in quasi-equilibrium without the need to excite the system. While chapter III demonstrates a new method, the following chapters focus on the use of an established technique, confocal FCS, to quantify binding processes.

Chapter IV identifies a confocal FCS measurement regime, which avoids refractive index mismatches that conventionally lead to artifacts and biased results. These findings also serve as a quality control for the subsequently presented experiments. More precisely, the polymerization of the tubulin-analogue FtsZ (filamenting temperature-sensitive mutant Z) and its interaction with the protein MipZ from *Caulobacter crescentus* are addressed by an FCS study in chapter V. Finally, chapter VI demonstrates a novel approach to measure diffusion kinetics of biomolecules in lipid monolayers at the air-water interface using confocal FCS, which is a major step towards the quantification of binding kinetics to lipid monolayers.

II

BASIC CONCEPTS

II.1 Diffusion and binding

II.1.1 Diffusion models

II.1.1.1 Brownian motion

The thermally induced random motion of microscopic particles immersed in a solvent is called Brownian motion and was first described by Robert Brown [Brown, 1828]. The solvent molecules are constantly moving at a temperature $T > 0$, resulting in frequent collisions with the immersed particles. The corresponding momentum transfers result in the motion of these particles. Moreover, on sufficiently long time scales, this motion is random and memoryless. An all-embracing discussion of all facets of Brownian motion clearly exceeds the scope of this introduction. A comprehensive compendium was published by Mazo [Mazo, 2002]. Brownian motion is ubiquitously found in almost all aspects of cellular and molecular biology [Codling et al., 2008, Sackmann and Merkel, 2010, Hoppe et al., 2012, Hänggi and Marchesoni, 2005] and hence plays an important role in the interpretation of many observations.

The research described in this thesis entirely encounters translational diffusion. Consequently, this paragraph will focus on this aspect of Brownian motion. The mathematical description goes back to work by Fick, Sutherland, Einstein and von Smoluchowski [Fick, 1855, Sutherland, 1905, Einstein, 1905, von Smoluchowski, 1906] and is centered around the diffusion equation:

$$\frac{\partial}{\partial t}\rho(\vec{r},t) = D\nabla^2\rho(\vec{r},t) \qquad \text{(II.1)}$$

Here, D is the diffusion coefficient, which in this work is assumed to be constant, i.e. has no spatiotemporal dependence within individual measurements. Equation II.1 has no restrictions on the dimensionality d of the system, although this thesis encounters only 2D and 3D cases. The solution $\rho(\vec{r},t)$ is found using the initial condition $\rho(\vec{r},0) = \delta(\vec{r}-\vec{r_0})$ and the boundary condition $\rho(\vec{r}\to\infty,t) = 0$. The solution $\rho(\vec{r},t)$ can be interpreted as the probability to find a diffusing particle at time t at the location $\vec{r}$, provided it was located at $\vec{r}_0$ at $t_0 = 0$. Taking into account a corresponding normalization $\int \rho(\vec{r}, t)\, \mathrm{d}^3\vec{r} = 1$, the solution to the diffusion equation in an infinite space reads:

$$\rho(\vec{r}, t) = (4\pi Dt)^{-\frac{d}{2}}\, e^{-\frac{\vec{r}^2}{4Dt}} \tag{II.2}$$

For convenience, the coordinate system was chosen such that $\vec{r}_0 = 0$. Although this Gaussian distribution widens with time, its center stays at $\vec{r} = \vec{r}_0 = 0$ for all times. Consequently, the mean displacement is $\langle \vec{r} \rangle = 0$. On the other hand, the mean squared displacement (MSD) reads:

$$\mathrm{MSD} = \left\langle \vec{r}^2 \right\rangle = \int \vec{r}^2 \rho(\vec{r}, t)\, \mathrm{d}^3\vec{r} = 2dDt \tag{II.3}$$

Sutherland, Einstein and von Smoluchowski came to the conclusion that the diffusion coefficient D depends on the temperature T and the friction constant ζ of the considered particles [Einstein, 1905, von Smoluchowski, 1906, Sutherland, 1905].

$$D = \frac{k_B T}{\zeta} \tag{II.4}$$

The discussed expressions to describe diffusion mathematically have direct practical implications. First, in the diffusion equation II.1, the spatial dimensions separate, which means that each dimension can be treated independently. Second, the probability function $\rho(\vec{r}, t)$ is a Gaussian with standard deviation $\sqrt{2dDt}$. Consequently, the probability that a particle leaves an observation volume within a time interval Δt is larger, the larger the diffusion coefficient. The FCS-based quantification of diffusion processes makes use of the temporal widening of $\rho(\vec{r}, t)$. Third, the linear relation between MSD and time implies that the measurement of a displacement of particles at different time points gives access to the diffusion coefficients. This is commonly exploited in single particle tracking (SPT).

II.1.1.2 Stokes-Einstein-Smoluchowski Equation

For simplicity, objects under study are often approximated as spherical objects. Ideally, for a spherical particle of hydrodynamic radius R_h immersed in a medium of much smaller solvent molecules and bulk viscosity η, the friction constant can be described by the Stokes relation $\zeta = 6\pi\eta R_h$. Combining with equation II.4 yields:

$$D = \frac{k_B T}{6\pi\eta R_h} \tag{II.5}$$

This expression is typically termed Stokes-Einstein-Smoluchowski or Stokes-Einstein relation. It is frequently used to relate measurements of the diffusion coefficient to the physical size of the observed particle. In practice, however, the objects under study, e.g. proteins, are not spherical, and thus the hydrodynamic radius is only an indicator for the size of this particle.

II.1.1.3 Diffusion of membrane inclusions

In the context of this thesis, the Stokes-Einstein-Smoluchowski is used to describe the diffusion of biomolecules in 3D. The surrounding medium is considered to be homogeneous. This assumption is not met when considering the diffusion of a membrane inclusion. Diffusion in lipid membranes is of key relevance to many biological processes, ranging from transmembrane protein diffusion to diffusion-limited reactions and the regulation of protein distributions. The most commonly used model to describe the diffusion of proteins in membranes was developed by Saffmann and Delbrück [Saffman and Delbrück, 1975, Saffman, 1976]. They considered a cylindrical membrane inclusion with radius a, which diffuses in a membrane of thickness h and surface viscosity η_s, as shown in figure II.1A. For a uniform slab of a viscous fluid with viscosity η and thickness h, the surface viscosity can be expressed as $\eta_s = \eta h$.

On both sides, the membrane is surrounded by media with the bulk viscosities η_1 and η_2. Although the SD-model describes 2D diffusion in a membrane, it is a 3D model in which the impact of the motion of a membrane inclusion is propagated to the surrounding media [Saffman and Delbrück, 1975, Saffman, 1976]. Moreover, similar to many other diffusion models, the SD-model assumes that the membrane inclusion itself is much larger than the lateral extension of the lipids. Based on these assumptions, Saffmann and Delbrück derived an expression for the diffusion coefficient D of the membrane inclusion:

$$D = \frac{k_B T}{4\pi\eta_s}\Delta \tag{II.6}$$

Here, k_B is the Boltzmann constant, T is the temperature, and Δ is referred to as the

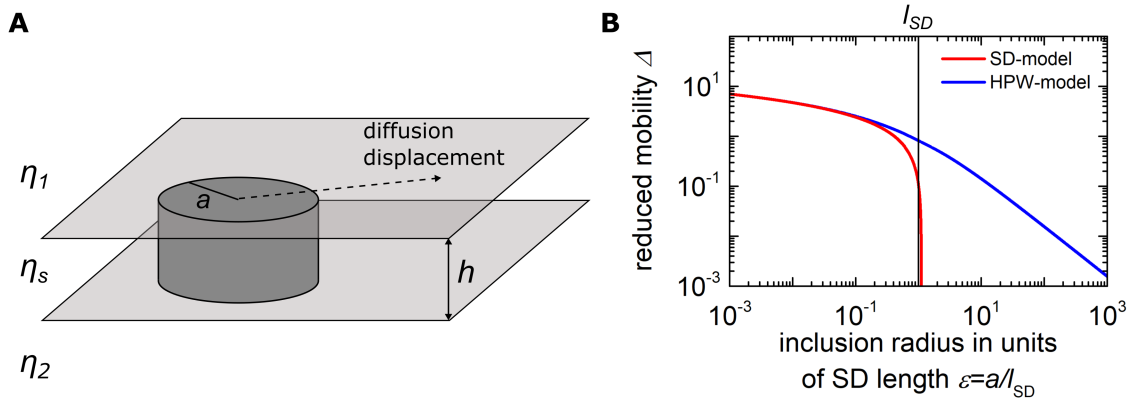

Figure II.1: Reduced mobilities of membrane inclusions according to Saffmann-Delbrück-model (SD-model) and Hughes-Pailthorpe-White-model (HPW-model). A) Conceptual basis: a cylindrical membrane inclusion with radius a diffuses freely in a 2D membrane of height h and surface viscosity η_s. The membrane is surrounded by two media of viscosity η_1 and η_2. B) For SD-model and HPW-model, the diffusion coefficient can be expressed as $D = \frac{k_B T}{4\pi\eta_s}\Delta$ [Saffman and Delbrück, 1975, Hughes et al., 1981, Petrov and Schwille, 2008b]. The reduced mobility Δ is identical for both models for inclusion sizes a much smaller than the Saffmann-Delbrück length l_{SD}. For $a \geq l_{\mathrm{SD}}$ only the HPW-model holds true. The curve for the HPW-model is calculated according to [Petrov and Schwille, 2008b].

reduced mobility, which for the SD-model reads:

$$\Delta_{\mathrm{SD}} = \ln\left(\frac{2l_{\mathrm{SD}}}{a}\right) - \gamma \tag{II.7}$$

γ is the Euler constant and the Saffmann-Delbrück length $l_{\mathrm{SD}} = \frac{\eta_s}{\eta_1+\eta_2}$ is the characteristic length scale of the system. Equation II.7 still meets the dependence predicted by Sutherland, Einstein and Smoluchowski (equation II.4). The SD-model was developed for membrane inclusions much smaller than l_{SD}, and appears to hold for many proteins, as shown by several experimental and simulation studies [Peters and Cherry, 1982, Ramadurai et al., 2009, Weiß et al., 2013, Guigas and Weiss, 2006]. Moreover, Guigas and Weiss showed that hydrophobic mismatches between the transmembrane part and the membrane itself induce only small deviations from the SD-model [Guigas and Weiss, 2008]. Interestingly, in the appropriate regime $a \ll l_{\mathrm{SD}}$ the diffusion coefficient shows only a weak dependence on the inclusion size.

The applicability of the SD-model needs to be evaluated for each membrane inclusion, because the model assumes at all times that on the one hand the lipids are much smaller than the inclusion and on the other hand $a \ll l_{\mathrm{SD}}$. On the lower limit, contradicting results were reported. Weiß *et al.* and Ramadurai *et al.* presented experimental evidence that the SD-model holds for membrane inclusions as small as $a < 0.5\,\mathrm{nm}$ in black lipid membranes (BLMs) [Weiß et al., 2013] and giant unilamellar vesicles (GUVs) [Ramadurai et al., 2009]. In contrast, Kriegsmann *et al.* and Gambin *et al.* published evidence for a relation $D \propto a^{-1}$, in line with the Stokes-Einstein-Smoluchowski relation (equation II.5) [Kriegsmann et al., 2009, Gambin et al., 2006]. At the other extreme, when $a \ll l_{\mathrm{SD}}$ is violated, the SD-model fails (figure II.1B), as reported for the diffusion of large membrane domains [Cicuta et al., 2007, Petrov et al., 2012]. For such cases, Hughes, Pailthorpe, and White derived a general description [Hughes et al., 1981]. The HPW-model covers arbitrary inclusion sizes, as long as the lipids are much smaller. Unfortunately, the publication by Hughes, Pailthorpe, and White does not provide a closed-form expression for D, but an analytical solution featuring infinite series with sign-varying terms, rendering numerical calculations very challenging. Therefore, Petrov and Schwille derived an empirical expression for the reduced mobility Δ_{HPW}, which describes the numerical results of the HPW-model with small errors and matches the asymptotic expressions from the analytical theory [Petrov and Schwille, 2008b]. For practical reasons, their analytical expression is used in this work:

$$\begin{aligned} \Delta_{\mathrm{HPW}} = &\left(\ln\left(\frac{2l_{\mathrm{SD}}}{a}\right) - \gamma + \frac{4a}{\pi l_{\mathrm{SD}}} - \frac{a^2}{2l_{\mathrm{SD}}^2} \ln\left(\frac{2l_{\mathrm{SD}}}{a}\right)\right) \\ &\times \left(1 - \frac{a^3}{\pi l_{\mathrm{SD}}^3} \ln\left(\frac{2l_{\mathrm{SD}}}{a}\right) + \frac{c_1 \frac{a^{b_1}}{l_{\mathrm{SD}}^{b_1}}}{1 + c_2 \frac{a^{b_2}}{l_{\mathrm{SD}}^{b_2}}}\right)^{-1} \end{aligned} \tag{II.8}$$

The empirical parameters $c_1 = 0.73761$, $b_1 = 2.74819$, $a_2 = 0.52119$, and $b_2 = 0.51465$ were found to describe the HPW-model best. The dependence of Δ_{HPW} on a/l_{SD} is shown in figure II.1B. In the limiting case $a/l_{\mathrm{SD}} \ll 1$, the HPW-model reproduces the SD-model and thus Δ_{HPW} has only a weak logarithmic dependence on the inclusion size. For very large membrane inclusions, the reduced mobility shows a much stronger, inversely proportional relation to the ratio a/l_{SD} and the diffusion coefficient becomes independent of the membrane viscosity [Hughes et al., 1981].

To put these models into perspective, it is worth estimating the l_{SD} for typical scenarios. In this thesis, free-standing lipid membranes in the shape of GUVs and lipid monolayers are the predominantly used model membrane systems. The Saffmann-Delbrück length for a lipid bilayer with $\eta_1 = \eta_2 \approx 1\,\mathrm{mPa\,s}$ and $\eta_s \approx 5 \cdot 10^{-7}\,\mathrm{mPa\,s\,m}$ [Peters and Cherry, 1982, Waugh, 1982,Herold et al., 2010] is 250 nm. For the lipid monolayer, the surrounding media are water ($\eta_1 \approx 1\,\mathrm{mPa\,s}$) and air ($\eta_2 \approx 0$). For the surface viscosity of lipid monolayers values around $\eta_s \approx 1 \cdot 10^{-7}\,\mathrm{mPa\,s\,m}$ have been reported [Wilke et al., 2010, Sickert and Rondelez, 2003]. Consequently, the Saffmann-Delbrück length for a lipid monolayer is on the order of 100 nm.

II.1.1.4 Free area model (FA-model)

While the diffusion models presented so far, describe the diffusion of particles that are much larger than the surrounding solvent molecules, the free area model (FA-model) has been used previously to describe the diffusion of lipids within a membrane [Galla et al., 1979, Peters and Beck, 1983]. The FA-model in its first form was introduced by Cohen and Turnbull and assumes a three-dimensional liquid of hard spheres in which empty spaces statistically open up and allow for diffusional displacements [Cohen and Turnbull, 1959]. The statistically generated free volume is filled by a sphere, which itself leaves a void at its previous position. This description gave an explanation for the empirical exponential relation between viscosity and free volume V_f: $\eta \propto e^{1/V_f}$, which was previously described [Doolittle, 1951]. Macedo and Litovitz enriched the model by an activation term, which accounts for temperature dependencies [Macedo and Litovitz, 1965], and Galla and colleagues adapted the FA-model for two-dimensional systems [Galla et al., 1979], yielding the following relation:

$$D = D_0 \exp\left(-\gamma \frac{A_c}{\mathrm{MMA} - A_0}\right) \tag{II.9}$$

Here, D_0 is a prefactor, which is approximately the product of the molecular diameter, the gas kinetic velocity and a geometric factor. Moreover, A_0 is the van der Waals area of an individual lipid, mean molecular area (MMA) is the area that is on average available per individual molecule, A_c is a critical free area a blank space needs to have such that displacements become possible, and γ is a factor accounting for the overlap of free areas ($0.5 < \gamma < 1$).

II.1.2 Simple binding kinetics

Generally, in this study binding reactions of the type

$$\mathrm{A} + \mathrm{B} \underset{k_d}{\overset{k_a}{\rightleftharpoons}} C \tag{II.10}$$

are considered. Two reaction partners A and B transiently form the product C with association rate k_a (unit [1/M/s]) and dissociation rate k_d (unit [1/s]). In equilibrium, the respective mean concentrations A, B, and C do not change, which does not mean that no reactions happen any longer, but that the rate of production and decay of C become equivalent:

$$\frac{\mathrm{d}}{\mathrm{d}t}C = k_a AB - k_d C = 0 \tag{II.11}$$

The corresponding dissociation constant K_D can be expressed either via the kinetic rates, or the equilibrium concentrations, using the law of mass action.

$$K_D = \frac{AB}{C} = \frac{k_d}{k_a} \tag{II.12}$$

One approach to determine K_D is a titration experiment, in which the total concentration (bound and unbound form) of A (or B) is kept constant $A + C = \mathrm{const}$, and the concentration of C is measured depending on the concentration of B.

$$C = \frac{\overbrace{(A + C)}^{\mathrm{const}} B}{K_D + B} \tag{II.13}$$

Alternatively, K_D can be determined by measuring k_a and k_d. The latter approach provides more insights about the system, as it describes kinetic rates, which also apply out of equilibrium.

Here, the binding kinetics of a simple reaction, e.g. transient receptor-ligand interaction, were described mathematically. These considerations can be generalized to also describe cooperative binding (Hill equation) or multivalent receptors. This study, however, studies only systems with one-to-one kinetics.

II.2 Fluorescence microscopy

The research fields of fluorescence microscopy and fluorescence itself, have attracted significant attention over the past 100 years. As such, the acquired knowledge is massive. Therefore, this section focuses exclusively on the aspects that are relevant to this work. More comprehensive textbooks on fluorescence (e.g. [Lakowicz, 2006, Valeur and Berberan-Santos, 2012, Haken and Wolf, 2013, Demtröder, 2013]) and light microscopy (e.g. [Kubitscheck, 2017, Pawley, 2006, Price and Jerome, 2011, Verveer, 2015, Hof et al., 2004, Diaspro, 2010, Kapusta et al., 2015, Mondal and Diaspro, 2013, Tinnefeld et al., 2015, Engelborghs and Visser, 2014]) do review the common knowledge in more detail.

II.2.1 Fluorescence as a tool for life science applications

A process, in which a physical many-body system emits a photon upon a preceding collective excitation is termed luminescence. Here, the focus is on the fluorescence of molecules. In this process, a molecule is excited from its ground state S_0 by a photon, and subsequently relaxes back to its ground state by the emission of a fluorescence photon. A detailed description of all underlying dynamics involved in this many-body problem, clearly exceed the scope of this introduction. Here, important properties of fluorescence that make it a suitable tool for life science applications, shall be mentioned.

First, the emitted fluorescence is red-shifted with respect to the excitation, a property commonly referred to as Stokes shift. Thus, excitation and emission light can be spatially separated by appropriate dichroic mirrors. Moreover, fluorescence excitation and emission can be performed in the visible wavelength range, at photon energies low enough to have little to moderate destructive impact on biological structures, depending on the flux rates, yet at sufficiently short wavelengths to avoid the absorption by water molecules. The visible range is also compatible with high-performance optical components, making fluorescence accessible with sensitive light microscopy, which is minimally invasive and provides the option to image in native environments, e.g. *in vivo*. Moreover, fluorophores can be chosen such that their excitation and emission spectra are separated from the autofluorescence that is omnipresent in biological systems. Finally, fluorophores can be selectively attached to target molecules. This is realized either by chemical coupling or partitioning of synthetic fluorophores, or by genetically encoded fluorescent proteins that are fused to a target protein.

The process of excitation of a fluorophore typically takes femtoseconds, whereas the fluorescence lifetime is on the order of nanoseconds. Thus, in an ideal case with high excitation rates, a single fluorophore can theoretically emit photons at 1 GHz, providing sufficiently high signals for detection. In fact, together with sensitive detectors, fluorescence-based single-molecule detection can be performed routinely.

On the other hand, the use of fluorescent labels has a few disadvantages. First, the introduction of a non-native tag is an alteration to the system under study. Careful controls need to be performed to ensure that observed effects do not originate from the fluorescent label (compare e.g. [Swulius and Jensen, 2012, Margolin, 2012]). Second, the use of excitation light and fluorophores may cause photo-induced damages that are potentially caused by energy deposition in the system, and the generation of reactive singlet oxygen, which is linked to the triplet state of fluorophores [Davidson, 1979, Wilkinson et al., 1994, Eggeling et al., 1999].

II.2.2 Confocal microscopy

In chapters IV, V, and VI a confocal microscope [Minsky, 1957] is used. While the basic concept of this microscope is reasonably simple, the developments around it, the theoretical description, the multi-facetted applications, and the limitations can fill entire books, e.g. [Pawley, 2006, Paddock, 2014]. For this thesis, confocal imaging is merely an auxillary tool, but another key aspect of the confocal microscope is exploited, namely the small open detection volume, which is beneficial for FCS applications (compare section II.3) [Rigler et al., 1993, Eigen and Rigler, 1994]. A schematic of a confocal setup is shown in section II.3. The small observation volume is generated by coinciding, narrowly focused excitation and detection profiles. Out-of-focus light is efficiently rejected using a pinhole in the image plane of the detection pathway. When operating at the diffraction limit and using a high-numerical aperture (NA) objective (typically NA $\simeq 1.2$), the effective observation volumes are typically on the order of femtoliters. Consequently, for a fluorescent tracer concentration of 10 nM, on average only six particles are in the observation volume at a time.

II.2.3 Total Internal Reflection Fluorescence Microscopy

Widefield and confocal microscopy are valuable tools for the life sciences. However, their axial resolution is limited, because the optical point spread function (PSF) has a typical axial extent on the order of 1 µm. Total internal reflection fluorescence (TIRF) microscopy pro-

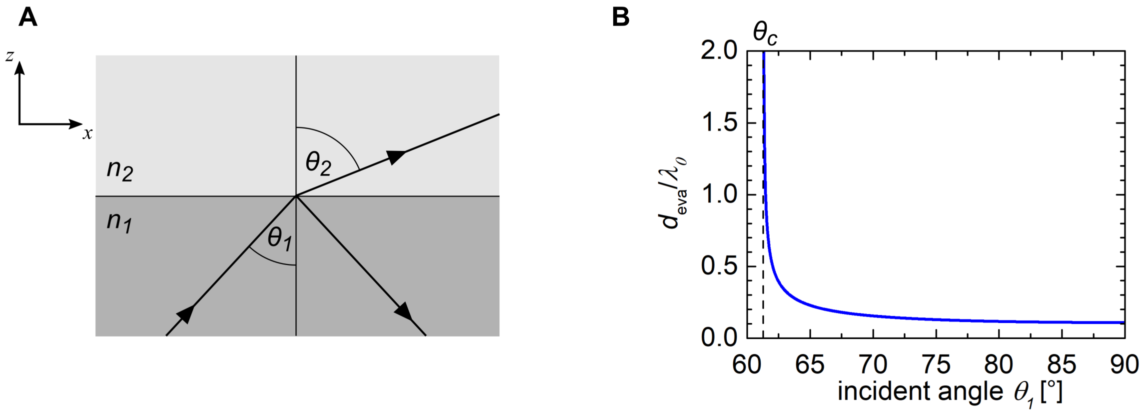

Figure II.2: Concept of total internal reflection. A) Refraction at a interface of two media with different refractive index. If $n_2 < n_1$, TIR occurs for incident angles θ_1 larger than the critical angle $\theta_c = \arcsin(n_2/n_1)$. B) Theoretical penetration depth d_{eva}, in units of the vacuum wavelength λ_0, according to equation II.17, assuming $n_1 = 1.52$ and $n_2 = 1.333$.

vides an alternative with an excitation that in theory decays exponentially within around 100 nm above a surface.

Total internal reflection (TIR) arises as a consequence of Snell's law, which describes the angle of refraction θ_2 for a light beam encountering a refractive interface.

$$n_1 \sin\theta_1 = n_2 \sin\theta_2 \tag{II.14}$$

Here, θ_1 is the incident angle, and n_1 and n_2 are the refractive indices of the two media, respectively (nomenclature as illustrated in figure II.2A). Above a critical incident angle $\theta_c = \arcsin(n_2/n_1)$, Snell's law yields $\sin\theta_2 > 1$, provided $n_2 < n_1$. In this regime, TIR occurs. On the other hand, Maxwell's equations require continuity of the fields across the interface. Considering plane waves $e^{i\vec{k}\vec{r}}$ with a wave vector $\vec{k}$, the transmitted wave vector k_t has a component $k_{t,z}$ normal to the interface (defined as z-direction), which becomes imaginary for TIR:

$$k_{t,z} = k_t \cos\theta_2 = k_t\sqrt{1 - \sin^2\theta_2} \overset{\theta_1 \geq \theta_c}{=} ik_t\sqrt{\sin^2\theta_2 - 1} \tag{II.15}$$

Applying the imaginary $k_{t,z}$ for a plane wave results not in a propagating, but an evanescent, exponentially decaying wave. The corresponding axial intensity profile reads:

$$I(z) = I_0 \exp\left(-\frac{z}{d_{\text{eva}}}\right) \tag{II.16}$$

$$d_{\text{eva}} = \frac{\lambda_0}{4\pi\sqrt{n_1^2 \sin^2\theta - n_2^2}} \tag{II.17}$$

In TIRF microscopy, this effect is exploited: An excitation laser beam is directed towards a coverslide-sample interface, where the sample typically has a refractive index similar to that of water. Consequently, TIRF microscopy selectively excites fluorophores close to the surface, as the evanescent wave decays exponentially away from the interface. Typically, d_{eva} is on the order of 100 nm. Thus, TIRF microscopy features a more confined observation volume in axial direction than confocal microscopy.

In practice, TIRF microscopy is typically performed using a prism-based [Axelrod, 1981] or an objective-based [Stout and Axelrod, 1989] approach. Applications of both have been reviewed elsewhere [Axelrod, 2001b, Fish, 2001, Toomre and Manstein, 2001]. For objective-type TIRF microscopy, the NA of the objective needs to be sufficiently large to achieve large incident angles θ_1. The theoretical minimum is NA $> n_1 \sin\theta_c = n_2$. However, in this extreme case, the incident beam may be partially clipped inside the objective. In practice, high-NA objectives with NA > 1.45 are typically used.

In TIRF microscopy, fluorescence is collected from dipole emitters close to a dielectric interface, e.g. a glass-water interface. Interestingly, the emission is distorted in such situations, resulting in a preferential emission towards the medium of higher refractive index. The angular emission profile also depends on the relative orientation of the dipole to the interface [Hellen and Axelrod, 1987, Enderlein et al., 1999, Enderlein, 2003, Enderlein and Ruckstuhl, 2005].

In this thesis, a custom-built TIRF microscope is presented (compare appendix A) and used in chapter III. This chapter also discusses further aspects of objective-based TIRF microscopy.

II.3 Fluorescence Correlation Spectroscopy

II.3.1 Information content of fluctuations

The study of complex systems by the observation of the response to an external perturbation is a common approach in the natural sciences. Prominent examples are pump-probe spectroscopy and concentration, pressure and temperature jump experiments. Typically, a system is driven out of equilibrium and its relaxation is observed by means of an appropriate read-out signal. An alternative approach, which does not require external perturbations, is the observation of fluctuations of a relevant quantity. Both approaches provide access to the same quantities and are related via the fluctuation-dissipation theorem [Kubo, 1966]. A famous example are the force dissipation by friction, and the random particle velocity due to Brownian motion. While the former is an effect observed in response to a non-equilibrium situation, the latter corresponds to fluctuations in equilibrium [Kubo, 1966]. Both are linked via the Einstein-relation [Einstein, 1905] and describe similar properties of the system.

To analyze the fluctuations of a system, two requirements have to be met. First, the fluctuation typically tend to zero for an infinitely large system. To make fluctuations observable, the system needs to be reasonably small. Moreover, an appropriate read-out signal is required. In FCS, both requirements are met by recording the fluorescence signal from a small detection volume using low concentrations of emitters.

The majority of dynamics described in this work correspond to equilibrium fluctuations, except for triplet dynamics, which are the result of the external light-induced excitation to higher energy levels [Petrášek and Schwille, 2009].

II.3.2 Principle of FCS

FCS is an optical method in which a fluorescence signal is collected from an observation volume and computationally analyzed with respect to its fluctuations. The typical duration of an individual fluctuation, for example a burst in signal, is of particular interest and is assessed by computing an autocorrelation of the fluorescence signal trace. An analysis of the correlation function can potentially provide insights into the dynamics that govern the signal fluctuations.

In the 1970s, Magde, Elson and Webb conducted the pioneering research to establish FCS [Magde et al., 1972, Elson and Magde, 1974, Magde et al., 1974]. The major breakthrough of FCS happened 20 years later, when more sensitive hardware had become available, but more importantly, FCS was demonstrated in combination with confocal microscopy [Rigler et al., 1993, Eigen and Rigler, 1994]. The resulting single-molecule sensitivity made FCS an important method for research in the life sciences, photophysics, polymer physics and many other areas. The historical development and applications of FCS have been discussed in a plethora of reviews, e.g. [Thompson, 1999, Webb, 2001, Schwille, 2001, Hess et al., 2002, Widengren and Mets, 2002, Thompson et al., 2002, Bacia and Schwille, 2003, Vukojević et al., 2005, Gösch and Rigler, 2005, Bacia et al., 2006, Kahya and Schwille, 2006, Kim et al., 2007, Bacia and Schwille, 2007, Petrov and Schwille, 2008a, Petrášek and Schwille, 2009, Mütze et al., 2010a, Mütze et al., 2010b, Elson, 2011, Nguyen et al., 2012, Rigler and Elson, 2012, Ries and Schwille, 2012, Melo et al., 2011, Weidemann et al., 2014, Machán and Wohland, 2014, Woll, 2014, Papadakis et al., 2014, Rigler and Widengren, 2017].

Typically, signal fluctuations arise either from brightness fluctuations of the fluorescent particles, or from fluorescent particles leaving and entering the detection volume [Petrov and Schwille, 2008a]. In both cases, the timescale of these fluctuations is related to the underlying process. For example, once a fast diffusing fluorescent particle statistically enters the confocal volume, it will cause an increase in signal, and on average will need a certain amount of time to leave the detection volume again. Considering the same scenario for a slowly diffusing particle, the mean dwell time in the detection volume will be larger. Consequently, analyzing the time scale of the fluctuations is a means to infer properties of the sample. To extract quantitative data from FCS measurements, the acquired autocorrelation curves are typically fitted by an appropriate closed-form model function. The reconstruction of entire distributions of decay times from the experimental autocorrelation curve (e.g. [Livesey and Brochon, 1987, Nyeo and Chu, 1989, Langowski and Bryan, 1991, Sengupta et al., 2003]) is less common, as it is an ill-posed inverse problem [Petrov and Schwille, 2008a].

In principle, every dynamic that reflects in fluctuations of the fluorescence signal can be investigated by FCS, provided the system under investigation is in quasi-equilibrium. This includes for example diffusion [Elson and Magde, 1974, Magde et al., 1974] and active transport [Magde et al., 1978] through the detection volume, reversible binding to immobile structures [Michelman-Ribeiro et al., 2009], but also blinking dynamics of the fluorophore. The latter may be caused by a multitude of processes, such as triplet transitions [Widengren et al., 1995], photo-isomerizations [Widengren and Schwille, 2000], reversible protonations [Haupts et al., 1998, Widengren et al., 1999], and transient Förster resonance energy transfer (FRET) [Torres and Levitus, 2007].

II.3.3 Derivation of the autocorrelation function of freely diffusing particles

In this section, the autocorrelation function for free diffusion is derived. The derivations for other dynamic systems follow the same strategy, but other differential equations need to be solved accordingly (compare e.g. chapter III). A more detailed description has been presented by [Krichevsky and Bonnet, 2002]. In the next section, the result derived here will be used to obtain the corresponding autocorrelation function for confocal detection volumes.

II.3.3.1 General considerations

FCS is based on the analysis of a fluorescence signal trace $F(t)$ and the fluctuation $\delta F(t)$ around its temporal mean $\langle F \rangle$:

$$F(t) = \langle F \rangle + \delta F(t) \tag{II.18}$$

Signal fluctuations and their relaxation times can be assessed using the autocorrelation of the signal. This approach is also used in dynamic light scattering (DLS), in which the scattering signal is autocorrelated [Pecora, 2013]. Throughout this work, the autocorrelation function is defined as:

$$G(\tau) = \frac{\langle \delta F(t) \delta F(t+\tau) \rangle}{\langle F \rangle^2} \tag{II.19}$$

The fluorescence signal is typically expressed as:

$$F(t) = Q \int \mathrm{d}^3\vec{r}\, I(\vec{r}) c(\vec{r}, t) \tag{II.20}$$

$$\delta F(t) = Q \int \mathrm{d}^3\vec{r}\, I(\vec{r}) \delta c(\vec{r}, t) \tag{II.21}$$

Here, Q is the product of excitation crosssection, detection efficiency of the microscope and the fluorescence quantum yield. In other words, Q is a measure for the photon collection and is thus termed the brightness. Moreover, the detection volume $I(\vec{r})$ and the concentration of fluorescent particles $c(\vec{r}, t)$ were introduced. For a static detection volume, the concentration is the only quantity that changes over time. Moreover, equation II.20 assumes a linear relation between the excitation and the corresponding fluorescence response. Deviations from this relation are typically referred to as saturation effects and will be discussed later. In addition, this derivation restricts itself to quasi-ergodic equilibrium systems for which the time average is equivalent to an ensemble average over all micro states. Consequently, equation II.19 can be expressed through an ensemble average.

$$G(\tau) = \frac{1}{\langle c \rangle^2 \left(\int \mathrm{d}^3\vec{r}\, I(\vec{r}) \right)^2} \int \mathrm{d}^3\vec{r} \int \mathrm{d}^3\vec{r}\,' I(\vec{r}) \underbrace{\langle \delta c(\vec{r},t) \delta c(\vec{r}\,', t+\tau) \rangle}_{\Phi(\vec{r},\vec{r}\,',\tau)} I(\vec{r}\,') \tag{II.22}$$

This autocorrelation function is expressed as a function of the temporal correlation of concentrations $\Phi(\vec{r}, \vec{r}\,', \tau)$. Depending on the underlying dynamics, an appropriate differential equation needs to be solved, e.g. for pure diffusion in d dimensions, the diffusion equation II.1.

II.3.3.2 Solution for diffusion in 3D

As for the fluorescence, the concentration at every point in time can be expressed as the sum of its mean and a fluctuation term $c(\vec{r}, t) = \langle c \rangle + \delta c(\vec{r}, t)$. Thus, the diffusion equation in three dimensions reads:

$$\frac{\partial}{\partial t} \delta c(\vec{r}, t) = D \nabla^2 \delta c(\vec{r}, t) \tag{II.23}$$

This differential equation is conveniently turned into a differential equation of first order in time

$$\frac{\partial}{\partial t} \delta \tilde{c}(\vec{q}, t) = -D q^2 \delta \tilde{c}(\vec{q}, t) \tag{II.24}$$

using the Fourier transforms:

$$\delta c(\vec{r}, t) = (2\pi)^{-3/2} \int \mathrm{d}^3\vec{q}\, e^{-i\vec{q}\vec{r}} \delta \tilde{c}(\vec{q}, t) \tag{II.25}$$

$$\delta \tilde{c}(\vec{q}, t) = (2\pi)^{-3/2} \int \mathrm{d}^3\vec{r}\, e^{i\vec{q}\vec{r}} \delta c(\vec{r}, t) \tag{II.26}$$

The solution is a single exponential $\delta \tilde{c}(\vec{q}, t) = \delta \tilde{c}(\vec{q}, 0) e^{-Dq^2 t}$, with a prefactor that is obtained from a suitable initial condition. For $\tau = 0$, only particles that are in identical positions can be correlated, which is accounted for by a Dirac delta function $\delta(\vec{r} - \vec{r}\,')$. In addition, diffusion is a Poisson process, and hence variance and mean are identical $\mathrm{var}(c) = \langle (\delta c(\vec{r}, 0))^2 \rangle = \langle c \rangle$. Thus, the initial condition $\Phi(\vec{r}, \vec{r}\,', 0) = \langle c \rangle\, \delta(\vec{r} - \vec{r}\,')$ needs to be met. Consequently, the 3D concentration correlation function in an infinite volume reads:

$$\Phi(\vec{r}, \vec{r}', \tau) = \langle c \rangle \, (4\pi D\tau)^{-3/2} \; e^{-\frac{(\vec{r}-\vec{r}')^2}{4D\tau}} \tag{II.27}$$

For 1D and 2D diffusion, the concentration correlation function are similar. In general, all spatial dimensions separate, and the solution in d-dimensional space reads:

$$\Phi(\vec{r}, \vec{r}', \tau) = \langle c \rangle \, (4\pi D\tau)^{-d/2} \; \prod_{j=1}^{d} e^{-\frac{\left(x_j - x'_j\right)^2}{4D\tau}} \tag{II.28}$$

II.3.4 Confocal single-point FCS

II.3.4.1 Autocorrelation from 3D diffusion and calibration of the confocal volume

To be sensitive to fluctuations of the fluorescence signal, the number of particles that contribute should be low. Typically, not more than 1000 particles are observed at a time. Such low numbers of particles are achieved by two strategies: The concentration of fluorescent particles should be low, and at the same time, the signal is collected from only a small detection volume. In the majority of FCS applications, the latter is achieved by using a confocal microscope, in which the effective detection volume is typically on the order of 1 fL [Rigler et al., 1993, Eigen and Rigler, 1994].

For confocal FCS, the detection volume is commonly approximated by a 3D Gaussian with the lateral $1/e^2$-width w_{xy}, and its axial counterpart $w_z = S w_{xy}$. Both are linked by the structure parameter S, which is a measure for the elongation of the detection volume.

$$I(x, y, z) = I_0 \, e^{-2\frac{x^2+y^2}{w_{xy}^2}} \; e^{-2\frac{z^2}{w_z^2}} \tag{II.29}$$

The description of the detection volume by Gaussian functions simplifies equation II.22, which together with the equation II.27 turns into:

$$\begin{aligned} G(\tau) &= \left(\langle c \rangle \, \pi^{3/2} S w_{xy}^3 \right)^{-1} \left(1 + \frac{\tau}{\tau_D}\right)^{-1} \left(1 + \frac{\tau}{S^2 \tau_D}\right)^{-1/2} \\ &= N^{-1} \left(1 + \frac{\tau}{\tau_D}\right)^{-1} \left(1 + \frac{\tau}{S^2 \tau_D}\right)^{-1/2} \end{aligned} \tag{II.30}$$

This is the well-known autocorrelation function for 3D diffusion in confocal FCS measure-

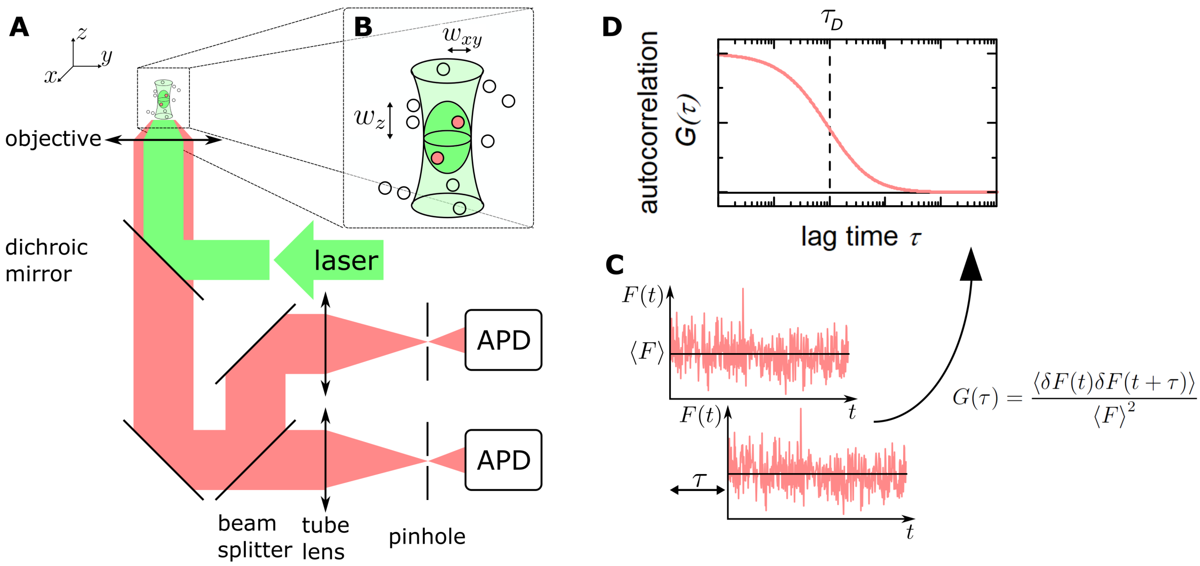

Figure II.3: Principle of confocal FCS. A) In confocal FCS, a collimated laser beam (green) is focused into a sample by an objective. Parts of the red-shifted fluorescence (red) emitted in response are collected by the same objective, spectrally separated from the excitation light and focused on an avalanche photodiode (APD). A 50:50 beam splitter enables pseudo-crosscorrelation. B) Schematic view of the confocal volume, which is typically described by a three-dimensional Gaussian with characteristic lateral (w_{xy}) and axial (w_z) widths. Fluorescent particles that are outside the confocal volume do not contribute to the detected signal. C) To compute the autocorrelation function, the acquired signals are first shifted by a lag time τ to each other. Subsequently, the time average of their product is calculated. This procedure is repeated for a set of lag times. D) The corresponding autocorrelation curve $G(\tau)$ is typically shown on a semilogarithmic scale and is, aside from some exceptions, a monotonically decaying function.

ments. Here, $G(\tau)$ is governed by three parameters: τ_D, N, and S, although in practice the dependence on the latter is only weak. These parameters may be obtained by fitting equation II.30 to an experimental autocorrelation curve.

The diffusion time τ_D is a key parameter of confocal FCS and is a measure for the mean dwell time of a fluorescent emitter in the detection volume.

$$\tau_D = \frac{w_{xy}^2}{4D} \tag{II.31}$$

If the confocal volume increases, or the diffusion coefficient decreases, the diffusion time increases accordingly. In practice, w_{xy} is determined by a confocal FCS calibration measurement. In detail, the diffusion time of freely diffusing fluorophores of known diffusion

Table II.1: Diffusion coefficients of fluorophores used for FCS calibrations. Reference diffusion coefficients in water at 25 °C. The diffusion coefficients at the experiment's temperature were calculated based on the Stokes-Einstein-Smoluchowski relation (equation II.4). The viscosities of water at the respective temperature were calculated based on an empirical equation by Kestin *et al.* [Kestin et al., 1978]. The diffusion coefficient for Alexa Fluor 546 was initially reported at 22.5 °C and was adjusted for 25 °C for this table.

fluorophore	D [µm^2/s] at 25 °C	reference
Alexa Fluor 488	414 ± 10	[Petrov et al., 2006]
ATTO488 carboxylic acid	405	this work, compare figure B.1
Alexa Fluor 546	364	[Petrášek and Schwille, 2008]
ATTO655 carboxylic acid	426 ± 8	[Dertinger et al., 2007]

coefficient is determined. The diffusion coefficients of the calibration fluorophores used in this study are shown in table II.1. These calibration measurements should be performed on a daily basis to be less sensitive to setup instabilities [Sherman et al., 2008]. Consequently, if w_{xy} is known, the diffusion times obtained from subsequent FCS experiments can be translated into the corresponding diffusion coefficients of the fluorescently labeled biomolecules of interest.

For small lag times $\tau \to 0$, the autocorrelation function converges to the inverse mean number of particles N^{-1} in the effective volume $V_{\text{eff}} = \pi^{3/2} S w_{xy}^3$ [Krichevsky and Bonnet, 2002, Rüttinger et al., 2007]. The amplitude of the autocorrelation function, i.e. N^{-1}, is typically a free fit parameter. Simultaneously, if w_{xy} and S are known, e.g. from a calibration measurement, N can be translated into the respective concentration $\langle c \rangle$.

II.3.4.2 Autocorrelation function for selected processes

In many confocal FCS measurements, the autocorrelation curve is not, or not exclusively governed by diffusion processes. A detailed derivation of the corresponding autocorrelation functions exceeds the scope of this introduction, but the derivations follow the same strategy as presented here for 3D diffusion [Krichevsky and Bonnet, 2002]. A summary of selected functions is provided in table II.2.

The single-focus, single-photon excitation approach discussed here is the predominant form of FCS, supposedly because several vendors provide commercial equipment for such experiments. It should be noted that over the past 20 years, many improvements and alterations to the standard confocal FCS approach have been proposed. This includes the introduction of fluorescence cross-correlation spectroscopy (FCCS), by which the in-

Table II.2: Analytical autocorrelation functions for confocal FCS. Examples of autocorrelation model functions that are frequently used in confocal FCS. The table covers free diffusion in 2D and 3D (models 2D, 3D) with and without a blinking dynamic of an individual fluorophore, e.g. triplet blinking (2D+T, 3D+T), the independent diffusion of C different species (3DC), and the diffusion with additional binding in a reaction-dominant system ($\tau_D \ll k_{\mathrm{on}}^{-1}$, 3D+binding). The model 3D+3D corresponds to the diffusion of two components of identical brightness ($Q_1 = Q_2$), and is thus a special case of the more general model 3DC. For details, compare e.g. [Krichevsky and Bonnet, 2002, Michelman-Ribeiro et al., 2009].

model	autocorrelation function	
2D	$G_{\mathrm{2D}}(\tau) = N^{-1}(1+\frac{\tau}{\tau_D})^{-1}$	(II.32)
2D+T	$G_{\mathrm{2D+T}}(\tau) = \left[1+\frac{T}{1-T}\exp\left(-\frac{\tau}{\tau_{\mathrm{T}}}\right)\right] G_{\mathrm{2D}}(\tau)$	(II.33)
3D	$G_{\mathrm{3D}}(\tau) = N^{-1}(1+\frac{\tau}{\tau_D})^{-1}(1+\frac{\tau}{S^2\tau_D})^{-1/2}$	(II.34)
3D+T	$G_{\mathrm{3D+T}}(\tau) = \left[1+\frac{T}{1-T}\exp\left(-\frac{\tau}{\tau_{\mathrm{T}}}\right)\right] G_{\mathrm{3D}}(\tau)$	(II.35)
3D+3D	$G_{\mathrm{3D+3D}}(\tau) = (N_1+N_2)^{-2}\sum_{j=1}^{2}\left[N_j(1+\frac{\tau}{\tau_{D,j}})^{-1}(1+\frac{\tau}{S^2\tau_{D,j}})^{-1/2}\right]$	(II.36)
3DC	$G_{\mathrm{3DC}}(\tau) = \left(\sum_{k=1}^{C} Q_k N_k\right)^{-2}\sum_{j=1}^{C} Q_j^2 N_j^2 G_{\mathrm{3D},j}(\tau)$	(II.37)
3D+binding $\tau_D \ll k_{\mathrm{on}}^{-1}$	$G_{\mathrm{3D+binding}}(\tau) = \frac{k_{\mathrm{off}}}{k_{\mathrm{on}}+k_{\mathrm{off}}} G_{\mathrm{3D}}(\tau) + N^{-1}\frac{k_{\mathrm{on}}}{k_{\mathrm{on}}+k_{\mathrm{off}}}\exp\left(-k_{\mathrm{off}}\tau\right)$	(II.38)

teraction of spectrally distinct species can be studied [Rička and Binkert, 1989, Schwille et al., 1997]. Other important developments were the introduction of two-photon FCS and FCCS [Berland et al., 1995, Heinze et al., 2000], scanning FCS [Berland et al., 1996, Ries and Schwille, 2006, Petrášek and Schwille, 2008], two-focus FCS [Brinkmeier et al., 1999, Dertinger et al., 2007], pulsed-interleaved excitation FCCS [Müller et al., 2005], and stimulated emission depletion (STED)-FCS [Kastrup et al., 2005, Eggeling et al., 2008].

II.3.4.3 Limitations of confocal FCS

FCS is a powerful method within its limitations. To obtain reliable results from confocal FCS, a range of factors, which will be briefly mentioned in the following, should be taken into account. Many of the effects described here, were also extensively discussed by Enderlein *et al.* [Enderlein et al., 2004, Enderlein et al., 2005, Gregor et al., 2005], and Petrov

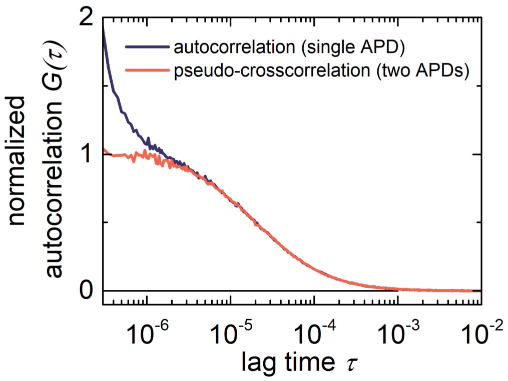

Figure II.4: Effect of afterpulsing in confocal FCS. Normalized experimental autocorrelation curve of ATTO488 carboxylic acid computed from single detectors (purple) and the cross-correlation of both (red). The measurements were taken in a low excitation irradiance ($I_0/2 = 0.05\,\mathrm{kW/cm^2}$ at 488 nm) regime where the triplet contribution can be neglected. For lag times above $\sim$3 µs both correlation curves become indistinguishable. At shorter time scales, however, afterpulsing adds a contribution to the autocorrelation curve.

and Schwille [Petrov and Schwille, 2008a]. Refractive index mismatches are not addressed in this section, but are subject to a detailed study in chapter IV.

Detector artifacts FCS experiments are commonly performed using APDs as detectors. Upon detection of a photon, these detectors feature a short dead time, on the order of 100 ns, during which no further photons can be detected. Consequently, at high photon count rates, typically above 1 MHz, the response of the APD becomes nonlinear. In essence, a doubling of the incoming photons does not result in a doubling of the detected events. The dead time limits not only the detector's time resolution, but also result in distortions of the autocorrelation curve [Schätzel, 1986], especially on the time scales of the dead time.

The more dramatic effect of APDs on the autocorrelation function is caused by afterpulsing, which in itself is correlated and thus shows as a contribution to the autocorrelation curve. This contribution typically decays on the sub-µs to µs time scale. Consequently, experiments on systems that show dynamics on this time scale, e.g. triplet dynamics [Widengren et al., 1995], or diffusion of small organic fluorophores through diffraction limited detection volumes, are effected by detector afterpulsing (figure II.4). The magnitude and decay time of the afterpusling contribution depend on the count rate and the detector characteristics.

In this work, the contribution of APD afterpulsing in confocal FCS is circumvented by a pseudo-crosscorrelation approach (figure II.3) [Burstyn and Sengers, 1983]. In brief, the fluorescence signal is split by a 50:50 beamsplitter and directed onto two independent APDs. The crosscorrelation of the signal from both detectors eliminates the contribution from afterpulsing, as the afterpulsing events from both detectors are not correlated. It should be noted, however, that the afterpulsing events still add as an uncorrelated background to the signal, which affects the amplitude of the autocorrelation curve. Atlernatively, the afterpulsing may be characterized by measuring the autocorrelation from a stable, uncorrelated light source at different count rates [Zhao et al., 2003]. Typically, a bi-exponential describes such experimental data sets well.

Measurement duration The computed autocorrelation curve is a biased estimator of the true autocorrelation [Oliver, 1979, Schätzel, 1987]. This bias becomes irrelevant for sufficiently long measurements. Too short measurements, on the other hand, result in a systematic underestimation of the diffusion time. For 3D diffusion in confocal FCS experiments, the measurement time should be around 10^3–10^4 times longer than τ_D [Tcherniak et al., 2009], depending on the required accuracy. It should be noted that this effect also depends on the shape of the autocorrelation curve. An example is discussed in detail in chapter III (figure III.6).

Gaussian shape of the detection volume The description of the detection volume by a 3D Gaussian is the predominant approach in confocal FCS. Although it is only a rough approximation, the effect on the outcome of confocal FCS measurements on probes diffusing in 3D is, compared to using the full model, typically negligible [Petrov and Schwille, 2008a]. The deviations of the autocorrelation curve depending on the precise shape of the confocal volume have been addressed before [Hess et al., 2002, Enderlein et al., 2005]. Alternatively proposed model functions for the shape of the detection volume typically include a Lorentzian [Dertinger et al., 2007]. In addition, several other effects may cause distortions of the detection volume. This includes e.g. astigmatism and refractive index mismatches [Enderlein et al., 2005].

Coverslide thickness The quality of the coverslide is a key parameter for accurate FCS measurements. Both, the diffusion time and the particle number are biased towards larger values with increasing coverslide thickness deviations. Importantly, deviations of around 10 µm may already have a considerable effect [Enderlein et al., 2005, Mütze et al., 2010b].

Consequently, the coverslides used for confocal FCS should have identical thicknesses across one batch, such that the detection volume does not change between several samples. Moreover, the coverslide thickness should not change across individual coverslides. This ensures that measurements are independent of the lateral position of the detection volume.

Optical saturation and photobleaching The derivation of the autocorrelation function assumes a linear dependence between the excitation and the emitted fluorescence. In case of optical saturation, this assumption is violated. Upon excitation, the fluorophores are not available for another excitation until they return to the ground state. Thus, at sufficiently high irradiances, a doubling of the excitation rate does not result in a doubling of the emitted photons anymore. This effect can already be observed in a simple two-state system (S_0, S_1) [Paddock, 2014], but occurs already at lower irradiances when a long-lived dark state, e.g. the triplet state, is involved [Widengren et al., 1994, Enderlein et al., 2005]. As a result, the detection profile effectively widens, resulting in overestimated diffusion times and particle numbers (compare figure B.2 in appendix B.2) [Widengren et al., 1994, Enderlein et al., 2005, Gregor et al., 2005, Petrov and Schwille, 2008a].

Photobleaching, on the other hand, has an opposite effect. When fluorophores bleach before leaving the detection volume, their diffusion time is underestimated [Widengren and Rigler, 1996]. Moreover, if the bleaching rate is larger than the rate by which fluorophores are replenished, the effectively measured particle number becomes smaller. As photobleaching and optical saturation have opposite effects on the outcome of confocal FCS experiments, their contributions can typically not be disentangled. Ideally, a power series should be performed for every system to identify the optimum regime of maximum photon count rate without the effect of photo-induced artifacts (compare figure B.2 in appendix B.2) [Petrov and Schwille, 2008a].

Uncorrelated background A collected fluorescence signal F always has a background contribution B, e.g. detector dark counts or afterpulsing-related counts. As long as B is uncorrelated, the decay of the autocorrelation curve is not affected. However, B decreases the correlation amplitude, leading to an overestimation of the particle number and thus the concentration. This effect becomes more dramatic, the larger the contribution of background to the total signal. However, a simple analysis yields that the autocorrelation curve of interest $G(\tau)$ can be recovered from the measured autocorrelation curve $G_{\mathrm{meas}}(\tau)$

if $\langle B \rangle$ is known, e.g. from a reference measurement [Thompson, 1999].

$$G_{\text{meas}}(\tau) = \frac{\langle (\delta F(\tau) + \delta B(\tau)) (\delta F(t+\tau) + \delta B(t+\tau)) \rangle}{\langle (F(t) + B(t)) \rangle^2} \tag{II.39}$$

$$G(\tau) = G_{\text{meas}}(\tau) \frac{\langle F \rangle^2}{(\langle F \rangle - \langle B \rangle)^2} \tag{II.40}$$

Correlated background Following the same reasoning as for uncorrelated background, a correction to the autocorrelation curve may be applied for correlated background. This step is, however, more severe and correlated background should be avoided by all means.

$$G(\tau) = G_{\text{meas}}(\tau) \frac{\langle F \rangle^2}{(\langle F \rangle - \langle B \rangle)^2} - G_B(\tau) \frac{\langle B \rangle^2}{(\langle F \rangle - \langle B \rangle)^2} \tag{II.41}$$

For this correction, the autocorrelation curve G_B of the background needs to be determined under identical conditions as the measurement of G_{meas}.

Estimation of concentrations As highlighted in equation II.30, a confocal FCS measurement on particles freely diffusing in 3D can provide access to the concentration of these particles via the amplitude of the correlation function $G(\tau \to 0) = N^{-1} = \left(\langle c \rangle \pi^{3/2} S w_{xy}^3 \right)^{-1}$. While this is theoretically possible, it should be noted that the autocorrelation function depends only very weakly on the structure parameter S, as illustrated in figure II.5. Consequently, the determination of S from the autocorrelation curve requires very low noise levels and a sufficiently small S. For values $S \gtrsim 10$, the correlation curve becomes virtually insensitive to S. Under these conditions, the detection volume approaches a Gaussian cylinder, and lateral diffusion becomes the only route for particle entry and exit. Consequently, precise determinations of S are challenging, which directly reflects on the relative error of the estimated concentration. Similarly, w_{xy} is determined with limited accuracy, but contributes to $\langle c \rangle$ to the third power. The determination of w_{xy} with a relative error of 5% and S with a relative error of 10% is under ideal conditions typically possible, but requires long and accurate measurement. Assuming these relative errors, they propagate to an error of 25% on $\langle c \rangle$. In practice, the situation may be even worse, because N also contributes to the error, and the aforementioned artifacts caused by e.g. refractive index mismatch and astigmatism may add an additional bias.

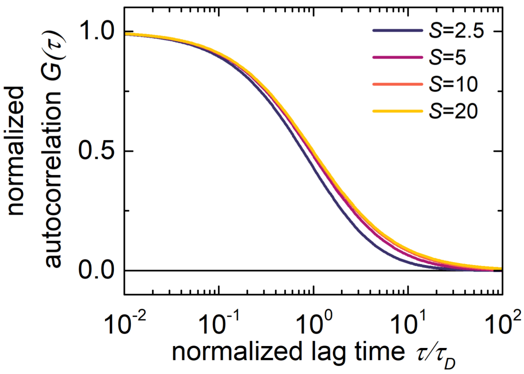

Figure II.5: Confocal FCS depends only weakly on the structure parameter. Theoretical normalized autocorrelation functions for 3D diffusion (equation II.34). The lag time is normalized to the common value of τ_D. The autocorrelation curves show only a weak dependence on the structure parameter S, and become virtually independent for $S \gtrsim 10$.

II.3.4.4 Confocal FCS on lipid membranes

For the study of diffusion in lipid membranes by FCS [Schwille et al., 1999], measurements are typically performed on planar (cell membranes, supported lipid bilayers (SLBs), lipid monolayers) or quasi-planar (GUVs) membranes, which are oriented normal to the optical axis (for reviews see [Kahya and Schwille, 2006, Machán and Hof, 2010]). The confocal volume is positioned on the membrane, such that maximum counts per particle (cpp) is achieved.

Importantly, the diffusion in the membrane is restricted to two dimensions. Consequently, the autocorrelation (equation II.32) decays slower than for 3D diffusion, as the lower dimensionality results in the loss of an exit direction. Moreover, membranes are typically considerably more viscous than aqueous media, resulting in considerably larger diffusion times.

As a follow-up to the limitations of FCS discussed above, the effect of defocused membranes on the outcome of FCS measurements needs to be briefly mentioned, as it is also for relevance for the measurements shown in chapter VI. When measuring confocal FCS on planar membranes, which are oriented perpendicular to the optical axis, the confocal volume needs to be positioned accurately. For a laser focus below or above the membrane, the cross-section of excitation and membrane increases, resulting in larger diffusion times and particles numbers, and lower cpp. To avoid this potential error source, z-scan FCS was introduced [Benda et al., 2003]. On the other hand, if the confocal volume is always precisely positioned on the membrane, conventional confocal FCS and z-scan FCS yield identical results, as expected [Heinemann et al., 2012].

II.3.4.5 Binding studies by confocal FCS

The key to binding studies by confocal single-color FCS is that under ideal conditions, two populations can be distinguished by their diffusion times and their stoichiometry can be determined, as indicated by equations II.36 (3D+3D model) and II.37 (3DC model). In fact, this approach performs best if a small, fluorescently labeled molecule binds to a much larger partner, such that the diffusion times of both states are clearly separated and the bound fraction can be inferred from the relative amplitudes of both components in the autocorrelation curve. Ideally, all diffusion times are determined individually, and the relative brightnesses of both species should be known [Meseth et al., 1999]. Moreover, the kinetics of binding and unbinding need to be slow compared to the diffusion time. Based on the stoichiometry accessible by FCS, many binding studies have been conducted, including hybridization of deoxyribonucleic acid (DNA) with DNA [Kinjo and Rigler, 1995] and ribonucleic acid (RNA) [Schwille et al., 1996], and the binding to lipid vesicles [Dorn et al., 1998].

This single-color approach requires considerable changes in diffusion coefficient upon binding. FCCS elegantly circumvents this limitation by labeling both reaction partners with spectrally distinct fluorophores and recording their respective fluorescence time traces [Schwille et al., 1997]. Interacting particles contribute to the cross-correlation amplitude, computed from both individual time traces.

The described studies provide access to the K_D via stoichiometric FCS or FCCS measurements. This is the predominant approach to binding studies by FCS. However, for the case of diffusion and binding to an immobile structure, recent studies also extracted kinetic rates from confocal FCS measurements [Michelman-Ribeiro et al., 2009, Bierbaum and Bastiaens, 2013].

III

QUANTIFICATION OF BINDING RATES BY SURFACE-INTEGRATED FLUORESCENCE CORRELATION SPECTROSCOPY

The results presented in this chapter are the outcomes of an equal-contribution collaboration with Philipp Blumhardt and have been previously published as:

Mücksch, J., Blumhardt, P.*, Strauss, M. T., Petrov., E. P., Jungmann, R., Schwille, P. (2018), Quantifying reversible surface binding via surface-integrated FCS. Nano Lett., 18(5): 3185-3192, doi: 10.1021/acs.nanolett.8b00875. *indicates equal contributions. A reprint permission has been granted by the publisher.*

Section III.4 is based on Christian Niederauer's Master's thesis, which was jointly supervised by Philipp Blumhardt and myself.

III.1 Introduction

The binding and partitioning of proteins to biologically relevant surfaces, especially to membranes, is of key importance for the function and control of cellular processes. An all-embracing understanding of such processes requires precise and accurate quantitative values of the association and dissociation rates. Thus, an accurate determination of surface binding rates and affinities is of great interest for basic research on cells and organisms, but also for biotechnological applications, often targeted towards creating and characterizing new efficient receptor ligands.

III.1.1 Demands on a method that quantifies surface binding

Many techniques have been released for the specific task of measuring surface affinities such as bio-layer interferometry (BLI) [Wallner et al., 2013,Frenzel and Willbold, 2014,Shah and Duncan, 2014], confocal FCS and FCCS [Magde et al., 1972,Eigen and Rigler, 1994,Schwille et al., 1997], imaging single-molecule binding events [Zhuang, 2005,Ditzler et al., 2007,Walter et al., 2008, Elenko et al., 2010], isothermal titration calorimetry (ITC) [Velazquez-Campoy and Freire, 2006, Freyer and Lewis, 2008, Ghai et al., 2012, Swamy and Sankhala, 2013, Velazquez-Campoy et al., 2015], microscale thermophoresis (MST) [Wienken et al., 2010, Jerabek-Willemsen et al., 2011, Jerabek-Willemsen et al., 2014], quartz crystal microbalance (QCM) [Dixon, 2008, Speight and Cooper, 2012, Nielsen and Otzen, 2013, Cho et al., 2010], potentially also with dissipation analysis, surface plasmon resonance (SPR) [Beseničar et al., 2006, Kooyman et al., 2008, Hodnik and Anderluh, 2013, Nguyen et al., 2015, Singh, 2016], switchSENSE® [Rant, 2012], and quantitative spectrophotometry and spectrofluorometry [Loura et al., 2003, Valeur and Berberan-Santos, 2012, Matos et al., 2010]. This list is far from exhaustive, and illustrates the unabated need for new methods to quantify binding dynamics.

For the study of membrane binding kinetics, the method of choice in principle strongly depends on the studied system and the parameters of interest. In the ideal case, the following conditions are met:

(i) minute sample volumes

(ii) applicability to surface binding processes

(iii) measurements in unperturbed equilibrium systems

(iv) specificity to perform in complex bio-fluids or live cells

(v) option to validate the membrane integrity

(vi) accessibility of not only binding affinities, but also binding rates

(vii) resolution of a wide range of kinetic rates, ideally from $1\,\mu s^{-1}$ to $1\,h^{-1}$

It should be mentioned that from a practical point of view, even more factors, such as measurement duration, passivation against unspecific binding, ease of use, unambiguous data analysis, costs of individual measurements, and the cost of acquiring the instrument play an important role. Despite the manifold of available techniques, all of them fall short of at least one of the aforementioned requirements. As an example, SPR and QCM, both frequently used tools to quantify surface binding rates, perform for perturbed systems relaxing into equilibrium. Especially SPR has become one of the most popular methods to quantify binding kinetics. Typically, in these experiments ligand is flushed into the sample chamber, upon which the number of bound ligands increases over time and eventually saturates. Similarly, upon constant buffer flow without any new ligands coming in, the bound ligand detaches and the read-out signal ideally goes back to its initial level. The characteristic times to reach these final levels are a measure for the association and dissociation rates, k_a and k_d, respectively. Clearly, such measurements are the response to a jump in ligand concentration, and are not performed in quasi-steady state, when the numbers of forward and backward reactions are more or less equilibrated and most binding sites feature a constant turnover of binders. On the other hand, this situation is physiologically most relevant, as it is frequently found in cellular environments. In other words, direct access to the rates of reversible surface binding in unperturbed, native systems has so far hardly been possible. From a historical point of view, the step to measure in equilibrated instead of perturbed systems is similar to the roots of FCS. Back then, the introduction of FCS provided an alternative to the observation of relaxations upon external pumping of a system, which was for instance done by temperature jump experiments [De Maeyer, 1960, Strehlow, 1972, Rigler and Widengren, 2017].

III.1.2 Review of previous TIR-FCS studies

For the desired method that meets the aforementioned conditions, total internal reflection fluorescence correlation spectroscopy (TIR-FCS) [Thompson et al., 1981, Thompson and Axelrod, 1983] is a propitious approach [Schwille, 2003]. On the one hand, FCS is an equilibrium method, which extracts a characteristic correlation time for quasi-ergodic fluctuating systems. Moreover, its maximum temporal resolution is only limited by the detector and the photon count rate. On the other hand, the use of TIRF microscopy provides improved surface selectivity compared to confocal FCS, as the evanescent field exponentially decays on the length scale of 100 nm away from the surface. Moreover, as a byproduct, a fluorescent tag provides a high specificity for the labeled ligand in potentially complex and diverse bio-fluids, and the quality of the surface, e.g. the membrane, can be validated by complementary imaging in a spectrally distinct channel.

The combination of FCS with TIR excitation has been first proposed by Thompson and colleagues in 1981 [Thompson et al., 1981]. During the following almost 25 years, TIR-FCS was rarely exploited and exclusively used on prism-type TIRF system in combination with photomultipliers for detection. A very limited number of studies addressed unspecific binding of immunoglobulin G (IgG) and insulin to serum albumin-coated surfaces [Thompson and Axelrod, 1983], fluorophores to C-18 modified silica surfaces [Hansen and Harris, 1998a, Hansen and Harris, 1998b], and several polyamidoamine dendrimers to silica surfaces [McCain et al., 2004a]. In addition, the diffusion of IgG above SLBs [Starr and Thompson, 2002], rhodamine 6G in sol-gel films [McCain and Harris, 2003], polyamidoamine dendrimers of variable sizes in sol-gel films and aqueous buffer [McCain and Harris, 2003, McCain et al., 2004b], polystyrene beads in water [Kyoung and Sheets, 2006], and vesicles above an SLB [Kyoung and Sheets, 2008] were measured by TIR-FCS. Many of these studies relied on the assumption of a single exponential shape of the axial excitation profile with a penetration depth d_{eva} that was estimated based on a rough measurement of the angle under which the excitation beam left the objective. Turning this argumentation around, Harlepp *et al.* measured the autocorrelation function of a fluorophore of known diffusion coefficient and extracted d_{eva} [Harlepp et al., 2004].

The concept of TIR-FCS was not only proposed by Nancy Thompson [Thompson et al., 1981], but considerable theoretical work was invested by her group towards TIR-FCS and the study of reversible binding [Thompson et al., 1981, Lagerholm and Thompson, 1998, Lagerholm and Thompson, 2000, Starr and Thompson, 2001]. In 2003, Lieto and colleagues build up on this work and reported for the first time dissociation rates for reversible receptor-ligand interactions measured by TIR-FCS [Lieto et al., 2003]. In detail, the reversible binding of a fluorescently-labeled monoclonal IgG with surface-bound mouse Fcγ RII receptor was studied.

The major breakthrough towards the availability of TIR-FCS to a broader community was achieved by switching from prism-type to objective-type TIRF microscopes [Stout and Axelrod, 1989, Axelrod, 2001a], an option that became available with the advent of high-NA objectives. Typically, objectives with NA > 1.4 are used. The combination of objective-type TIRF and FCS with photon-counting point detectors is in theory compatible with commercial setups [Yordanov et al., 2011], or only requires the placement of a multimode fiber for detection on one of the microscopes camera ports. Moreover, it features full sample accessibility on an inverted microscope, and was first demonstrated in a range of studies by the group of Theo Lasser [Anhut et al., 2005, Hassler et al., 2005a, Hassler et al., 2005b], including a proof-of-principle study of TIR-FCCS [Leutenegger et al., 2006]. In a range of other communications, objective-type TIR-FCS with point-detectors was applied to study lateral diffusion in membranes *in vivo* [Ohsugi et al., 2006], triplet blinking close to dielectric interfaces [Blom et al., 2009], flow above a surface [Schmitz et al., 2011], and the effect of surfactant on the unspecific binding of bovine serum albumin (BSA) and lipase (*Thermomyces lanuginosus*) to C18-modified silica surfaces [Sonesson et al., 2008]. Moreover, modifications of regular objective-type TIR-FCS with point-detection, ranging from pulsed excitation with a time correlated single photon counting (TCSPC) unit [Weger and Hoffmann-Jacobsen, 2017], to interfering evanescent waves [Otosu and Yamaguchi, 2017], and an advanced combination of STED with TIR-FCS [Leutenegger et al., 2012], were reported. Despite the increased interest on TIR-FCS upon introduction of objective-type TIRF microscopes, to the best of our knowledge only one published study investigated kinetic rates. Namely, Hassler and colleagues addressed the enzyme kinetics of surface-immobilized horseradish peroxidase [Hassler et al., 2007].

Very shortly after the introduction of objective-type TIR-FCS, the group of Thorsten Wohland introduced electron-multiplying charge-coupled device (EMCCD) camera detection instead of point detectors [Kannan et al., 2007]. The massive parallel detection boosts the multiplexing by exploiting the widefield excitation in TIRF microscopy, but comes at the cost of lower time resolution, and to date still lower quantum yield of the detector, compared to point-detectors. In detail, the integrated signals from a set of region of interests (ROIs) are autocorrelated to sample the local dynamics. Thus, this approach has the potential to resolve maps of dynamics. Moreover, as the ROIs are defined during post-processing, their size can be systematically varied, based on which Bag *et al.* elegantly circumvented the need for calibration measurements before 2D diffusion measurements in SLBs [Bag et al., 2012]. To date, the potential of camera-based TIR-FCS was demonstrated in several studies [Guo et al., 2008, Sankaran et al., 2009, Bag et al., 2012, Lim et al., 2013, Bag et al., 2014, Huang et al., 2015]. It should be noted that in our view camera-based TIR-FCS is conceptually identical to the differently termed methods binned imaging FCS (bimFCS) [Lim et al., 2013, Huang et al., 2015], and temporal image correlation spectroscopy (TICS) using TIRF microscopy [Wiseman, 2013, Wiseman, 2015]. Camera-based TIR-FCS has developed into an powerful tool to measure lateral membrane diffusion, but except for the reported k_d for doublecortin from surface immobilized microtubules [Brandão et al., 2014] has not been employed to study binding kinetics.

The mathematical description of a ligand-receptor system is highly complex, and to our knowledge no analytical solution to the coupled diffusion-reactions equations has been found. In many cases, the measured autocorrelation curve may be governed by 3D ligand diffusion, 2D receptor diffusion, reversible binding, and potentially photophysics [Thompson et al., 1981]. The situation becomes even more complicated when all optical effects, i.e. supercritical angle fluorescence (SAF), correct shape of the lateral and axial detection profile are fully taken into account [Ries et al., 2008a]. Thompson *et al.* compiled a guide for successful TIR-FCS to navigate through the manifold of parameters that influence TIR-FCS measurements [Thompson et al., 2011]. Taken together, more than 30 years after the first demonstration of TIR-FCS, the method has developed into a useful tool to characterize lateral membrane diffusion, but has been hardly used to measure reversible binding rates.

III.1.3 Concept of SI-FCS

As discussed, the analysis of TIR-FCS, especially with binding and diffusion contributions, is highly complex. On the other hand, the major difficulty comes from the contributions of lateral and axial ligand diffusion, which are not of particular interest when the focus is on the determination of binding rates. Based on this realization, this work introduces surface-integrated FCS (SI-FCS) in which a spatially integrated signal recorded from a surface is subject to an autocorrelation analysis. To validate this approach, the reversible hybridization of short single-stranded DNA (ssDNA) to the surface-immobilized complementary strands is characterized (figure III.1A).

Considering a fluorescently labeled ligand diffusing above a surface to which it binds occasionally, information about the binding kinetics can be only extracted if there are means to distinguish the signals of bound and unbound states. In the easiest case, the unbound state does not contribute to the fluctuating signal, which can be for instance achieved by FRET between receptor and ligand [Auer et al., 2017]. Alternatively, the change of second harmonic signal [Sly et al., 2013, Sly and Conboy, 2014] or fluorescence lifetime upon binding may be analyzed. However, the latter two options are typically incompatible with widefield illumination and massive parallel detection on a camera and can thus not sample many locations in parallel. In this work, bound and unbound state are distinguished by the timescale on which the correlation is lost. We study binding kinetics that are much slower than the 3D diffusion through the detection volume, i.e. occur on time scales on which diffusion is equilibrated. Hence, as long as no diffusion occurs on the surface, diffusion is not relevant to this chapter, which means that SI-FCS is calibration free and the area of the surface over which the integration is performed only depends on signal-to-noise considerations.

In this work, FCS and TIRF excitation are combined with fluorescence detection with a highly sensitive camera to study reversible binding. TIRF microscopy is a useful tool to reduce the signal contribution of freely diffusing ligand compared to confocal or widefield imaging. Nonetheless, the concept of SI-FCS is not limited to TIR excitation. Any time-resolved imaging scheme rendering reversible binding as fluctuating signal separable from

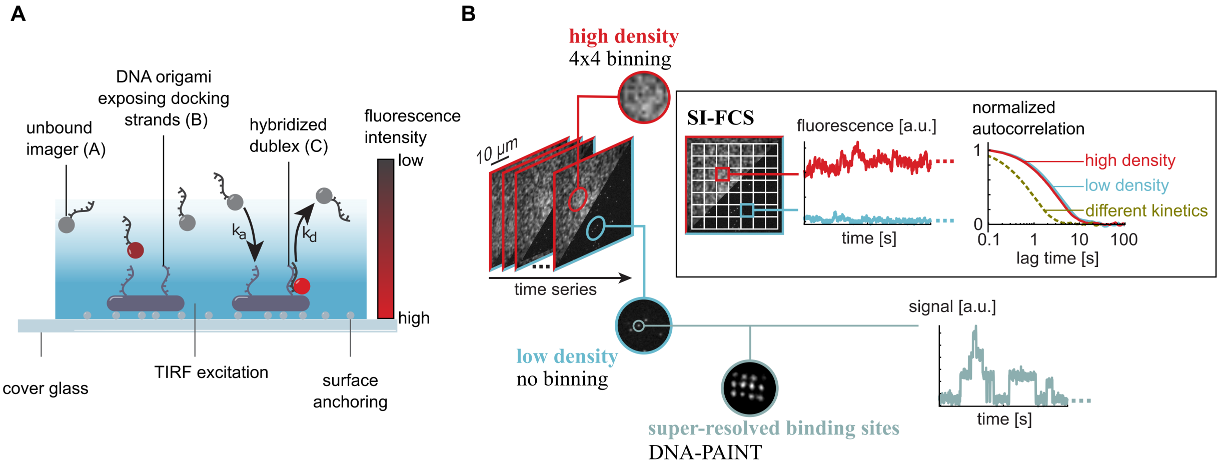

Figure III.1: Concept of SI-FCS. A) The system under study comprises surface-immobilized rectangular DNA origami structures, which exhibit ssDNA docking strands on their surface. The complementary imager strand is fluorescently labeled, diffuses in solution and occasionally hybridizes with the docking strand. Thus, this system mimics a reversible receptor ligand interaction, which is highly tunable by the nucleotide overlap. The entire system is imaged by TIRF microscopy. B) For SI-FCS, a stack of images is acquired and subdivided into several ROIs in which the signals are integrated. For every ROI a signal trace is extracted and autocorrelated. The characteristic decay time of the autocorrelation curve reflects on the underlying binding kinetics and is independent of the receptor density. For the system in A), the imaging can also be performed at low DNA origami and imager concentrations, such that individual binding events can be localized to render a super-resolved DNA-points accumulation for imaging in nanoscale topography (PAINT) image [Jungmann et al., 2010] or to potentially count the binding sites on one DNA origami [Jungmann et al., 2016].

diffusion, is compatible with this approach. Potential examples include FRET to surface-attached acceptors [Auer et al., 2017] and SAF microscopy [Ruckstuhl and Verdes, 2004, Barroca et al., 2012, Brunstein et al., 2017].

The basic principle of SI-FCS is shown in figure III.1. The fluorescence signal from a surface binding system, here reversible DNA hybridization, is imaged using TIRF microscopy. A set of such images with equidistant temporal spacing is acquired. The images are tiled with ROIs. Each of them serves as a surface over which the acquired pixel values are integrated. The obtained signal trace is autocorrelated and the characteristic decay time of the autocorrelation curve should reflect on the reversible binding kinetics. SI-FCS performs in low and high density regimes of receptors. This study uses rectangular DNA origamis [Rothemund, 2006, Schnitzbauer et al., 2017] that expose ssDNA for hybridization on the surface. At very low densities of binding events, not only SI-FCS analysis can be performed, but also a super-resolved image of the binding sites can be acquired using DNA-PAINT [Jungmann et al., 2010].

For this work, a TIRF microscope was built with the sole purpose to perform high-quality SI-FCS. As a byproduct, this microscope is also compatible with single-molecule and regular TIRF imaging. A detailed description, including a novel method for a focus stabilization, can be found in appendix A.1. The theoretical basis of SI-FCS is derived and followed by a series of measurements on reversible hybridization kinetics of DNA. The association and dissociation rates are extracted from ligand titration experiments. Finally, as SI-FCS is a new technique, an entire section is attributed to thorough quality controls, comprising experiments and simulations.

III.2 SI-FCS to characterize binding kinetics

III.2.1 Theoretical considerations

III.2.1.1 Derivation of the autocorrelation function

Considerable effort has been previously put into the derivation or approximation of an all-embracing correlation function which covers lateral 2D diffusion, 3D diffusion and reversible binding [Ries et al., 2008a, Thompson et al., 1981, Starr and Thompson, 2001]. Despite the previous work, to date no closed analytical autocorrelation function, which covers all these dynamics, has been found. Thompson and colleagues derived an expression, which requires a numerical inverse Laplace transform, which is however a classically ill-posed problem. Moreover, the full autocorrelation depends on at least four time parameters (axial and lateral 3D diffusion time, lateral 2D diffusion time, inverse association rate, inverse dissociation rate), which are intrinsically difficult to obtain simultaneously from one correlation curve.

This work focuses on the quantification of binding rates. Therefore, a simplified approach is followed here. Throughout this work, surface-immobilized binding sites are considered. SI-FCS studies describing lateral diffusion and reversible binding will be subject to a future study. Thus, we consider a bimolecular reactions of the type A+B$\rightleftharpoons$C, where A is the ligand, freely diffusing above a surface, B is the unbound receptor, which is immobilized at a surface, and C is the bound receptor-ligand pair (compare figure III.1A). Moreover, we assume that the detected fluorescence signal $F(t)$ from a detection volume can be expressed by its mean $\langle F \rangle$ and the temporal fluctuations $\delta F(t)$ around it.

$$F(t) = \langle F \rangle + \delta F(t) = \underbrace{\langle F_C \rangle + \delta F_C(t)}_{\text{bound ligands}} + \underbrace{\langle B_g \rangle + \delta B_g(t)}_{\text{uncorrelated background}} \tag{III.1}$$

$F(t)$ is made up by signal contributions from bound molecules $F_C(t)$ and an uncorrelated background $B_g(t)$, which results in a measured autocorrelation curve $G_{\text{meas}}(\tau)$.

$$G_{\text{meas}}(\tau) = \frac{\langle \delta F_C(0) \delta F_C(\tau) \rangle}{(\langle F_C \rangle + \langle B_g \rangle)^2} \tag{III.2}$$

In the context of the SI-FCS measurements presented here, the uncorrelated background can be not only background noise or stray light, but also the signal contribution from freely diffusing ligand. The latter can be considered as uncorrelated background if the 3D diffusion of labeled ligand through the detection volume is occurring on a much shorter timescale than the considered binding dynamics. This assumption significantly simplifies the theoretical autocorrelation function, but needs to be verified for each system under study. A more detailed discussion and an estimation of accessible time scales are discussed in section III.3.1.

In addition to the temporal component that correlated background adds to the autocorrelation curve, background in general lowers the autocorrelation amplitude, as it contributes to the normalization of G_{meas}. It is rather relevant to measure the correlation curve $G_{CC}(\tau)$ based on $\delta F_C(t)$ and normalize to the mean of $F_C(\tau)$. Provided that the background can be measured in a separate blank control sample, $G_{CC}(\tau)$ can be calculated easily [Thompson, 1999]:

$$G_{CC}(\tau) = G_{\text{meas}}(\tau) \frac{\langle F \rangle^2}{(\langle F \rangle - \langle B_g \rangle)^2} \tag{III.3}$$

It is worth noting that the temporal decay of the autocorrelation curve is not altered by uncorrelated background.

To obtain an expression for $G_{CC}(\tau)$, the common scheme of derivations for confocal FCS is followed [Krichevsky and Bonnet, 2002]. Time and ensemble average are equal for quasi-ergodic system and the collected fluorescence is proportional to the number of fluorophores in the detection volume. Thus, $G_{CC}(\tau)$ reads:

$$G_{CC}(\tau) = \frac{\int \mathrm{d}^3\vec{r} \int \mathrm{d}^3\vec{r}' \Phi_{CC}(\tau)\delta(\vec{r} - \vec{r}')}{\langle C \rangle^2 \left(\int \mathrm{d}^3\vec{r}\right)^2} \tag{III.4}$$

The integrals cover the entire detection volume. $G_{CC}(\tau)$ was expressed in terms of the concentration correlation function $\Phi_{CC} = \langle \delta C(0)\delta C(\tau)\rangle$, which is calculated once an expression for $\delta C(\tau)$ is known.

Under the assumption that all diffusion dynamics through a considered region of interest are equilibrated, the change of the concentration of conjugates C is governed by a source and a sink term.

$$\frac{\mathrm{d}C}{\mathrm{d}t} = \underbrace{k_a AB}_{\text{source}} - \underbrace{k_d C}_{\text{sink}} \tag{III.5}$$

Here, the association rate k_a, and the dissociation rate k_d were introduced. Both parameters are directly linked to the mean dwell and association times, $\tau_d = k_d^{-1}$ and $\tau_a = k_a^{-1} \langle A \rangle^{-1}$, which describe the average duration of a single binding event and the average time between two consecutive binding events, respectively. The ratio of these rates is the well-known dissociation constant:

$$K_D = \frac{k_d}{k_a} = \frac{\langle A \rangle \langle B \rangle}{\langle C \rangle} \tag{III.6}$$

As the total number of surface binding sites is constant $S = \langle B \rangle + \langle C \rangle = \text{const}$, it is evident that a decrease of receptor-ligand pairs will results in an increase of free receptor by the same magnitude: $\delta B = -\delta C$. Therefore, the differential equation III.5 for C is easily transformed into a differential equation for Φ_{CC}:

$$\frac{\mathrm{d}\Phi_{CC}(\tau)}{\mathrm{d}\tau} = -\left(k_a A + k_d\right)\Phi_{CC}(\tau). \tag{III.7}$$

Differential equations of this kind are very well known and have the simple solution

$$\Phi_{CC}(\tau) = \Phi_0 \, e^{-\tau/\tau_c} \tag{III.8}$$

The obtained exponential function decays with the characteristic time constant τ_c, which can be expressed in terms of the association and dissociation rates.

$$\tau_c = \left(k_a \langle A \rangle + k_d\right)^{-1} = \left(\tau_a^{-1} + \tau_d^{-1}\right)^{-1} \tag{III.9}$$

An expression for Φ_0 is obtained from the initial condition $\Phi_{CC}(\tau = 0) = \Phi_0 = \langle \delta C^2 \rangle$. This quantity is known as the variance. To find the underlying distribution, it is worth realizing that for every given point in time, each surface receptor occupies one out of two states: bound to a ligand or unbound. Provided that all receptors are independent, this corresponds to a binomial distribution, which has the variance $\Phi_0 = S\beta(1-\beta)$ [Thompson et al., 1981]. Here we introduced the fraction of bound receptors β, which can be interpreted as the success probability of the binomial distribution. Accordingly, the fraction of unoccupied receptors is $(1 - \beta)$.

$$\beta = \frac{\langle C \rangle}{\langle B \rangle + \langle C \rangle} = \left(1 + \frac{k_d}{k_a \langle A \rangle}\right)^{-1} = \frac{\tau_c}{\tau_a} \tag{III.10}$$

$$(1-\beta) = \frac{\langle B \rangle}{\langle B \rangle + \langle C \rangle} = \left(1 + \frac{k_a \langle A \rangle}{k_d}\right)^{-1} = \frac{\tau_c}{\tau_d} \tag{III.11}$$

Therefore, the variance of the binomial distribution reads

$$\Phi_0 = \langle C \rangle \frac{\tau_c}{\tau_d} = \langle C \rangle (1 - \beta), \tag{III.12}$$

and finally, inserting equations III.8 and III.12 into equation III.4 yields

$$G_{CC}(\tau) = \frac{1}{N_C} \frac{\tau_c}{\tau_d} e^{-\tau/\tau_c} = \frac{1}{N_S} \frac{1-\beta}{\beta} e^{-\tau/\tau_c} \tag{III.13}$$

In accordance with the nomenclature C and S for the surface concentrations of bound receptors and the total receptor concentration, N_c and N_S are the corresponding absolute numbers in the detection volume. Alternatively, equation III.13 can be obtained as a limiting case of the advanced derivation of the full autocorrelation by Thompson and colleagues [Thompson et al., 1981]. Interestingly, the amplitude $G_0 = \lim_{\tau \to 0} G_{CC}(\tau)$ of the correlation is not only proportional to the absolute number of occupied binding sites, but also depends on the kinetic rates. However, if $\tau_a \gg \tau_d$, i.e. in the case of low concentration of labeled ligand $\langle A \rangle \ll K_D$, the number of occupied binding sites can be obtained directly as the inverse of the correlation amplitude. It is important to realize that for any extraction of information from the correlation amplitude, the mean background signal

$\langle B_g \rangle$ has to be carefully measured. This work focuses exclusively on the temporal decay of the autocorrelation curves. Therefore, it is noted that the correlation amplitude of SI-FCS carries valuable information, but the exploitation is left for future studies.

III.2.1.2 Conclusions for the experimental design from the theoretical autocorrelation function

The obtained exponential for the autocorrelation function is not surprising, as the considered blinking upon binding is a random telegraph process, which is known to be described by an exponential, provided many transitions between both states were sampled [Bingemann, 2006]. Similar observations have been made for the blinking of surface-immobilized red fluorescent proteins [Schenk et al., 2004]. In the case of SI-FCS, provided the receptors do not diffuse laterally, the situation is very similar: blinking molecules are conceptually switching between two states (bright and dark), and the transitions are governed by the characteristic rate $k_a \langle A \rangle$ and k_d.

The characteristic decay time τ_c of the exponential (equation III.9) can be obtained by fitting the model function to experimental autocorrelation curves. Interestingly, in the limit of very low ligand concentrations, i.e. $\langle A \rangle \ll K_D = k_d/k_a$, τ_c equals the inverse dissociation rate k_d. Therefore, SI-FCS measurement in a regime of low imager concentrations can give direct access to the dissociation rate.

Moreover, if the experiments can be supported by predictions of the binding free energy ΔG, the association constant k_a can be estimated via:

$$k_a = \frac{k_d}{K_0} e^{\frac{\Delta G}{RT}} \tag{III.14}$$

Here, the gas constant R and a reference constant $K_0 = 1\,\mathrm{M}$ were introduced. Equation III.14 follows directly from the well-known equation $\Delta G = -RT \ln \frac{K_D}{K_0}$. Consequently, in an ideal scenario, both rates, k_d and k_a, may be obtained from a single experiment, if predictions of ΔG are accessible.

Another important feature of τ_c is its dependence on the ligand concentration $\langle A \rangle$. Consequently, a set of SI-FCS measurements at different ligand concentrations yields different τ_c. This dependence can be fitted by equation III.9, providing direct access to the rates k_d and k_a.

III.2.2 Measurement of reversible DNA hybridization

III.2.2.1 Temporal resolution of 7 nt, 8 nt, 9 nt and 10 nt hybridizations

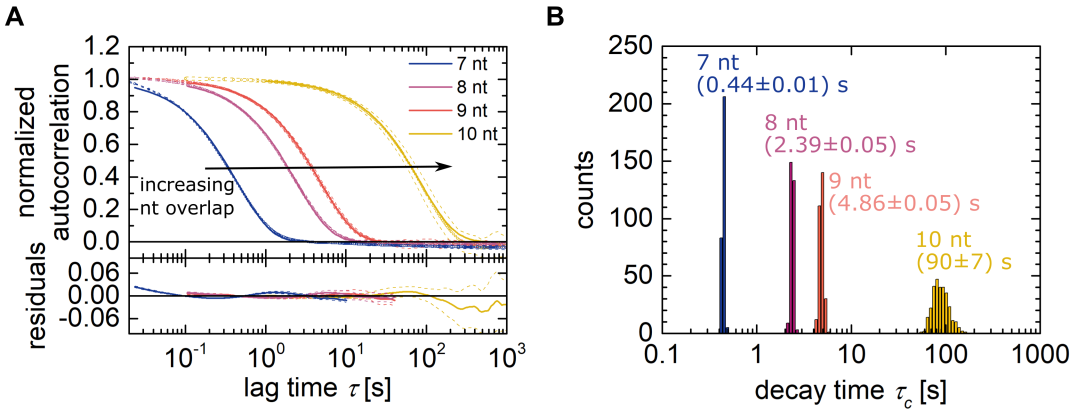

Figure III.2: Resolution of reversible DNA hybridizations by SI-FCS. A) Representative autocorrelation curves of four individual SI-FCS measurements of the hybridization of 7, 8, 9 and 10 nucleotide (nt) base pair overlaps. Each curve shows the mean (circles) and standard deviations (dashed lines) of 49 autocorrelation curves, which were measured in parallel in different ROIs. All autocorrelation curves were fitted by a single exponential (solid lines), which described the experimental data with residual well below 4% of the maximum autocorrelation amplitude. B) Corresponding histograms of characteristic decay times τ_c. The results from 6 measurements per duplex overlap are shown, each of them comprising the autocorrelation curves from 49 ROIs.

To experimentally explore the kinetics accessible to SI-FCS, four different DNA origamis, which together with fluorescently labeled ssDNA (imager strand) formed a 7 nt, 8 nt, 9 nt and 10 nt overlap respectively, were designed (compare Materials and Methods section in appendix A.2). To keep these initial experiments as simple as possible, the concentrations of imager strand were chosen very low, such that $\langle A \rangle \ll K_D$. To obtain an estimate of K_D, the binding free energies (table III.1) were estimated using the NUPACK tool [Zadeh et al., 2011]. Based on theses theoretical predictions, imager concentrations of 10 nM for 7 nt, 8 nt, and 9 nt, and 1 nM for 10 nt hybridizations respectively, were chosen. Consequently, the experiments were expected to be in a regime where the decay time of the autocorrelations curve is governed by the imager dwell time $\tau_d = k_d^{-1}$ at the surface.

Figure III.2A shows corresponding representative autocorrelation curves. Evidently, the different hybridization kinetics result in clearly resolvable different timescales on which the autocorrelation curves decay. The autocorrelation curve for 7 nt hybridizations decays fastest. With increasing nt overlap, the correlation decays at larger lag times. This is in line with the expected increasing binding time for an increasing nt overlap. Having demonstrated the capability of SI-FCS to resolve differences in the number of nucleotide overlaps, one can immediately conclude that single base pair mismatches are also resolvable. According to calculations (data not shown), the free energy of DNA hybridization decreases to a larger extent by the introduction of a single base pair mismatch than by the removal of a terminal base pair [Zadeh et al., 2011].

In the approach presented here, the acquired images were tiled with 7x7 square ROIs, each of them covering 31x31 pixels. Accordingly, each measurement yielded 49 autocorrelation curves, which sampled the hybridization kinetics across the entire image. All measurements were taken at sufficiently low illumination, such that photobleaching was negligible (compare section III.3). Figure III.2A shows the means (circles) and standard deviations (dashed lines) of the autocorrelations from these 49 ROIs for 7 nt, 8 nt, 9 nt and 10 nt hybridizations. Remarkably, the standard deviations are small, indicating that all ROIs yield identical results. This was to be expected, as the hybridization kinetics are independent of the lateral sample positions, but highlights that SI-FCS can precisely measure binding kinetics of a freely diffusing ligand to a surface-immobilized receptor.

The acquired autocorrelation curves were fitted using a single exponential fit model, as derived above (equation III.13). Strikingly, this model function describes the experimental data well with overall residuals below 3% of the amplitude. Interestingly, the residuals show only very minor systematic residuals, which are only visible, because no noise, i.e. random residuals, are visible in the residuals. These low random deviations originate from the large number of binding events that is sampled by this SI-FCS approach. Overall, the residuals are smallest for 8 nt and 9 nt hybridizations. For 7 nt, the fit is slightly below the experimental curve at short lag times below 100 ms. This deviation can be attributed to the correlation from 3D diffusion of imager strand in solution, which is known to have a long tail [Thompson et al., 1981, Ries et al., 2008a]. The autocorrelation of 7 nt is most affected by solution diffusion, as this kinetic is fastest of all measured hybridizations, and thus the characteristic decay time is closest to the diffusion time. At the other end of the spectrum, the 10 nt hybridization shows almost no residuals at lag times below the characteristic decay time. In this case, the whole dynamics take place at large lag times where the correlation from solution diffusion is lost. On the other hand, the 10 nt autocorrelation shows larger residuals and larger standard deviations at lag times above 100 s. Here, the deviations originate from two effects: First, at large lag times, the statistics are worse, as less binding events with long dwell times can be sampled within the measurement duration. Secondly, the computed autocorrelation curve is a biased estimator, which only approaches the real case for infinitely long measurements. This effect is discussed in more detail in section III.3, which deals with the quality control of SI-FCS measurements. Although the discussed systematic residuals show minor deviations between the exponential fit model and the experimental data, it is worth noting, that these residuals supposedly affect the outcome of the analysis to a minor degree, and are only visible because of the outstanding signal-to-noise ratios of the presented measurements.

Table III.1: Estimation of the kinetic rates for 7-10 nt hybridizations based on single SI-FCS experiments. SI-FCS measurements (compare figure III.2) were performed in a low ligand concentration regime, such that $\langle A\rangle \ll K_D$ and thus $\tau_c \approx k_d$. For each hybridization sequence, the binding free energy ΔG was predicted using the NUPACK software tool [Zadeh et al., 2011] with the following settings: $T = 296.15\,\mathrm{K}$, concentration of Na^+ 50 mM, concentration of Mg^{2+} 9 mM. Using this hybrid approach of measuring τ_c and predicting ΔG, estimates of k_a and k_d were obtained from single shot experiments. The experiments were performed at 23 °C, the sequences exposed on the DNA origamis were 5′-TT**ATACATC**-3′ (7 nt), 5′-TT**ATACATCT**-3′ (8 nt), 5′-TT**ATACATCTA**-3′ (9 nt), and 5′-TT**ATACATCTAG**-3′ (10 nt), with the hybridized sequences in bold.

sample	ligand concentration $\langle A\rangle$ [nM]	predicted ΔG in [kJ mol^{-1}]	measured τ_c [s]	measured k_d [s^{-1}]	estimated $k_a \cdot 10^6$ [M^{-1}s^{-1}]
7 nt	10	36.03	0.44 ± 0.01	2.27 ± 0.05	5.15 ± 0.12
8 nt	10	37.83	2.39 ± 0.05	0.418 ± 0.009	1.97 ± 0.04
9 nt	10	41.98	4.86 ± 0.05	0.206 ± 0.002	5.23 ± 0.05
10 nt	1	48.98	90 ± 7	0.0111 ± 0.0009	4.84 ± 0.39

The characteristic decay times τ_c obtained from the fits of the autocorrelation function range from less than 440 ms for 7 nt to 90 s for 10 nt hybridizations, thus covering more than two orders of magnitude (figure III.2B). The corresponding values of τ_c are presented in table III.1. As the imager concentration was low compared to K_D, τ_c equals the inverse dissociation rate k_d^{-1}. The values of k_d obtained from these experiments are comparable to previously reported rates [Peterson et al., 2016b,Dupuis et al., 2000,Jungmann et al., 2010]. Small differences can likely be attributed to the effect of different sequences and ion concentrations in the buffer, which are known to affect the formation of secondary structures (for reviews see [Woodson, 2005,SantaLucia and Hicks, 2004]). The obtained characteristic decay times reflect on the number and type of the base pairing, as an increased nt overlap results in larger τ_c. Moreover, the relative increase of τ_c from 9 nt to 10 nt is by far the largest, which can be attributed to the addition of a stronger binding GC-pair from 9 nt to 10 nt, whereas in the other cases a weaker binding AT-pair was added. The results are highly reproducible, with standard deviations of less than 3% of the mean characteristic decay times for 7 nt, 8 nt and 9 nt samples. The 10 nt hybridizations show a slightly larger relative standard deviation below 7%, supposedly because of the slightly larger scatter in the autocorrelation curves. Nonetheless, the results presented here, show that SI-FCS can precisely measure dissociation rates over more than two orders of magnitude with high statistical accuracy.

DNA hybridization has been subject to many theoretical studies, which have been reviewed elsewhere [SantaLucia and Hicks, 2004, Zuker, 2000, Mathews, 2006, Lorenz et al., 2016]. The thermodynamic modeling enabled the development of software tools to estimate hybridization parameters, such as the free binding energy ΔG [Zadeh et al., 2011]. Here, the SI-FCS measurements of k_d were supplemented by theoretical predictions of ΔG to estimate the association rates k_a (table III.1). The calculations were performed based on the parameters provided by SantaLucia [SantaLucia, 1998], which did not perfectly match our buffer conditions, and had to be adjusted. To describe our conditions best, we used the minimum concentration of Na^+ compatible with ref. [SantaLucia, 1998], which compensated partially for the Tris in our buffer. The remaining Na^+ could be accounted for by lowering the Mg^{2+} concentration, although the relevant equivalent amount of Mg^{2+} is be small [Owczarzy et al., 2008, von Ahsen et al., 2001, Mitsuhashi, 1996]. Following this approach, the obtained estimates of k_a are in line with previously reported values [Peterson et al., 2016b, Lang and Schwarz, 2007, Jungmann et al., 2010, Dupuis et al., 2000, Jungmann et al., 2016]. Moreover, all estimated association rates appear to be similar, regardless of the base pair overlap. The same observation was recently reported for 9 nt and 10 nt hybridization by Jungmann and colleagues [Jungmann et al., 2010].

Here, single SI-FCS experiments were supported by theoretical predictions to obtain k_a and k_d. Alternatively, these parameters are accessible by titration of the imager strand concentration $\langle A \rangle$. This approach does not rely on estimates, but is independent of external estimates. The corresponding experiments are presented in section III.2.3.

III.2.2.2 Parallel discrimination of multiple binding kinetics

In the previous section, it has been demonstrated that SI-FCS can resolve the dissociation rates of reversible DNA hybridizations. Based on these findings, the question arises whether

SI-FCS can resolve the presence of several binding species in one sample. From an analysis point of view, this corresponds to the question whether and under which conditions the superposition of two exponential decays can be resolved. Conceptually, the same question is of relevance to fluorescence lifetime measurement with two decay times. A clear criterion based on which it can be judged whether two exponentials can be separated is not known, because the separation depends on too many parameters: the signal-to-noise ratio, the nature of the noise, the ratio of both characteristic decay parameters, and the ratio of the amplitudes of the exponentials.

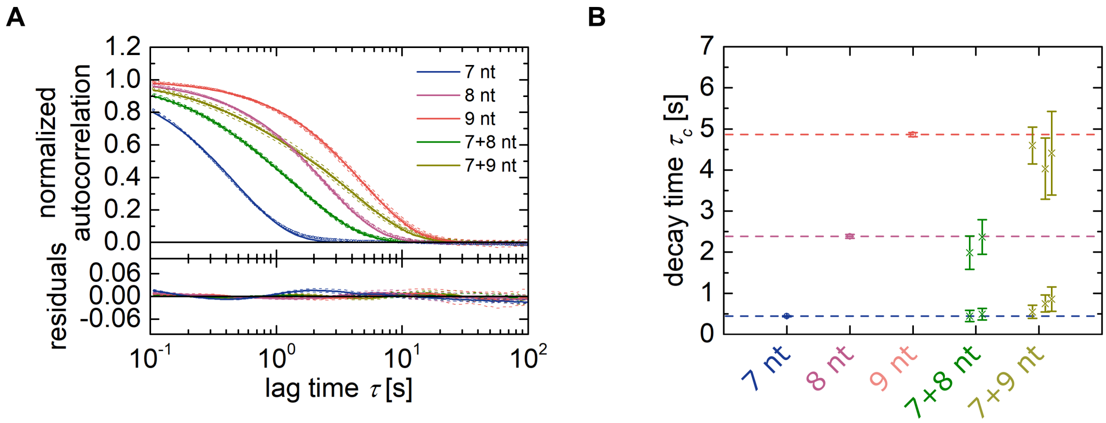

Figure III.3: Resolution of multiple binding species by SI-FCS. Representative experimental autocorrelation curves of samples with single hybridization kinetics (7, 8, 9 nt) and two hybridization kinetics present (7+8 nt, 7+9 nt). Each curve shows the mean (circles) and standard deviations (dashed lines) of 49 autocorrelation curves, which were measured in parallel in different ROIs. The samples with two hybridization kinetics were appropriately described by a bi-exponential fit (solid lines), whereas the samples with only one hybridization kinetic are adequately described by single exponential fits (solid lines). B) Characteristic decay times for samples with only one kinetic and with mixed kinetics. Error bars correspond to the means and standard deviations of the results from 49 ROIs. For mixed samples, two distinct decay times were found and the anticipated decay times (dashed lines) were reproduced with minor biases.

To address this question experimentally in the relevant context of SI-FCS measurements, we prepared samples with mixed populations of DNA origamis. The imager strand can hybridize with strands exposed on both kinds of DNA origamis, albeit with different kinetic rates. In detail, surfaces were prepared, such that 7 nt and 8 nt complementary strands to the imager strands were exposed on different surface-immobilized DNA origamis. Similarly, for another set of measurements, DNA origamis for 7 nt and 9 nt hybridizations were in parallel immobilized. The expected values of τ_c for the mixed binding kinetics differ by less than an order of magnitude (compare figure III.2B), which makes them intrinsically difficult to distinguish. The corresponding experimental autocorrelation curves are shown together with single species measurements (7, 8, 9 nt) in figure III.3A. Clearly, the mixed samples show a much broader decay than the single species measurements, corresponding to the sum of two exponentials that decay on different time scales. Consequently, these curves were fitted with bi-exponentials, which yielded low residuals and were therefore adequately describing the experimental data sets. The obtained characteristic decay times are presented in figure III.3B and show that the decay times from single component binding experiments were reproduced with deviations of less than 20%. These results demonstrate that SI-FCS can distinguish the presence of multiple binding species in one sample. Their characteristic decay times may differ by only a factor of 5, and can still be separated. The distinction solely relies on the differences in binding kinetics, and does not require any spectral discrimination.

III.2.3 Precise quantification of association and dissociation rates by SI-FCS

III.2.3.1 Titration experiments

To demonstrate that SI-FCS has indeed the capability to determine association and dissociation rates of reversible binding kinetics, as proposed in the theoretical preconsiderations (section III.2.1), titration experiments were performed for 9 nt and 10 nt DNA hybridizations.

For this purpose, the sample chambers were prepared as usual, but solutions with different concentrations of ligand (imager strand) were loaded. To verify that the target concentration of ligand was reached in solution, confocal FCS measurements were performed in solution above the surface. Indeed, the measured concentrations are identical to the target concentrations, as shown in figure A.4 in appendix A.3. Only at sub-nanomolar concentrations of ligand, a relative deviation of the concentration is discernible, which may be attributed to afterpulsing photons, as discussed in the context of figure A.4. Consequently, it is not clear, whether and to which extent these deviations are real. Sub-nanomolar concentration regimes are difficult to characterize, especially in this case, were an *in situ* measurement of the concentrations was desired. Following the famous Hagen-Poiseuille law, flow chambers have a flow profile (measured e.g. in reference [Gösch et al., 2000]).

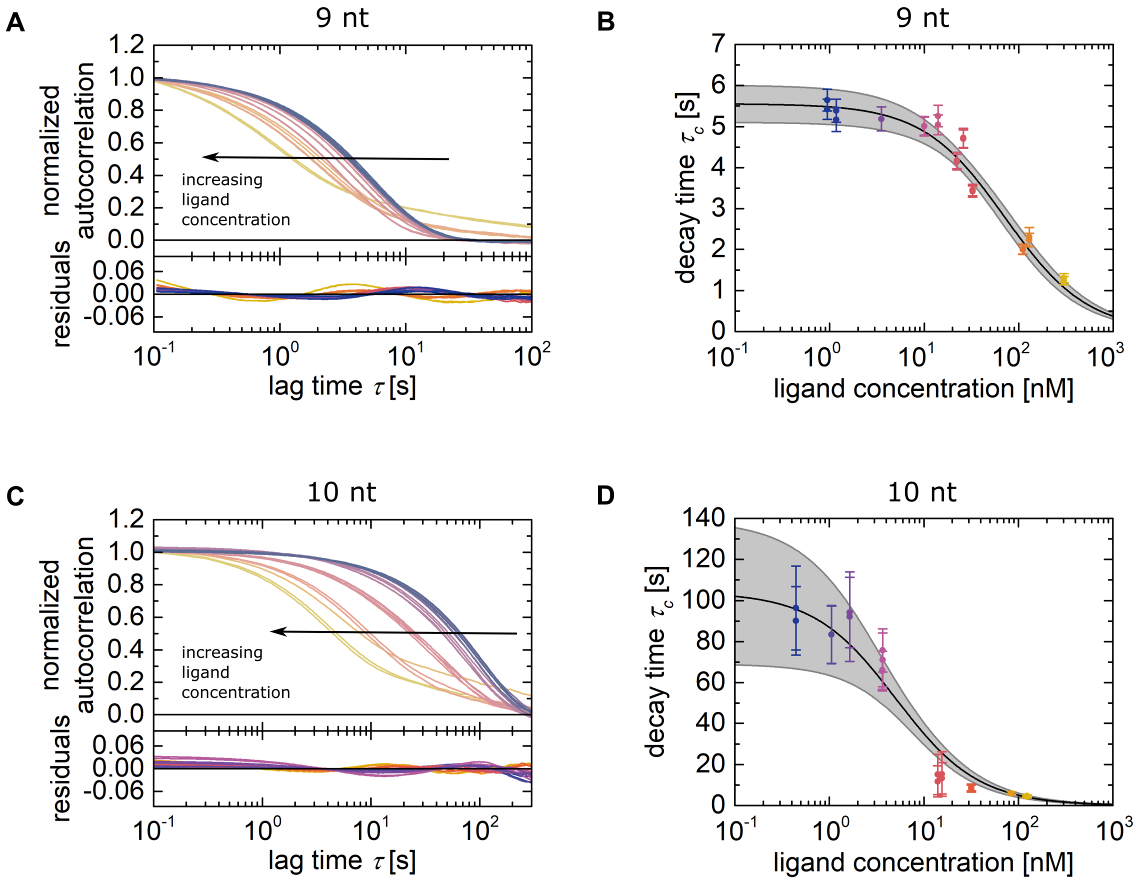

Figure III.4: Quantification of association and dissociation rates by SI-FCS. A) Autocorrelation curves of reversible 9 nt hybridizations at different concentrations of ligand (imager strand). With increasing ligand concentrations, the autocorrelation curves shift to shorter decay times. For clarity, only the experimental autocorrelation curves are shown. Below a ligand concentration of 100 nM, the autocorrelation curves were fitted by a single exponential, above 100 nM by a bi-exponential. The quality of the fits is illustrated by the residuals. B) Characteristic decay times obtained from the autocorrelation curves in A) decrease with increasing ligand concentration. The dependence was fitted using equation III.9 (black line with 95% confidence interval in gray). C) Autocorrelation curves of reversible 10 nt hybridizations at different concentrations of ligand. As in A), the autocorrelation curves decay at shorter lag times with increasing ligand concentrations, although overall the kinetics occur on longer time scales than the 9 nt hybridizations. For clarity, only the experimental autocorrelation curves are shown. The residuals indicate a good fit quality. Autocorrelations above ligand concentrations of 10 nM were fitted by a bi-exponential. D) Titration curve showing the characteristic decay times for 10 nt hybridizations. The dependence was fitted using equation III.9 (black line with 95% confidence interval in gray). The association and dissociation rates obtained by the fits in B) and D) are presented in table III.2.

Thus, it is not granted that the liquid is exchanged efficiently throughout the sample. The confocal FCS measurements performed here demonstrate however that the target concentration was reached over more than two orders of magnitude. Moreover, the deviations for sub-nanomolar concentrations only affect the determination of k_a and k_d if the dissociation constant K_D is also in this regime.

Table III.2: Association and dissociation rates for reversible 9 nt and 10 nt hybridizations measured by SI-FCS. The kinetic rates were obtained from titration experiments and subsequent fitting of the dependence of τ_c on the ligand concentration (figure III.4B,D). The errors correspond to the 95% confidence bounds of the fits. K_D and ΔG were directly calculated from k_a and k_d. The experiments were conducted at 23 °C.

sample	k_d [s^{-1}]	$k_a \cdot 10^6$ [$M^{-1}s^{-1}$]	K_D [nM]	ΔG [$kJ\,mol^{-1}$]
9 nt	0.180 ± 0.012	2.5 ± 0.5	72 ± 16	40.5 ± 0.6
10 nt	0.009 ± 0.002	2.1 ± 0.4	4.2 ± 1.8	47.5 ± 1.1

Strikingly, the autocorrelation curves of 9 nt and 10 nt DNA hybridizations shift to shorter lag times with increasing ligand concentration, as demonstrated by the experimental data sets shown in figure III.4A,C. This is in good agreement with the theoretical model (equation III.9). For ligand concentrations higher than 100 nM for 9 nt and 10 nM for 10 nt, respectively, a second component appeared at large lag times in the autocorrelation and was accounted for by a second exponential decay in the fitting model. The origin of this contribution is currently unclear, but one may speculate that this second component originates from unspecific binding, which becomes more pronounced with an increasing number of binders, i.e. the ligands. Regardless of the nature of this second component, the faster of the two decays, which corresponds to the kinetics of interest, was insensitive to changes in the fitting of the slower component. Moreover, the residuals of the autocorrelation fits are reasonably small, across all measured ligand concentrations.

In accordance with the shifts of the autocorrelation curves to shorter lag times with increasing ligand concentration, the characteristic decay time τ_c decreases (figure III.4B,D). The dependence of τ_c on the ligand concentration $\langle A \rangle$ was fitted by equation III.9 with k_a and k_d as free parameters. The values obtained for theses rates are presented in table III.2. Remarkably, the dissociation rates are in good agreement with the rates estimated from measurements with low ligand concentrations (table III.1), showing that for the previous measurements the assumption $\langle A \rangle \ll K_D$ was justified. This is further supported by the K_D calculated from the titration experiments (table III.2). As expected, the K_D for

10 nt DNA hybridizations is considerably lower than for 9 nt. The association rates are within the error identical for both hybridization kinetics, an observation already made by others [Jungmann et al., 2010], and in the previous section III.2.2. Finally, the binding free energy was directly calculated from K_D (table III.2) and reproduced the theoretical predictions from table III.1 within 10%. Thus, SI-FCS titration experiments have been shown to reproduce previous results and theoretical predictions, demonstrating that this method can adequately measure the kinetic rates of reversible binding.

III.2.3.2 Minimal set of SI-FCS experiments to measure kinetic rates

The previous section demonstrated that SI-FCS can accurately and precisely measure the kinetic rates of binding to a surface. These measurements come however at the cost of considerable experimental effort. In detail, each point in figure III.5B,D corresponds to a separate sample preparation and an independent measurement that lasts 5 h. To increase the throughput of SI-FCS measurements, several strategies were followed. A reduction of the measurement duration is discussed in chapter III.3, the parallelization of experiments is currently work in progress, and the reduction of the number of experiments is addressed in this chapter.

The determination of k_a and k_d relies on the measurement of τ_c, which depends on top of these two rates, also on the ligand concentration $\langle A \rangle$ (equation III.9). As $\langle A \rangle$ is controlled by the operator, the measurement of τ_c at two different ligand concentrations is in principle sufficient to determine the two parameters k_a and k_d. Compared to a full titration series, this approach would save precious samples and measurement time, but comes at the cost of lower precision. Intuitively, the most accurate results should be obtained for pairs of ligand concentrations $(\langle A_1 \rangle, \langle A_2 \rangle)$ that fulfill $\langle A_1 \rangle \ll K_D$ and $\langle A_2 \rangle \gtrsim K_D$. In this case, τ_c would be in one experiment dominated by the dwell time $\tau_d = k_d^{-1}$ and in the other experiment the association time $\tau_a = k_a^{-1} \langle A \rangle^{-1}$ would significantly contribute to τ_c. On the other hand, $\langle A_2 \rangle$ should not be too large for several reasons: when τ_c is close to zero, its relative error becomes large; fluctuations become more difficult to observe; and the contribution of 3D ligand diffusion to the autocorrelation curve may become non-negligible. Following the idea to extract binding rates from only two SI-FCS measurements, the individual experiments from figure III.4 were reanalyzed in pairs of different concentrations. The kinetic rates k_a and k_d obtained from this approach were related to the results from the full titration experiments by calculating the relative differences $\left| k_{a/d} - k_{a/d,\text{titration}} \right| / k_{a/d,\text{titration}}$. The corresponding results for 9 nt and 10 nt DNA hybridizations are shown in figure III.5.

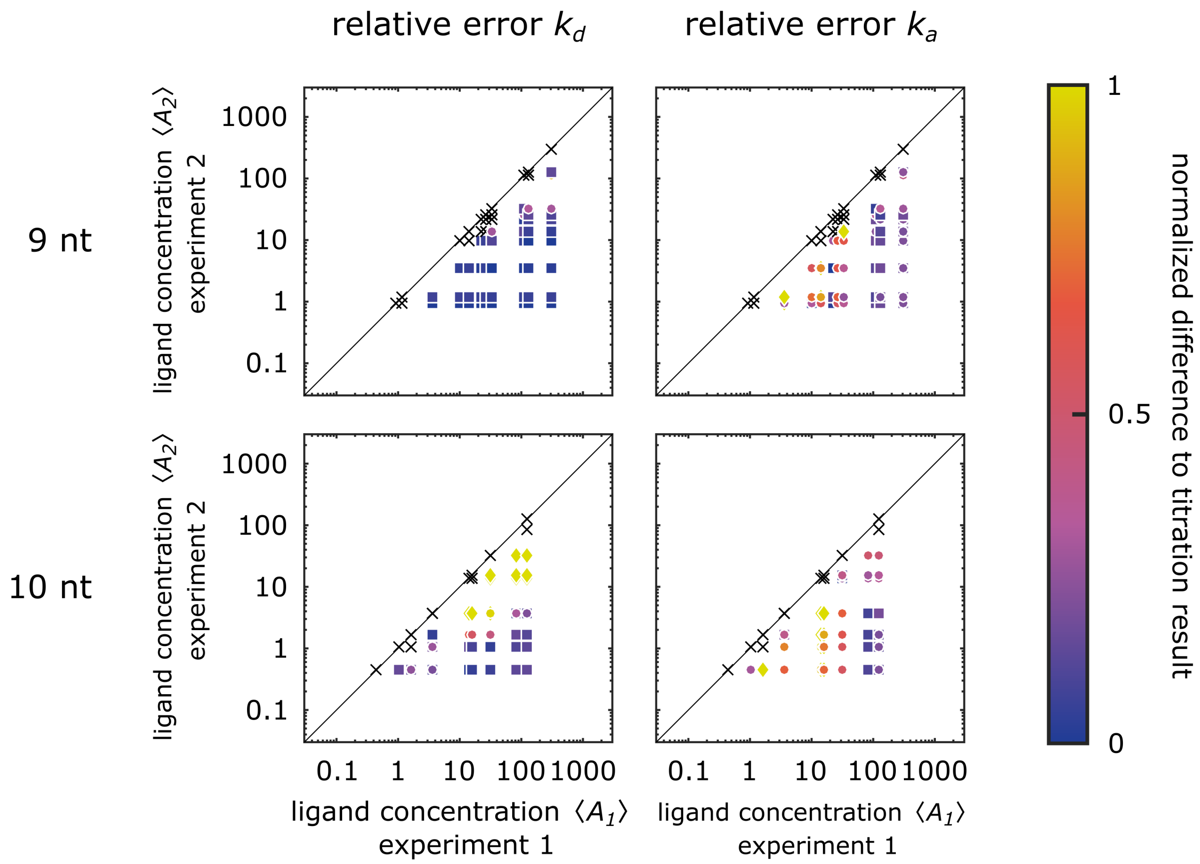

Figure III.5: Quantification of association and dissociation rates from a minimal set of SI-FCS measurements. Based on equation III.9, the measurement of τ_c at two different ligand concentrations $(\langle A_1 \rangle, \langle A_2 \rangle)$ is in theory sufficient to determine k_a and k_d. The relative difference to the results from the titration $k_{a/d,\text{titration}}$ (figure III.4) $\left|k_{a/d} - k_{a/d,\text{titration}}\right| / k_{a/d,\text{titration}}$ is color coded for the individual points. If the two concentration covered the regimes $\langle A_1 \rangle \ll K_D$ and $\langle A_2 \rangle \gg K_D$ (or vice versa), the rates from the titration experiments were recovered with an error below 20% (squares). Pairs of concentrations which were differing by less than a factor of two were excluded from the analysis and marked as crosses. Concentration pairs leading to a relative error of more than 100% saturated the chosen color scale and were marked as diamonds. The graphs are symmetric with respect to the diagonal and therefore only the lower half is shown.

Evidently, the experiments with only two ligand concentrations reproduce the k_d from the full titration series best, when one of the ligand concentrations is small compared to K_D, in line with the previous discussions (section III.2.1). The association rate is reproduced best in the bottom right of the respective panels, i.e. for $\langle A_1 \rangle \ll K_D$ and $\langle A_2 \rangle \gtrsim K_D$, as expected. Although finding good choices for $\langle A_1 \rangle$ and $\langle A_2 \rangle$ may be challenging if K_D is completely unknown, The results presented in figure III.5 clearly show, that two SI-FCS experiments can be sufficient to accurately measure the kinetic reaction rates k_a and k_d.

III.3 Quality control

The previous sections demonstrated the potential of SI-FCS to quantify association and dissociation rates. The hybridization kinetics measured here accurately reproduced theoretical predictions and were in line with the experimental results of other studies [Peterson et al., 2016b, Lang and Schwarz, 2007, Jungmann et al., 2010, Dupuis et al., 2000, Jungmann et al., 2016]. As SI-FCS is a novel method, measurement conditions which do not introduce artifacts and are realizable in routine experiments had to be established. This section presents strategies and solutions for finding the optimal experimental settings for SI-FCS measurements, which is of major importance for the accurate application of SI-FCS.

III.3.1 Time scales accessible to SI-FCS

III.3.1.1 Minimal duration of individual SI-FCS measurements

Each of the previously presented autocorrelation curves was computed from almost 5 h long measurements. This long measurement duration was initially taken to ensure that the overall duration is much longer than the characteristic decay time of the autocorrelation curve. Monte Carlo simulations of autocorrelation curves for lateral diffusion showed that measurements should be at least 10^3 to 10^4 times longer than the diffusion time (data not shown) [Ries, 2008]. This necessity arises partially from the fact that to describe an average of kinetics, the slow contributions also need to be sample adequately and must not be cut off by too short measurements. More importantly, the computed autocorrelation curve is a biased estimator, which only converges to the real ensemble averaged autocorrelation in the limit of sufficiently long measurements [Oliver, 1979, Schätzel et al., 1988, Schätzel, 1987, Saffarian and Elson, 2003]. This effect has also been described for confocal FCS measurements on freely diffusing particles [Saffarian and Elson, 2003, Tcherniak et al., 2009].

In real experiments, short measurements are desirables, as samples may slowly degrade over time, and long acquisitions limit the throughput and require valuable time on the microscope. Thus, an optimal measurement duration, which introduces only an acceptable bias and is as short as possible, had to be found. To this end, Monte Carlo simulations were

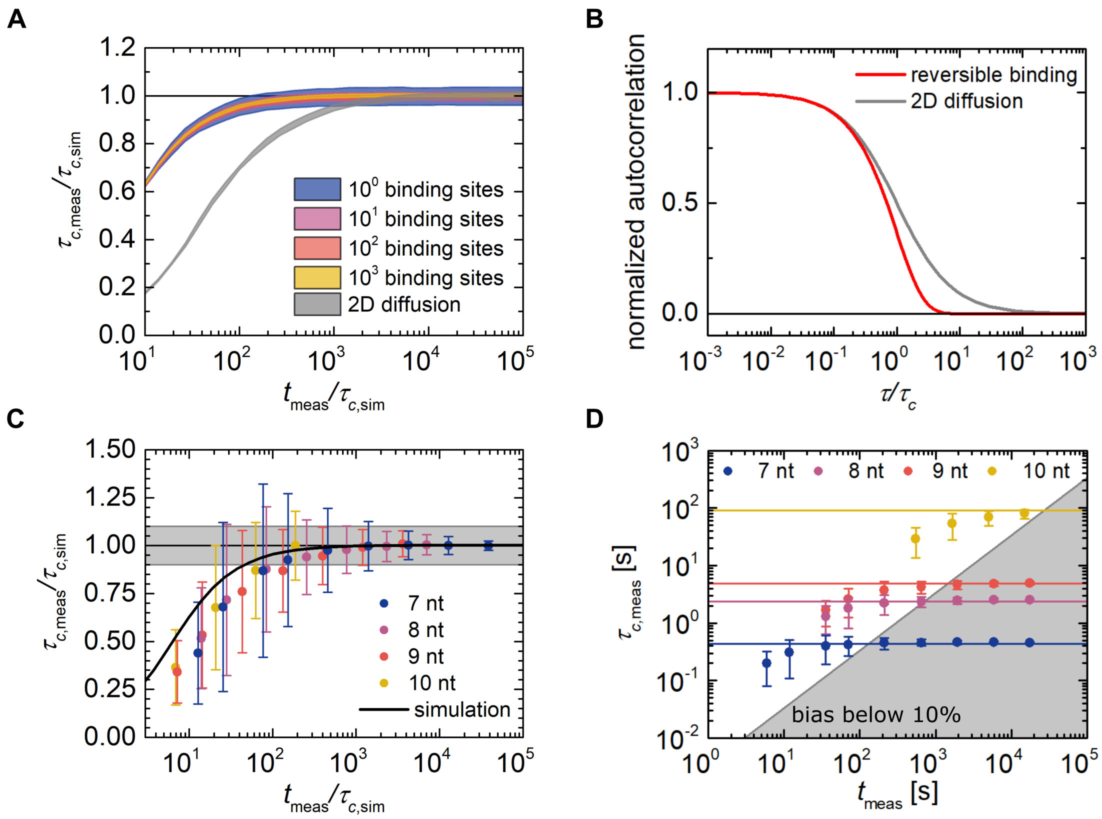

Figure III.6: Required measurement duration for SI-FCS experiments. A) The relative error of the obtained characteristic decay time depends on the duration of the SI-FCS experiment. The shaded areas represent means and standard deviations of ten independent simulations (for more details see main text) for different numbers of binding sites. The convergence does not depend on the number of sampled binding events. As a reference, similar simulations were performed for 2D diffusion through a confocal volume. Compared to binding measurements by SI-FCS, 2D diffusion requires much longer measurement durations to achieve similarly small biases on the characteristic decay time (τ_D in the case of diffusion). B) The slower convergence originates from the longer tail of the 2D diffusion autocorrelation curve compared to a single exponential for reversible binding (theoretical curves are shown). C) Individual SI-FCS measurements from figure III.2 were cut into shorter traces, reanalyzed and superimposed with the mean from simulations (solid line). The experiments show a slightly higher bias on the obtained τ_c compared to simulations, but follow the same trend. For measurement durations at least 300 times longer than τ_c, the simulated decay time $\tau_{c,\text{sim}}$ is recovered with a bias below 10% (region shaded in gray). D) Representation of panel C) without normalization to the simulated decay time allows for the direct visual judgment whether a particular measurement has a bias below the required accuracy. The gray area corresponds to measurements that are at least 300 times longer than the characteristic decay time $t_{\text{meas}} > 300 \cdot \tau_{c,\text{meas}}$. Points in the gray area have a bias below 10%.

performed for 1, 10, 100, and 1000 binding sites in a detection volume. Each simulation was repeated ten times. The total duration t_{meas} of the simulated measurements was 10^5 times longer than the simulated characteristic decay time $\tau_{c,\mathrm{sim}}$, which is expected to set the relevant time scale when assessing the required measurement duration [Schätzel et al., 1988, Saffarian and Elson, 2003]. To evaluate the effect of the measurement duration on the measured $\tau_{c,\mathrm{meas}}$, each simulation was split into shorter acquisitions which were independently autocorrelated and fitted by a single exponential. Finally, all obtained $\tau_{c,\mathrm{meas}}$ for one measurement duration were averaged. By this approach, $\tau_{c,\mathrm{meas}}$ was determined for a range of ratios $t_{\mathrm{meas}}/\tau_{c,\mathrm{sim}}$, yet all results corresponded to the same amounts of binding events sampled. As an example, consider N events were sampled in a full simulation with $t_{\mathrm{meas}}/\tau_{c,\mathrm{sim}} = 10^5$. To determine $\tau_{c,\mathrm{meas}}$ for a measurement duration $t_{\mathrm{meas}}/\tau_{c,\mathrm{sim}} = 10^1$, the original trace was cut into 10^4 independent traces, which were all analyzed to obtain mean and standard deviation of τ_c from 10^4 measurements. Consequently, the total number of sampled binding events is maintained.

The obtained decay times normalized to the simulated value $\tau_{c,\mathrm{meas}}/\tau_{c,\mathrm{sim}}$ are shown in figure III.6A. As expected, for sufficiently long measurements, the simulated decay time is recovered $\lim\limits_{t_{\mathrm{meas}}/\tau_{c,\mathrm{sim}}\to\infty} \tau_{c,\mathrm{meas}}/\tau_{c,\mathrm{sim}} = 1$. Interestingly, the convergence does not depend on the number of binding sites, which directly corresponds to the number of sampled binding events. Thus, the bias in the obtained decay times is not an effect of sampling statistics, but solely originates from the computed biased estimator of the autocorrelation curve. Remarkably, the situation for reversible binding is more convenient than for 2D diffusion, which requires much longer measurement durations to describe the diffusion time as adequately. This finding is very reasonable when comparing the shape of the autocorrelation functions for reversible binding (equation III.13) and 2D diffusion through a confocal volume (equation II.32). The autocorrelation function for 2D diffusion diffusion has a much longer tail (figure III.6B), which requires longer measurement durations to be adequately described. Importantly, in none of the cases, the averaging of many short measurements is equivalent to an individual long measurement.

To relate these simulations to experimental data, we reanalyzed the previously presented measurements on the DNA hybridization of 7-10 nt overlaps (section III.2.2). As for the simulations, measurements were cut into shorter segments and reanalyzed. The obtained τ_c was normalized to the obtained value for the longest measurements, i.e. the previously presented results (table III.1). In figure III.6C, the experimental data points are superimposed with the mean of the simulation with 1000 binding sites, without any further parameter adjustment. Although simulated and experimental data sets originate from entirely different sources, they follow the same trend, indicating that this convergence is a universal relation. The experimental results are systematically slightly below the simulated convergence, which can be attributed to the noise in real experiments. Very importantly, figure III.6C provides a relation between bias on $\tau_{c,\mathrm{meas}}$ and the required measurement time. Based on this, the measurement duration can be adjusted with respect to the required accuracy. For example, a systematic bias below 10% requires measurement durations that are at least 300 times longer than the characteristic decay time of the autocorrelation function. In figure III.6D, the same data set is replotted without any normalizations. This graph provides a tool for the quick visual inspection of the required measurement duration. After a measurement of duration t_{meas}, which yielded a value $\tau_{c,\mathrm{meas}}$, the bias is below 10% if the point lies in the gray area.

III.3.1.2 Minimal frame rate of individual SI-FCS measurements

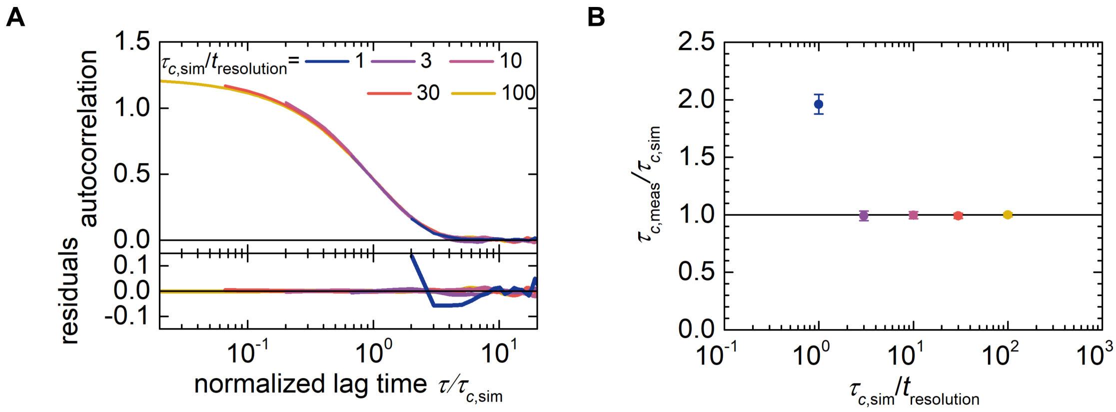

Figure III.7: Effect of the frame rate on SI-FCS measurements. A) Simulate autocorrelation curves (solid lines) with time resolutions (correspond to frame rates) that were up to 100 times longer than the simulated decay times $\tau_{c,\mathrm{sim}}$. For clarity, only the simulated autocorrelation curves are shown. The data sets were fitted by single exponentials. B) For time resolutions that are at least three times shorter than the characteristic decay time, the simulated decay times are recovered. Mean and standard deviations of 10 independent simulations each are shown.

The quality of SI-FCS measurements not only depends on the duration of individual experiments, but also on the time resolution, i.e. the frame rate of the acquisition. Intuitively, the time $t_{\mathrm{resolution}}$ between two consecutive frames needs to be shorter than the characteristic decay time of the autocorrelation curve to properly describe the dynamics. If this is not the case, but $t_{\text{resolution}} > \tau_c$, the situation is similar to the contribution of 3D diffusion to the SI-FCS experiments presented above in sections III.2.2 and III.2.3: the dynamics are equilibrated on the sampled time scales and are no longer observed as a decay in the autocorrelation curve. Moreover, a tuning of the time resolution is not only a useful tool to minimize the amount of acquired data, as higher frame rates requires more hard disk space, but also may reduce photobleaching in the sample. An example was already considered in section III.2.2 for 10 nt DNA hybridizations where τ_c was on the order of 100 s. To minimize photobleaching, the frame rate was set to 10 Hz instead of 85 Hz, which was used for all other samples (compare Materials and Methods in appendix A.2).

Similarly to the previous section, the required minimal time resolution was determined by Monte Carlo simulations of reversible binding kinetics. Figure III.7A shows representative autocorrelation curves with time resolutions ranging from 100 times longer than τ_c to equivalent to τ_c. Except for the very extreme of $t_{\text{resolution}}/\tau_c = 1$, the fits of all simulated autocorrelation curves recovered the assumed characteristic decay time $\tau_{c,\text{sim}}$. Thus, the concluded rule of thumb is that the time resolution of the acquisition needs to be 3 to 10 times smaller than the characteristic decay time. Retrospectively, these simulations validates the frame rates used for the 7-10 nt hybridizations in section III.2.2.

III.3.1.3 Conclusions for the accessible time scales

From the discussed practical considerations for the timing parameters and the underlying dynamics, the temporal regimes that are accessible to SI-FCS can be concluded. On short time scales, two major limitations are discernible. First, the time resolution of the detector clearly restricts the fastest dynamics that can be resolved. For modern EMCCDs, the frame rate for camera-based FCS applications can be readily reduced to the low to sub-ms regime [Sankaran et al., 2009, Bag et al., 2012, Capoulade et al., 2011] by reducing the pixel number. This comes at the cost of larger image files, less collected photons per pixel and thus lower signal-to-noise ratios. However, it should be noted that the autocorrelation curves presented in figures III.2, III.3 and III.4 have no discernible random noise contributions, which suggests that compromises can be made in this direction. Secondly, at short lag times, the ligand diffusion in 3D contributes to the autocorrelation function. Unfortunately, this contribution decays only slowly [Ries et al., 2008a]. An example for the effect of 3D diffusion on the autocorrelation curve is illustrated by the results of a Monte Carlo simulation in figure III.8. Clearly, the simulated full autocorrelation (black line)

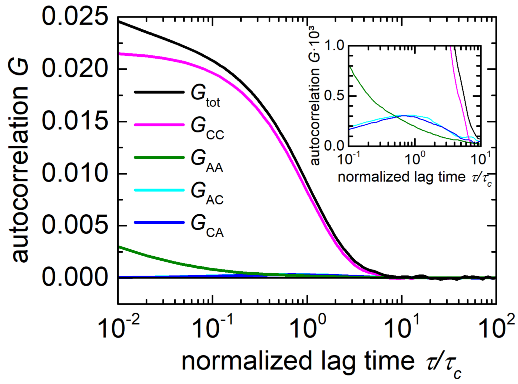

Figure III.8: Simulated autocorrelation curve for SI-FCS with 3D diffusion and reversible binding. The curves were computed from Monte Carlo simulations, which allowed to track whether a detected signal originated from free (state A) or bound ligand (state C, compare figure III.1A): $F(t) = F_{\mathrm{A}}(t) + F_{\mathrm{C}}(t)$. Thus, the individual contributions to the autocorrelation curve could be disentangled. For the assumed settings, the total autocorrelation curve (G_{tot}, black line) is dominated by reversible binding, which corresponds to the blinking of surface binding events (G_{CC}, magenta). On the other hand, at short lag times there is a significant contribution from free ligand diffusion (G_{AA}, green). In this particular case, the cross-terms G_{AC} and G_{CA} are negligible (blue, cyan, magnified inset). This graph has only an illustrative purpose, as the contribution of ligand diffusion and cross-terms depend on a range of factors. The detailed settings of this simulation are nonetheless provided in appendix A.2.

has not only a contribution from reversible binding (magenta), but also from 3D diffusion (green line). The specific magnitude of the contribution depends on the ligand concentration, the number of surface binding sites, and the characteristic times of lateral diffusion $\tau_{xy} = \frac{a^2}{4D}$, axial diffusion $\tau_z = \frac{d_{\mathrm{eva}}^2}{4D}$ and reversible binding τ_c. Here, the side length a of the ROIs was introduced. To estimate, which values of τ_c are accessible, we assume τ_c needs to be at least one order of magnitude larger than the 3D diffusion times. For the imager strand used in this study, $D \approx 200\,\mu\mathrm{m}^2/\mathrm{s}$ was measured (figure A.4 in appendix A.3), which for $d_{\mathrm{eva}} = 100\,\mathrm{nm}$ and $a = 5.12\,\mu\mathrm{m}$ (32 pixels á 160 nm) yields $\tau_z = 12.5\,\mu\mathrm{s}$ and $\tau_{xy} = 33\,\mathrm{ms}$. Thus, values of τ_c down to around 400 ms can be considered resolvable. The characteristic decay times measured here (table III.1) meet this criterion. Nonetheless, the effect of diffusion is already discernible in the autocorrelation curves of 7 nt hybridizations (figure III.2A). Similarly, for the 27 kDa protein green fluorescent protein (GFP) with $D \approx 90\,\mu\mathrm{m}^2/\mathrm{s}$ [Petrášek and Schwille, 2008], this estimate yields that $\tau_c > 750\,\mathrm{ms}$ ($\tau_z = 28\,\mu\mathrm{s}$, $\tau_{xy} = 73\,\mathrm{ms}$) should be resolvable. These estimations of the lower limit of accessible characteristic decay times can be potentially pushed to significantly shorter times if the ligand diffusion in 3D is accommodated in the analysis of the autocorrelation curve (compare section III.4).

It needs to be mentioned that the presented discussion is a very simplified view for illustrative purposes. For a more quantitative analysis, the full autocorrelation curve needs to be considered. Moreover, the lateral diffusion time can be tuned by adjusting the ROI size. Ideally, for a ROI much larger than the axial penetration depth, the axial direction becomes the only route for molecule to enter and escape the detection volume, which simplifies the axial autocorrelation function [Ries et al., 2008a]. On the other hand, the autocorrelation function for 1D diffusion decays very slowly and a large ROI corresponds to a larger detection volume, which reduces the relative contribution of reversible binding to the measure autocorrelation curve. Thus, when accounting for diffusion, the size of the detection volume needs to be finely tuned, and potentially also systematically varied [Bag et al., 2012]. Similar arguments hold when lateral receptor diffusion occurs.

At the other end of the spectrum, the maximum τ_c that is accessible to SI-FCS is governed by photobleaching and the measurement duration. The latter solely depends on the accessible time at the microscope, as well as setup and sample stability. The effect of photobleaching will be discussed in the following section. Overall, this study shows that decay times on the order of 100 s are readily accessible to SI-FCS.

III.3.2 Effect of photobleaching

Photobleaching poses a major problem for quantitative fluorescence-based binding studies. Regardless of the method used, e.g. dwell time measurements through SPT, or autocorrelation approaches, the apparent observed dynamics is artificially shortened by photobleaching. In essence, bound particles that are photobleached cannot be distinguished from unbinding events and contribute to the analysis in the same way. Moreover, one pathway of triplet relaxation of the fluorophore is accompanied by the generation of singlet oxygen [Davidson, 1979, Wilkinson et al., 1994, Eggeling et al., 1999], which is highly reactive. Thus, this reactive oxygen species is generated in very close proximity to the fluorophore and the observed receptors, and may potentially alter both of them. To minimize photobleaching-related artifacts, several approaches are commonly followed. First, oxygen may be depleted from the buffer, either by degassing or more commonly by enzymatic oxygen removal, e.g. through the most frequently used glucose oxidase catalase system [Benesch and Benesch, 1953]. A recently developed system [Swoboda et al., 2012] even

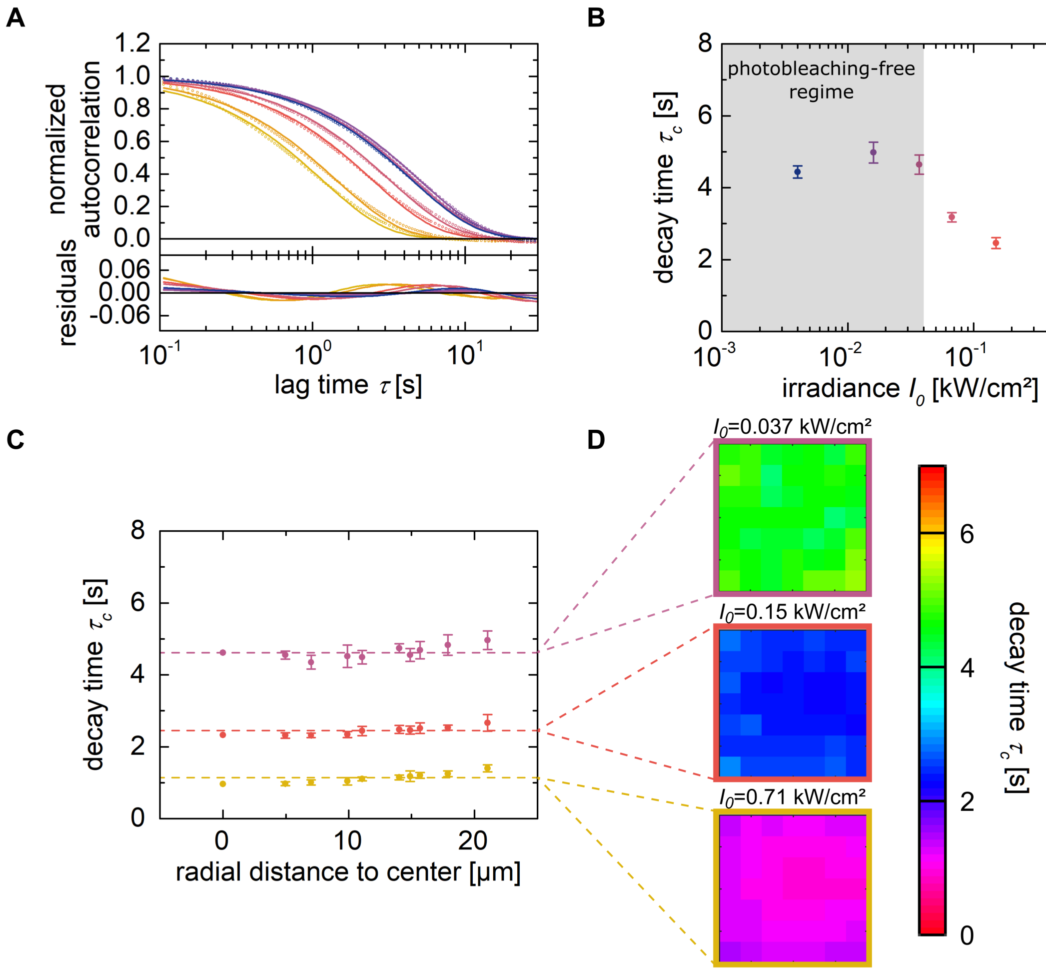

Figure III.9: Identification of a photobleaching-free regime. A) Mean measured autocorrelation curves (circles) of 9 nt hybridizations with 10 nM imager strand at different irradiances. Each autocorrelation curve corresponds the mean from 49 different ROIs and was fitted by single exponentials. B) Characteristic decay times τ_c obtained from the data sets in A). At peak irradiances above 0.04 kW/cm^2, the measured τ_c decreases with increasing irradiance, indicating photobleaching. C) Radial distribution of τ_c measured in ROIs with different distances to the center of illumination. At high irradiances, a spatial dependence is discernible, corresponding to the Gaussian illumination profile. D) Corresponding maps of the obtained decay times show shorter decays in the center of illumination, except for the lowest displayed irradiance, which shows no obvious spatial dependence of τ_c.

circumvents the sample acidification typically found for enzymatic oxygen removals [Shi et al., 2010, Kim et al., 2012]. Importantly, the removal of oxygen requires the addition of another triplet quencher to maintain the fluorophore brightness [Rasnik et al., 2006, Vogelsang et al., 2008, Dave et al., 2009]. Alternatively, recently developed organic fluorophores feature *in situ* triplet quenchers, which are chemically linked to the fluorophore [Altman et al., 2011, van der Velde et al., 2016, Zheng et al., 2014, Juette et al., 2014]. In this study, none of these approaches was used, as the excitation irradiance was carefully tuned to a regime where the autocorrelation curves are not affected by the irradiance.

The aforementioned shortening of the observed characteristic decay time can be used to identify a photobleaching-free regime. To this end, a set of experiments was performed with different powers of the excitation light, which was conveniently controlled through the transmission of the acousto optical tunable filter (AOTF) (compare figure A.1 in appendix A.1). As the width of the Gaussian excitation profile was constant, such a power series can be directly related to the applied peak irradiances. The corresponding autocorrelation curves and the single exponential fits for 9 nt DNA hybridizations are shown in figure III.9A. Clearly, for decreasing irradiances, the autocorrelation curves shift to longer lag times until a certain limit is reached. Moreover, the overall residuals of the single exponential fit become larger for increasing irradiances, indicating that in the presence of photobleaching the model of reversible binding as derived in section III.2.1 does not apply. The obtained decay times are shown in figure III.9B, together with the identified regime $I_0 < 0.04\,\mathrm{kW/cm^2}$ where the obtained decay time is not affected by the irradiance. In this regime, no photobleaching artifacts are observed for the 9 nt samples, and consequently, the faster dynamics of the 7 nt and 8 nt hybridizations should similarly be free of photobleaching artifacts for $I_0 < 0.04\,\mathrm{kW/cm^2}$. For the 10 nt hybridizations, a similar power series was performed (data not shown). Based on this power series, the measurements of 10 nt hybridization were conducted with a lower frame rate of 85 Hz, as compared to 100 Hz for 7–9 nt.

The small standard deviations of the autocorrelation curves (compare figure III.2) from several ROIs across the excitation volume already indicated that at sufficiently low irradiances, the autocorrelation curves are spatially invariant. This is the desired situation, as the sample has binding sites homogeneously distributed on the surface. At high irradiances however, the decay times are shortest in the center of illumination, corresponding to the Gaussian shaped excitation profile, which causes higher bleaching rates in the center. The obtained maps of τ_c, obtained from the 7x7 ROIs, demonstrate that for 9 nt hybridizations no spatial dependence of the outcome is discernible for irradiances $I_0 < 0.04\,\mathrm{kW/cm^2}$. Thus, the autocorrelation curves from these ROIs sample the same kinetics and can be averaged.

III.3.3 Reproducibility of individual SI-FCS measurements

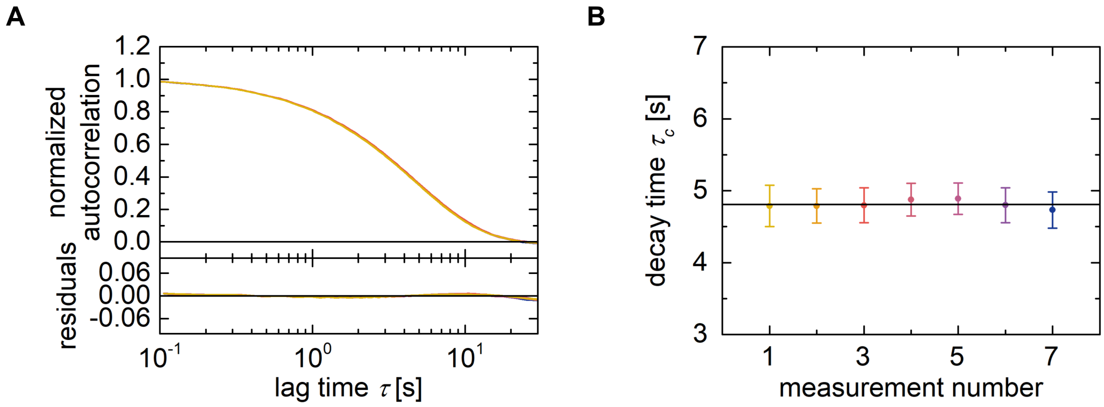

Figure III.10: Reproducibility of individual SI-FCS measurements. A) Overlay of seven independent, yet indistinguishable autocorrelation curves of 9 nt hybridization with 10 nM imager strand. Each autocorrelation curve corresponds to the mean from 49 ROIs. For clarity, only the experimental curves are shown. The quality of the single exponential fits can be inferred from the residuals, which are below 2% of the amplitude at all times. B) Corresponding decay times obtained from the fits in A) show only little scatter around the mean (black line) and are highly reproducible. Data points correspond to mean and standard deviation from 49 ROIs.

Having shown that the autocorrelation curves across the entire field of view are indistinguishable, the investigation of the reproducibility across samples was the next step towards the qualification of SI-FCS as a reliable method to quantify surface binding. Obviously, this method is only a reliable tool if the results reproduce with small scatter. The underlying system of reversible binding aside (here 9 nt reversible DNA hybridization), only the temperature, the buffer composition, i.e. salt concentration [Owczarzy et al., 2003, von Ahsen et al., 2001, Mitsuhashi, 1996, Lang and Schwarz, 2007], and the precision of the method are expected to influence the outcome. As identical buffers were used for all experiments, the salt concentration can be considered constant across all measurements. Similarly, the temperature of the optical laboratory was globally controlled and kept constant at 23 °C.

The autocorrelation curves obtained from seven independent measurement are superimposed in figure III.10A, and are indistinguishable. Consequently, the obtained characteristic decay times show almost no scatter around the mean and reproduce (figure III.10B). Remarkably, when calculating the overall weighted mean and standard deviation of τ_c from all seven measurements, with the individual standard deviations as weights, one obtains

$\tau_c = (4.81 \pm 0.03)$ s. This is not only reproducing the results presented in figure III.2, but also corresponds to a standard deviation of less than 1% of the mean.

III.3.4 Robustness of SI-FCS against defocused image acquisitions

In the majority of FCS experiments, the temporal loss of correlation originates from the diffusion of fluorescent particles into and out of the detection volume. For such systems, the knowledge of the shape and size of the detection volume is crucial to translate the measured diffusion time, a setup dependent parameter, into a diffusion coefficient, a universal physical quantity. Typically, the shape of the detection function is inferred from theoretical predictions and estimations, whereas the physical size is determined by a calibration measurement. Not only does the initial calibration consume valuable measurement time, it also adds an experimental error to all measurements that rely on this calibration, and requires the assumption of a function describing the detection profile. The evanescent excitation field in objective-type TIR-FCS is usually assumed to be a single exponential (e.g. [Lieto et al., 2003, Lieto and Thompson, 2004, McCain and Harris, 2003, Harlepp et al., 2004, Anhut et al., 2005, Hassler et al., 2005b, Hassler et al., 2007, Blom et al., 2009, Thompson and Steele, 2007]), which may often not be the case (compare section III.4) [Hlady et al., 1986, Oheim and Schapper, 2005, Mattheyses and Axelrod, 2006, Brunstein et al., 2014a, Brunstein et al., 2014b].

In this work, SI-FCS is used to measure reversible binding kinetics, where the signal fluctuations are fully attributed to binding and unbinding events. Consequently, no spatial information is required or assumed for this approach. Thus, as long as diffusion does not contribute to the autocorrelation curve, SI-FCS is a calibration-free method. For a more complex system with lateral receptor diffusion in 2D, the internal calibration for camera FCS proposed by Bag *et al.* may be used [Bag et al., 2012]. Only if the ligand diffusion in 3D is of relevance to SI-FCS experiments, a calibration may be required.

Not only does SI-FCS not require calibrations, its spatial robustness also implies that it is invariant to slightly defocused samples. If the sample is not perfectly in focus, the PSF is wider and the projection of the detection volume, here an individual ROI which corresponds to an assembly of pixels, into the sample appears more blurred and is thus widened. To investigate the effect of such defocused acquisitions, we performed a series of 8 independent measurements on one sample with 9 nt DNA hybridizations. Each measurement lasted 5 h. The sample was initially brought into focus, and was subsequently moved

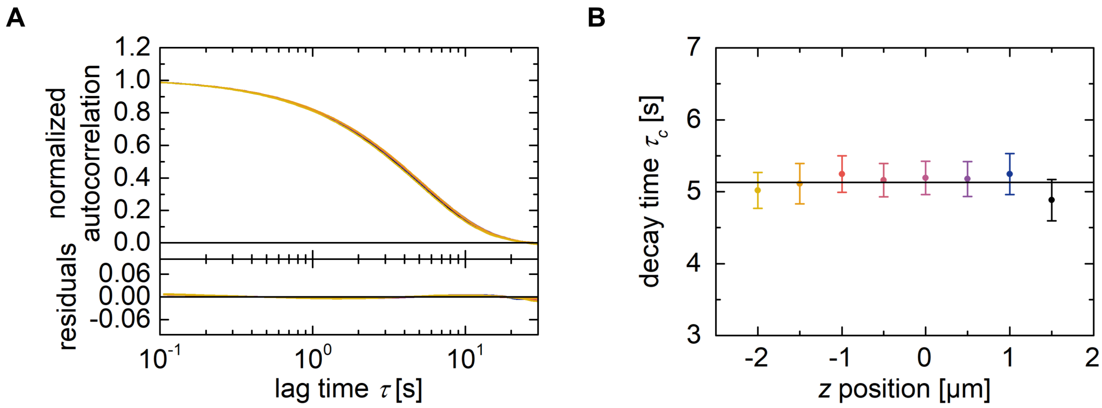

Figure III.11: Robustness of SI-FCS to defocused image acquisitions. A) Overlay of eight independent autocorrelation curves, measured for a range of axial sample positions. For clarity, only the experimental autocorrelation curves are shown. The quality of the single exponential fits is highlighted by the residuals. B) Corresponding decay times, obtained for different axial sample positions relative to the objective's detection PSF. The decay times reproduce over the full range of investigated axial sample positions, although the signal-to-noise ratio differs between the measurements.

2 µm down to start the first acquisition. After each measurement, the sample was moved up by 0.5 µm, until a position 1.5 µm above the focus position was reached. The focus stabilization ensured that the sample was kept at the respective target positions relative to the objective's focus. Thus, the range of covered z-positions supposedly covers much more than the axial extent of the objective's detection function. The autocorrelation curves obtained from these measurements are indistinguishable, and the obtained characteristic decay times are highly reproducible (figure III.11), albeit the signal-to-noise lowers considerably when the sample is out of focus. Consequently, SI-FCS for the quantification of reversible binding is robust to defocused imaging. Moreover, as a byproduct, this series of measurements indicate that these samples are stable at 23 °C for at least 40 h of acquisition.

III.4 Direct characterization of the evanescent field

So far, this chapter omitted any contributions of 3D ligand diffusion to the autocorrelation curve. This approach is useful, because it massively simplifies the otherwise complex analysis of the full autocorrelation curve [Thompson et al., 1981, Ries et al., 2008a]. Moreover, any approach that takes the diffusion in axial direction into account requires precise knowledge of the excitation and detection profiles. For these considerations, for the first time in this work the microscopy scheme needs to be taken into account for SI-FCS, which in this study is TIRF microscopy. Ideally, the characteristics of SAF emission [Lukosz and Kunz, 1977b, Lukosz and Kunz, 1977a, Hellen and Axelrod, 1987, Enderlein et al., 1999, Enderlein, 2003] are also taken into account. Despite the potential challenges, a description of 3D ligand diffusion coupled with binding kinetics by SI-FCS is a rewarding goal, because it would make even shorter binding kinetics in the millisecond to second regime accessible. The precise characterization of the evanescent field, as required for axial diffusion dynamics in TIR-FCS has been subject to several studies. Typically either a single exponential was assumed for the evanescent wave profile and the characteristic decay length was determined, or the actual shape of the evanescent profile was measured.

III.4.1 Shortcomings of existing methods

Assuming a single-exponential excitation profile, previous studies calculated the penetration depth d_{eva} based on measurements of the incident angle [Fish, 2001, Schwarz et al., 2011, Burghardt, 2012, Müller, 2012, Brunstein et al., 2014b] between the incoming beam and the cover slide. It should be noted that these approaches are very sensitive to the refractive indices (compare equation II.17), which need to be known very accurately. Other studies used TIR-FCS to calculate the penetration depth from the free diffusion of fluorophores of known diffusion coefficient [Harlepp et al., 2004], an inclined coverslide with immobilized fluorophores [Fiolka et al., 2008], or the image of a sphere superseding fluorophores in solution [Schwarz et al., 2011]. While all these approaches provide rough estimates of the penetration depth, they are insensitive to deviations from a single exponential. These deviations are however frequently found in TIRF microscopy [Hlady et al., 1986, Oheim and Schapper, 2005, Mattheyses and Axelrod, 2006, Brunstein et al., 2014b, Brunstein et al., 2014a], likely to originate from scattered light and diverging beam contributions, and result in an extended axial excitation profile. These effects are particularly pronounced in objective-type TIRF microscopy [Oheim and Schapper, 2005, Brunstein et al., 2014b].

For the quantification of axial diffusion by SI-FCS the excitation profile needs to be known, and thus a direct sampling of the excitation field in different heights above the coverslide would be preferable. In the past, several of such methods have been developed [Steyer and Almers, 1999, Mattheyses and Axelrod, 2006, Gell et al., 2009, Saffarian and Kirchhausen, 2008, Liu et al., 2009, Sarkar et al., 2004, Oreopoulos and Yip, 2008, Ramachandran et al., 2013, Brutzer et al., 2012, Graves et al., 2015, Seol and Neuman, 2018, Unno et al., 2015, Unno et al., 2017, Cabriel et al., 2018]. Unfortunately, all of these methods either do not perform at the refractive index of biologically relevant samples [Steyer and Almers, 1999, Mattheyses and Axelrod, 2006], need demanding sample preparations [Gell et al., 2009], or require advanced equipment, potentially with laborious calibrations, that is not standard to the vast majority of TIRF microscopes [Saffarian and Kirchhausen, 2008, Liu et al., 2009, Sarkar et al., 2004, Oreopoulos and Yip, 2008, Ramachandran et al., 2013, Brutzer et al., 2012, Graves et al., 2015, Seol and Neuman, 2018]. Unno and colleagues made an attempt to position fluorescent emitters on polymer blocks of defined heights, using polymers of refractive index 1.33 [Unno et al., 2015, Unno et al., 2017]. However, their approaches required advanced equipment, featured only few sampling heights, and were performed with fluorescent particles that had a diameter similar to the size of the penetration depth.

III.4.2 Preparation protocol of a novel calibration slide

Due to the lack of an easy tool to calibrate the evanescent field, we spent considerable efforts to develop an approach for the manufacturing of a calibration slide (figure III.12). This slide was designed to meet the following requirements: sampling of the excitation field in multiple heights, matching of the refractive index in typical biological samples, easy to use, compatible with standard TIRF microscopes, no additional equipment required, long shelf-life. To this end, we developed a multistep calibration slide using the polymer MY133-MC (MY Polymers Inc., Ness Ziona, Israel), which has a refractive index of 1.33. In an initial step, the bottom side of a conventional #1.5 coverslide was coated with a protective layer of the chemical First Contact (Photonic Cleaning Technologies, Wisconsin, USA) that can be easily stripped off. The MY133-MC polymer was subsequently applied by repetitive dip coating of the coverslide in a solution of MY133-MC (figure III.12B, for more details see Materials and Methods in appendix A.2). At each iteration, the depth by which the coverslide was dipped into the polymer solution was decreased, resulting in a staircase-like polymer profile on both sides of the coverslide. To clear the bottom side, the initially deposited protective layer was stripped off. Finally, the calibration slide was cured at ambient temperature and humidity.

To measure the heights of the individual steps, atomic force microscopy (AFM) was used. Each of the steps was scratched by a blade (figure III.12C), which served two purposes: First, a scratched cross acted as a fiducial marker to ensure that AFM and

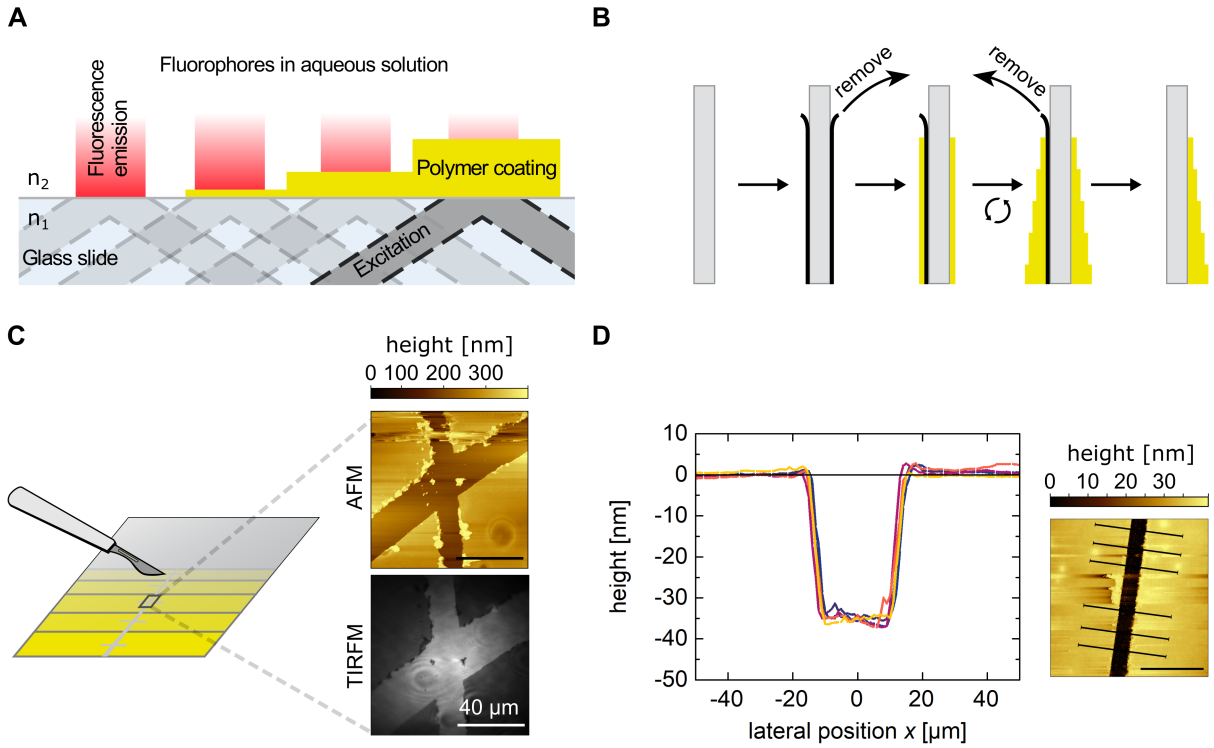

Figure III.12: Multistep calibration slide for the direct calibration of the evanescent field. A) Conceptual idea of a calibration slide: A cover slide is coated with polymer steps (yellow) with a refractive index matching that of water ($n = 1.333$). The coated slide is loaded with free fluorophores in solution, or point-like emitters are immobilized on the polymer steps. With increasing height of the polymer steps, the fluorescence detected by TIRF imaging decreases. B) Preparation procedure of the calibration slide: a cover slide is coated with a removable protective layer (black) on one side and subsequently dip coated several times with a polymer that has the refractive index of water. For each iteration of dip coating, the slide is immersed less into the polymer solution, yielding discrete steps. The final removal of the protective layer clears the lower side of the cover slide. C) Fiducial markers that are visible in AFM and TIRF microscopy are generated on each slide by scratching with a blade. D) Height profiles across a scratch through one polymer step. The height of each polymer step is measured relative to the cover slide surface, which is made accessible by the scratch. Such measurements are performed for every step height. All scale bars correspond to 40 µm. Figure adopted from [Niederauer, 2018].

TIRF imaging were performed in the same positions. Second, the scratching removed the polymer, thereby uncovering the glass surface, which served as a reference to measure the step heights by AFM (figure III.12D). The height profile across such a scratch was highly reproducible. Notably, when performing AFM imaging on one polymer plateau, the height varies within on field of view (FOV) (approximately 100x100 μm^2) with a standard deviation of around 1 nm ([Niederauer, 2018], data not shown). In between two plateaus, the dip coating preparation procedure comes with a transition region of around 100 µm ([Niederauer, 2018], data not shown), which me be reduced by an op

III.4.3 Direct measurement of the evanescent field profile

By immobilization of point-like emitters on the individual steps, this calibration slide can be used to directly sample the excitation profile, convolved with SAF effects, at different heights above the coverslide. Here, a slightly simpler approach that does not require any immobilization is demonstrated. Similar to Mattheyses and Axelrod [Mattheyses and Axelrod, 2006], we assumed that the excitation profile is a bi-exponential with relative amplitudes f_1 and f_2. In this picture, the first decay corresponds to the evanescent field, whereas the second decay covers propagating and evanescent contributions from scattered light, but may potentially be also effected by the shape and size of the objective's detection PSF. Correspondingly, this second decay is expected to have a significantly larger decay length. Although there is no physical justification to describe a potentially propagating beam with a single exponential decay away from the interface, this approach adequately described the experimental data (figure III.13).

The calibration slide was loaded with aqueous solution of fluorescent dye and imaged with the described TIRF microscope (compare appendix A.1). As the axial extent of the objective's detection PSF is much larger than the decay of the evanescent field, the signal acquisition corresponds to an integration over the axial coordinate z from the step height h to infinity:

$$\begin{aligned} I(h) &= I_0 \int_h^\infty \left[f_1 \exp\left(-z/d_{\text{eva}}\right) + f_2 \exp\left(-z/d_{\text{rest}}\right)\right] \, \mathrm{d}z \qquad \text{(III.15)} \\ &= I_0 \left[f_1 d_{\text{eva}} \exp\left(-h/d_{\text{eva}}\right) + f_2 d_{\text{rest}} \exp\left(-h/d_{\text{rest}}\right)\right] \end{aligned}$$

Thus, although the camera detection equals an integration over the axial excitation, the bi-exponential shape is maintained.

Figure III.13A shows representative background-corrected TIR images of Alexa488 diffusing in water above several coating heights. As expected, the detected fluorescence intensity decreases with increasing thickness of the coating. Moreover, these images reconfirm the need to measure the shape of the excitation volume. The central evanescent

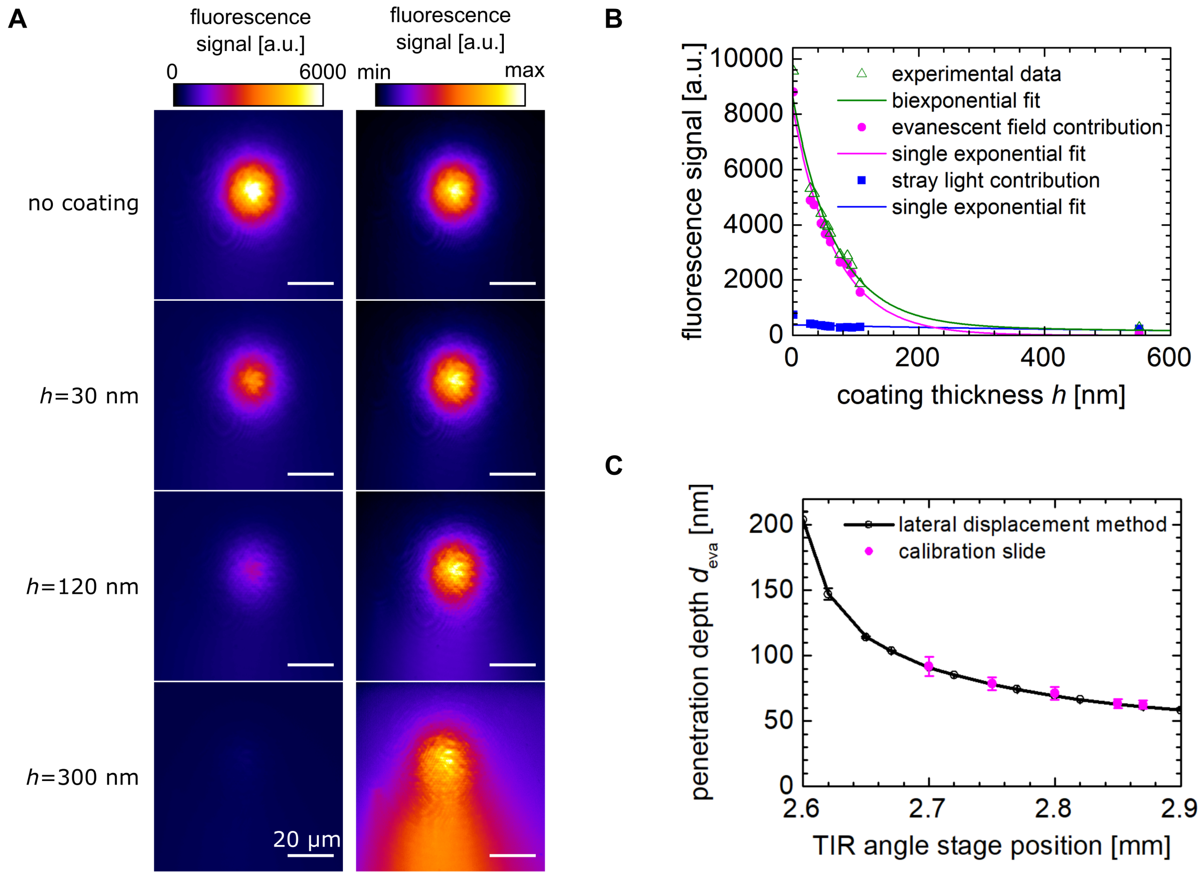

Figure III.13: Direct characterization of the evanescent field with the newly developed calibration slide. A) Representative images of 5 µM Alexa488 diffusing above different coating thicknesses of MY133-MC. The images are shown with a common color scale (left column), highlighting the decrease of fluorescence intensity with increasing cover-slide distance, and an individual color coding, covering the range of each individual image. The latter highlights the contribution of the non-evanescent field, which has an increasing relative contribution with increasing distance to the coverslide. In contrast to the presented SI-FCS measurements, these images were taken without a 3x magnification telescope in the excitation pathway (compare figure A.1 in appendix A.1). The scale bars correspond to 20 µm. B) Fluorescence signal (triangles) decreases with increasing coating thickness. Each point has an evanescent (circles) and a propagating (squares) wave contribution. The evanescent wave contribution follows a single exponential decay, from which the penetration depth can be obtained by a corresponding fit. The propagating distribution decays very slowly, and dominates for heights $h \gg d_{\text{eva}}$. This graph was taken for an incident angle of 71.71°. The imaging was performed using another calibration slide than in panel A and therefore, other heights were sampled. C) The obtained d_{eva} reproduces the values expected from the incidence angles measured with the lateral displacement method for a range of TIR angle stage positions (compare figure A.1 in appendix A.1).

excitation profile is superimposed with another contribution, which starts dominating with increasing coating thickness. Moreover, this contribution does not appear to have a common lateral center with the evanescent excitation. These observations demonstrate a second, non-evanescent contribution to the excitation profile. First, the relative amplitude of this contribution starts to dominate far away from the glass-water interface, because the intensity of a propagating beam ideally does not decrease while penetrating the sample, whereas the evanescent wave quickly decays. Secondly, the propagating excitation wave separates more from the evanescent wave with increasing coating thickness, because it still has a lateral k-vector, whereas the evanescent wave only has an imaginary k-vector normal to the interface. Consequently, close to the surface, the evanescent excitation is dominant, but far away from the surface, the propagating beam is the primary excitation source. As the detection PSF of the objective is much larger than d_{eva}, all the corresponding fluorescence contributions are integrated by the objective, which in return means that also fluorophores that are much further than d_{eva} away from the interface contribute to the overall signal. For the contribution of 3D diffusion to TIR-FCS autocorrelation functions, this extended axial excitation profile results in longer diffusion times.

For the quantification of the axial excitation profile, ROIs of 32x32 pixels, over which the signal was integrated, were defined. By imaging a fluorophore solution above the steps of coating heights, $I(h)$ was experimentally sampled and fitted by a bi-exponential. As an example, for a position of the TIR angle stage, which was determined to correspond to an incident angle of 71.71° by the lateral displacement method (compare Materials and Methods in appendix A.2), the evanescent wave was determined to have a decay length $d_{\mathrm{eva}} = 66.7\,\mathrm{nm}$. The second exponential was found to have a decay length $d_{\mathrm{eva}} = 2.6\,\mu\mathrm{m}$. This long-range exponential is a formal approximation, but does not reflect the physical origin of the effect. The corresponding data set is shown in figure III.13B.

These measurements were repeated for several TIR angle stage positions, yielding a range of penetration depths for the respective evanescent excitation profiles. Moreover, the incident angles θ between the normal to the coverslide and the incoming excitation beam were measured for different TIR angle stage positions using the lateral displacement method (compare Materials and Methods in appendix A.2). From the knowledge of θ, d_{eva} can be calculated for ideal conditions using equation II.17. Thus, d_{eva} was obtained using two independent methods. The results are overlaid in figure III.13C and appear to yield identical results. Based on this result, two major conclusions can be drawn. First, the developed calibration slide recovers the expected penetration depth of the evanescent wave for TIRF microscopy and therefore appears to be a suitable tool for the axial sampling of the excitation profile. Second, this calibration slide outperforms methods that assume a single exponential excitation profile, because it also samples deviations from this assumption.

As a next step, the axial excitation profile that was determined here should be used for the analysis of 3D ligand diffusion in SI-FCS measurements with TIRF excitation. The performance of the calibration slide may be further optimized by immobilizing point-like emitters on the individual polymer steps, which would directly sample the local excitation profile without any axial integration. Moreover, such a calibration slide may be used to directly quantify the effect of SAF and the effect it has on an effective penetration depth to describe the convolution of excitation and detection profiles [Ries et al., 2008a].

Finally, the developed calibration slide has two major byproducts. First, with such a slide in hand, the evanescent field and the optics alignment can be routinely validated, which is important to ensure the quality and reproducibility of imaging data [Deagle et al., 2017]. A similar calibration slide is available for the quality control of lateral imaging parameters in fluorescence microscopy [Royon and Converset, 2017], but to the best of our knowledge, no such calibration slide has been developed for the assessment of the excitation field in TIRF microscopy. Second, the developed calibration slide may have great potential for 3D single-molecule localization microscopy. Typically, the precise axial localization relies on an initial calibration of the PSF performed on surface immobilized fluorescent beads or single-molecules [Huang et al., 2008, Juette et al., 2008, Pavani et al., 2009]. However, the PSF of a bead in water is different compared to the surface [Hell et al., 1993, Deng and Shaevitz, 2009, Backer and Moerner, 2014]. The calibration slide presented here allows for the sampling of the PSF in arbitrary heights at the refractive index of water without any advanced equipment and thus circumvents this potential error source and eliminates the need for advanced aberration corrections [Deng and Shaevitz, 2009, Izeddin et al., 2012, Bratton and Shaevitz, 2015, Shechtman et al., 2015]. Moreover, intensity-based axial super-resolution methods, e.g. TIRF incidence angle scanning [Boulanger et al., 2014], may directly benefit from this calibration slide.

III.5 Discussion of SI-FCS in relation to other methods

An extensive comparative study of all methods frequently used to characterize binding kinetics does not exist to the best of my knowledge, and would clearly exceed the scope of this thesis. Consequently, in the following SI-FCS will be compared to Localization studies of single molecules, which is methodologically among the closest methods to SI-FCS. A few paragraphs will be also spent on a comparison to BLI, QCM with dissipation (QCM-D) and SPR, before finally relating SI-FCS to confocal FCS.

III.5.1 Localization of single particles

Over the years, several methods have been developed to quantify binding. From all these methods, the determination of dwell times by SPT is supposedly the closest to SI-FCS. Both involve the fluorescence signal-based discrimination of bound and unbound particles. Moreover, SPT and SI-FCS are compatible with imaging modalities, can be conducted in identical sample chambers, and are commonly performed on TIRF microscopes. On the one hand, SPT relies on the detection of individual particles, which locally contribute more photons to a few camera pixels than rapidly diffusing particles, thus appearing as bright spots in a camera image. On the other hand, correlation-based approaches discriminate the binding events from other dynamics through the typical time scale on which these events occur. The computation of a correlation does not require the localization of individual particles in every image frame.

To highlight this fact, SI-FCS image stacks were simulated using the Picasso software tool [Schnitzbauer et al., 2017]. In these simulations, the surface densities of receptors were varied over almost five orders of magnitude, ranging from 3 to 10^5 binding sites within a 3.84x3.84 µm^2 area (figure III.14). For SPT the number of binding sites is not of particular importance, but rather the density of simultaneously bound sites per resolution unit (compare Materials and Methods in appendix A.2). As shown in figure III.14B, the simulated characteristic decay time is recovered for the whole range of simulated bound sites per resolution disk. The error bars correspond to the standard deviations from 10 independent simulations and decrease steadily, as the number of sampled binding events increases linearly with the number of surface receptors.

Figure III.14C gives an overview of typical images from the image stacks simulated for different densities of binding sites. Clearly, already above on average 0.1 bound sites per resolution disk, multiple binding events become optically irresolvable. The computed autocorrelation curve was not affected by these effects (figure III.14B), but clearly SPT starts failing. In contrast, as shown by the simulations, SI-FCS still performs adequately when the density of bound sites increases by another two orders of magnitude.

The results obtained for different receptor densities are confirmed by experimental data.

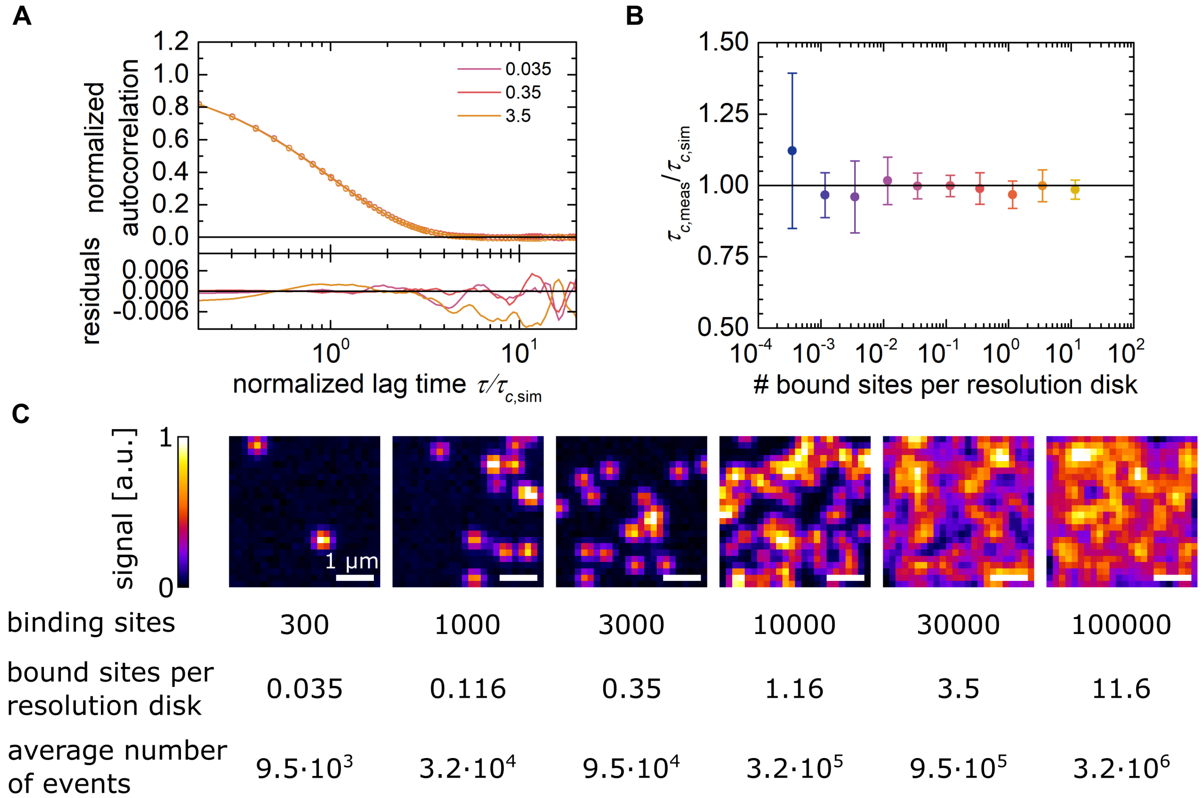

Figure III.14: Simulation of SI-FCS experiments at different surface receptor densities. A) Representative simulated normalized autocorrelation curves (circles) for different numbers of bound receptors per resolution disk. The autocorrelation curves were fitted using a single exponential (solid lines and residuals below). All simulations were performed using the same settings, but different numbers of binding sites, ranging from 3 to 10^5, were assumed (see Materials and Methods in appendix A.2). B) Obtained characteristic decay times for different densities of bound receptors approaches the simulated target value even for low densities of binding sites. The error bars correspond to means and standard deviations of 10 independent simulations. The standard deviations get successively smaller with increasing density of binding sites, as the number of sampled binding events steadily increases from around 300 for the least binding sites to almost 10^7 for 10^5 binding sites. C) Representative images, taken 100 s into each measurement. The color coding was adjusted for each image independently to give an impression of the density of binding events. Starting at on average 0.116 bound sites per resolution disk, individual events started overlapping in the simulated image and become unresolvable for single particle detection approaches. SI-FCS yields reliable results even at two orders of magnitude higher densities.

We prepared samples with 9 nt DNA hybridizations as usual, but varied the incubation concentration of DNA origamis $c_{\text{incubation}}$ as a means to control the final receptor density,

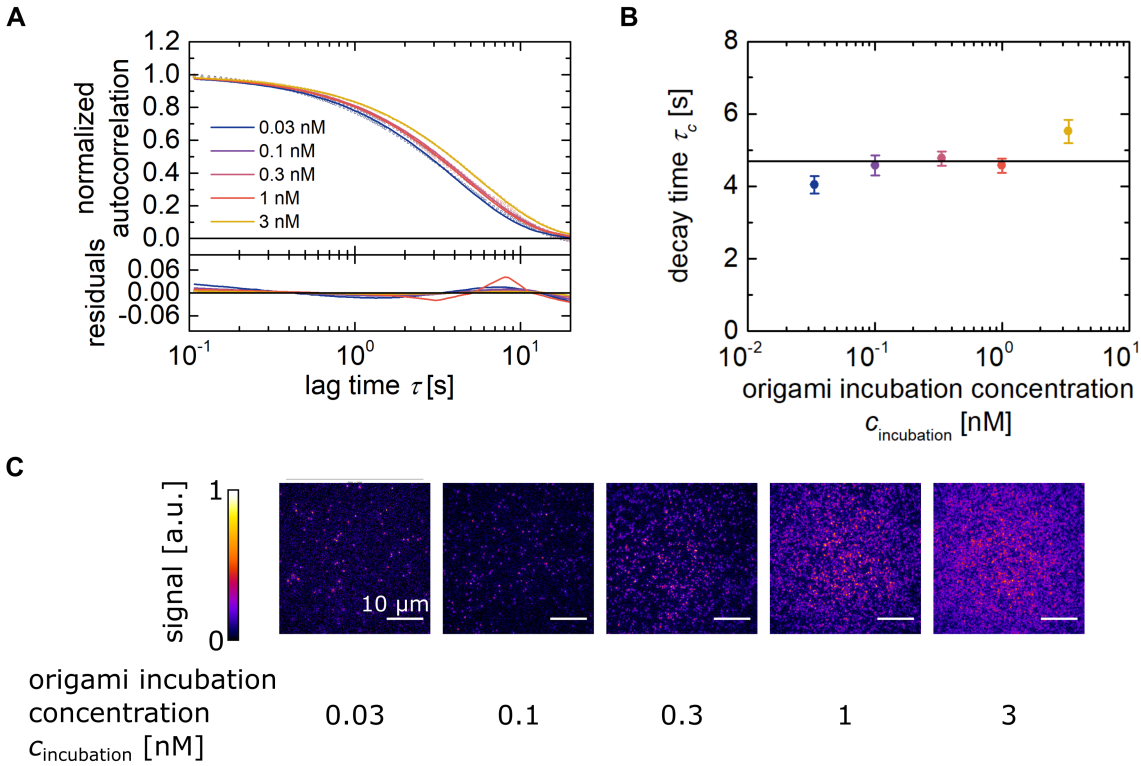

Figure III.15: SI-FCS experiments at different surface receptor densities. A) Representative autocorrelation curves (circles) for 9 nt hybridization kinetics. The sample chambers were prepared as usual (compare Materials and Methods in appendix A.2), but the samples were incubated with different DNA origami concentrations $c_{\text{incubation}}$. All previous experiments were conducted with $c_{\text{incubation}} = 0.5\,\text{nM}$. As usual, the autocorrelation curves were fitted with a single exponential (solid lines). B) Characteristic mean decay times and standard deviations from 49 different ROIs show only a small dependence on the origami concentration during incubation. C) Representative images show that the density of surface immobilized DNA origamis strongly depends on $c_{\text{incubation}}$ (compare figure A.5 in appendix A.3). At $c_{\text{incubation}} = 0.1\,\text{nM}$, the detection of individual binding events is already challenging because of the high mean surface density of bound imager strands. At higher surface densities, SI-FCS still yields identical τ_c, while methods based on single molecule registrations would clearly fail. The color coding was adjusted for each image independently to give an impression of the density of binding events.

i.e. the density of immobilized DNA origamis. The amount of receptors increases with increasing $c_{\text{incubation}}$, as shown in figure A.5 in appendix A.3. The overall brightness of the acquired images scales roughly linearly with $c_{\text{incubation}}$, indicating that not all streptavidin binding sites are saturated. However, the exact quantification of the receptor density is challenging, as the detected signal amplitude depends on a multitude of parameters, such as focus position, excitation irradiance, background level and detection efficiency. Therefore, the extraction of information about the underlying receptor density would require cumbersome calibrations [Weidemann et al., 2003, Galush et al., 2008]. Here, such steps were not performed, because we only aim to qualitatively assess the performance of SI-FCS at different receptor densities. The representative images displayed in figure III.15 already illustrate that for $c_{\text{incubation}} \gtrsim 100\,\text{pM}$ the conditions applied here are incompatible with single-molecule localizations. In contrast, SI-FCS yields consistent characteristic decay times across all these densities of receptors (figure III.15B). An increased receptor density also has the potential advantage to increase the relative contribution of binding dynamics to the autocorrelation curve, thereby suppressing contributions from diffusion dynamics, which were omitted when applying a single exponential model function (compare figure III.8).

As SI-FCS also performs at much higher densities of bound receptors, more events can be sampled in less time, which makes the detection of statistically significant numbers of events readily accessible. On the other hand, single-molecule localization experiments are not based on the biased estimator of the autocorrelation, but only need to ensure that slow contributions to the overall kinetics are adequately sampled. Consequently, tracking-based approaches converge to the true rates faster than SI-FCS.

The analysis of image stacks for SI-FCS is straightforward and leaves little room for tuning of parameters: ROIs are defined, the corresponding signal traces are calculated, the autocorrelation curves are calculated and finally fitted by a single exponential. Thus, the outcome does not depend on subjective assessments by the operator. For SPT-based approaches, the situation is significantly different, and the operator needs to tune several parameters which affect the outcome of the analysis. In the easiest case, the rough size of the PSF needs to be known, and the minimal brightness or intensity gradient of the particles need to be defined [Chenouard et al., 2014]. Depending on the algorithm, a manifold of other parameters may require tuning. To extract binding kinetics based on appearing and disappearing bright spots, the signal from one individual binding site may be transformed into a binary signal, i.e. on and off state. The time for which individual states are populated is sampled several thousand times and analyzed as histograms [Yang et al., 2004, Kubitscheck et al., 2005, Bowen et al., 2005, Elenko et al., 2010, Gebhardt et al., 2013, Loose et al., 2011, Schnitzbauer et al., 2017]. Consequently, the algorithm needs to be tuned such that particles are on the one hand found with a very high efficiency, yet statistical peaks in noise are not identified as a bound particle. In other words, the rate of true positives should be large, while the false negative rate needs to be low. This is corresponds to the classical receiver operating characteristic method, through which the performance of diagnostic tools can be evaluated [Fawcett, 2006]. Whenever a binding event that spans several image frames is not detected in one frame, the single binding event is registered as two independent events of shorter dwell time, which biases the determined histogram of bright and dark times. Thus, the tuning of the detection parameters has a tremendous impact on the outcome of localization based quantifications of binding kinetics.

Moreover, the image-based detection of individual single-molecules requires a high signal-to-noise ratio, which in return requires larger irradiances than SI-FCS. Thus, the regime where the results are not affected by the irradiance is broader for SI-FCS. The situation in localization-based approaches becomes even more challenging when several binding species are present. To resolve 7 nt and 9 nt hybridizations in one sample, as done by SI-FCS in the context of figure III.3, single-molecules need to be tracked at high frame rates around 100 Hz, with high signal to noise, yet other molecules need to be followed for more than 10 s, i.e. twice the mean dwell time of 9 nt hybridizations. Consequently, particles need to be readily tracked at high signal-to-noise ratios for 1000 frames without any photobleaching, which is very demanding.

The situation for localization-based measurements of binding rates is even more complicated, when several binding sites within one resolution disk get populated at the same time, or the receptors diffuse laterally. For the latter, the analysis is complicated, because the blinking receptors are potentially lost in their unbound state. Multiple binding events within one resolution unit on the other hand, may potentially distort the histograms of residence time and off time [Taylor et al., 2018]. For SI-FCS in contrast, multiple binding events within one ROI do not bias the autocorrelation curve (figures III.14 and III.15). Diffusing receptors on the other hand manifest as an additional decay in the autocorrelation curve and can be accounted for, as long as the diffusion time through the detection volume (ROI) is significantly larger than τ_c. Moreover, the lateral diffusion time can be tuned in SI-FCS during post-processing by adjusting the size of the detection volume.

III.5.2 BLI, QCM-D and SPR

SI-FCS determines kinetic rates of reversible binding in equilibrium. In contrast, BLI, QCM-D and SPR monitor the change of a signal in response to a sudden jump in ligand concentration. A quantitative comparison of these methods with SI-FCS for a range of receptor-ligand pairs would be desirable, but also potentially biased, as these methods have been optimized over decades and commercialized.

Nonetheless, there are some obvious differences. The sample chamber used in this study has a total volume far below 20 µL, which could potentially be reduced even further. The small required sample volume is unmatched by the other methods. Moreover, for experiments with concentration jumps, the precise timing can be difficult. Namely, these methods need to define a start time t_0 for the concentration jump. As this start time is not clearly defined e.g. in a flow chamber, very fast kinetics in the low second and sub-second regime are inaccessible. This study showed on the other hand that sub-second dynamics can be resolved by SI-FCS.

For membrane-binding studies, SI-FCS provides a direct imaging option to validate the membrane integrity. It shall be mentioned that QCM-D and SPR have been combined with fluorescence imaging, but require additional equipment, whereas SI-FCS naturally comes with an imaging option. On the other hand, the membrane formation over the entire chip can be monitored in QCM-D. Moreover, QCM-D measures the dissipation, which together with appropriate modeling can potentially provide information about the viscoelasticity of the adhered layer, a property inaccessible to all other methods.

All of the methods discussed here are based on a different read-out parameter. The detailed discussion of the advantages and disadvantages clearly exceeds the scope of this work. Nonetheless, it shall be mentioned that BLI, QCM-D and SPR perform without any fluorescent label, which circumvents artifacts caused by the fluorophore. On the other hand, this label-free advantage comes at the cost of no specificity to the target ligand. Neither BLI, nor QCM-D, nor SPR have the potential to perform in complex bio-fluids like cell lysates or even *in vivo*, whereas these systems are potentially accessible to SI-FCS.

III.5.3 Confocal FCS

Typical confocal FCS binding studies (compare chapter II) and SI-FCS follow very different approaches to quantify binding. While SI-FCS measures binding rates, classical FCS follows a stoichiometric approach based on relative abundances in multicomponent diffusion, which provides access to K_D, but not to the reaction rates. For the study of membrane binding, confocal FCS may additionally require a solubilization of the membrane.

In much less frequent cases, confocal FCS has been used to measure binding rates to immobile structures [Michelman-Ribeiro et al., 2009,Bierbaum and Bastiaens, 2013]. Compared to SI-FCS, this approach samples less binding events and has a larger contribution from 3D ligand diffusion. When using small ROIs, SI-FCS with TIRF excitation features smaller detection volumes compared to confocal FCS and thus allows for experiments at higher, more physiological concentrations [Li et al., 2017]. Because of the parallel detection in many pixels over more than 100 µm^2, SI-FCS provides outstanding statistics and has the potential to generate maps of binding rates. Moreover, the TIRF excitation used in this study is particularly convenient for the study of SLBs.

III.6 Conclusion

In this chapter, a new method for the quantification of surface binding rates has been demonstrated. Starting from the conceptual idea of SI-FCS, which integrates the signal over a surface, a camera-based combination of TIRF excitation and FCS was identified as one potential setup for the application of SI-FCS. In the following, the theoretical framework for the autocorrelation function was derived and shown to describe the reversible DNA hybridizations of 7–10 nt adequately. A set of experiments with different ligand concentrations was demonstrated to provide access to the association and dissociation rates, and hence the dissociation constant.

The characterization of binding rates by camera-based TIR-FCS, or SI-FCS in general, has to the best of my knowledge not been performed, and is thus far away from being a routinely used method. Thus, considerable work has been invested to develop strategies and find criteria for the identification of artifact-free measurement conditions. Namely, the required measurement durations, the camera frame rate, the effect of photobleaching, the reproducibility, and the surface receptor density have been addressed.

This work describes first steps towards the incorporation of 2D and 3D diffusion into the analysis of SI-FCS measurements. Moreover, the implementation of SI-FCS demonstrated here can be adapted on any TIRF microscope with a focus stabilization, which has become a standard equipment in many life science laboratories and imaging facilities. The small sample volumes required for SI-FCS, the compatibility with imaging modalities, and its steady-state operation without the need for external perturbations are the major advantages of the approach. The application of SI-FCS for the quantification of surface binding has the potential to make a major contribution towards understanding important biological systems on the quantitative level.

III.7 Outlook and future directions

This work provides a proof-of-principle of SI-FCS, from which a manifold of further developments can be envisioned. To encourage further development of SI-FCS, but also to highlight the potential of this method, this section outlines possible future directions.

The quantification of membrane binding is certainly one of the most promising future directions. Such experiments have to deal with the lateral 2D diffusion of ligand upon membrane binding, which could be addressed by several strategies: First, the lateral diffusion could be accounted for in the autocorrelation function, which would however limit the measurement to values of τ_c that are smaller or on the order of the lateral diffusion time. On the other hand, the lateral diffusion time can be adjusted to the specific experimental condition by adapting the ROI sizes during post-processing. Second, the contribution of lateral diffusion to the autocorrelation function could be suppressed by the preparation of laterally confined membrane patches. Possible strategies include the bursting of single vesicles [Chiaruttini et al., 2015, Miyagi et al., 2017], patterned membrane surfaces [Groves et al., 1997, Nair et al., 2011], and lipid nanodiscs [Bayburt et al., 2002, Nath et al., 2007, Bayburt and Sligar, 2010] on the surface. Lipid nanodiscs may also be immobilized on functionalized polyethylen glycol layers, circumventing potential surface interactions and paving the way towards the application of SI-FCS to transmembrane receptors. In all cases, the key idea is to generate lateral membrane sizes that are smaller than an optimized ROI, such that the detection volume cannot be left or entered by lateral 2D diffusion. Any of these approaches may be initially validated using the same DNA origami structures and hybridization kinetics as this work, but instead of biotin, lipophilic anchors may be bound to the lower facet to facilitate membrane binding [Pfeiffer and Höök, 2004, Chan et al., 2009, Langecker et al., 2014].

To make even shorter binding kinetics accessible to SI-FCS, the 3D ligand diffusion potentially needs to be considered in the autocorrelation function. To simplify the analysis, it would be helpful to neglect the contributions of cross-terms from bound to unbound and vice versa to the autocorrelation curve. Thus the final autocorrelation function would only consist of a term for pure 3D diffusion and binding-unbinding, i.e. transient population of the surface bound state. In how far these cross-terms can be neglected should be evaluated by computer simulations (compare figure III.8). Alternatively, the potential of an analysis in k-space, similar to k-space image correlation spectroscopy (ICS) [Kolin et al., 2006b, Brandão et al., 2014], may be investigated. Additionally, there are many possibilities to circumvent or minimize the contribution from 3D diffusion. If the sample allows, FRET upon surface binding may be used to completely eliminate background from diffusing ligand [Auer et al., 2017]. Alternatively, SI-FCS may be combined with a dual-color cross-correlation approach [Rička and Binkert, 1989, Schwille et al., 1997, Leutenegger et al., 2006] to investigate sequential surface binding. This approach may be of interest for systems where a molecule reversibly binds to a surface and recruits another molecule upon binding. From a technological perspective, SAF emission close to the dielectric surface may be exploited by back-focal plane (bfp) imaging and selective analysis of the SAF emission into large angles [Ruckstuhl et al., 2003, Ruckstuhl and Verdes, 2004, Ries et al., 2008b, Deschamps et al., 2014, Brunstein et al., 2017]. This approach provides an increased surface sensitivity, which comes at the cost of lost spatial information. In parallel, the undercritical part of the fluorescence may be also correlated to gain for instance the ligand concentration in diffusion. For this, it should be considered to detect the undercritical fluorescence on a separate, faster point-detector [Winterflood and Seeger, 2016]. In parallel, the camera frame rates may be pushed to even shorter acquisition times. This study is still far away from reaching the time resolution limits of EMCCD cameras. To acquire images even faster, a recently developed back-illuminated complementary metal-oxide-semiconductor (CMOS) camera and single-photon avalanche diode (SPAD)-arrays are exciting options [Buchholz et al., 2012, Singh et al., 2013]. As long as no spatial information is required, the signal may also be detected with either large area detectors (e.g. hybrid photomultiplier tubes (PMTs)) or APDs (compare figure A.1 in appendix A.1). For the latter, the projected size of the pinhole into the sample may be increased to the experiment's requirements by the collection optics. These detection schemes are set up. The initial experiments are not presented in this work. For detectors compatible with TCSPC, the surface confinement of SI-FCS may be even further increased by the application of pulsed excitation, lifetime measurements and appropriate lifetime filters for the calculation of the autocorrelation curve [Böhmer et al., 2002, Kapusta et al., 2007, Felekyan et al., 2012]. This idea exploits the dependence of the fluorescence lifetime on the distance of the dipole emitter to a dielectric surface [Enderlein, 1999, Enderlein, 2003, Karedla et al., 2014].

Based on the work presented here, the exploitation of competitive binding shows promising potential for SI-FCS. A non-fluorescent competitor would alter the fluorescence trace obtained from a labeled binder [Lieto and Thompson, 2004, Peterson et al., 2016a]. This way, SI-FCS may under certain circumstances serve as a label-free method to quantify binding kinetics. Alternatively, if unlabeled and labeled ligand were, except for the fluorescent label, identical competitors, the fraction of labeled ligand may get reduced by this approach.

Recent developments enabled the imaging of label-free single proteins by interferometric scattering [Ortega Arroyo et al., 2014, Piliarik and Sandoghdar, 2014, Young et al., 2017]. Potentially, the scattered signal from reversible binding events should also yield a fluctuating signal, where the time scale of the fluctuation reflects on the binding rates. Thus the autocorrelation of interferometric scattering signals may circumvent the need for the introduction of fluorescent labels.

Considerable work has been invested into surface functionalization for QCM-D and SPR studies. The range of potential applications of SI-FCS could be massively increased by introducing such surface modifications. Similarly, the sample volume can be further reduced by decreasing the sample chamber size, which so far has not been subject to any optimization. Furthermore, SI-FCS measurements with different conditions may be parallelized by fitting several microfluidic channels into one FOV. However, care needs to be taken that the evanescent excitation field is not altered by the material that separates the different compartments. Microchannels in polymers with the refractive index of water, e.g. MY-133MC, the polymer used for the calibration slide presented in this study, may circumvent this issue.

Finally, the potential information contained in the amplitude of the SI-FCS autocorrelation function was outlined in section III.2.1, but so far not experimentally exploited. After careful background correction, the amplitude should be governed by the binding rates and the density of bound receptors, from which for a reaction of the type $A+B \rightleftharpoons C$ the total number of surface receptors can be inferred. Again, the rectangular DNA origamis used in this work are a suitable platform to validate this approach, because the number of binding sites on a single origami is known. This way, the fluctuating signal from a single origami may be monitored in a low density regime. The obtained number of binding sites could be directly compared with qPAINT [Jungmann et al., 2016].

IV

DISENTANGLING EFFECTS OF VISCOSITY AND REFRACTIVE INDEX MISMATCH IN SINGLE-FOCUS FCS

IV.1 Introduction

The measurement of diffusion coefficients of fluorescent molecules and colloidal particles is one of the intended applications of confocal FCS. The standard single-focus FCS technique however, does not allow one to measure absolute diffusion coefficients directly. This only becomes possible if the measurements are supplemented with an initial calibration measurement, which is typically performed using an aqueous solution of organic fluorophore with a known diffusion coefficient. This way, the size of the FCS detection volume can be determined using equation II.31. As long as the target sample represents an aqueous medium with a refractive index equal or close to the refractive index in the calibration measurement, the diffusion coefficient can be determined via the ratio of diffusion times obtained from the sample (τ_D) and the reference ($\tau_{D,\mathrm{ref}}$): $D = D_{\mathrm{ref}}\, \tau_{D,\mathrm{ref}}/\tau_D$.

On the other hand, it is frequently required to perform FCS measurements in media differing from pure water. Such a change of the medium between the initial calibration and the subsequent measurement is accompanied by two effects: First, the viscosity of the new medium can be different compared to water. Second, the refractive index may change upon a change of medium. As FCS is an optics-based method, the results of FCS measurements are potentially affected by changes in the refractive index, which is, however, often neglected. Typically, FCS measurements are performed using water immersion objectives, which are optimized for their performance in samples that have the refractive index of water. Consequently, if the refractive index differs from that of water, the size of the detection volume may differ considerably from the one obtained with the same setup using water as medium [Hell et al., 1993, Booth et al., 1998, Diaspro et al., 2002, Enderlein et al., 2005]. The simultaneous change of both viscosity and refractive index with the change of medium may therefore be problematic for the correct interpretation of experimental results, as both parameters affect the diffusion time τ_D, and their quantitative effects on the diffusion time cannot be easily disentangled.

A mismatch in the refractive index typically results in a larger detection volume, which inherently increases the diffusion time. Simultaneously, the center of the detection volume shifts axially, meaning that the nominal focus position (NFP) and the actual position of the detection volume above the coverslide may not coincide. Not only it is very challenging to predict the extent of the confocal volume for different refractive indices, but the expansion also depends on the optical path length through the solvent: The further the focus is in the sample with a refractive index different from water, the larger the focal volume will be. Consequently, it is not straightforward to extract information about tracer diffusion in arbitrary solvents from FCS measurements, as long as the measured diffusion time may be affected by refractive index mismatches.

The effect of the refractive index in FCS measurements has been subject to a theoretical study by Enderlein and colleagues [Enderlein et al., 2005], who came to the conclusion that the refractive index mismatch can introduce tremendous errors on the determined diffusion coefficient. Some other studies acknowledged the problem and followed a more pragmatic approach and suggested to account for a refractive index mismatch by the adjustment of the objective's correction collar [Chattopadhyay et al., 2005, Banachowicz et al., 2014, Połatyńska et al., 2017]. In more recent publications, single-focus FCS measurements in aqueous solutions of sucrose were described [Junghans et al., 2016], and the danger of misinterpreting FCS measurements taken at refractive index mismatches was highlighted [Lehmann et al., 2015]. On the other hand, Sherman *et al.* claimed that they could reliably conduct FCS experiments in media with refractive indices as high as 1.46 [Sherman et al., 2008]. Moreover, a plethora of FCS studies neglects the potential artifacts related to the refractive index mismatch or considers them to be unimportant. The extent to which such assumptions are justified is often difficult to assess retrospectively, because important parameters like viscosity, refractive index and NFP are often not reported.

In this chapter, it is explored under which conditions single-focus FCS can be employed to measure diffusion coefficients accurately, despite refractive index mismatches. An identification of conditions in which unbiased artifact-free confocal FCS measurements can be performed is of interest for all applications of single-focus FCS. Thus, the results presented here are also of relevance for the conduction of the experiments presented in chapters V and VI.

IV.2 Results and discussion

IV.2.1 Bias of typical FCS measurements in case refractive index mismatch effects are not taken into account

The assessment of the diffusion process is one of the major strengths of FCS. In such experiments, the diffusion time τ_D is the key parameter, as it relates to the diffusion coefficient D:

$$\tau_D = \frac{w_{xy}^2}{4D} \tag{IV.1}$$

Clearly, the $1/e^2$-width w_{xy} of the Gaussian detection volume is an optics-related quantity and thus should also depend on the refractive index $w_{xy}(n)$. On the other hand, it is not clear how strong this dependence typically is, and whether it can be neglected, as often done in FCS experiments.

To assess whether the refractive index is of practical and not only theoretical relevance, we start with the naive assumption that the refractive index mismatch does not play a role in FCS measurements. Assuming that the fluorescent tracer's hydrodynamic radius is the same in different media, diffusion times measured at the same temperature in water $\tau_{D,\text{water}}$ and another arbitrary medium $\tau_{D,\text{medium}}$ can be related using the Stokes-Einstein-Smoluchowski relation (equation II.4) [Einstein, 1905, von Smoluchowski, 1906]:

$$\eta_{\text{FCS}} = \frac{\tau_{D,\text{medium}}}{\tau_{D,\text{water}}}\eta_{\text{water}} \tag{IV.2}$$

Here, η_{FCS} is the viscosity of the medium as determined by FCS, and η_{water} is the viscosity of water. To verify whether the oversimplified assumption to ignore the refractive index mismatch is justified, the diffusion times of Atto655 were measured in a set of aqueous solutions, spanning a wide range of viscosities. Typically, the FCS detection volume is positioned 50 µm to 200 µm into the sample (compare e.g. [Carl Zeiss Microscopy GmbH, 2012, Wohland et al., 1999, Rusu et al., 2004, Posokhov et al., 2008, García-Sáez and Schwille, 2008, Rzepecki et al., 2004, Ringemann et al., 2009, Melo et al., 2011, Melo et al., 2014]) to avoid unwanted interactions with the coverslide surface. Therefore, these initial measurements were performed at NFP = 100 µm (see Materials and Methods in appendix appendix B.1). As expected, the FCS autocorrelation curves progressively shift to larger lag times with an increase in solution viscosity, which is exemplified in figure IV.1 for

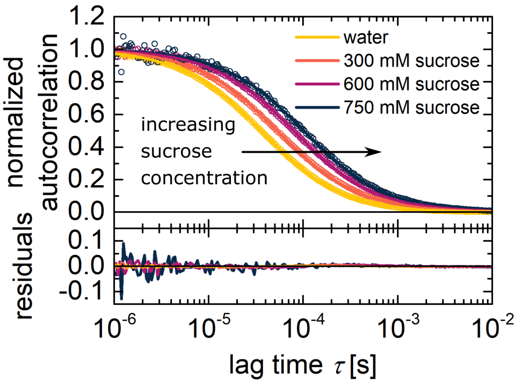

Figure IV.1: Normalized autocorrelation curves of Atto655 in aqueous solutions of sucrose. With increasing sucrose concentration, the autocorrelation curves shift to larger lag times, potentially caused by an increase in viscosity or an increased mismatch of refractive indices. The experimental autocorrelation curves (circles) were fitted using a simple 3D diffusion model (equation II.34), yielding random residuals across all conditions. Measurements were taken at 28 °C and NFP = 100 µm.

aqueous sucrose solutions. Qualitatively similar results are observed for aqueous solutions of glycerol, urea, ethanol and methanol (data not shown).

The increase of the diffusion time with the sucrose concentration observed in figure IV.1 may originate from an increasing sample viscosity and an increased size of the detection volume. The magnitude by which both effects contribute to these measurements is unclear. On the other hand, if the simple relation provided by equation IV.2 holds, the viscosity η_{FCS} obtained by FCS should recover the bulk viscosity η as measured with a conventional viscometer (compare Materials and Methods in appendix B.1). This is however clearly not the case, as demonstrated by figure IV.2A, which shows the ratio of η_{FCS} and η for a range of aqueous solutions. This data set appears to scatter massively without showing any clear trend, while at the same time the FCS measurements appear to overestimate the viscosity systematically. The scatter by far exceeds the typical experimental scatter of the FCS measurements themselves, which is for reference provided in figure B.3 in appendix B.2. Interestingly, within one kind of aqueous solution, the points in figure IV.2A appear to follow clear trends. In urea solutions, FCS overestimate the bulk viscosity even if the viscosity is close to that of water, whereas in ethanol, even at a viscosity twice that of water, η_{FCS} reproduces the bulk viscosity with a bias below 10%. The other points appear to fall in between these two extremes. The reason for this distribution is easily explained when considering the viscosities and refractive indices of these solutions in parallel. Qualitatively, for urea, a large increase in refractive index is accompanied by

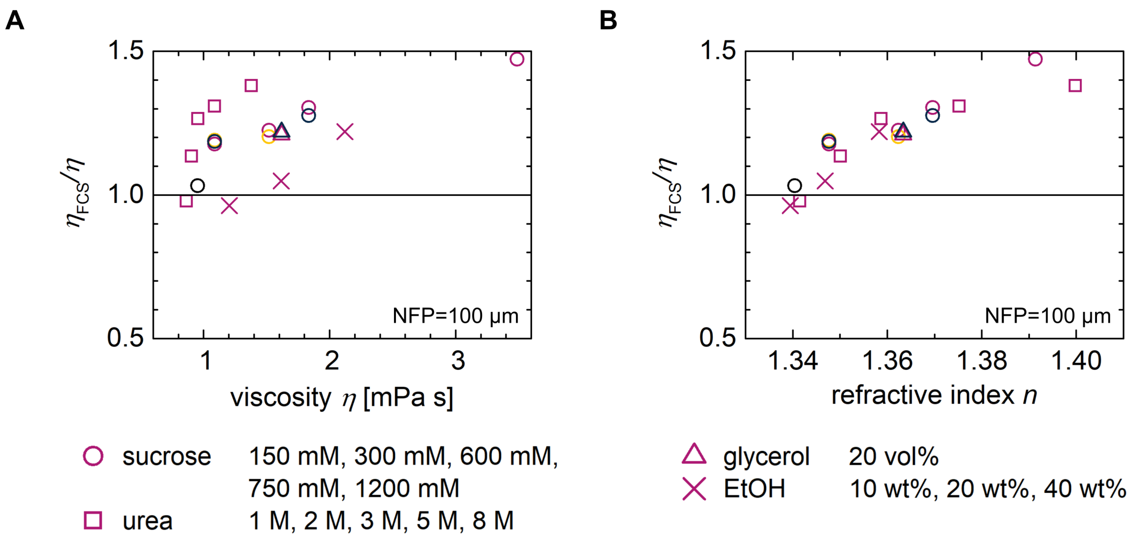

Figure IV.2: Bias of the viscosity measured by FCS 100 µm above the coverslide. A) At NFP = 100 µm, FCS overestimates the bulk viscosity for a range of aqueous solutions. The points follow no clear trend but exhibit a large scatter. B) Same data set as in A), but plotted against the refractive index. The bias of the viscosity follows a clear trend. At refractive indices close to that of water, the bias is small and increases with increasing refractive index mismatch. Symbols encode for the type of aqueous solution. Within the covered concentration ranges, η and n monotonously increase with the concentration, thus enabling to identify the respective solution concentrations of each point. Red points were measured using Atto655, yellow corresponds to Atto488, and black symbols were acquired using crimson beads.

a moderate increase in viscosity. For ethanol this is quite the opposite, and many other common aqueous solutions of e.g. sucrose, tris(hydroxymethyl)aminomethane (Tris), or NaCl fall in between these extremes (compare figure B.4 in appendix B.2).

The large scatter of obtained viscosities from figure IV.2A dissolves when plotting these data sets against the refractive index, as shown in figure IV.2B. Clearly, the bias on the viscosity obtained by FCS increases with increasing refractive index mismatch. The larger the refractive index compared to water, the larger the detection volume becomes, which directly manifests as an overestimated viscosity, if equation IV.2 is used. Clearly, at NFP = 100 µm FCS measurements above $n = 1.34$ yield viscosities η_{FCS} that overestimate the true value by more than 10%.

Notably the effects presented in figure IV.2 do not originate from chromatic aberrations. This has been tested by using Atto488 instead of Atto655 as a fluorescent tracer, thus blue-shifting the experiments. The experiments for 20 vol% glycerol, and 300 mM and 600 mM sucrose were repeated with Atto488 (yellow symbols in figure IV.2) and yielded identical results as with Atto655. Similarly, the use of crimson beads (radius 13 nm, black symbols in figure IV.2) reproduced the results obtained using Atto655.

IV.2.2 Effect of the nominal focus position

Having realized that there are situations where the refractive index cannot be neglected, it is very likely that the optical path length through the medium of a particular refractive index also plays a role, as this is a purely optical effect. In other words, one should expect very little effect of the refractive index mismatch at the surface of the coverslide and a much larger impact deep into the sample.

Previous calculations addressed the confocal volume in refractive index mismatch conditions. The axial extent and the actual focus position of the PSF, that is the distance of the focus to the top coverslide surface, were primarily considered. Both quantities were predicted to increase with increasing NFP. Interestingly, the widening is not symmetric [Hell et al., 1993, Török et al., 1997, Sheppard and Török, 1997, Egner and Hell, 1999]. Another study made similar observations by imaging beads in different distances to the coverslide surface [Diaspro et al., 2002]. In the context of single-focus FCS, however, the issue of refractive index mismatch has to the best of our knowledge not been addressed in a quantitative experimental manner. Enderlein and colleagues performed respective simulations, but focused only on one large NFP of 200 µm [Enderlein et al., 2005]. Based on these previous studies, we performed FCS experiments on freely diffusing Atto655 in sucrose and urea solutions at different NFPs above the coverslide. Both media are used as means to control the refractive index (compare table B.1 in appendix B.3). The obtained ratios $\tau_{D,\mathrm{medium}}/\tau_{D,\mathrm{water}} = \eta_{\mathrm{FCS}}/\eta_{\mathrm{water}}$ are shown in figure IV.3C,D.

When the FCS experiments are performed in water, the water immersion objective yields, as expected, the same diffusion time for all probed distances of the confocal volume to the coverslide surface, as can be seen in figure IV.3. For all other media, a dependence of the diffusion time on the axial position of the detection volume is discernible. Moreover, this dependence is stronger the larger the refractive index mismatch relative to water. As a reference, the refractive indices and viscosities are shown in table B.1 in appendix B.3. Interestingly, for all investigated cases, the diffusion time converges to a constant value for each series in a particular solution when approaching the coverslide surface. These findings are particular interesting when recalling that in a typical single-focus FCS experiment the effects of a change in viscosity and refractive index cannot be disentangled (compare figure

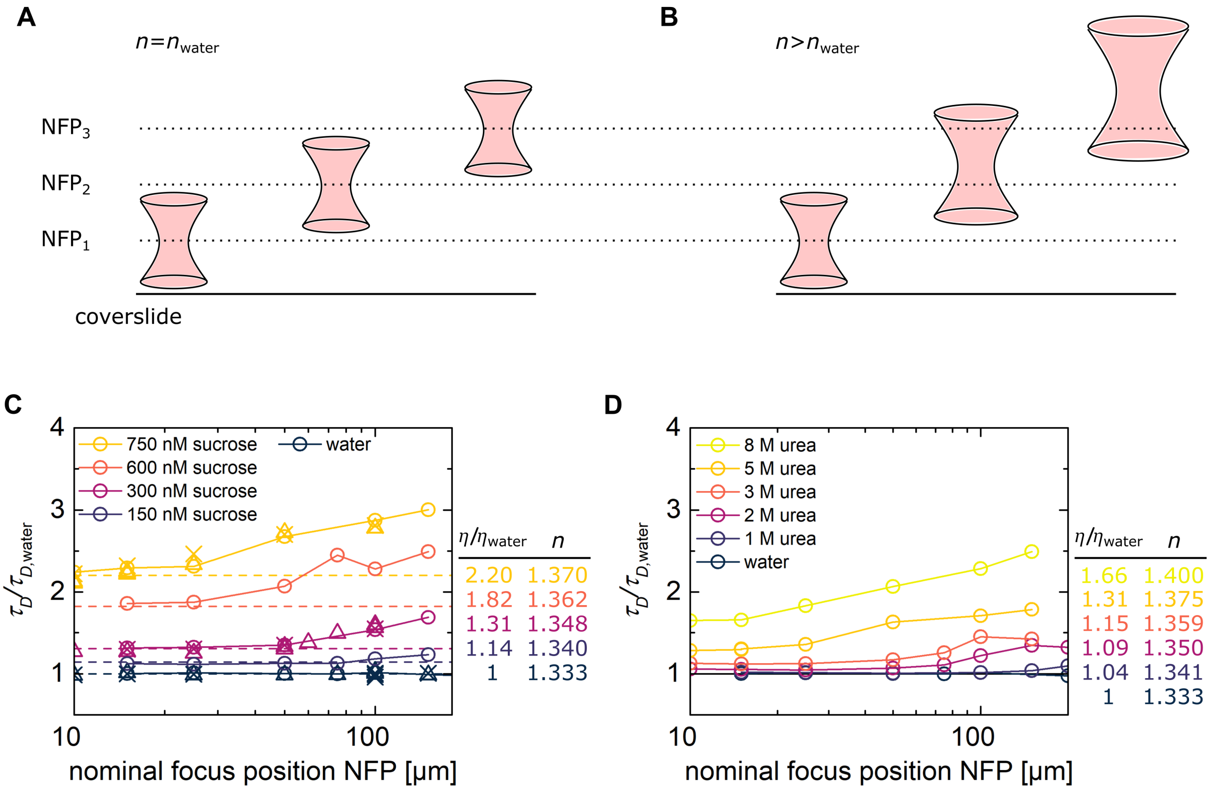

Figure IV.3: FCS diffusion time depends on the NFP in media with a refractive index mismatch. A,B) Schematic of the detection volume at different NFPs without and with refractive index mismatch. For the latter ($n > n_{\mathrm{water}}$), the detection volume increases with increasing NFP and becomes asymmetric (not depicted here). At the same time, the actual focus position becomes larger than the NFP. C) Diffusion times τ_D of Atto655 in different sucrose concentrations measured at different NFPs, relative to the diffusion time in water $\tau_{D,\mathrm{water}}$. The data points from one concentration of sucrose are connected as a guide to the eye. Except for the measurements in water, the diffusion times show a dependence on the NFP, but converge to a constant when approaching the coverslide surface. This constant coincides with the medium's viscosity relative to water (dashed lines). Similar measurements with Atto488 (triangles) and crimson beads (crosses) are superimposed and reproduce these results. For reference, the viscosities relative to water and the refractive indices of the aqueous solution of sucrose are shown (compare appendix B.3). D) As in C), but measurements were taken in different concentrations of urea. The dependencies of the diffusion time on the NFP are qualitatively similar to the measurements in sucrose, but converge to smaller values when approaching the coverslide surface. For clarity, the viscosities relative to water are not highlighted by dashed lines. The respective values for the relative viscosity and the refractive index are displayed (compare appendix B.3). The structure parameters obtained from the measurements shown in panels C) and D) are shown in figure B.5 in appendix B.2.

IV.2). Figure IV.3 shows the axial dependence of the diffusion time, which can only originate from an optical effect, because the viscosity and the refractive index are the same throughout the homogeneous sample.

As all curves in figure IV.3C,D converge to a constant value, the convergence value may potentially be free of any optical artifacts. This is in line with the aforementioned considerations: Firstly, the optical effect should disappear at the coverslide surface as the optical path length through the medium goes to zero. Secondly, the convergence appears already further away from the surface if the refractive index mismatch relative to water is small. Following these arguments, it would be desirable to place the detection volume right at the coverslide surface. However, this is experimentally unfeasible. The measurements would be affected by axial focus drifts and surface interactions. The surface drag, on the other hand, is not expected to be relevant for a detection volume spanning around 1 µm to 2 µm in axial direction and small organic fluorophores as fluorescent probes [Happel and Brenner, 2012, Schäffer et al., 2007]. A series of identical FCS measurements on Atto655 in water at different NFPs showed no differences for NFPs ranging from 5 µm to 100 µm (data not shown), suggesting that measurements as close as 5 µm to the coverslide surface still yield correct results.

As a byproduct, the FCS measurements presented in this section demonstrate how severely experimental results may be corrupted by refractive index mismatches. As an example, we consider 600 mM sucrose ($n = 1.362$, $\eta = 1.519$ mPa s at 28 °C, compare table B.1 in appendix B.3) and NFP = 150 µm. For these settings, the viscosity is overestimated by 37%, which is in line with the results by Enderlein and colleagues, who calculated for $n = 1.36$ and NFP = 200 µm a 50% bias [Enderlein et al., 2005]. The situation is even worse when the experiments are aimed at the determination of concentrations, which also requires a precise knowledge of the structure parameter S. For refractive index mismatches, the detection volume becomes asymmetric and the confinement deteriorates in axial direction much more severely than laterally [Hell et al., 1993]. This is also observed in the confocal FCS measurements presented here (figure B.5 in appendix B.2). Not only does the structure parameter increase, it also shows a large scatter. Single-focus FCS measurements are intrinsically rather insensitive to changes in S, but practically independent of S for $S \gtrsim 10$. In this case, the detection volume is similar to an infinitely long cylinder where lateral diffusion is the dominant route of entry and escape. Consequently, as the measurements become insensitive to S, the concentration cannot be determined reliably.

IV.2.3 Accurate viscosity measurements by single-focus FCS

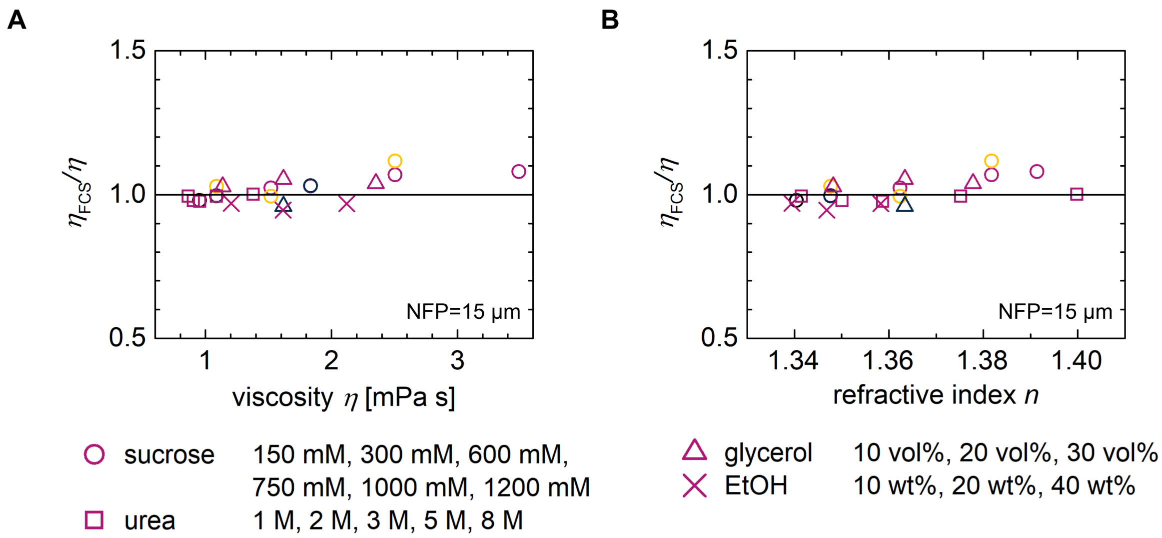

Figure IV.4: Lack of bias of the viscosity measured by FCS 15 µm above the coverslide. A) Relative error comparing the viscosity obtained by FCS measured 15 µm above the coverslide surface and obtained by a bulk measurement using a rolling ball viscometer. The viscosity obtained by FCS measurements reproduces the viscosity measured by a bulk viscometer with an accuracy of 5-10%. B) Same data set as in A), but plotted against the refractive index. The experimental scatter neither depends on the solution's viscosity nor on the solution's refractive index. Symbols encode for the type of aqueous solution. Within the covered concentration ranges, η and n monotonously increase with the concentration, thus enabling to identify the respective solution concentrations of each point. Red points were measured using Atto655, yellow corresponds to Atto488, and black symbols were acquired using crimson beads.

Following the hypothesis that all curves in figure IV.3C,D would converge to a diffusion time that only reflects the viscosity, rather than the change in the refractive index, another set of FCS measurements, similar to the experiments presented in figure IV.2, was performed. This time, however, the detection volume was placed 15 µm above the coverslide surface. As before, the viscosity was calculated from the diffusion time, using equation IV.2, and related to the bulk viscosity. The results are shown in figure IV.4. Strikingly, when the detection volume is placed 15 µm above the coverslide surface, FCS reproduces the viscosities measured with a bulk viscometer with an error less than 5-10% for the investigated solutions. Moreover, for the investigated refractive indices ranging from 1.33 to 1.4, no noteworthy dependence of the viscosity measured by FCS on the refractive index is discernible (figure IV.4B). This is in contrast to the previously presented results in figure IV.2B, where the confocal detection volume was placed 100 µm above the coverslide surface. Thus, FCS can be used to measure viscosities of small-volume samples reliably, under the condition that the confocal volume is placed as close as 15 µm to the coverslide surface. These results demonstrate this capability for refractive indices ranging from 1.33 to 1.4.

It is worth noting, that the majority of cells have an average refractive index of 1.36-1.38 [Rappaz et al., 2005, Choi et al., 2007, Schürmann et al., 2016, Brunstein et al., 2017]. On the other hand, FCS experiments in cells are usually performed in adherent cells, which are typically not higher than 10 µm. Consequently, the results presented in this chapter indicate that FCS experiments in adherent cells are most likely not affected by artifacts originating from the refractive index mismatch.

IV.2.4 Refractive index mismatch in FCS measurements on 2D diffusion in GUVs

Optical distortions are of course not a unique problem of FCS measurement on freely diffusing particles in 3D. Another popular application of FCS is the study of mobility in lipid membranes, typically GUVs. These model membranes are a suitable tool to study biological phenomena in a minimalistic unadulterated system [Lagny and Bassereau, 2015]. Moreover, GUVs provide frre-standing membranes, circumventing potential interactions with a support [Dertinger et al., 2006, Przybylo et al., 2006]. A popular protocol for the generation of GUVs involves initial electroformation on platinum wires and the subsequent transfer to a sample chamber in which the GUVs settle to the bottom where they can be imaged. This is typically achieved by forming the GUVs in sucrose solutions and their final transfer into a glucose solution of the same osmolarity. As a result, the GUVs are often filled with 300 mM aqueous solution of sucrose [García-Sáez et al., 2010], but significantly higher concentrations up to 1.5 M have also been used [Doeven et al., 2005]. For FCS measurements, the confocal volume is placed on the top pole of the GUV, which means that for excitation and fluorescence detection the light has to travel through the optically dense sucrose solution.

To investigate the effect of refractive index mismatches on the outcome of such FCS experiments, the diffusion of the lipid probe Atto655DOPE and the lipid analog fast3,3'-Dilinoleyloxacarbocyanine Perchlorate (DiO) were measured. The GUVs were prepared by electroformation on indium tin oxide (ITO)-coated coverslides (see Materials and Methods in appendix B.1 for details) [Angelova and Dimitrov, 1986, Méléard et al., 2009, Herold

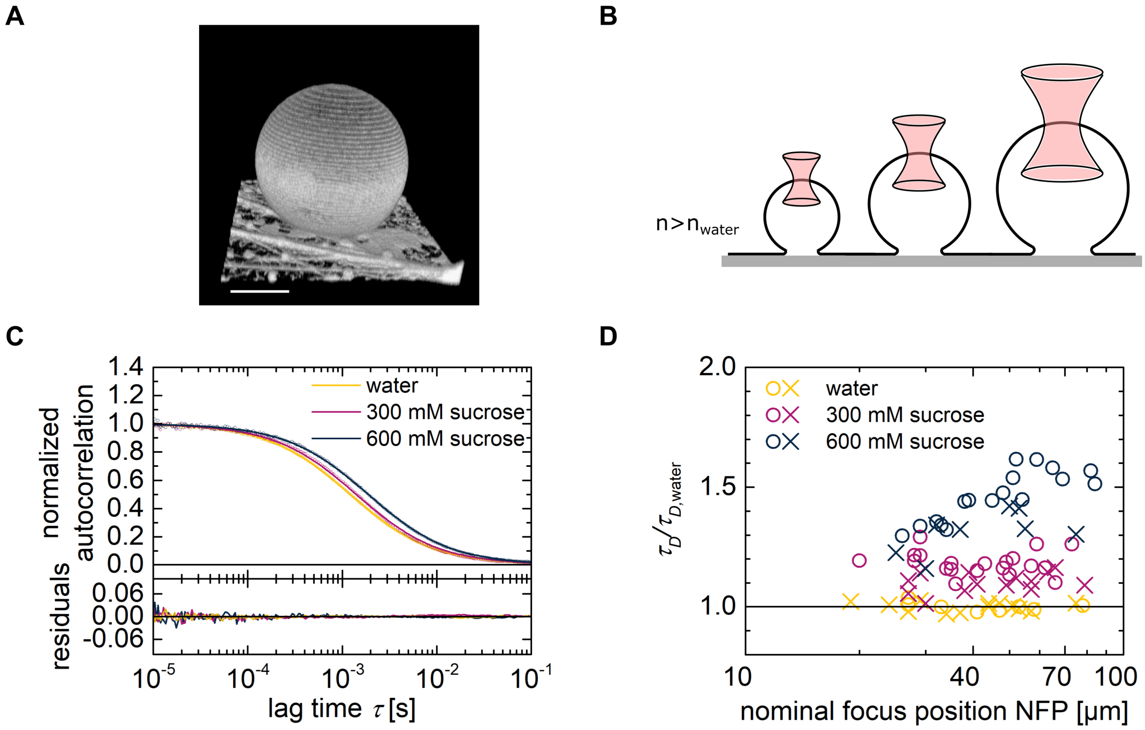

Figure IV.5: FCS on GUVs filled with aqueous solutions of sucrose. A) 3D reconstruction of a dome-shaped GUV adhered to an ITO-coated coverslide. The scale bar corresponds 10 µm. B) Schematic of the positioning of the confocal volume on the top pole of GUVs, which naturally grow in different sizes. C) Representative normalized autocorrelation curves of 0.001 mol% Atto655DOPE in GUVs of 1,2-dioleoyl-sn-glycero-3-phosphocholine (DOPC). The GUVs were grown in different aqueous solutions of sucrose. The experimental autocorrelation curves (circles) were fitted (solid lines) using a simple 2D diffusion model (equation II.32), which describes the adequately with residuals well below 3% of the correlation amplitude. D) Diffusion times of Atto6551,2-dioleoyl-sn-glycero-3-phosphoethanolamine (DOPE) (circles) and fastDiO (crosses) depend on the viscosity of the surrounding media. Especially for 600 mM sucrose concentration and GUVs larger than 40 µm, an additional dependence on the NFP is discernible. Each point corresponds to an independent FCS measurement (total measurement time at least 12 min) on one GUV.

et al., 2012]. Although this preparation is slightly different to the initially mentioned popular method of GUVs formation on wires, the problem of refractive index mismatch is identical in both cases.

Independent of the preparation protocol, GUVs are typically not monodisperse but come in a range of sizes. Thus, FCS measurements on the top pole of a set of GUVs can sample a range of actual focus positions, and thus a range of NFPs. However, the range of accessible GUV sizes is limited. In this study, the top poles of GUVs were typically not higher than 100 µm above the coverslide surface. On the other hand, it is difficult to carry out FCS measurements on vesicles with a diameter below 20 µm, because of a limited reservoir of fluorophores (unavoidable residual photobleaching). Figure IV.5D shows the apparent diffusion times τ_D normalized to the diffusion times $\tau_{D,\mathrm{water}}$ measured for GUVs grown in pure water. As for freely diffusing fluorophores (figure IV.3C), the ratio $\tau_D/\tau_{D,\mathrm{water}}$ increases with increasing sucrose concentration. This is reasonable, because the diffusion of the lipid probes is expected to be affected by the viscosity of the surrounding bulk viscosities. Although not directly applicable to small lipid probes, the SD-model indicates that the 3D bulk viscosities affect diffusion in the membrane [Saffman and Delbrück, 1975].

Remarkably, the diffusion times of the lipid probes show no NFP dependence at 300 mM sucrose, but only at 600 mM. In contrast, for fluorescent tracers diffusing in 3D, the diffusion time showed a dependence on the NFP for both of these concentrations of sucrose (figure IV.3). On the other hand, the FCS measurements on GUVs filled with 300 mM aqueous solution of sucrose exhibit a slightly larger scatter, such that a potential NFP-dependence of the diffusion time may be masked. To achieve stronger effects, FCS measurements may be performed on larger GUVs.

The results presented here suggest that FCS measurements performed on GUVs filled with 300 mM sucrose (e.g. following the protocol by García-Sáez and colleagues [García-Sáez et al., 2010]) were most likely not affected by artifacts induced by refractive index mismatches. Of course this conclusion only holds provided the optical system of the particular study was similar to this work.

Interestingly, the ratio $\tau_D/\tau_{D,\mathrm{water}}$ seems to be slightly, but consistently smaller for DiO than for Atto655DOPE. Potentially, this effect may originate from the different structures of these probes. While DiO is located entirely in the membrane, Atto655 is attached to the polar head group of DOPE and therefore exposed to the surrounding bulk. Thus, DiO may be less sensitive to changes of the 3D bulk viscosity.

IV.3 Conclusion

This chapter addressed the potential artifacts that may arise during FCS measurements because of refractive index mismatches. In general, refractive index mismatches may potentially cause severe overestimations of viscosities and concentrations. Moreover a regime where standard single-focus FCS can be used without optical artifacts was identified. In the presence of refractive index mismatches, the dependence of the diffusion time on the axial position of the detection volume can be used to find a regime where the confocal volume size in a particular medium is the same as in water. This reasoning can also be reversed: assuming a known viscosity throughout the sample and a Gaussian-shaped confocal volume, the lateral beam waist w_{xy} can be calculated for every axial position. This is a fairly rough approximation of the confocal volume, but considering that precise focus field calculations are complicated, even for the paraxial approximation [Richards and Wolf, 1959], this may be a helpful tool to estimate the size of the confocal volume at different positions when facing refractive index mismatches.

The results presented here demonstrate the importance of refractive index and NFP for the outcome of FCS measurements. Therefore, these parameters are, among others, key to assess the quality and potential error sources in FCS studies, and should be commonly reported.

Notably, among the investigated solutions were urea and ethanol. For urea, large changes in refractive index are accompanied by a small change in viscosity, whereas for ethanol already small changes in refractive index relate to large changes in viscosity [Haynes, 2014]. The vast majority of commonly used media, including aqueous solutions of sucrose, falls in between these extreme cases. Thus, the findings of this chapter are likely to be applicable to most liquids commonly used in the life-sciences. This is also a strong indication that FCS experiments in adherent cells are most likely not affected by artifacts because of refractive index mismatch.

V

CHARACTERIZATION OF FTSZ DYNAMICS FROM *C. CRESCENTUS* BY FCS

V.1 Introduction

Although cell division is orchestrated by a manifold of regulatory mechanisms across bacteria, most of them target the key divisome protein: filamenting temperature-sensitive mutant Z (FtsZ). FtsZ is not only a tubulin homologue, but also is essential for cell division, which makes it a promising target for the development of new antibiotics [Haranahalli et al., 2016]. Although it has been reported almost 30 years ago that FtsZ forms a ring, termed the Z-ring, at the division site in *E. coli* [Bi and Lutkenhaus, 1991], its exact role during cytokinesis is still a matter of debate. It is, however, known that FtsZ is a GTPase [Mukherjee and Lutkenhaus, 1994], which forms filaments and performs treadmilling [Loose and Mitchison, 2013,Bisson-Filho et al., 2017,Yang et al., 2017]. The Z-ring appears to serve as a recruitment platform for other proteins involved in cell division, but was also suggested to actively drive cell division by locally inducing cell wall synthesis or force generation by ring contraction (for reviews see [Adams and Errington, 2009,Erickson et al., 2010,Lutkenhaus et al., 2012,Eun et al., 2015,Haeusser and Margolin, 2016,Coltharp and Xiao, 2017]).

In this chapter, the focus is on the *in vitro* study of the essential cell division proteins FtsZ and MipZ from *C. crescentus*. The crystal structure of FtsZ from *C. crescentus* has to date not been solved. However, as FtsZ is conserved across almost all bacteria (compare appendix C.2), the solved crystal structures from other bacteria can be used to predict the structure of FtsZ from *C. crescentus* (figure V.1). Similar to other bacteria, the protein has separately folded C- and N-terminal domains, which are linked by one helix [Oliva et al., 2004,Adams and Errington, 2009]. The nucleotide binding site is located in the N-terminal domain (grove on the top facet in figure V.1) [Raymond et al., 2009,Adams and Errington, 2009]. Often, FtsZ proteins are separated into four regions: the N-terminus, a core region, the C-terminal linker (Ctl), and the C-terminus [Vaughan et al., 2004]. Most relevant for this study is the Ctl (magenta), which is terminated by the C-terminal conserved peptide (green). The Ctl has not been resolved in previous crystal structures of FtsZ [Löwe

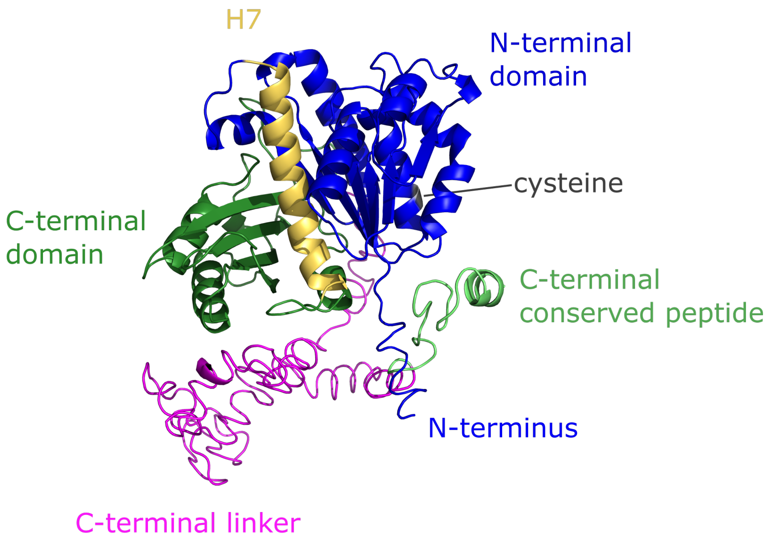

Figure V.1: FtsZ crystal structure. Predicted crystal structure of FtsZ from *C. crescentus*, as computed by the I-TASSER platform [Zhang, 2008, Roy et al., 2010, Yang et al., 2014]. The protein shows two separately folded N-terminal (blue) and C-terminal (green) domains, which are connected by one helix (yellow) [Adams and Errington, 2009]. FtsZ from *C. crescentus* has a large (∼150 aa) unstructured C-terminal linker (Ctl) (magenta), and is terminated by the C-terminal conserved peptide (light green), which is essential for the regulation of FtsZ.

and Amos, 1998, Leung et al., 2004, Oliva et al., 2004, Oliva et al., 2007, Haydon et al., 2008, Raymond et al., 2009, Tan et al., 2012, Matsui et al., 2012, Fujita et al., 2017, Wagstaff et al., 2017] and is thus expected to be unstructured [Erickson et al., 2010]. The length of the Ctl varies considerably across bacteria [Vaughan et al., 2004]: in *C. crescentus* it comprises around 150 amino acids, whereas in *E. coli*, it is only around 50 amino acids long. The role of the Ctl has been subject to studies in *E. coli* [Gardner and Farzan, 2017], *B. subtilis* [Buske and Levin, 2013], and *C. crescentus* [Sundararajan et al., 2015]. The latter suggests that the Ctl plays a key role in the regulation of cell wall synthesis. A recent *in vitro* study suggest that the presence of the Ctl alters the lateral interaction of FtsZ protofilaments [Sundararajan and Goley, 2017b].

Although FtsZ is conserved across almost all bacteria, its spatiotemporal distribution is regulated by different mechanisms in different organisms. While for example in *E. coli* FtsZ is confined to the mid-cell by its inhibitor MinC, which follows the pole-to-pole oscillations of the protein pair MinD and MinE [Raskin and de Boer, 1999, Hu and Lutkenhaus, 1999, Lutkenhaus, 2007], in *C. crescentus* the protein MipZ is the key inhibitor of FtsZ polymerization [Thanbichler and Shapiro, 2006] (for reviews see [Thanbichler and Shapiro, 2008, Thanbichler, 2009, Kiekebusch and Thanbichler, 2014, Lasker et al., 2016]). Like MinD, MipZ is a P-loop ATPase [Kiekebusch et al., 2012, Leipe et al., 2002]. In contrast to MinD, however, MipZ does not oscillate between the cell poles, but co-localizes with chromosomal DNA. Upon chromosome segregation, the spatial distribution of MipZ has a minimum at mid-cell, and thus FtsZ assembles at the cell center [Thanbichler and Shapiro, 2006]. The resulting Z-ring has been only recently imaged in *C. crescentus* using super-resolution microscopy [Biteen et al., 2012, Holden et al., 2014]. FtsZ filaments are shortened and form arc-like structures upon interaction with MipZ [Thanbichler and Shapiro, 2006]. This interaction was reported to only work effectively upon formation of MipZ dimers [Kiekebusch et al., 2012].

In this chapter, the polymerization of FtsZ filaments and their shortening by MipZ are followed by FCS in real-time. Moreover, the effect of the Ctl on FtsZ-FtsZ interaction is investigated. Filaments typically exhibit a length distribution instead of a unique size. Consequently, an appropriate model for the autocorrelation curve is derived and applied to experimental FCS data.

V.2 Results and Discussion

V.2.1 Semiquantitative real-time observation of FtsZ filament formation and shortening

V.2.1.1 Filament formation

FtsZ is a guanosine triphosphate (GTP)ase and forms filaments upon addition of GTP [Mukherjee and Lutkenhaus, 1994, Mukherjee and Lutkenhaus, 1999, Chen and Erickson, 2005, Hou et al., 2012]. Under such conditions, monomers are attaching on one end of the filament with a rate k_{on} and are detaching on the other end with a rate k_{off} (figure V.2A), resulting in the characteristic treadmilling [Loose and Mitchison, 2013, Bisson-Filho et al., 2017, Yang et al., 2017]. Until a steady state is reached, the filament formation itself is clearly not an equilibrium process, which violates one of the major prerequisites for an FCS analysis. However, if the polymerization was reasonably slow, short FCS measurements arguably sample a quasi-equilibrium in which the system does not change over the measurement time. Another possiblity is to qualitiatively describe filament formation by

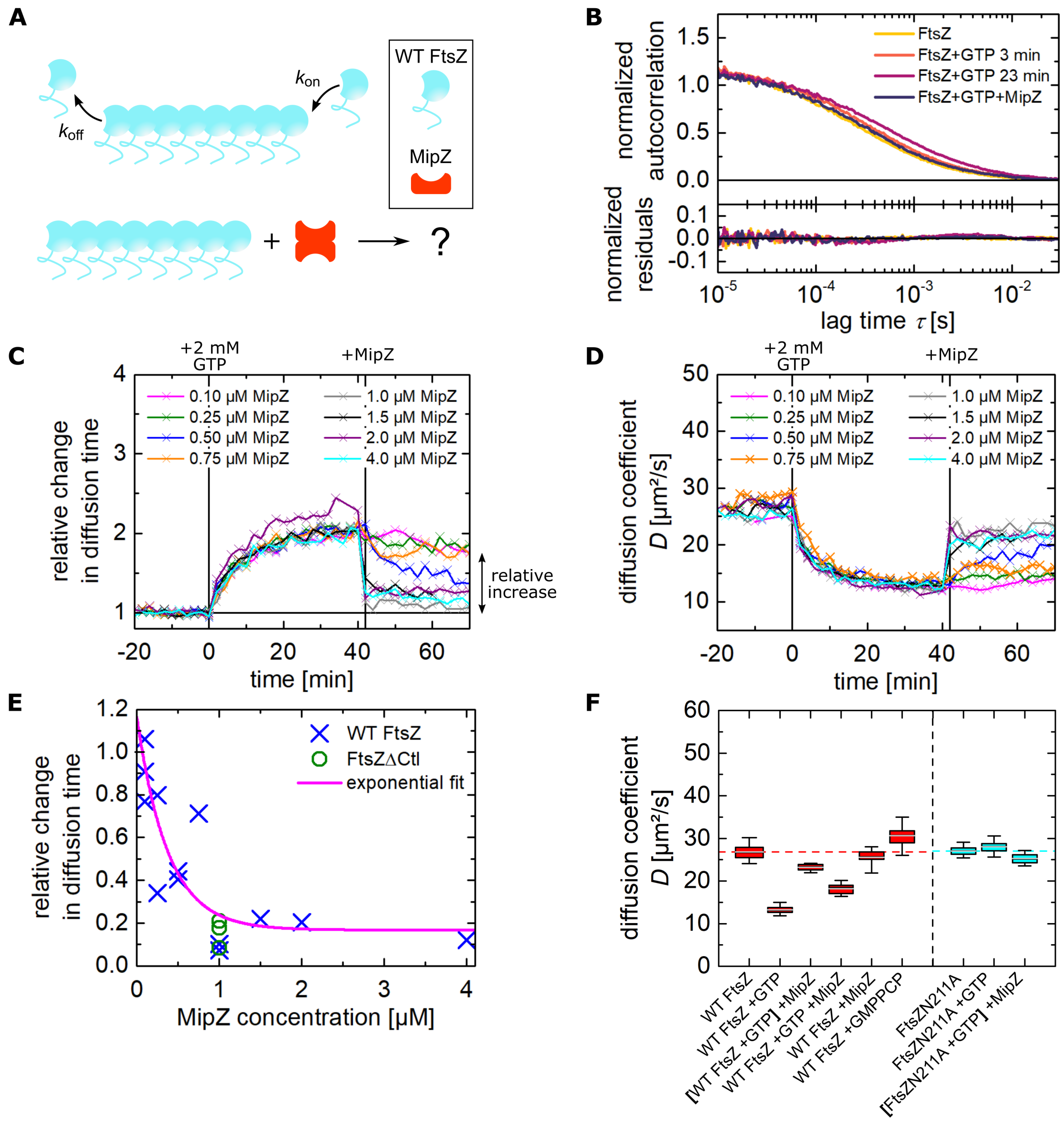

Figure V.2: FtsZ filament formation and break down by MipZ. A) FtsZ performs treadmilling upon addition of GTP, but the exact product of interaction with MipZ is not known. B) Representative autocorrelation curves for WT FtsZ shift to larger lag times upon addition of 2 mM GTP and shift back to a shorter lag time after addition of 2 µM MipZ. For clarity, the fits are not shown. The residuals appear to be random and small compared to the amplitude. C,D) Time evolution of the diffusion times and the corresponding diffusion coefficients of WT FtsZ. Addition of 2 mM GTP ($t = 0$) induces a reproducible decrease in the diffusion coefficient of FtsZ. The subsequent addition of MipZ increases the diffusion coefficient again, but the initial value is not recovered. E) Relative increase in diffusion time comparing initial and final state in C) depends on the amount of MipZ added. F) Diffusion coefficients of WT FtsZ and the monomeric mutant FtsZN211A in different mixtures. Squared brackets denote a pre-incubation for 40 min. FtsZ was used at 2 µM with 10% labeled fraction, GTP was used at 2 mM.

observing the shift to larger lag times in the autocorrelation curves when filaments are forming. Here, all experiments were performed 50 µm above a BSA-coated coverslide surface to reduce unspecific surface binding. Therefore, the results presented here reflect on the FtsZ dynamics in bulk. The autocorrelation curves presented in this section were analyzed using a model function for two diffusing components (equation II.36, for details see Materials and Methods in appendix C.1).

The formation of filaments results in an increase of the average particle size, which should result in larger diffusion times. This behavior is indeed observed, as shown in figure V.2B. Starting from WT FtsZ without any GTP (yellow), the autocorrelation curve shifts to larger lag times upon addition of GTP. The system does not instantly reach an equilibrium, as the representative autocorrelation curves 3 min and 23 min after GTP addition are clearly different. After adding MipZ, the autocorrelation curve (dark blue) shifts back to shorter lag times, in line with the reported shortening of FtsZ filaments by MipZ [Thanbichler and Shapiro, 2006]. The measured autocorrelation curves are adequately described by a model with two freely diffusing species, indicated by the random, non-systematic residuals. One of the two diffusion times was fixed to the diffusion of free Alexa488 to minimize the amount of free parameters (compare Materials and Methods in appendix C.1).

To evaluate the time evolution of the system more systematically, we performed a time series of FCS measurements, each of the measurements lasting for 2 min. Figure V.2C shows the corresponding changes in diffusion time for a set of experiments, which are all identical until $t = 42$ min. In the beginning of each series, the diffusion time of FtsZ was determined in the absence of GTP, serving as a baseline ($t < 0$ in figure V.2C,D). All other diffusion times in a time series were normalized to the mean of the initial diffusion times (figure V.2C). In a next step, GTP was spiked into the sample to reach a final concentration of 2 mM. As discussed for the autocorrelation curves, the diffusion time starts increasing upon addition of GTP, which is in line with the well-known GTP-dependent polymerization of FtsZ [Mukherjee and Lutkenhaus, 1994, Mukherjee and Lutkenhaus, 1999, Chen and Erickson, 2005, Hou et al., 2012]. Qualitatively, the diffusion time increases and finally saturates at around two times larger values than the initial state, which was FtsZ without any GTP. Remarkably, these measurements are highly reproducible, with standard deviations of only around 10% of the mean. Although FtsZ from *E. coli* has been subject to FCS studies [Reija et al., 2011, Monterroso et al., 2012, Montecinos-Franjola et al., 2012, Monterroso et al., 2013, Ahijado-Guzmán et al., 2013, Mikuni et al., 2015], this is the first time that the polymerization is observed by this method in real time. To roughly quantify the time scale on which the polymerization occurs, the diffusion times from 0 min to 40 min were extracted and fitted by a logistic function with an offset, as shown in figure C.3 (red line, appendix C.2). The obtained characteristic time constant is (11.1 ± 1.2)min, which is in agreement with a DLS study of the polymerization of WT FtsZ from *C. crescentus* [Hou et al., 2012]. Interestingly, the time within which the maximum polymerization state of such a system is reached differs for FtsZ from different organisms. FtsZ from *Mycobacterium tuberculosis* was reported to fully polymerize within less than 10 min [White et al., 2000, Chen et al., 2007], whereas for FtsZ from *E. coli* the polymerization appears to happen almost instantaneously [Mukherjee and Lutkenhaus, 1999]. As the size of the detection volume was calibrated on each measurement day, the diffusion times can be easily transformed into diffusion coefficients. The corresponding data sets are shown in figure V.2D. The average diffusion constant remains around $25\,\mu m/s^2$ to $30\,\mu m/s^2$ before addition of GTP, and decreases upon filament formation.

Interestingly, we did not observe any formation of filaments when FtsZ was mixed with GMPPCP, a non-hydrolysable form of GTP. However, when 2 mM GTP were added to a mixture of 2 µM FtsZ and 4 mM GMPPCP, filaments started forming (compare appendix C.2, figure C.4), but the overall increase in diffusion time was only around half of what has been observed if only 2 mM GTP are added (figure V.2C,D). These results indicate that although some of the FtsZ proteins seem to have bound GMPPCP they are not available for polymerization in this state. As the affinity of FtsZ to GTP is larger than to GMPPCP, one may hypothesize that GTP slowly replaces GMPPCP over time and consequently FtsZ becomes available for polymerization. The lack of FtsZ filaments in the presence of only GMPPCP has been observed in several independent experiments, but is not in agreement with a recent study [Sundararajan and Goley, 2017b]. Moreover, polymerizations were observed by transmission electron microscopy (TEM) and sedimentation assays[1]. The reason for this discrepancy is currently unclear and requires further investigation.

Next, we performed a similar experiment on the chimeric protein FtsZ-YFP-mts. In detail, this construct comprises the first 366 amino acids of FtsZ from *E. coli*, followed by YFP-Venus [Nagai et al., 2002] and the membrane targeting sequence (mts) from *E. coli* MinD [Szeto et al., 2003, Osawa et al., 2008]. This construct is lacking the Ctl of FtsZ. Upon addition of GTP, FtsZ-YFP-mts also polymerizes, but the degree of polymerization is much weaker than observed for WT FtsZ from *C. crescentus*, as shown in appendix

[1]Personal communication Laura Corrales Guerrero, PhD (Thanbichler lab, Philipps University Marburg, Germany)

C.2 (figure C.5). Moreover, previous studies on chemically labeled WT FtsZ from *E. coli* found significantly longer polymers [Reija et al., 2011, Monterroso et al., 2012]. These results indicate that either the lacking Ctl, YFP, the mts, or combinations of them alter the polymerization properties of *E. coli* FtsZ. Knowing that YFP (28.1 kDa) is almost as large as FtsZ from *E. coli* (40.3 kDa) [UniProt Consortium., 2017], whereas the mts consists of only a few amino acids [Szeto et al., 2002, Hu and Lutkenhaus, 2003, Szeto et al., 2003], it is conceivable that YFP interferes with the polymerization. Moreover, many fluorescent proteins tend to dimerize at high effective concentrations, e.g. when they are fused to monomers that form polymers, or when they are membrane-confined [Zacharias et al., 2002, Day and Davidson, 2009]. The effect of dimerized YFP on the polymerization and depolymerization dynamics of FtsZ has not been characterized, but may be an interesting tool to tune the rate of FtsZ depolymerization. Thus, a more thorough study of this chimeric protein is required.

V.2.1.2 Effect of MipZ on FtsZ filaments

The ATPase MipZ has been shown to interact with FtsZ, yielding significantly shorter and arc-like structures than polymerized FtsZ [Thanbichler and Shapiro, 2006]. However, to date, the interaction between FtsZ and MipZ has not been monitored in real time. Here, this process is addressed using FCS. To this end, a defined amount of MipZ was added to polymerized FtsZ filaments (after 40 min in figure V.2C,D). The interaction between MipZ and FtsZ is only efficient upon dimerization of MipZ. The fission of these dimers requires ATP hydrolysis [Kiekebusch et al., 2012]. Therefore, we used a mutant of MipZ (D42A), which has a low ATP hydrolysis rate. Moreover, all experiments were performed with non-hydrolysable ATPγS, which locks MipZ in its dimerized state. Clearly, the addition of MipZ induced a decrease in the diffusion time of FtsZ, which is interpreted as a reduction in particle size (figure V.2C,D). Interestingly, the diffusion time appears to level within around 5 min to 10 min after addition of MipZ. Moreover, this final value of the diffusion time depends on the concentration of MipZ. This effect itself is not surprising, because in the limit of no MipZ, no effect is expected. On the other hand, it is interesting to realize that between 1 µM and 4 µM of MipZ there appears to be no difference in the time evolution of the diffusion time, at least not within the resolution of this approach. Consequently, a saturation is reached. To investigate this effect more systematically, we quantified the saturation dependence of the final diffusion time of FtsZ on the concentration of MipZ. To this end, the final diffusion time was related to the diffusion time in the absence of

GTP and MipZ τ_D(FtsZ+GTP+MipZ)/τ_D(FtsZ-GTP-MipZ) − 1, termed relative change in diffusion time in the following. As shown in figure V.2E, this quantity depends roughly exponentially on the MipZ concentration. In detail, a fit by an exponential function with offset yields

$$\frac{\tau_D(\text{FtsZ+GTP+MipZ})}{\tau_D(\text{FtsZ-GTP-MipZ})} - 1 = 1.00 \cdot \exp\left(-[\text{MipZ}]/376\,\text{nM}\right) + 0.17 \qquad (\text{V.1})$$

The characteristic concentration of the exponential decay is 376 nM. Interestingly, when approximating a single *C. crescentus* as a cylinder of diameter $d = 0.75\,\mu\text{m}$ and length $l = 3.5\,\mu\text{m}$ [Wright et al., 2015], and estimating the copy number of MipZ proteins per cell as 1000 [Thanbichler and Shapiro, 2006], a similar concentration of 230 nM is obtained. Although many other factors, like interfaces, the MipZ gradient, the FtsZ concentration, which depends on the cell state in *C. crescentus* [Quardokus et al., 1996], and protein mobility render the considered dynamics *in vivo* much more complex, the agreement of physiological MipZ concentration and the obtained characteristic concentration hint that indeed hundreds of nM of MipZ are sufficient to achieve an effective length regulation of FtsZ filaments.

The offset of 0.17 indicates that at an excess of MipZ ([MipZ] $\to \infty$) the resulting FtsZ structures are still ~17% larger than in the initial state without any GTP and MipZ. This observation could be explained by two scenarios: MipZ may sequester FtsZ, or FtsZ forms larger structures in the presence of GTP and MipZ, compared to the absence of both. Interestingly, Thanbichler and Shapiro observed by TEM that FtsZ forms short arc-like structures upon action of MipZ [Thanbichler and Shapiro, 2006]. On the other hand, this study was performed at higher $MgCl_2$ concentrations, which stabilizes filaments. Recent TEM images, relating to comparable conditions to this study, suggest the presence of short oligomers[2]. A direct answer which of the two scenarios applies could be obtained by FCCS measurements where both, MipZ and FtsZ, are fluorescently labeled with spectrally distinct fluorophores.

As a next step, we compared the obtained diffusion coefficients for FtsZ in the presence and absence of GTP, and MipZ with other mixtures (figure V.2F). Surprisingly, the final diffusion coefficient of FtsZ is slightly smaller when FtsZ, GTP and MipZ are mixed at the same time (FtsZ+GTP+MipZ), as compared to initial filament formation and subsequent addition of MipZ ([FtsZ+GTP]+MipZ). Consequently, on average FtsZ structures become

[2]Personal communication Laura Corrales Guerrero, PhD (Thanbichler lab, Philipps University Marburg, Germany)

larger when all three components are mixed from the start. The reason for this observation is currently unclear. Moreover, an incubation of WT FtsZ with MipZ and without GTP shows no clear reduction of the diffusion coefficient, indicating that MipZ either does not sequester WT FtsZ at all, or at least not in the absence of GTP. Interestingly, the monomeric mutant FtsZN211A, which has an impaired capability to form filaments, also shows a slight decrease of the diffusion coefficient upon incubation first with GTP and then with MipZ ([FtsZN211A+GTP]+MipZ). These results suggest that GTP may be essential for MipZ binding to FtsZ. A validation of this hypothesis and the exact lifetime of such heterodimers may be accessible by FCCS or single-molecule imaging techniques.

V.2.2 Quantitative insights into FtsZ dynamics in the absence of GTP

V.2.2.1 Revisited selection of an appropriate model for the autocorrelation

Typically, FCS experiments of diffusing objects are analyzed assuming one of the following models: single-component diffusion in three dimensions (termed 3D model, equation II.34), single-component diffusion with triplet blinking (3D+T model, equation II.35), or two-component diffusion (3D+3D model, equation II.36). So far, all measurements were analyzed using a 3D+3D model, where the faster component was attributed to freely diffusing fluorescent label. To minimize the number of free fit parameters, the respective short diffusion time was measured for free Alexa488, adjusted to the respective size of the detection volume on the measurement day, and was kept fixed in the 3D+3D fit. To determine whether the choice of the fit model has an impact on the determined diffusion coefficients, we reanalyzed the experiments of FtsZ in the absence of GTP. The corresponding results are shown in figure V.3.

The 3D model shows shorter diffusion times and larger residuals than both other models, although the fitted range was chosen to start at larger lag times. Evidently, there appears to be a short time contribution to the autocorrelation curve, which is not accounted for by the 3D model. This also explains, why in this case the nonlinear least square algorithm yields a smaller diffusion time, corresponding to a trade-off between faster and slower dynamic in the autocorrelation. Interestingly, 3D+T and 3D+3D model yield identical results for the slow diffusion component, indicating that the faster decay can be either described by a triplet decay or a diffusion contribution. This may be surprising at first, because both functions have different shapes, but phenomenologically, both account for

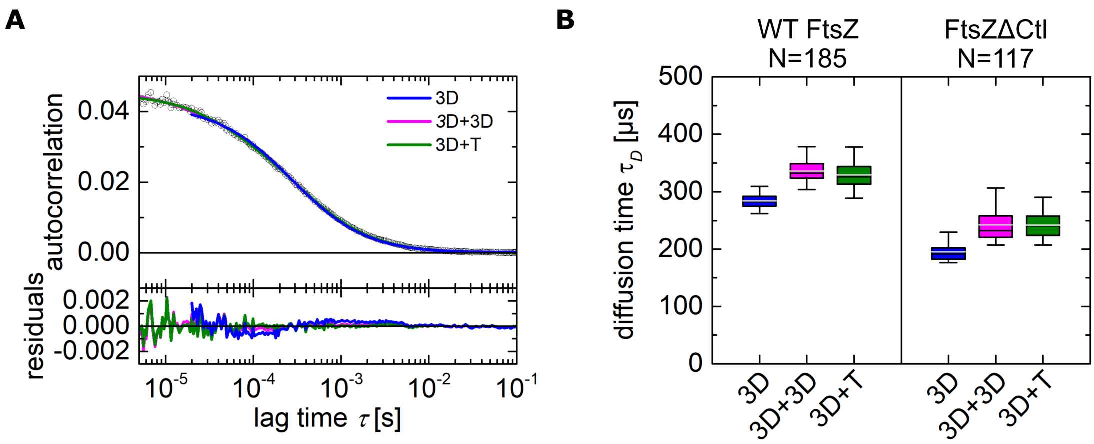

Figure V.3: FtsZ autocorrelation curves appear to be well described by several models. A) Representative autocorrelation curve (circles) of WT FtsZ in the absence of GTP fitted by model functions based on a single diffusing component (3D, blue), two non-interacting diffusing components, with the faster diffusion time fixed to that of free dye (3D+3D, magenta), and a single diffusing species with an additional triplet dynamics (3D+T, green). A single-component diffusion model shows the largest systematic residuals, but also has the least free fit parameters. B) Boxplot of the diffusion times for WT FtsZ and FtsZΔCtl obtained from the three fitting models obtained in A). The means (gray lines) and medians (black lines) are indicated. Both models, two-component diffusion and single-component diffusion with triplet yield similar diffusion times. All previously presented results for FtsZ were obtained using the 3D+3D model.

the first decay in the autocorrelation curve, which allows for the other diffusion component to adequately describe the second decay. For the 3D+T model, the triplet decay times are typically far above 30 µs, which is much larger than expected for triplet blinking [Widengren et al., 1994]. Consequently, one can assume that the fast component corresponds to freely diffusing fluorophores, rather than photophysics processes. The same holds for the mutant FtsZΔCtl, which has a deleted Ctl (compare Materials and Methods in appendix C.1) and will be of relevance in the following sections.

The facts that both models, 3D+3D and 3D+T, yield similar diffusion coefficients for FtsZ and both describe the experimental autocorrelation curves well, emphasize that prior knowledge about the underlying system is crucial. An unreflected analysis with a triplet contribution could easily lead to the conclusion that there was only one diffusing species in the system. The model-driven analysis of FCS autocorrelation curves is the predominant form to analyse such data, because the recovery of an underlying distribution of dynamics is an ill-posed inverse problem, where the stability of the solution is a major concern [Petrov and Schwille, 2008a].

In the analysis of the previous sections, we assumed that there is only one species of FtsZ that diffuses with a defined diffusion coefficient. This was done, regardless of whether FtsZ was expected to be filamentous or monomeric. The same approach has been previously followed for FtsZ [Reija et al., 2011, Hou et al., 2012, Monterroso et al., 2012, Montecinos-Franjola et al., 2012, Monterroso et al., 2013, Ahijado-Guzmán et al., 2013, Mikuni et al., 2015]. For monomeric FtsZ, we expect this approach to yield a good estimate of the hydrodynamic radius. On the other hand, for polymerized FtsZ the assumption of a single diffusing component potentially allows for a rough estimation of the mean diffusion coefficient of a mixture of filaments, but comes with a significant bias, which originates from the nature of FCS measurements. Namely, the contribution of each species to the total autocorrelation curve is weighted by its relative abundance and its squared brightness. Consequently, bright long filaments contribute more to the autocorrelation curve, resulting in an overestimation of the mean filament length. This effect is discussed in more detail in section V.2.3.

V.2.2.2 Hydrodynamic radius of FtsZ in the absence of GTP exceeds the monomer radius

In section V.2.1, the filament formation of FtsZ and the action of MipZ were observed and semiquantitatively described using FCS. Based on the calibration measurement, the diffusion coefficient for WT FtsZ can be calculated. Moreover, using the Stokes-Einstein-Smoluchowski relation (equation II.5), the hydrodynamic radius R_h can be estimated. This work finds $D = (27 \pm 2)\ \mu\text{m/s}^2$ for WT FtsZ from *C. crescentus* in the absence of GTP, which is in good agreement with previously presented DLS measurements [Hou et al., 2012]. Table V.1 shows a collection of diffusion coefficients and physical sizes of FtsZ measured by different studies. Interestingly, all reports where the hydrodynamic radius was estimated from measurements of the diffusion coefficient, yield much larger values than the physical sizes predicted by other studies. This effect is particularly pronounced for WT FtsZ from *C. crescentus*. Moreover, in the absence of GTP, the diffusion coefficient measured for WT FtsZ from *C. crescentus* is aroundtwo times smaller than the diffusion coefficient of the chimeric protein FtsZ-YFP-mts (compare table V.1, figure C.5 in appendix C.2). This is particularly surprising, as the molecular mass of WT FtsZ from *C. crescentus* is 54 kDa, whereas FtsZ-YFP-mts has a considerably larger molecular mass of 69 kDa. Similarly, table V.1 shows differences between the diffusion coefficients of WT FtsZ from *E. coli*

(40 kDa) and *C. crescentus* (54 kDa), which by far exceed what would be expected from the differences in molecular weight. Assuming spherical particles of similar mean density, one would expect that WT FtsZ derived from *E. coli* has a roughly 10% larger diffusion coefficient, corresponding to the third root of the ratio of the molecular weights. The reported diffusion coefficients differ however by a factor of 2 to 4, suggesting that the differences are not exclusively caused by different monomer sizes.

This indication is further supported by theoretical predictions based on the approximations of FtsZ by convex hulls. We predicted the protein structures of FtsZ from *C. crescentus* (compare figure V.1) and *E. coli* using the I-TASSER tool [Zhang, 2008, Roy et al., 2010, Yang et al., 2014]. The obtained structures were described by convex hulls for which the diffusion coefficient was calculated using the HullRad tool [Fleming and Fleming, 2018]. The results are shown in table V.1. Interestingly, in these shape-based predictions WT FtsZ from *E. coli* has a 15% larger diffusion coefficient than WT FtsZ from *C. crescentus*. This result is in line with the estimated 10% difference between both diffusion coefficients, which was based on the molecular weights. Moreover, the predicted diffusion coefficient for monomeric WT FtsZ from *C. crescentus* is almost three times larger than the diffusion coefficient measured in this work.

To identify the origin of the discrepancy between the anticipated size of WT FtsZ from *C. crescentus* and its diffusion coefficient, three potential sources are addressed. First, to translate the diffusion coefficient into the hydrodynamic radius, the temperature and the bulk viscosity are assumed to be known. Here, the temperature at the objective ($T = 300\,\mathrm{K}$) is assumed to be the sample temperature, which is expected to be accurate with a relative error below 1%. Moreover, the viscosity of the used buffer (P buffer) at this temperature was measured by a rolling ball viscosimeter together with a densiometer, and found to be $\eta = 0.878\,\mathrm{mPa\,s}$, which is only 3% higher than the viscosity of water [Kestin et al., 1978]. Hou *et al.* in contrast, measured viscosities of $2\,\mathrm{mPa\,s}$ to $3\,\mathrm{mPa\,s}$ [Hou et al., 2012]. As a reference, an aqueous solution of 850 mM sucrose would yield similar viscosities [Haynes, 2014]. Neither the buffer conditions used here, nor the conditions used in [Hou et al., 2012] support such high bulk viscosities. One may speculate however, that the charged beads, whose diffusion coefficients were determined by Hou and colleagues to obtain the bulk viscosity, may have gotten interconnected by FtsZ polymers. Regardless of the origin, the different bulk viscosities between [Hou et al., 2012] and this study perfectly explain why similar diffusion coefficients were found in both cases, but the concluded filament sizes (compare section V.2.3) and hydrodynamic radii of monomers (this section)

Table V.1: Diffusion coefficients and hydrodynamic radii of FtsZ in the absence of GTP. The respective quantities were calculated for 25 °C, using equation II.5, assuming a single diffusing species and the viscosity of water with a temperature dependence as described in [Kestin et al., 1978]. The underlined values highlight the quantities that were measured in the respective work. For AFM measurements, the hydrodynamic radius was estimated from height and lateral extent of surface-confined FtsZ filaments. For ref. [Hou et al., 2012], the viscosity of water was assumed instead of the surprisingly high reported viscosity. In ref. [Montecinos-Franjola et al., 2012], the temperature at which experiments were conducted is not reported, and 23 °C was assumed. All reported values were experimentally measured, except for the HullRad method [Fleming and Fleming, 2018], which relies on the description of the protein by a convex hull. The underlying protein structures were predicted using I-TASSER [Zhang, 2008, Roy et al., 2010, Yang et al., 2014]. The obtained diffusion coefficients were adjusted for 25 °C in water.

	diffusion coefficient D [µm/s^2] at 25 °C	hydrodynamic radius R_h [nm]	method
WT FtsZ (*C. crescentus*) this work	$\underline{27 \pm 2}$	9.6 ± 0.7	FCS
FtsZΔCtl (*C. crescentus*) this work	$\underline{39 \pm 5}$	6.3 ± 0.8	FCS
WT FtsZ (*C. crescentus*) [Hou et al., 2012]	$\underline{35}$ 94 ± 11	7.8 $\underline{2.6 \pm 0.3}$	DLS TEM
WT FtsZ (*E. coli*) [Reija et al., 2011]	$\underline{53 \pm 5}$	4.6 ± 0.4	FCS
WT FtsZ (*E. coli*) [Montecinos-Franjola et al., 2012]	$\underline{60 \pm 1}$	3.9 ± 0.1	FCS
WT FtsZ (*E. coli*) [González et al., 2005]	88 ± 2 123	$\underline{2.8 \pm 0.1}$ (width) $\underline{2}$ (height)	AFM
WT FtsZ (*E. coli*) [Mukherjee and Lutkenhaus, 1999]	70	$\underline{3.5}$ (width)	TEM
FtsZ-YFP-mts (*E. coli*) this work	$\underline{50 \pm 13}$	4.7 ± 1.2	FCS
FtsZ-W319Y-His$_6$ (*M. jannaschii*) [Huecas et al., 2008]	91 ± 17	$\underline{2.7 \pm 0.5}$ (width)	cryoTEM
WT FtsZ (*C. crescentus*)	78.3	3.1	HullRad
FtsZΔCtl (*C. crescentus*)	89.8	2.7	HullRad
WT FtsZ (*E. coli*)	90.1	2.7	HullRad

are very different. There is no indication that the temperature and viscosity measured for this study are not accurate, and thus the discrepancy between diffusion coefficient-based estimations of the FtsZ monomer size and the directly measured physical dimension persists.

The second potential reason for this discrepancy may be that the observed FtsZ particles in fact are not monomers. In order to assess whether we observed polymerized FtsZ, potentially induced by leftover nucleotides from the protein purification, we incubated FtsZ with ethylenediaminetetraacetic acid (EDTA) to remove Mg^{2+}, which affects the dynamic behavior of FtsZ [Mukherjee and Lutkenhaus, 1999, Monterroso et al., 2012]. Using a similar approach, Monterroso and colleagues found for FtsZ from *E. coli* that only monomers of FtsZ are present at high concentrations of EDTA [Monterroso et al., 2012]. Here however, we observed no changes in the diffusion time of FtsZ upon addition of EDTA, as shown in figure C.6 in appendix C.2. This result indicates that a potential interaction may be of different origin than the classical polymerization. The following sections will further pursue this hypothesis.

Third, FtsZ from *C. crescentus* has a relatively large unstructured Ctl (compare figure V.1), which contributes to the viscous drag and thus reduces the diffusion coefficient. To address this contribution, we generated a mutant FtsZΔCtl which lacks the Ctl (compare Materials and Methods in appendix C.1). It needs to be mentioned that the deletion of the Ctl may potentially also alter interactions between FtsZ monomers [Sundararajan and Goley, 2017b]. Thus, the effects of the Ctl on viscous drag and lateral interactions require careful disentanglement.

V.2.2.3 Effect of the C-terminal linker of FtsZ on diffusion dynamics

As previously discussed, FtsZ from *E. coli* and *C. crescentus* differ only slightly in mass, but show large differences in diffusion coefficients in the absence of GTP. To identify potential origins of these differences, we performed a sequence alignment, including also other organisms (compare appendix C.2). Interestingly, all sequences are very similar, including a conserved C-terminal peptide, which is essential for the regulation of FtsZ and the anchoring to membranes through other cell division proteins [Ma and Margolin, 1999, Sundararajan and Goley, 2017a]. However, across the compared organisms, *C. crescentus* FtsZ has by far the largest C-terminal-linker domain. This domain is unstructured [Erickson et al., 2010] and appears to be essential for cell division in *C. crescentus* [Sundararajan et al., 2015]. To test, whether this Ctl causes interactions between individual FtsZ

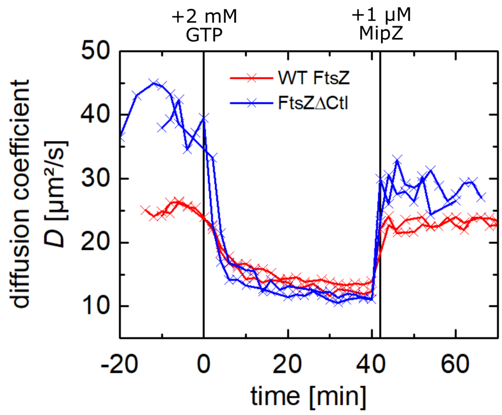

Figure V.4: Functionality of FtsZ without C-terminal linker domain. Time evolution of the diffusion coefficient as in figure V.2D. 2 mM GTP and 1 µM MipZ were added at 0 min and 40 min, respectively. WT FtsZ and FtsZΔCtl were used at 2 µM with 10% labeled fraction.

monomers, which may potentially give rise to the large differences in diffusion coefficient between FtsZ from *E. coli* and *C. crescentus* (table V.1), but also to assess the effect of the Ctl on the diffusion coefficient, we generated and purified a mutant FtsZΔCtl of FtsZ from *C. crescentus*, which lacks the Ctl (amino acids 336–480 deleted, compare figure V.1 and appendix C.2). For a slightly different deletion region of the Ctl, Sundararajan and colleagues reported a reduced GTP hydrolysis rate and increased lateral interaction of protofilaments compared to WT FtsZ [Sundararajan and Goley, 2017b]. Before quantifying the diffusion properties of FtsZΔCtl, we repeated the experiments from section V.2.1, i.e. filament growth and subsequent breakage by MipZ, to assess the functionality of this mutant.

The mutant FtsZΔCtl is still capable of filament formation upon addition of GTP. Although the initial diffusion coefficient without GTP is much larger than for WT FtsZ, in the steady state of polymerization, this mutant forms filaments that diffuse slightly slower than the wild type (figure V.4). This observation may potentially originate from slightly longer filaments formed by the FtsZΔCtl mutant. On the other hand, Sundararajan and Goley recently suggested that the Ctl may act as a repelling brush and that Ctl deficient mutants of FtsZ form wider filaments because of an increased lateral interaction [Sundararajan and Goley, 2017b]. The FtsZΔCtl mutant reported here has, however, a smaller region of the Ctl deleted. Whether this particular mutant also exhibits a lateral interaction of protofilaments needs to be addressed in future work.

The steady state of filament length is reached slightly faster for FtsZΔCtl than for the wildtype, as shown in figure C.3 (appendix C.2). Finally, the interaction of MipZ with FtsZ does not appear to depend on the Ctl.

Qualitatively, figure V.4 shows that the addition of MipZ shortens the mean filament length of FtsZΔCtl, just as it does for WT FtsZ. Even more interestingly, comparing the initial state without GTP and the final state after addition of GTP and MipZ, the relative increase in diffusion time is identical for the wild type and the ΔCtl mutant, as shown in figure V.2E (green circles). The obtained diffusion coefficients are summarized in figure C.5 in appendix C.2. Qualitatively, WT FtsZ and FtsZΔCtl show the same effects: they polymerize upon addition of GTP and the structures become smaller again upon addition of MipZ. Interestingly, as for the wild type, FtsZΔCtl forms on average larger structures when incubated with GTP and MipZ from the beginning, as compared to an initial polymerization with GTP and a subsequent degradation by MipZ (figure C.5 in appendix C.2). Finally, in the absence of GTP, the diffusion coefficient of FtsZΔCtl does not appear to depend on MipZ, indicating no permanent interaction. If FtsZΔCtl and MipZ would co-diffuse, the diffusion coefficient of FtsZ should change, as both are mixed in the same quantities (1 µM each) and both have similar molecular masses (MipZ 30.8 kDa [Thanbichler and Shapiro, 2006], FtsZΔCtl 38.3 kDa).

According to this semiquantitative analysis, WT FtsZ and FtsZΔCtl behave very similarly. However, a thorough quantitative analysis of the diffusion coefficient of the supposedly monomeric case (no GTP) still yields surprisingly large hydrodynamic radii. In detail, the mutant FtsZΔCtl has a molecular mass of 38.3 kDa, which is similar to the molecular mass of WT FtsZ from *E. coli*. However, the diffusion coefficients obtained by FCS differ still significantly, suggesting that the hydrodynamic radius of FtsZΔCtl is approximately two times larger (table V.1). On the other hand, FtsZΔCtl has a larger diffusion coefficient than WT FtsZ, as expected. Again, the difference in diffusion coefficient cannot be solely attributed to the differences in molecular mass, which only account for a difference of around 12%. The unstructured Ctl may explain this discrepancy. Consequently, as in the previous section, a hybrid approach of structure prediction and estimation of the diffusion coefficient (I-TASSER [Zhang, 2008, Roy et al., 2010, Yang et al., 2014] and Hull-Rad software tools [Fleming and Fleming, 2018]) was performed (compare table V.1). The predicted diffusion coefficients for *C. crescentus* WT FtsZ and FtsZΔCtl are both more than twice as large as the values measured by FCS. Moreover, the hybrid approach yields a 15% larger diffusion coefficient for FtsZΔCtl compared to WT FtsZ, whereas the FCS measurements yield a 45% difference. Thus, the physical size and the viscous drag of the

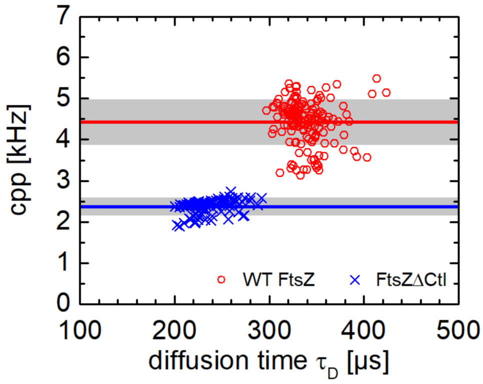

Figure V.5: cpp of WT FtsZ and a Ctl deficient mutant in the absence of GTP. Scatter plot of the diffusion times and the respective cpp of WT FtsZ (red circles) and FtsZΔCtl (blue crosses) from *C. crescentus* in the absence of GTP. Each point corresponds to a 2 min FCS measurement with 2 µM FtsZ out of which 10% were labeled with Alexa488. The means (solid lines) and standard deviations (gray shaded areas) are cpp $= (4.4 \pm 0.5)$ kHz and cpp $= (2.4 \pm 0.2)$ kHz for WT FtsZ and FtsZΔCtl, respectively. The autocorrelation curves were analyzed using a model with two freely diffusing species, one of them corresponding to free Alexa488 (compare Materials and Methods in appendix C.1). The deletion of the Ctl results not only in a shorter diffusion time, but also in a lower cpp. This indicates that the average particles are brighter in the case of the wild type, suggesting that WT FtsZ forms oligomers in the absence of GTP.

unstructured Ctl do not to fully explain the different diffusion coefficients of WT FtsZ and FtsZΔCtl.

To further investigate whether this discrepancy originates from the change in monomer size or a Ctl-mediated interaction between several monomers, we analyzed the cpp of the individual measurements (figure V.5). As before, the autocorrelation curves were analyzed with a model comprising two freely diffusing species, out of which one was assigned to freely diffusing Alexa488. The corresponding fits yield the particle numbers of both species, which together with the count rate of the detectors can be used to calculate the overall cpp. Interestingly, WT FtsZ has not only a larger diffusion time than FtsZΔCtl, but also has on average an almost two times higher cpp, although all measurements were performed at the same irradiance. The latter is remarkable, especially because only 10% of the FtsZ proteins were labeled. Consequently, assuming that the intrinsic brightness of Alexa488 is identical, regardless of whether it is bound to WT FtsZ or FtsZΔCtl, we conclude that in the absence of GTP WT FtsZ forms oligomers. The degree of oligomerization is significantly decreased when the Ctl is deleted.

In conclusion, both WT FtsZ and FtsZΔCtl have in the absence of GTP hydrodynamic radii that suggest structures that are much larger than the monomers. Consequently, it is conceivable that oligomers are the predominant state. The mean size of these oligomers is larger for the wild type, suggesting that the unstructured Ctl induces a lateral interaction. This is an interesting finding, because Sundararajan and coworkers proposed that the Ctl acts as a repulsive brush, reducing the lateral interaction of protofilaments [Sundararajan and Goley, 2017b].

Having realized that WT FtsZ forms oligomers in the absence of GTP, it would be interesting to deduce an average size. The straightforward approach would be to calculate the diffusion coefficient and the hydrodynamic radius. Unfortunately, this assumes a single diffusing component of spherical particles with a distinct brightness. In reality, however, it is more likely to find a size and brightness distribution. Moreover, especially when FtsZ grows into filaments, the diffusing particles are rather rod-like than spherical. To accommodate these effects, the next two sections will be used to derive an appropriate model function to analyze the autocorrelation curves of a distribution of filaments. This novel approach will be applied to FtsZ in the absence and presence of GTP in sections V.2.2.6 (page 119) and V.2.3.2 (page 123).

V.2.2.4 Diffusion of rod-like particles

To quantitatively interpret the equilibrium results for FtsZ in the presence and absence of GTP, it would be advantageous to translate the diffusion coefficient into an estimated number of monomers. A straightforward approach is to estimate the filament length through the hydrodynamic radius obtained from the Stokes-Einstein-Smoluchowski relation (equation II.5) [Reija et al., 2011, Monterroso et al., 2013]. However, this assumes spherical particles, which is clearly a non-ideal description of filaments. In a first step towards finding a model function for the autocorrelation curve of a distribution of filaments, we find an expression for the diffusion coefficient of a rod-like particle, based on previously reported models.

Hou and colleagues recently studied the filament formation and degradation of FtsZ from *C. crescentus* using DLS [Hou et al., 2012]. They applied models for diffusing rod-like particles to their experimental results. In detail, they used models by Bloomfield and colleagues [Bloomfield et al., 1967], Van de Sande and Persoons [Van de Sande and Persoons, 1985], and Seils and Pecora [Seils and Pecora, 1995], and found only little to moderate differences between these models. Consequently, it is sufficient to pick one of these models. Therefore, here only the model of a stiff cylinder is considered [Seils and

Pecora, 1995]. In detail, a polymer, made up of j spherical monomers of radius r_0 is treated as a cylinder of width $2r_0$ and length $L = 2r_0 j$. The coordinate system is chosen such that one axis points along the long axis of the cylinder and thus the diffusion coefficient D_j of a j-mer separates into three contributions.

$$D_j = \frac{1}{3}\left(2D_\perp + D_\parallel\right) \tag{V.2}$$

According to the work by Seils and Pecora [Seils and Pecora, 1995], the perpendicular and parallel diffusion coefficients $D_\perp$ and $D_\parallel$ are given as:

$$D_\perp = \frac{k_B T}{4\pi\eta L}\left(\ln(j) + \nu_\perp\right) \tag{V.3}$$

$$D_\parallel = \frac{k_B T}{2\pi\eta L}\left(\ln(j) + \nu_\parallel\right) \tag{V.4}$$

with the end corrections

$$\nu_\perp = 0.839 + 0.185 j^{-1} + 0.233 j^{-2} \tag{V.5}$$

$$\nu_\parallel = -0.207 + 0.980 j^{-1} - 0.133 j^{-2} \tag{V.6}$$

Taken together, the expression for D reads:

$$D_j = \underbrace{\frac{k_B T}{6\pi\eta r_0}}_{D_{j=1}} \frac{1}{2j}\left(2\ln(j) + \nu_\perp + \nu_\parallel\right) \qquad j = 2, 3, 4 \ldots \tag{V.7}$$

Interestingly, the diffusion coefficient of a cylindrical model polymer can be expressed in terms of the diffusion coefficient of the monomer $D_{j=1}$ multiplied by an empirical expression that depends solely on the number of monomers forming the chain. Moreover, as j^{-1} decays faster than the logarithm grows, the diffusion coefficient for infinitely long cylinders ($j \to \infty$) tends to zero, as expected. It should be noted, that for the FCS measurements, it is assumed that the FtsZ structures are much smaller than the extension of the detection volume. Moreover, rotational diffusion is neglected in the analysis as the filaments are sufficiently short.

V.2.2.5 Autocorrelation function of linear filaments with a known length distribution

The assumption of one diffusing species gives only an estimate of the mean diffusion coefficient, and suffers from a brightness-related bias. When assuming, however, the co-existence of several oligomer states, a more realistic model would comprise a superposition of several species (compare equation II.37):

$$G(\tau) = \frac{1}{\left(\sum\limits_{k=1}^{C} Q_k N_k\right)^2} \sum_{j=1}^{C} Q_j^2 N_j G_j(\tau) \tag{V.8}$$

$$G_j(\tau) = \left(1 + \frac{\tau}{\tau_{D,j}}\right)^{-1} \left(1 + \frac{\tau}{S^2 \tau_{D,j}}\right)^{-1/2} \tag{V.9}$$

$$\tau_{D,j} = \frac{w_{xy}^2}{4D_j} \tag{V.10}$$

Here, we derive an autocorrelation fitting function, which accounts for a superposition of an arbitrary number C of species, yet has only two free fit parameters. This is achieved, by assuming that the FtsZ oligomers assemble in a linear fashion, i.e. form filaments. In such a scenario, the diffusion time $\tau_{D,j}$ of each j-mer can be expressed based on equation V.7.

$$\tau_{D,j} = \tau_{D,j=1} \frac{2j}{2\ln(j) + \nu_\perp + \nu_\parallel} \qquad j = 2, 3, 4 \ldots \tag{V.11}$$

Equations V.8–V.11 provide a framework for calculating the individual autocorrelation curve G_j of diffusing multimers, assuming the diffusion time of the monomer is known. For a mixture of multimers of different lengths, each j-mer has a weighted contribution to the overall autocorrelation amplitude (equation V.8). The individual weights depend not only on the relative abundance of the respective multimer, but also on the brightnesses Q_j.

To find an expression for these weights, a simple theory for filament size distributions is used. FtsZ has been shown to undergo treadmilling *in vitro* [Loose and Mitchison, 2013] and *in vivo* [Bisson-Filho et al., 2017, Yang et al., 2017] in the presence of GTP. In the absence of GTP, FtsZ from *C. crescentus* forms oligomers due to an unknown interaction, as shown above. For the latter case, we also assume a linear assembly of proteins. For other scenarios, the approach presented here can still be used, but the underlying size distribution would need to be adjusted. Consequently, a filament that grows and shrinks by one monomer at a time with attachment and detachment rates k_{on} and k_{off} is considered (compare figure V.2A). The addition of a monomer not only depends on the on-rate, but also on the monomer concentration c_1. A derivation of the corresponding size distribution was first presented by Flory [Flory, 1936]. Four dynamics affect the concentration c_j of a j-mer: addition of a monomer to a $(j-1)$-mer and detachment of a monomer from a $(j+1)$-mer increase the concentration c_j, whereas any monomer attachment or detachment to or from a j-mer reduces the concentration c_j.

$$\frac{\mathrm{d}c_j}{\mathrm{d}t} = k_{\text{off}}c_{j+1} + k_{\text{on}}c_{j-1} - \left(k_{\text{on}}c_1 + k_{\text{off}}\right)c_j \overset{\text{steady state}}{=} 0 \tag{V.12}$$

In equilibrium, a steady state is reached and the concentration of a j-mer does not change over time. The ansatz $c_j = A\lambda^j$ satisfies the steady state condition for $\lambda = \frac{k_{\text{on}}}{k_{\text{off}}}c_1$ and $\lambda = 1$ [Edelstein-Keshet and Ermentrout, 1998]. The latter is, however, unphysical, as it corresponds to an equal concentration of all filament lengths, including extremely long filaments. The proportionality constant A is not relevant for this study, but can be calculated from appropriate boundary conditions. The ansatz is a geometric distribution, which can be easily expressed in terms of an exponential.

$$c_j = A\lambda^j = A\,e^{-jE} \tag{V.13}$$

$$E = -\ln\lambda \tag{V.14}$$

Here, E may be conceived as an activation energy, in units of k_BT, for the addition of a monomer. Moreover, it is important to realize that equation V.13 can be interpreted as a size distribution, with the mean filament length $\langle l\rangle = E^{-1}$. Figure V.6A shows the normalized probability distribution for $l = 2$ and $l = 5$.

For the calculation of a multicomponent autocorrelation function, the brightness of every component needs to be known. In fact, as shown in equation V.8, the individual autocorrelation G_j of each component is weighted by a factor $w_j = Q_j^2 N_j$. It is sufficient to know w_j up to a prefactor, because the prefactor cancels out upon normalization in equation V.8. From equation V.13, it follows that $N_j \propto e^{-jE}$. For the brightness Q_j of a j-mer, two important cases are considered. In the very best case, each monomer carries exactly one fluorescent label of identical brightness. In this case, the weighting factor is simply $w_j \propto j^2 e^{-jE}$. However, a perfect labeling efficiency of 100% is typically not achieved. A genetically encoded fluorescent protein at the N-terminus may get close, because truncated proteins may not be functional, but photobleaching and incomplete maturation deteriorate the labeling efficiency. With synthetic fluorescent labels, the yield is typically even lower, and a one-to-one labeling is not guaranteed. In the experiments presented here, labeled and unlabeled FtsZ are mixed at a ratio of $\alpha = 1/10$. Assuming that the fluorescent label does not alter the activity, for the addition of every monomer, there is a chance α that the new monomer is labeled. This is exactly the definition of the well-known binomial distribution. Consequently, for a j-mer the mean number of fluorescent labels is $j\alpha$ and thus $w_j \propto j^2 e^{-jE}$. Hence, the autocorrelation function is invariant to the labeling efficiency of the monomers. The normalized, brightness weighted length distributions w_j for $l = 2$ and $l = 5$ are shown in figure V.6A. As w_j features a quadratic growth and an exponential suppression, the distribution has a local maximum.

Based on this derivation, the final fit function reads:

$$G(\tau) = G_0 \sum_{j=1}^{C} j^2 e^{-jE} G_j(\tau) \tag{V.15}$$

Here, the amplitude is expressed as a constant G_0 and G_j was previously presented in equation V.9.

To highlight the importance of the brightness distribution, a simple test was performed: Autocorrelation curves with values of E ranging from 1 to 100 were computed based on equation V.15. These autocorrelation curves, which reflect upon distributions of filament sizes, were fitted by a single-component diffusion model. From the obtained diffusion time, the mean filament length was estimated (see figure C.7 in appendix C.2). If the brightness distribution is not considered, the estimated filament length is strongly overestimated by more than a factor of two. Longer and thus brighter filaments contribute more to the total autocorrelation function. This issue is reflected only to a minor degree in the residuals of the fit. In the example in figure C.7, the maximum residuals are around 1% of the amplitude, which would most likely be masked by noise in most FCS measurements. We conclude that for a distribution of diffusing particles with varying brightnesses, the knowledge of the underlying distribution is essential to obtain unbiased estimates of the diffusion coefficients.

It should be noted that this model does not render all previous results invaluable. Relative changes, such as the formation of filaments and the subsequent shortening by MipZ, can be observed, even if the absolute numbers are not exact.

V.2.2.6 Size distributions of FtsZ in the absence of GTP

Although the newly derived fitting function (equation V.15) comprises an arbitrary number of diffusing components C, it only depends on two free parameters: E and G_0. To calculate the autocorrelation curve, the diffusion time of the monomer needs to be known, and is calculated using the Stokes-Einstein-Smoluchowski relation (equation II.5). To get a rough estimate of the hydrodynamic radius, we revisited an AFM study of surface confined FtsZ filaments (*E. coli*) [González et al., 2005], which found the filaments to be 4 nm in height and (5.6 ± 0.1) nm in width. We calculated the effective radius to be $(2 \cdot 5.6\,\mathrm{nm} + 4.0\,\mathrm{nm})/2/3 = 2.5\,\mathrm{nm}$, knowing that this was only a very rough estimate. This value is similar to the results of others (compare table V.1).

The derived autocorrelation function (equation V.15) comprises a sum over the individual autocorrelation functions of j-mers. In practice, only a limited filament length can be considered for computational reasons. The cutoff polymer size should be much larger than the mean of the underlying size distribution: $C \gg \langle l \rangle$. Here, a cutoff of $C = 100$ was consistently implemented.

Unfortunately, the autocorrelation curves for WT FtsZ and FtsZΔCtl in the absence of GTP appeared to have also another short time decay, which is not accounted for by this model (compare figure V.3). This contribution is easily explained by the diffusion of unbound free Alexa488. To account for this effect, another diffusing component was added to the fit. As before, to keep the number of fit parameters to a minimum, the diffusion time of Alexa488 was fixed (compare Materials and Methods in appendix C.1). After accounting for free dye diffusion, the experimental autocorrelation curves for WT FtsZ and FtsZΔCtl are well described by the derived model function, as shown for two representative 2 min measurements in figure V.6B.

The obtained values for E and the corresponding mean number of monomers per filament are presented in table V.2 and figures V.6C,D. As already indicated by the previously used model, the deletion of the unstructured C-terminal domain reduces the mean filament length. For FtsZΔCtl less than a dimer is obtained on average. WT FtsZ forms on average trimers to tetramers in the absence of GTP. A similar analysis was performed for the monomeric mutant FtsZN211A, which appears to form on average trimers, in very good agreement with the results for the wild type. This agreement once more emphasizes that the interaction found here is of different origin than the classical GTP-dependent polymerization of FtsZ.

The results presented here are in themselves consistent, but based on a novel analysis

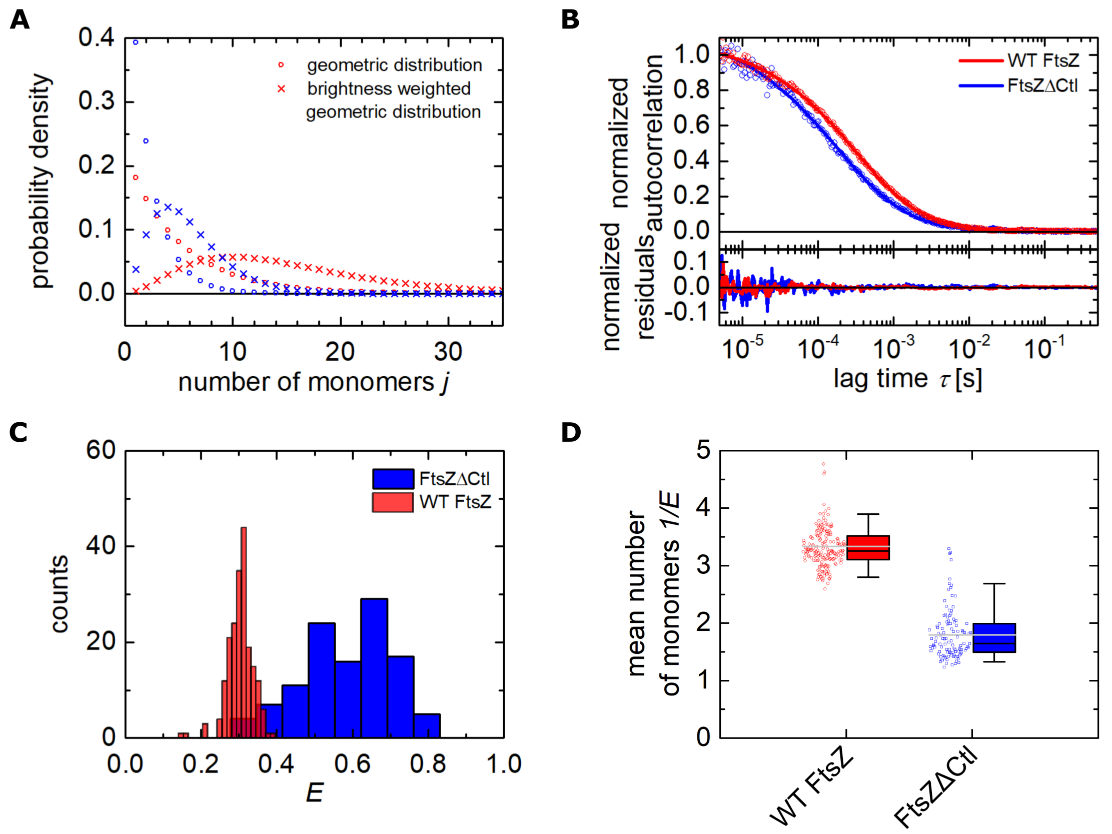

Figure V.6: C-terminal linker in FtsZ appears to introduce protein interaction. A) Theoretical geometric length distributions (circles) and the corresponding brightness weighted distributions w_j (crosses) for dimers (blue, $E = 0.5$) and pentamers (red, $E = 0.2$) as mean. B) The proposed model for the autocorrelation function (equation V.15), together with a term for free diffusion of fluorescent label, describes the experimental data well, with random residuals. Each autocorrelation curve corresponds to a 2 min measurement. The fit has three free parameters: E and the overall amplitudes of the FtsZ autocorrelation and the free diffusion of free fluorescent dye. The FtsZ monomers were assumed to be spheres with hydrodynamic radii $R_h = 2.5$ nm. C) Histograms of E as obtained from the fits of 199 and 113 2 min measurements on WT FtsZ and FtsZΔCtl, respectively. Clearly, a deletion of the Ctl reduces the average filament size. D) Corresponding mean number of monomers in one filament, showing individual measurements and the corresponding boxplots with median (black lines) and mean (gray lines). The whiskers of FtsZΔCtl are slightly skewed towards an increased size because of occasional aggregates diffusing through the confocal volume. For WT FtsZ the average number of monomers in one filament is found to be between 3 and 4. For FtsZΔCtl, only less than 2 monomers are forming on average. As indicated in panel A), these values only correspond to mean values. The filaments are assumed to obey a geometric distribution. All measurements were taken in the absence of GTP.

Table V.2: Sizes of FtsZ oligomers in the absence of GTP. Experimental FCS data were fitted by equation V.15, yielding a value for E for each measurement. The mean number of monomers per particle are obtained by taking the inverse of E. In size exclusion measurements the molecular mass was determined relative to a set of reference proteins. The average number of monomers in one structure was estimated by dividing the molecular mass by the expected monomer masses, which are 54.2 kDa and 38.3 kDa for WT FtsZ and FtsZΔCtl, respectively.

	FCS			size exclusion chromatography	
	number of measurements	E	mean number of monomers	molecular mass [kDa]	mean number of monomers
WT FtsZ	199	0.30 ± 0.03	3.3 ± 0.4	180 ± 6	3.3 ± 0.1
FtsZN211A	15	0.32 ± 0.03	3.2 ± 0.3	158 ± 21	2.9 ± 0.4
FtsZΔCtl	113	0.58 ± 0.12	1.7 ± 0.4	65 ± 2	1.7 ± 0.1

of FCS autocorrelation curves. To confirm that this approach yields correct results, we performed size exclusion chromatography[3] to estimate the mean size of the investigated FtsZ proteins, based on their retention time. Strikingly, this mechanistically completely different approach yields identical mean oligomer sizes as the FCS-based approach, as shown in table V.2. We conclude that the derived model, which assumes a geometric size distribution of oligomers is applicable to describe FtsZ in the absence of GTP. As indicated by the different cpp (figure V.5), the different diffusion coefficients of WT FtsZ and FtsZΔCtl are not exclusively the result of the Ctl. Accordingly, the Ctl of FtsZ appears to play a major role in the formation of FtsZ oligomers in a non-GTP dependent manner.

V.2.3 Quantitative insights into FtsZ dynamics in the presence of GTP

V.2.3.1 Estimation of the FtsZ filament length using a single-component diffusion model

The potential artifacts when treating a distribution of particle sizes with an effective single component has been theoretically discussed in section V.2.2.5. Despite the potential bias towards larger filament sizes, this approach will be used in this section for two reasons.

[3]Experiments by Laura Corrales Guerrero, PhD (Thanbichler lab, Philipps University Marburg, Germany)

First, the description of filaments with a single diffusing component has been frequently used in the past [Reija et al., 2011, Hou et al., 2012, Monterroso et al., 2012, Montecinos-Franjola et al., 2012, Monterroso et al., 2013, Ahijado-Guzmán et al., 2013, Mikuni et al., 2015] and is to date the standard procedure to analyze such data sets. Second, we will subsequently analyze the same data set with the newly derived fitting model (equation V.15) and compare both results.

When assuming that the experimental autocorrelation can be described by an effective single species that diffuses in 3D, we translate the diffusion time into a diffusion coefficient. Subsequently, one may calculate the corresponding effective hydrodynamic radius. On the other hand, equation V.7 expresses the diffusion coefficient of a rod-like particle and can be used to find the effective number of monomers that corresponds to the determined diffusion coefficient. Unfortunately, equation V.7 cannot be explicitly solved for j. However, a numerical approach provides an estimate of j, similar to the estimation of the membrane insertion size from the HPW-model that will be used in chapter VI. In detail, Newton's method was used to estimate the value of j at which the difference between measured and theoretical diffusion coefficient is zero.

The experimental diffusion coefficient of filaments formed from *C. crescentus* WT FtsZ (data from 30 min to 40 min after GTP injection) was $D = (13.3 \pm 0.9)\,\mu\mathrm{m/s}^2$ (mean and standard deviation), which is only slightly higher than previously reported DLS results [Hou et al., 2012]. Following the aforementioned approach based on equation V.7, the corresponding number of monomers could be computed, provided that the hydrodynamic radius of FtsZ monomers was known. As discussed in section V.2.2.6, we assume $r = 2.5\,\mathrm{nm}$ [González et al., 2005]. Finally, using the bulk viscosity of water $\eta = 0.851\,\mathrm{mPa\,s}$ at the temperature of the experiment ($T = 300\,\mathrm{K}$) [Kestin et al., 1978], the mean number of monomers was found to be $\langle j \rangle = 29 \pm 3$. Accordingly, the mean filament length was estimated to be $\langle l \rangle = (145 \pm 14)\,\mathrm{nm}$. It should be noted that the optical detection volume was a Gaussian with a typical $1/e^2$-width of around 210 nm. Although the assumption was that the filaments were much shorter than the size of the detection volume, no obvious deviations were found in the fit of the theoretical model to the experimental data. The average filament length found here is significantly longer than previously reported, although the obtained diffusion coefficients were similar [Hou et al., 2012]. This discrepancy originates from significantly different viscosities, as discussed in section V.2.2.2. A similar study found four to five-fold longer filaments using FtsZ derived from *E. coli* [Reija et al., 2011]. A comparison to the lengths of FtsZ filaments reported on surfaces [Mingorance et al., 2005] is challenging, as a surface may have significant impact on the polymerization dynamics [Hamon et al., 2009]. The system described here, is however imagined to be closer to *in vivo* conditions than surface-confined polymerizations.

V.2.3.2 Average filament size of FtsZ from *C. crescentus*

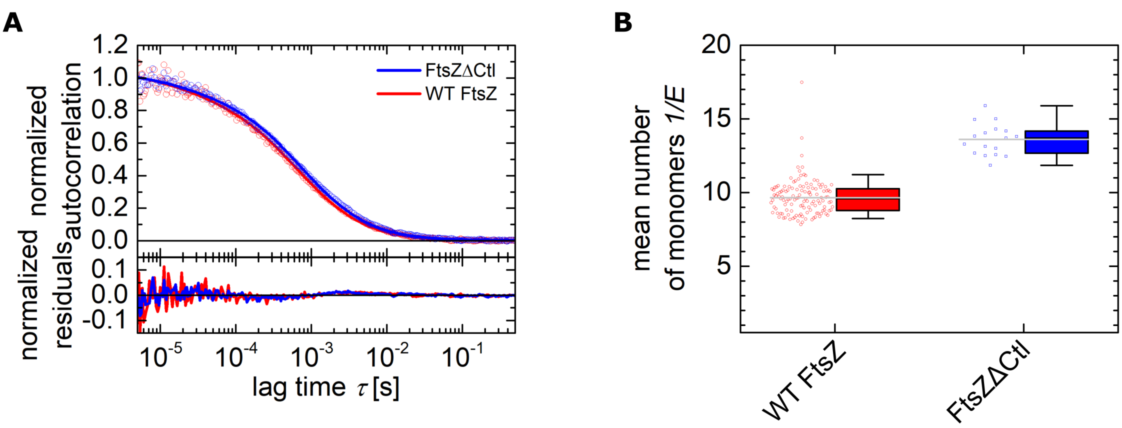

Figure V.7: Average filament size of FtsZ from *C. crescentus*. A) Representative autocorrelation curves of WT FtsZ and FtsZΔCtl in their fully polymerized state 30 min to 40 min after addition of GTP. The experimental data sets were acquired for 2 min each and were fitted by equation V.15, with an additional contribution from freely diffusing fluorophores. The model function describes the autocorrelation curves adequately. B) Corresponding mean filament lengths for WT FtsZ ($N = 128$) and FtsZΔCtl ($N = 17$). glsFCS measurement were performed at 2 µM FtsZ out of which 10% were labeled with Alexa488. GTP was used at 2 mM.

In section V.2.2.5, a model function for the analysis of diffusing filaments has been derived. The logical next step is to apply this analysis to fully polymerized FtsZ filaments. Therefore, autocorrelation curves that were acquired for 2 min in a time window from 30 min to 40 min after injection of GTP were considered. During this time, a steady state is reached and the filament size is considered to be constant, as shown in figure C.3 (appendix C.2). The corresponding results are shown in figure V.7. In detail, this work found that the average filament comprises $\langle j \rangle = 9.5 \pm 1.0$ ($E = 0.105 \pm 0.011$) and $\langle j \rangle = 13.5 \pm 1.0$ ($E = 0.074 \pm 0.006$) monomers for WT FtsZ and FtsZΔCtl, respectively. Assuming again a monomer radius $r = 2.5$ nm, these values translate to physical lengths of $\langle l \rangle = (48 \pm 5)$ nm and $\langle l \rangle = (68 \pm 5)$ nm.

As expected, the estimated mean filament length of WT FtsZ is considerably shorter than the estimation from the previous section, which does not consider a distribution of filament lengths. As shown in a simulation (figure C.7 in appendix C.2) and demonstrated by the comparison with size exclusion chromatography (table V.2), the distributions of filament lengths and brightnesses need to be considered in the analysis to yield unbiased results. Thus, the results from this section are believed to be more accurate.

The deletion of the Ctl resulted in the formation of slower diffusing filaments. While there is no indication that WT FtsZ shows a lateral interaction between protofilaments, Sundararajan and Goley reported that their Ctl-deficient FtsZ mutant exhibited a lateral interaction [Sundararajan and Goley, 2017b]. Thus, the cross-section of FtsZΔCtl may have a larger diameter than assumed, which would result in a potentially shorter filament length than estimated in this work. Interestingly, FtsZ from *E. coli* forms longer filaments than FtsZ from *C. crescentus*, while at the same time having a much shorter Ctl. Whether this correlation between length of the Ctl and mean length of the filaments holds across all prokaryotic versions of FtsZ is an interesting question for future studies.

V.3 Conclusion

In this chapter, FtsZ from *C. crescentus* was studied by FCS. In the first part, the polymerization of FtsZ was monitored through the time evolution of the diffusion time, a fit parameter of classical FCS analysis. For the first time, the effect of MipZ on the diffusion properties of FtsZ was investigated. As expected, MipZ breaks FtsZ filaments into shorter fragments, which are however considerably larger than monomers. Interestingly, the process required the presence of GTP. Without GTP, MipZ had little to no effect on the diffusion time of FtsZ.

In the second part of this chapter, a discrepancy between the diffusion coefficient of FtsZ in the absence of GTP and the physical monomer size was described. Upon deletion of the Ctl of FtsZ, the diffusion time shortened considerably, suggesting that the Ctl introduces an interaction between individual FtsZ proteins. To extract also quantitative information about FtsZ filaments from the FCS measurements, a novel fitting function, which assumes a geometric length distribution of filaments, was derived and successfully applied for FtsZ in presence and absence of GTP. For the latter, the results were verified by size exclusion chromatography experiments. Moreover, we extracted the size distributions of fully polymerized FtsZ in the steady state.

V.4 Outlook

The newly derived fitting model for the size distribution of filaments was cross-validated with size exclusion chromatography. To further proof the validity of this approach, cryo-electron tomography may be used to track filaments in 3D. By this approach the actual filament length distribution could be measured without forcing the filaments to a 2D surface, which potentially introduces a bias. It would be interesting to compare the size distributions from cryo electron tomography with the geometric distribution characterized by FCS. As FtsZ is a tubulin homoloque, it would be interesting to see how this model performs on similar filament forming proteins like tubulin and actin.

On a mechanistic level, future studies should further address the interaction of FtsZ and MipZ. As a next step to this work, MipZ should be labeled fluorescently, to perform FCCS between MipZ and FtsZ. This approach may potentially answer whether MipZ sequesters FtsZ. Once the system is understood at this level, further interactions of MipZ, e.g. with ParB and DNA may be addressed by FCS or single-molecule imaging studies.

VI

FCS STUDY OF PROTEIN MOBILITIES IN LIPID MONOLAYERS

The data sets related to figures VI.2 and VI.7 were acquired by Franco Conci. The results presented in this chapter are the outcomes of an equal-contribution collaboration with Alena Khmelinskaia and have been recently communicated:

Khmelinskaia, A., Mücksch, J.*, Conci, F., Chwastek, G., Schwille, P. (2018), FCS analysis of protein mobility on lipid monolayers. Biophys. J., 114: 2444-2454. doi: 10.1016/j.bpj.2018.02.031, *indicates equal contributions. A reprint permission has been granted by the publisher.*

VI.1 Introduction

Over the past decades, several model membrane systems have been developed, studied and characterized. While they all share the self-assembly of lipids, arising from their amphiphilic character, they differ in many other features. Especially for the study of protein-lipid interactions performed *in vitro*, the choice of the model membrane highly depends on the system and the parameters to be studied. For example, an investigation of membrane curvature-dependent binding does require curved membranes, e.g. small unilamellar vesicles (SUVs) or large unilamellar vesicles (LUVs), fluorescence microscopy studies with high background solution may preferably be conducted on SLBs, which are compatible with TIRF microscopy, and transmembrane proteins are best studied using free-standing membranes. In cells, the interaction of proteins and membranes also depends on the lipid packing density and mobility. *In vivo*, both are regulated by the local lipid composition and by lateral organization [Holthuis and Menon, 2014, Bigay and Antonny, 2012, van den Brink-van der Laan et al., 2004]. In *in vitro* lipid bilayers, the lipid mobility can be altered by membrane composition, ambient bulk viscosities temperature and ionic strength [Machán and Hof, 2010, Böckmann et al., 2003]. However, such changes alter at least two parameters at the same time, which makes it difficult, if not impossible, to disentangle the effects of changes introduced [Brockman, 1999]. The possibility to study the effects of lipid packing and mobility on protein-membrane interactions in an unobstructed manner, is a unique feature of lipid monolayers. Moreover, the lipid composition of the monolayer can be changed over a much wider range compared to bilayers without adding effects of membrane curvature (for reviews see e.g. [Brockman, 1999, Stefaniu et al., 2014]). On the other hand, lipid monolayers are well suited to study the change of lateral pressure in the membrane upon binding of biomolecules, or based on that, to distinguish external membrane association from insertion. These features make lipid monolayers an interesting system for the study of interactions of biomolecules with lipids.

Several of such studies have been conducted using a wide range of approaches. Brewster angle microscopy (e.g. [Hönig and Moebius, 1991, Angelova et al., 1996, Wu et al., 1998, Seoane et al., 2000, Mandal et al., 2016]), infrared spectroscopy (e.g. [Maltseva et al., 2005, Meister et al., 2006, Amado et al., 2008, Dittrich et al., 2011, Travkova et al., 2013]) and X-ray-based methods (e.g. [Majewski and Stec, 2010, Dittrich et al., 2011, Watkins et al., 2011, Jones et al., 2012, Travkova et al., 2013, Abuillan et al., 2013]) have been commonly employed, but measurements of the surface pressure using Langmuir-Blodgett troughs are still the predominant tool (e.g. [Diakowski and Sikorski, 2002, Vitovič et al., 2008, Nieto-Suárez et al., 2008, Dittrich et al., 2011, Jones et al., 2012, Travkova et al., 2013]), most likely because it is the simplest, best established, and least costly approach. On the other hand, the Langmuir-Blodgett approach requires considerable changes in surface pressure to study binding effects, which can be achieved in two ways: either the binding biomolecules have an extremely large insertion size and only few molecules are required or the insertion size is small and many biomolecules need to bind to the monolayer to measure an effect on the surface pressure. In practice, the latter may apply in many cases, which limits the sensitivity of the assay. Moreover, a large scale insertion of biomolecules into the monolayer changes the MMA of the lipids, the key tuning parameter of the lipid monolayer. Consequently, it would be desirable to study the interaction of biomolecules and lipid monolayers with higher sensitivity to circumvent the aforementioned limitations.

Another parameter that has been widely neglected in the past is the mobility within the lipid monolayer. This parameter is of interest for two reasons: first, the viscosity in the monolayer is expected to be a monotonic function of the MMA [Gudmand et al., 2009]. This implies that a measurement of the diffusion coefficient of a biomolecule in the lipid monolayer or the viscosity of the lipid monolayer can be used to infer the MMA. Second, the reaction rate of membrane bound biomolecules strongly depends on their collision rate, which is directly related to their diffusion coefficients in the lipid monolayer. Consequently, the diffusion of lipid monolayer-associated biomolecules is a key parameter to understand their interaction dynamics.

Taken together, the study of lipid monolayers would benefit from a method that provides a high sensitivity for binding of biomolecules, preferably even small ones, and ideally also quantifies mobilities. Microscopy-based techniques like SPT, confocal FCS, fluorescence recovery after photobleaching (FRAP), and TICS, including raster image correlation spectroscopy (RICS), have become routinely used tools with single-molecule sensitivity. All of these methods have the potential to quantify mobilities in the lipid monolayer. FRAP has been applied for lipid monolayer studies [Huang et al., 1992], but is not considered here, because the initial bleaching may cause local chemical modifications of the air-exposed lipids and the expected diffusion in lipid monolayers is relatively fast, which causes fast recoveries and makes FRAP approaches challenging. On the other hand, SPT has been used to study lipid diffusion in lipid monolayers [Ke and Naumann, 2001, Sickert and Rondelez, 2003, Sickert et al., 2007], but typically needs to be combined with widefield microscopy. While parallel acquisition is possible with camera-based widefield approaches, they reject fluorescence from the subphase less efficiently than confocal microscopes. Especially in the perspectives of future studies on protein binding, titration experiments may have to cope with considerable signal from unbound proteins. The major advantage of correlation-based methods is the ability to directly extract particle numbers from the autocorrelation function of purely diffusing species [Magde et al., 1972], which is a direct consequence of the underlying Poissonian statistics. However, particle numbers and densities are only correctly estimated provided the size of the detection volume is known, and bleaching and background signal are negligible, or properly corrected for [Thompson, 1999, Costantino et al., 2005, Kolin et al., 2006a, Digman et al., 2005, Digman et al., 2009]. ICS-based approaches are particularly powerful in the context of spatial information. RICS has been performed on free-standing membranes [Gielen et al., 2009a], but the spatial information is not required for the study of lipid monolayers, which are supposed to be homogeneous. Consequently, this chapter focuses on the implementation of confocal FCS for the study of biomolecules interactions with lipid monolayers. So far, FCS has been employed exclusively to investigate lipid diffusion in lipid monolayers at the air-water interface [Gudmand et al., 2009, Chwastek and Schwille, 2013]. In their pioneering work, Gudmand and colleagues for the first time showed the relation between MMA and lipid diffusion in 1,2-dimyristoyl-sn-glycero-3-phosphocholine (DMPC) monolayers. They proposed a respective behavior for monolayer-bound biomolecules, but this hypothesis has never been investigated.

One of the main drawbacks of Langmuir-Blodgett troughs is the large volume in the range of at least 50 mL of conventionally used troughs (e.g. by Kibron Inc., Helsinki, Finland, [Kibron, 2018], or Binolin Scientific AB, Stockholm, Sweden, [BiolinScientific, 2018]). Therefore, relatively large amounts of protein are required, which is incompatible with minute amounts of proteins that are purified on a laboratory scale. Consequently, small chambers with tunable MMA are desirable. Moreover, as discussed above, such chambers should be compatible with fluorescence microscopy. A straightforward solution would be a miniaturized Langmuir-Blodgett through, which however comes with considerable engineering effort and costs. Duschl and colleagues proposed an alternative approach to control the interface area at small sample volumes: they exploited the known droplet geometry of a subphase droplet of known size [Duschl et al., 1998]. However, the droplet is subject to evaporation, which implies that the MMA is not constant over time. Recently, Chwastek and Schwille presented a different strategy, in which they use a miniaturized chamber with an air-water interface of constant area and control the MMA by the amount of lipid deposited on the interface [Chwastek and Schwille, 2013]. They studied the diffusion of a lipid probe at different MMAs and found a good agreement with the previously presented findings by Gudmand *et al.* [Gudmand et al., 2009].

In this chapter, the diffusion of a set of biomolecules associated to a lipid monolayer is investigated using FCS. To minimize the amount of required sample, miniaturized chambers inspired by [Chwastek and Schwille, 2013] are used. We cover a wide range of biomolecules from a small peptide (membrane proximal external region (MPER)), which is derived from the envelope glycoprotein gp41 of HIV-1, to rod-like DNA-based nanostructures. The diffusion of these biomolecules is discussed, also in the context of the Saffmann-Delbrück-model (SD-model) and the Hughes-Pailthorpe-White-model (HPW-model). Finally, empirical relations between lipid diffusion, monolayer viscosity and MMA are presented. Moreover, we exploit the amplitude information of the autocorrelation function to characterize the binding of the pentameric β subunit of cholera toxin (CtxB) to monolayers containing various amounts of CtxB's specific binding partner ovine brain ganglioside (G_{M1}).

VI.2 Results and Discussion

VI.2.1 Qualification of the miniaturized monolayer chambers

The MMA is a key parameter that characterizes the monolayer. It corresponds to the total area that on average is available to an individual lipid molecule. Thus, the MMA is expressed as the ratio of the total interface area A_{tot} and the total number of lipid molecules $N_{\text{lipid,tot}}$.

$$\text{MMA} = \frac{A_{\text{tot}}}{N_{\text{lipid,tot}}} \tag{VI.1}$$

In a conventional Langmuir-Blodgett trough, $N_{\text{lipid,tot}}$ is kept constant and the total available area is varied by moving two parallel barriers. Here, miniaturized chambers made of polytetrafluoroethylene (PTFE) are used instead of Langmuir-Blodgett troughs (figure D.2A in appendix D.1). The customized miniaturized chamber features a roughly three orders of magnitude smaller volume than conventional Langmuir-Blodgett through. This comes at the cost of no means to vary the interface area, which is exclusively determined by the shape of the meniscus and the physical dimensions of the chamber. Following equation VI.1, the MMA in these miniaturized chambers is controlled by the amount of lipids that is deposited on the air-water interface, while A_{tot} is kept constant. In principle, this approach is simple and straightforward, but at second glance, it is not necessarily clear that controlling $N_{\text{lipid,tot}}$ at a constant interface area is equivalent to compressing a constant $N_{\text{lipid,tot}}$ in Langmuir-Blodgett troughs. Namely, in a Langmuir-Blodgett trough the lipids initially spread over a large area and the initial monolayer is in its gas phase before compression. Hence, upon slow compression the monolayer slowly transits into the liquid-extended phase by slow lateral arrangement of lipids. For the miniaturized chambers, the situation is fundamentally different. Here, the lipids are dissolved in chloroform and subsequently deposited on the air-water interface. The chloroform evaporates very quickly, leaving only little time for the lipids to arrange into a liquid-extended phase. To demonstrate that the MMA can be controlled accurately by controlling the amount of lipids deposited on the air-water interface in miniaturized microchambers, two independent validations are performed. First, the pressure Π is measured in miniaturized microchambers with different target MMAs and compared to the pressures measured in Langmuir-Blodgett troughs. Second, the diffusion coefficient of a lipid probe is measured in several DMPC monolayers of different target MMAs. The results are analyzed by means of the FA-model [Cohen and

Turnbull, 1959, Galla et al., 1979] and compared to previously reported results [Gudmand et al., 2009, Chwastek and Schwille, 2013, Ke and Naumann, 2001].

VI.2.1.1 Interface area in miniaturized microchambers

The miniaturized microchambers are made of PTFE, which is plasma cleaned before use. PTFE that was not plasma cleaned shows a lotus effect with water. In contrast, the PTFE treated as described in the Materials and Methods section (appendix D.1) is hydrophilic and shows a small contact angle with water. Consequently, the air-water interface forms a concave meniscus, as illustrated in figure VI.1A.

In the previous study by Chwastek and Schwille [Chwastek and Schwille, 2013], the air-water interface area was not characterized but assumed to be equivalent to the cross-section of the miniaturized microchamber, which is given as πR^2. Since the air-water interface forms a meniscus, its area is larger than the cross-section of the chamber. This is particularly important in miniaturized microchambers where the ratio of boundary to bulk increases with increasing degree of miniaturization. As a result, the actual MMA is larger than predicted from the amount of lipid deposited, which directly reflects in an overall lower Π. The extent of this effect is however unknown. Ideally, the magnitude of the effect should be predicted by a theoretical model. However, while the meniscus shape in capillaries (i.e. cavity radius much smaller than the height of the liquid) has been subject to theoretical studies (e.g. [Erikson, 1965, Kashin et al., 2011]), no analytical expression is known for a cylindrical well structure as used in this study. Additionally, the contact angle of aqueous buffer and plasma cleaned PTFE is unknown. Finally, the effect of the lipids themselves on the meniscus shape has not been characterized.

To address the unknown interface area, several tile images were taken on a confocal laser scanning microscope (LSM) with a low magnification objective and stitched together during post-processing. This process was repeated in several axial planes (for details see Materials and Methods in appendix D.1). Once the focal plane is above the lowest point of the meniscus, the obtained images show circles, which correspond to the cross-section of the confocal plane and the convex interface (figure VI.1A,B). Two different approaches were pursued: detection of fluorescence from fluorescently labeled lipids located at the interface and detection of laser light back-reflected from the air-water interface. It is tempting to use the latter approach, because it is label-free. However, in practice, the back-reflection cannot be detected efficiently close to the boundary where the interface is not perpendicular to the optical axis. Moreover, for the same reason, the back-reflection is more prone to

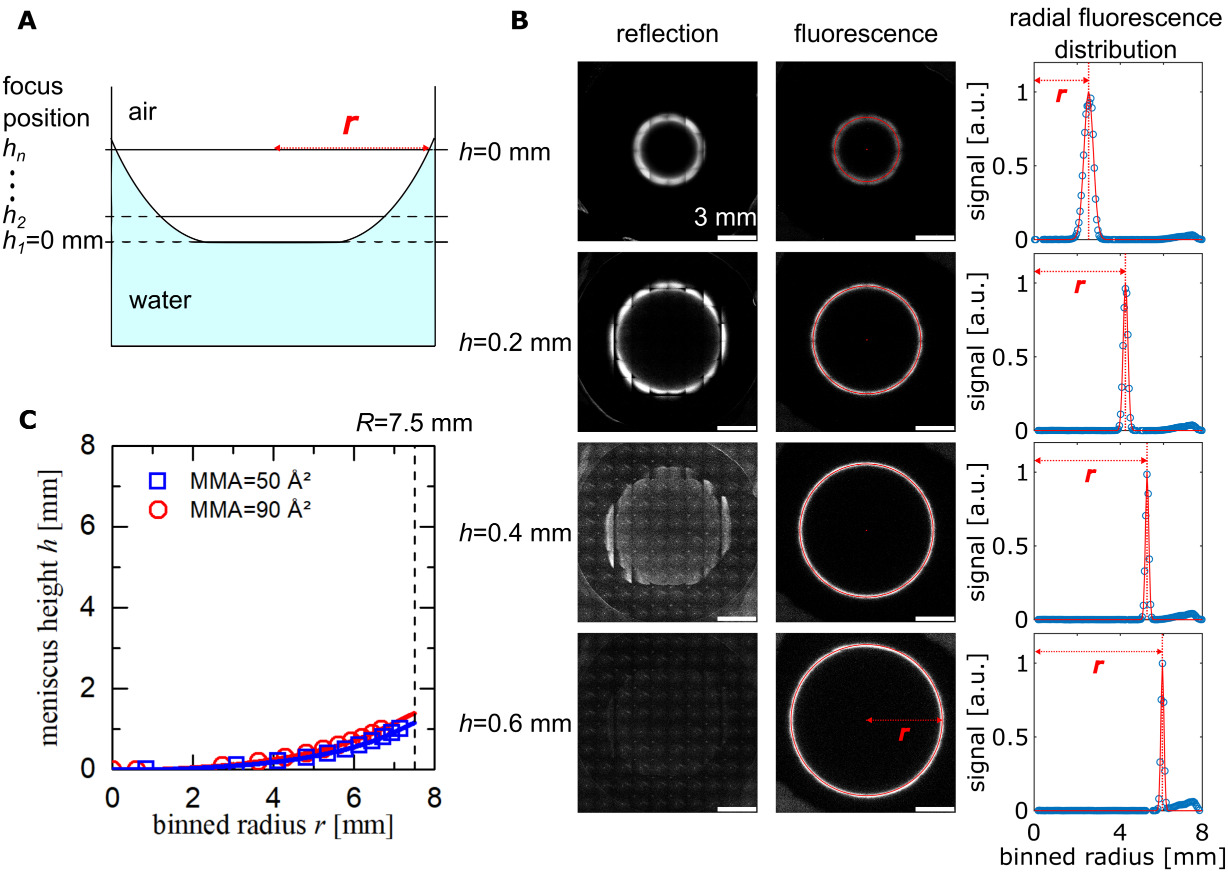

Figure VI.1: Determination of the air-water interface area. A) The air-water interface is not entirely flat, but forms a meniscus, which leads to an effective increase in interface area. B) Tile scans of the entire monolayer chamber in different heights. The interface area cannot be determined based on the back reflection from the air-water interface, as small surface waves and non-paraxial reflections yield unreliable results. Above the lowest point of the interface, the fluorescence image of Atto655-DOPE yields rings, which correspond to the overlap of the air-water interface and the corresponding optical section. The radius of this circles is determined through the radial distribution. C) Corresponding meniscus shape. The effective interface area is around 5% larger than the cross-section of the monolayer chamber and shows only a weak dependence on the lipid density.

show surface undulations. The fluorescence signal does not show these effects. The radius of each circle increases with increasing height h of the focus (figure VI.1B). The radial intensity distributions showed distinct peaks at the radii r of the corresponding circles, which were located to compute a radial meniscus profile $h(r)$ (see figure VI.1, for details see Materials and Methods in appendix D.1). Based on the radial meniscus profile, the meniscus area can be calculated, assuming azimuthal symmetry:

$$A_{\text{tot}} = 2\pi \int_0^R r \sqrt{1 + \left| \frac{\partial h(r)}{\partial r} \right|^2} \mathrm{d}r \tag{VI.2}$$

Here, $R = 7.5\,\mathrm{mm}$ is the radius of the miniaturized microchamber. To estimate the shape of $h(r)$ close to the walls, an extrapolation was performed. The radial meniscus profile is well-behaved and hence the integration can be performed numerically. Remarkably, at MMA $= 50\,\text{Å}^2$ the obtained meniscus area is only 4% larger than the cross-section of the chamber. At MMA $= 90\,\text{Å}^2$ the increase is only $(4 \pm 1)\,\%$ (mean and standard deviation), as obtained from four independent samples. These results indicate that the meniscus shape is reproducible, and the interface area depends only very weakly on the lipid concentration at the interface, at least for the measured MMAs ($50\,\text{Å}^2$ to $90\,\text{Å}^2$). To validate that the numerical integration yielded the corrected results, the radial meniscus profiles $h(r)$ were fit by polynomials of 4th order, on which the integration in equation VI.2 can be performed analytically. This ad hoc approach yielded identical results as the numerical integration. Two major conclusions are drawn from these results. First, the MMA of DMPC affects the meniscus shape within the investigated regime only to a minor degree. Second, to account for the meniscus shape, all target MMAs, which are intuitively calculated according to equation VI.1, are from now on multiplied by a factor 1.04 to yield a better estimate of the true MMA.

VI.2.1.2 Comparison of surface pressures in miniaturized microchambers and Langmuir-Blodgett troughs

The physical compression of DMPC monolayers in Langmuir-Blodgett troughs is accompanied by a gradual increase in pressure Π. The pressure onsets at an MMA slightly below $100\,\text{Å}^2$. The phase transition from the liquid extended (LE) phase to the liquid condensed (LC) phase occurs at around $40\,\text{Å}^2$ to $50\,\text{Å}^2$, with surface pressures above $40\,\mathrm{mN/m}$ (figure VI.2, black line). This compression isotherm is in line with previously reported isotherms for DMPC monolayers [Gudmand et al., 2009, Chwastek, 2013, Nielsen et al., 2007, Kubo et al., 2001]. Slight differences may be attributed to the different temperatures used, to which the DMPC monolayer is particularly sensitive at room temperature as the critical temperature was reported to be at $20\,^\circ\mathrm{C}$ [Nielsen et al., 2007].

The monolayers deposited in the miniaturized microchambers follow the general trend

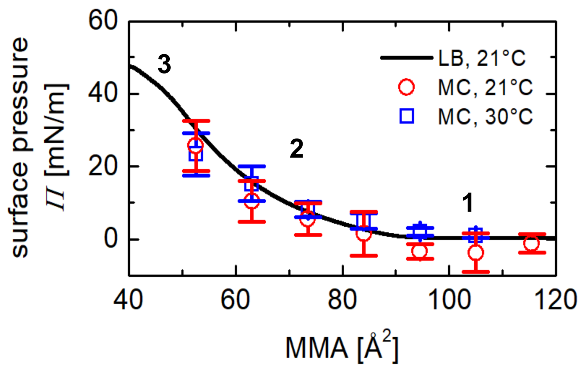

Figure VI.2: Surface pressure measurements in miniaturized monolayer chambers reproduce conventional Langmuir-Blodgett isotherms. Surface pressures were measured with a dyne probe in a conventional Langmuir-Blodgett trough (black line) and in individual miniaturized monolayer chambers at room temperature (21 °C, red circles) and 30 °C (blue squares). The isotherms measured in miniaturized chambers reproduce the Langmuir-Blodgett isotherm and exhibit no temperature dependence in the investigated temperature regime. The Langmuir-Blodgett isotherm was measured twice, all other points correspond to mean and standard deviation from at least four different samples are shown. The MMA was corrected for the effective interface area (see figure VI.1). Upon compression, the pressure onsets at an MMA around 100 Å^2 (1) and rises up to more than 40 mN/m (2) until a phase transition is encountered (3). This data set was in parts presented in Franco Conci's Master's thesis [Conci, 2016].

of the Langmuir isotherm and confirm the reproducibility of the deposition protocol. This applies for both temperatures (21 °C and 30 °C) at which these measurements were performed. Apparently, even at low MMA, the sampled monolayers were still too far from the phase transition to see effects of the temperature. The small but consistent discrepancies between the Langmuir isotherm and the miniaturized microchambers at low MMA can be attributed to the different physical processes of monolayer formation. In a Langmuir monolayer, the lipids rearrange upon slow physical compression, whereas in the fixed-area chambers, lipid molecules need to incorporate and find their arrangement during the much faster process of lipid spreading on the interface upon organic solvent evaporation. Consequently, when depositing low MMA lipid monolayers, a fraction of the lipid molecules may not insert into the monolayer, resulting in an effective increase of the MMA and a lower pressure than expected. Nonetheless, the compression isotherms measured in the miniaturized microchambers are in remarkably good agreement with the isotherm obtained in a conventional Langmuir-Blodgett trough. This agreement has not been shown before and justifies the used deposition method.

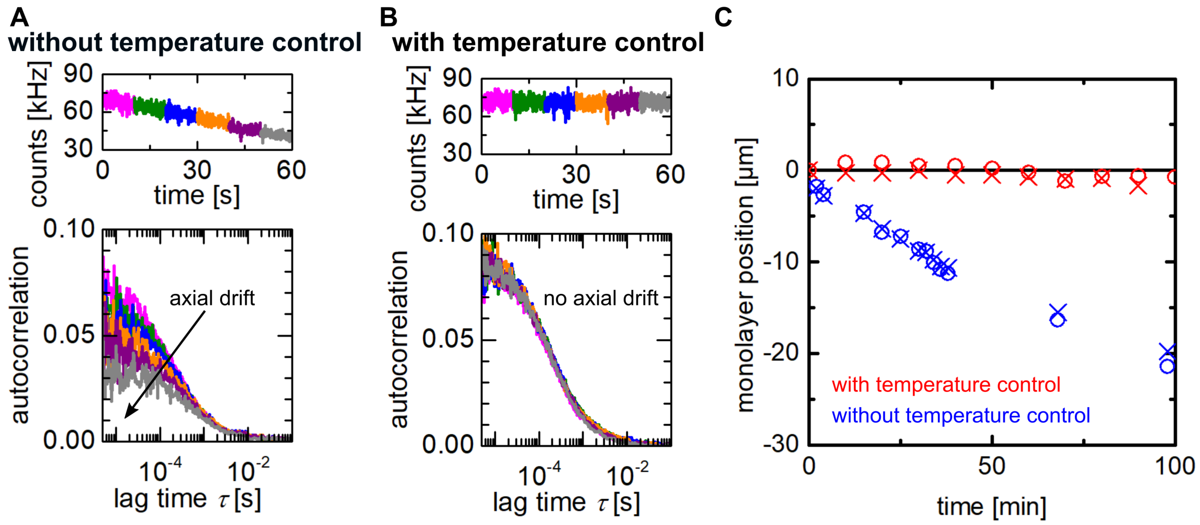

Figure VI.3: Temperature control stabilizes monolayer interface. A) Intensity trace and corresponding autocorrelation curves of 10 s measurements show significant axial drift of the monolayer interface. B) Same as in A), but the miniaturized monolayer chamber is heated to 30 °C to avoid temperature gradients and condensation on the top coverslide. The measured autocorrelation curves shown no drift and reproduce. C) Temporal evolution of the axial drift of the monolayer with (red) and without (blue) heating of the monolayer chamber above ambient temperature. The axial positions were determined by z-scans. Circles and crosses correspond to individual experiments.

VI.2.1.3 Stabilization of the monolayer position

When performing FCS on 2D systems, such as lipid membranes, the axial z-position of the confocal volume needs to be accurately adjusted to the membrane position, as axial mismatches between both bias the obtained particle number N and diffusion coefficient D [Benda et al., 2003, Gielen et al., 2009b, Machán and Hof, 2010, Gudmand et al., 2009]. For monolayers formed at the air-water interface in the miniaturized microchambers, it is particularly challenging to keep the confocal volume axially centered on the monolayer. As the total subphase volume comprises only 200 µL and the surface area to volume ratio is fairly large, evaporation of the subphase plays a major role and results in a lowering of the air-water interface and hence the monolayer. This effect is particularly pronounced when using the presented miniaturized chambers on commercial microscopy setups, which typically host active elements, i.e. electronics. Such microscopes internally heat up above room temperature, which exposes the chamber to a temperature gradient: the bottom, which is in touch with the immersion fluid is warmer than the lid of the chamber. Consequently, subphase evaporates, and partially condensates on the top lid, which prevents a humidity-saturated state of the gas phase. The resulting permanent axial drift of the monolayer with respect to the confocal volume renders long high-quality FCS measurements almost impossible and wastes valuable measurement time, as the operator constantly needs to re-focus on the lipid monolayer. Figure VI.3A highlights this issue through a series of six subsequent 10 s FCS measurements without adjustment of the axial position of the focal volume. Not only does the fluorescence signal constantly decrease, but also the amplitude of the corresponding correlation curve decreases and the decay time of the autocorrelation curves shifts towards longer lag times. All these observations are directly attributed to the aforementioned permanent evaporation of subphase, which is accompanied by biases in N and τ_D.

Having realized that subphase evaporation and re-condensation at the top lid impairs the quality of FCS measurements on lipid monolayers, I was seeking a way to minimize these effects. A preparation of monolayers in humidity-saturated air at the microscope temperature from the very beginning was reasonable, but impractical. Alternatively, the monolayer was formed as usual, but for FCS measurements, the miniaturized microchamber was hosted in a temperature controlled chamber, which was heated to 30 °C, which is above the objective temperature of roughly 27.5 °C. This time, the mean fluorescence signal stays fade and individual curves reproduce, as shown in figure VI.3B. These observations imply that the subphase evaporation was massively reduced. In fact, when tracking the axial monolayer position by z-scans of the confocal volume over a time of almost two hours, the heated monolayer axially drifts by less than 1.5 µm. During the same time, the monolayer system without temperature control shows a unidirectional drift of around 20 µm (figure VI.3C).

The stable positioning of the focus with respect to the monolayer allows for considerably longer measurements. This is important for two reasons: first, less time needs to be spent on readjustment of the focus positions, which maximizes the time that is spent on actual measurements. Second, stable focus positioning allows for the reliable measurement of long correlation times, e.g. due to low diffusion coefficients, which require respectively long measurement times [Oliver, 1979, Schätzel et al., 1988, Tcherniak et al., 2009]. Gudmand and colleagues had previously taken advantage of the natural subphase evaporation to apply a modification of z-scan FCS [Benda et al., 2003] to determine lipid mobility in monolayers [Gudmand et al., 2009]. In their approach, each series of intensity trace measurements starts with the lipid monolayer above and finishes below the fixed focus position, such that the maximum autocorrelation amplitude and cpp can be found. While this approach is simple and elegantly makes use of the inherent evaporation, it comes at the cost of very long measurement times (30 min). In contrast, the approach of focus stabilization presented here and point FCS analysis maximizes the counts per particle, as the lipid monolayer is constantly in focus, and thus reduces the total measurement time per sample considerably. Nonetheless, both approaches are expected to yield identical results [Heinemann et al., 2012].

VI.2.1.4 FCS study of lipid diffusion in lipid monolayers

The previously presented measurements of the surface pressure Π validated the use of miniaturized microchambers for the study of lipid monolayers of different MMAs. Albeit possible, these pressure measurements are cumbersome and impractical in combination with confocal microscopy. It would be beneficial if similar conclusions could be drawn from FCS measurements.

The imaging capability of fluorescence microscopy is very handy for the study of monolayers as the initial condition of the monolayer can be inspected visually. Therefore, inadequate samples, e.g. contaminated by dirt at the air-water interface, can be identified and justifiably discarded. For the typical range of MMAs that were used in this study ($50\,\text{Å}^2$ to $100\,\text{Å}^2$), intact monolayers appeared homogeneous in the fluorescence channel (figure VI.4A), as expected for the liquid-extended phase.

The autocorrelation curves of a lipid probe in a DMPC monolayer for different MMAs differ significantly with respect to amplitude and decay time. Figure VI.4B shows representative autocorrelation curves at five different MMAs. Clearly, a low MMA yields smaller correlation amplitudes than a higher MMA. Nonetheless, all curves are excellently described by a 2D diffusion model without any additional dynamics (equation II.32). The particle number N obtained from the fit decreases monotonically with increasing MMA (figure VI.4C), which is expected. The higher the MMA, the less dense the packing of lipids, the less lipids are found on average in the detection volume. In accordance with equation VI.1, N scales inversely proportional with the MMA, as highlighted by the fit (black line) in figure VI.4C. In theory, the expected number of particles could be directly calculated from the interface area, the MMA and the fraction of labeled lipids (gray line, figure VI.4C). However, for unclear reasons, this theoretical dependence predicts consistently higher N than measured, although the experiments reproduce an inverse proportionality between N and MMA. This discrepancy is seen for the whole range of investigated MMAs, which suggests that the process of monolayer formation, which is most prone to failing lipid insertion

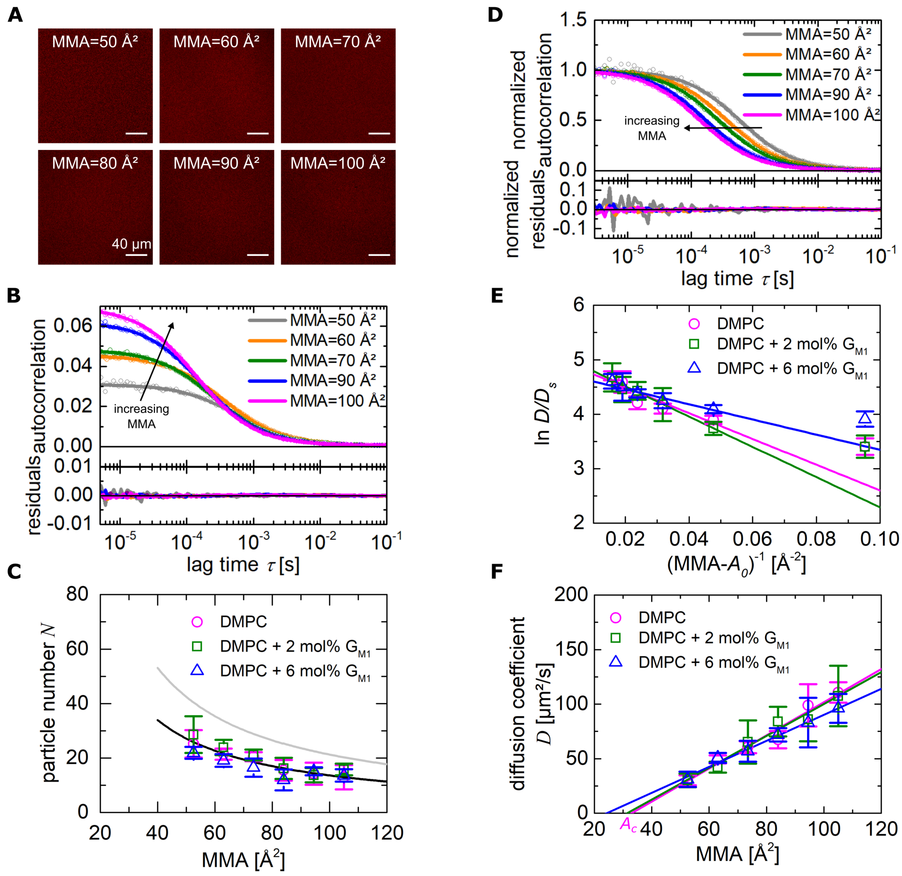

Figure VI.4: FCS study of lipid diffusion in DMPC monolayers A) LSM images of DMPC monolayers with 0.01 mol% ATTO655-DOPE appear homogeneous for all MMAs considered. Scale bar corresponds to 40 µm. B) Fluorescence autocorrelation curves and corresponding fits with 2D diffusion model for 0.01 mol% ATTO655-DOPE in DMPC monolayers. The larger the MMA, the larger the amplitude of the autocorrelation curve, corresponding to fewer particles in the detection volume. C) Particle numbers obtained from the fits of autocorrelation functions for different monolayer compositions. Doping the DMPC monolayer with 2 to 6 mol% of G_{M1} does not alter the obtained particle numbers. The particle number is inversely proportional to the MMA (black line, fit), although the overall particle number is slightly lower than expected from the molar fraction of lipids (gray line). Both lines are only plotted down to MMA = 40 Å^2, because the phase transition occurs in this regime. D) Normalized autocorrelation curves from B). With increasing MMA, the autocorrelation curves shift to shorter decay times. E) Linear fits of the ln of the lipid diffusion coefficients (normalized to a standard value $D_s = 1\,\mu m^2/s$) vs. the inverse free area per lipid. A van der Waals area of 42 Å^2 was assumed. The obtained fit parameters are summarized in table VI.1. F) Diffusion coefficients obtained from FCS measurements. The diffusion coefficient scales linearly with the MMA, the corresponding fits are shown. An extrapolation to $D = 0\,\mu m^2/s$ yields an estimate of the critical area A_c (see table VI.2). All measurements were performed at 30 °C. The error bars correspond to the standard deviations from at least four independent samples.

at high lipid packings, is not the cause. Moreover, imaging of entire chambers showed no indication for accumulations of lipids on the border of the chamber. Photobleaching may also reduce the number of observed particles, but has been excluded by an initial power series to identify an irradiance regime of minimal photobleaching. It is discernible that the stock of fluorescent lipids did not match the target concentration. Despite the discrepancy in absolute number, the expected inverse proportionality between N and MMA is properly recovered, which has not been demonstrated for a lipid monolayer in previous FCS studies [Gudmand et al., 2009, Chwastek and Schwille, 2013]. Notably, doping the monolayer with 2 mol% or 6 mol% G_{M1} yields identical results.

An increasing MMA is not only accompanied by a decrease in N, but also by a shortening of the diffusion time τ_D. To highlight the latter effect, figure VI.4D shows the same autocorrelation curves as in figure VI.4B, but this time normalized to their inverse particle number, i.e. in the absence of dark state contributions, all autocorrelation curves approach 1 for zero lag time $\lim_{\tau\to 0} G(\tau) = 1$. Clearly, the autocorrelation curves decay at shorter lag times, the larger the MMA. The differences in τ_D are significant, ranging from roughly 580 µs at MMA $= 50\,\text{Å}^2$ down to around 150 µs at MMA $= 100\,\text{Å}^2$. Based on the initial calibration measurement and the obtained values of τ_D, the diffusion coefficients D of the lipid probes are calculated (figure VI.4E,F).

To obtain more insights from the measured diffusion coefficients, it is worth discussing these results in the context of the free area model (FA-model) [Cohen and Turnbull, 1959, Galla et al., 1979], which deals with the diffusion in the context of available free area (see section II.1.1 in chapter II). According to the FA-model, the diffusion coefficient D of lipids, which are treated as hard rods, scales as $D \propto e^{-\gamma \frac{A_c}{\mathrm{MMA}-A_0}}$ (equation II.9), with a constant factor γ, A_0 being the van der Waals area of a lipid, and A_c being the critical area, below which no diffusion is possible. Consequently, plotting $\ln D/D_s$ vs $(\mathrm{MMA} - A_0)^{-1}$ should yield a straight line with the slope $-\gamma A_c$. Several studies confirmed this relation and thereby validated the FA-model for lipid monolayers [Peters and Beck, 1983, Kim and Yu, 1992, Tanaka et al., 1999, Ke and Naumann, 2001, Gudmand et al., 2009] . The standard diffusion coefficient $D_s = 1\,\mu\text{m}^2/\text{s}$ is introduced only to take the logarithm of a dimensionless quantity. The corresponding fit is shown in figure VI.4E and the corresponding fit parameters are given in table VI.1. To perform the linear fit, a van der Waals area of $42\,\text{Å}^2$ has been assumed, based on other studies where van der Waals areas of $42\,\text{Å}^2$ to $44\,\text{Å}^2$ fitted well for phosphocholines [Peters and Beck, 1983, Kim and Yu, 1992, Tanaka et al., 1999, Ke and Naumann, 2001, Gudmand et al., 2009, Boguslavsky et al., 1994]. The

Table VI.1: Free area model fit of D at different MMAs. Based on equation II.9, the lipid diffusion coefficient D obtained by FCS is plotted versus the inverse free area (figure VI.4E), The slope is a measure for the critical area A_c. All measurements were performed at 30 °C.

monolayer composition	γA_c [Å^2]	$\ln D_0/D_s$
DMPC	23.72 ± 5.01	4.97 ± 0.17
DMPC + 2 mol% G_{M1}	27.82 ± 1.58	5.07 ± 0.06
DMPC + 6 mol% G_{M1}	13.92 ± 1.86	4.74 ± 0.06

points at low MMA, corresponding to large values of $(\text{MMA} - A_0)^{-1}$, deviate from the linear dependence and are thus discarded from the fit. This finding is interesting, because these points are measured reasonably close to the phase transition where the FA-model is predicted to fail. Gudmand and colleagues reported a surprisingly good agreement of measurements close to the phase transition with the FA-model [Gudmand et al., 2009]. Despite this minor difference, they obtained and identical slope $\gamma A_c = 23$ Å^2. As γ is a dimensionless correction factor between 0.5 and 1, the critical area A_c of DMPC is estimated to be between 23 Å^2 to 46 Å^2.

As a next step, the relation between D and MMA is analyzed (figure VI.4F). This work finds a linear dependence between D and MMA, which is in agreement with previous FCS studies on DMPC monolayers [Gudmand et al., 2009, Chwastek and Schwille, 2013], but also can be conjectured from older work [Kim and Yu, 1992]. The corresponding fit parameters are presented in table VI.2. Conceptually, the FA-model does not accept diffusion for MMAs below the critical area A_c. Consequently, an extrapolation of the linear dependence $D \propto \text{MMA}$ to $D = 0\,\mu\text{m}^2/\text{s}$, ignoring the phase transition, yields an estimate of A_c. Again, the obtained values are in very good agreement with previous studies [Gudmand et al., 2009, Chwastek and Schwille, 2013, Ke and Naumann, 2001], but also with the result discussed above in the context of figure VI.4E and table VI.1. Notably, not only pure DMPC, but also other DMPC mixtures with low content of the ganglioside G_{M1} followed similar linear trends.

So far, it has been shown that the miniaturized microchambers reproduce many aspects of different previously reported studies, which can be considered a solid validation of the approach. The surface pressure measurements presented above show a good agreement between conventional Langmuir-Blodgett troughs and miniaturized chambers. However, the acquisition of such data sets is very tedious and impractical. Consequently, it would

Table VI.2: Critical area of DMPC monolayers with small fractions of G_{M1}. The measured diffusion coefficient of a lipid (here ATTO655-DOPE) follows a linear dependence on the MMA of the monolayer: $D = m \cdot \mathrm{MMA} + n$, as shown in figure VI.4E. The corresponding values for slope m and offset n of the linear fits are given with 95% confidence intervals for monolayers of DMPC with small dopings of G_{M1}. The critical area corresponds to the tightest packing of lipids in the monolayer and is calculated based on the linear fits and their values at $D = 0\,\mu m^2/s$. All measurements were performed at 30 °C.

monolayer composition	critical area A_c [Å^2]	$m \cdot 10^{-8}$ [s^{-1}]	n [µm^2/s]
DMPC	33.0 ± 8.0	1.52 ± 0.14	-50.11 ± 11.20
DMPC + 2 mol% G_{M1}	31.4 ± 7.4	1.46 ± 0.12	-45.80 ± 10.04
DMPC + 6 mol% G_{M1}	24.3 ± 4.6	1.19 ± 0.07	-28.91 ± 5.24

be desirable to have a fast alternative to judge the quality and state of a monolayer. A visual inspection of the homogeneity of the lipid monolayer is a first step towards this goal, but does not provide any information on the MMA. This shortcoming is overcome by the bijective map between the lipid diffusion coefficient and the MMA provided in table VI.2. Consequently, the quality and the MMA of a DMPC monolayer can be characterized on the fly using FCS and the linear dependence $\mathrm{MMA} = (D - n)/m$ presented here. This comes in handy when monitoring the monolayer state during FCS measurements on biomolecules binding to lipid monolayers.

VI.2.2 Protein aggregation at the lipid monolayer

It has been proposed that the mobility of protein components in membranes is influenced by lipid packing [Gudmand et al., 2009]. Moreover, very little is known about the mobility of proteins at the monolayer. As a first step, this work aims to characterize protein diffusion at different MMAs.

A common problem when working with purified proteins are clustering and aggregation. The presence of protein clusters precludes quantitative FCS measurements, because such clusters have statistically ill-defined size and brightness distributions, which distorts both amplitude and shape of the autocorrelation curve. Moreover, in FCS, particles are weighted with their squared brightness, which emphasizes aggregates even more. Under special circumstances, the effect of aggregates can be corrected by post-processing of the photon-arrival times or many individual short FCS measurements [Persson et al., 2009, Laurence et al., 2007, Ries et al., 2010]. However, even these approaches only deal with the effect of very bright particles passing through the center of the confocal volume. Slow, but bright aggregates that pass the outer sphere of the confocal detection volume may not appear as a spike in the fluorescence signal trace, but still contribute a slow component to the autocorrelation function. Generally, it is advisable to spend considerable efforts to prevent the formation of aggregates or to remove aggregates.

Interestingly, the aggregation behavior of proteins at the lipid interface cannot be simply inferred from the molecules' propensity to aggregate in solution. Nonetheless, for all amphipathic proteins, there is a potential of aggregation upon contact with an air-water interface, which may induce a non-native conformation. The hydrophobic regions are exposed and aggregation may occur through interactions of these exposed regions [Browne et al., 1973, Maa and Hsu, 1997, Carpenter et al., 1999]. Aggregation is not unique to large flat air-water interfaces, but may also happen at entrained air-water interfaces (e.g. [Kiese et al., 2008]), and other interfaces (e.g. [Jiang et al., 2009, Thirumangalathu et al., 2009]), to name only a few examples.

Here, a range of biomolecules is tested for their compatibility with lipid monolayer experiments, see table VI.3. Independently of the nature of the interaction with the lipid monolayer, the studied molecules can be divided into two groups: homogeneously distributed, or aggregated at the lipid interface. Interestingly, the free fluorescent proteins mCherry and mNeonGreen tend to aggregate at the monolayer. This effect is of particular interest for solution studies with fluorescent proteins where the precise concentration needs to be known. Further studies are required to estimated the degree of aggregation, also at air-water interfaces without lipids. Nonetheless, for such studies it appears to be advisable to keep the interface areas to a minimum and to passivate surfaces, e.g. with BSA (see below). Concerning membrane binding biomolecules, interactions through lipid head groups and hydrophobic insertions are discussed in table VI.3. It appears that the proteins derived from MinD, which insert through hydrophobic interactions are collectively aggregating at the monolayer. From the tested biomolecules that interact with the monolayer through a hydrophobic moiety, only MPER and cholesterol-anchored DNA origami do not aggregate at the monolayer. This is a reasonable finding, as both, the short peptide MPER and cholesterol lack a higher order structure, which may potentially get unfolded upon encountering the interface. The detailed investigation of the highly complex aggregation processes themselves and possible reversibility exceeds the scope of this study, but is of relevance to a broad variety of fields, ranging from formulation of pharmaceutical biologics to foams (for reviews see e.g. [Wang, 2005, Wang et al., 2010, Roberts et al., 2011, Amin

Table VI.3: Compatibility of a range of biomolecules with lipid monolayers at the air-water interface. A biomolecule is considered aggregated, when clusters are seen in fluorescence images of the interface, a bleached region does not recover after photobleaching (FRAP), or FCS measurements are impossible to perform because of aggregate transits. Experiments were performed on DMPC monolayers at MMA = 70 Å^2.

biomolecule	nature of membrane binding	aggregation at monolayer
6xHis-mCherry		yes
6xHis-mNeonGreen		yes
ATTO488-MPER	hydrophobic moiety	no
CtxB-Alexa488	head group	no
(*E. coli*) mts(MreB)-mCherry	hydrophobic moiety	yes
(*B. Subtilis*) mCherry-mts(MinD)	hydrophobic moiety	yes
(*E. coli*) mCherry-mts(MinD)	hydrophobic moiety	yes
(*E. coli*) mCherry-MinD	hydrophobic moiety	yes
(*E. coli*) eGFP-MinD	hydrophobic moiety	yes
(*E. coli*) MinD-LD650	hydrophobic moiety	yes
(*M. musculus*) 6xHis-VCA(NWASP)-Alexa488	head group	no
(*M. musculus*) 10xHis-VCA(NWASP)-Alexa488	head group	yes
(*M. musculus*) miniNWASP-GFP	head group	yes
DNA origami-Alexa488	hydrophobic moiety	no

et al., 2014, Roberts, 2014, Murray, 2007]).

The large degree of aggregation at the air-water interface appears to be a common feature of many proteins. Interestingly, a control experiment shows that CtxB, which specifically binds to the sugar moieties of the ganglioside G_{M1}, aggregates at the air-water interface, but the presence of a low-density lipid monolayer can per se considerably reduce this aggregation, as shown in figure VI.5A. Several studies similarly found that surfactants can mitigate the aggregation at interfaces, for reviews see [Wang, 2005, Arnebrant and Wahlgren, 1995]. On the other hand, the bacterial MinD protein strongly aggregates at the lipid monolayer interface, even at an MMA of 50 Å^2 (figure VI.5B). An efficient passivation of the interface is achieved by an extremely tightly packed lipid monolayer (MMA = 30 Å^2). Although difficult to characterize, at an MMA of 30 Å^2 the interface contains excess of lipids and is believed to be fully covered by a tightly packed monolayer, with Π and effective MMA resembling that of a lipid bilayer [Israelachvili et al., 1980]. At

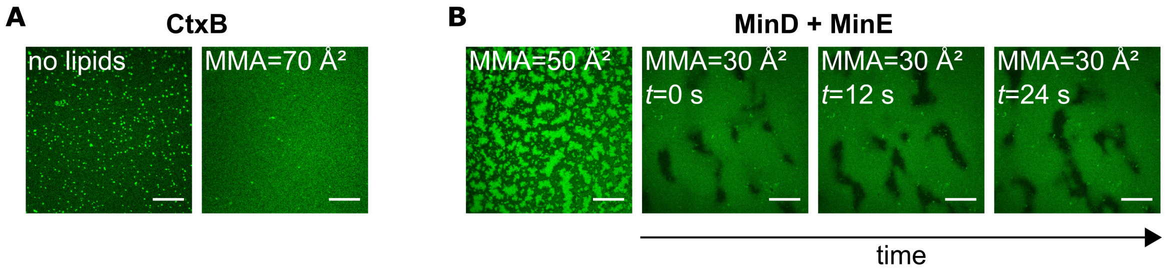

Figure VI.5: Air-water interfaces may be passivated against protein aggregation by lipids. A) 10 nM of CtxB labeled with Alexa488 aggregate at the air-water interface, but the aggregation disappears in the presence of a DMPC monolayer (here MMA = 70 Å^2). B) The proteins MinD and MinE together are known to form patterns on SLBs [Loose et al., 2008], but form large aggregates and show no spatio-temporal pattern for monolayers with 50 Å^2 MMA or higher. The spatio-temporal patterns only form at 30 Å^2 MMA, at which the lipids are expected to be maximally packed and form partially multilayer structures [Israelachvili et al., 1980]. Images were taken on monolayers of *E. coli* polar extract, with 1 µM MinD (10% eGFP-MinD) and 1 µM MinE. The scale bars correspond to 40 µm.

this condition, the membrane system is not fully controlled, but characteristic dynamic Min waves can be reconstituted upon addition of the partner proteins MinD and MinE (figure VI.5B) [Zieske et al., 2016] and no aggregation is observable any longer. However, using such a passivation method eliminates the key feature of monolayers, the possibility to vary lipid density and mobility.

A common passivation approach routinely used in lipid bilayer experiments in order to eliminate unspecific interactions with the interface is the addition of a high concentration of BSA to the working buffer. This approach successfully passivates a DMPC monolayer at MMA = 70 Å^2, as shown in figure VI.6A,B. However, passivation by BSA is not a suitable tool for experiments on lipid monolayers. Despite the fact that the use of BSA in solution reduces protein clustering and unspecific binding to the interface, BSA significantly slows down the diffusion of the lipids (figure VI.6C), as previously reported for ovalbumin and bovine prothrombin fragment 1 at similar concentrations [Huang et al., 1992]. The local lipid density is increased due to unspecific insertion of BSA into the monolayer, and as a result, the ranges of effective lipid density and mobility available for analysis are drastically reduced. By the same reasoning, any passivation approach comes with major drawbacks, as every unspecific larger scale insertion into the lipid monolayer alters the main parameter of interest, the lipid packing. Without any passivation tools available, lipid monolayer studies

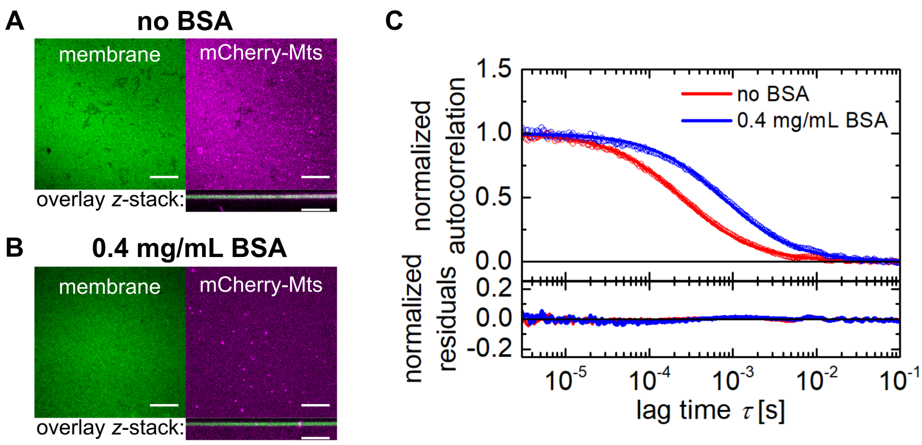

Figure VI.6: Monolayer passivation by BSA. A,B) Confocal LSM images of 70 Å^2 MMA DMPC monolayers (green) and mCherry-mts of the protein MinD from *Bascillus subtilis* (magenta) without and with prior incubation with BSA. The presence of BSA reduces the interface binding and aggregation of mCherry-mts. The scale bars correspond to 40 µm. C) Autocorrelation curves of ATTO655-DOPE in DMPC (MMA = 70 Å^2) before and after addition of 0.4 mg/mL BSA. The lipid diffusion is slowed down by the addition of BSA.

are only compatible with a limited set of well-behaved biomolecules.

VI.2.3 FCS study of differently sized biomolecules in lipid monolayers

The prominent aggregation of many proteins at the lipid monolayer interface poses a major restriction on the study of protein-monolayer interactions. Nonetheless, in this chapter the lateral diffusion of monolayer-bound biomolecules is studied by confocal point FCS. To cover a broad range of physical molecule sizes, the relatively small peptide MPER, the pentameric protein CtxB, and a rod-like DNA origami nanostructure are investigated. All measurements are performed in a low concentration regime, where the lipid packing in the monolayer is not altered upon binding and all biomolecules are assumed to be bound, i.e. no residual diffusion in solution occurs. Controlling that the monolayer is not significantly altered upon binding is particularly important to avoid any uncontrolled feedback.

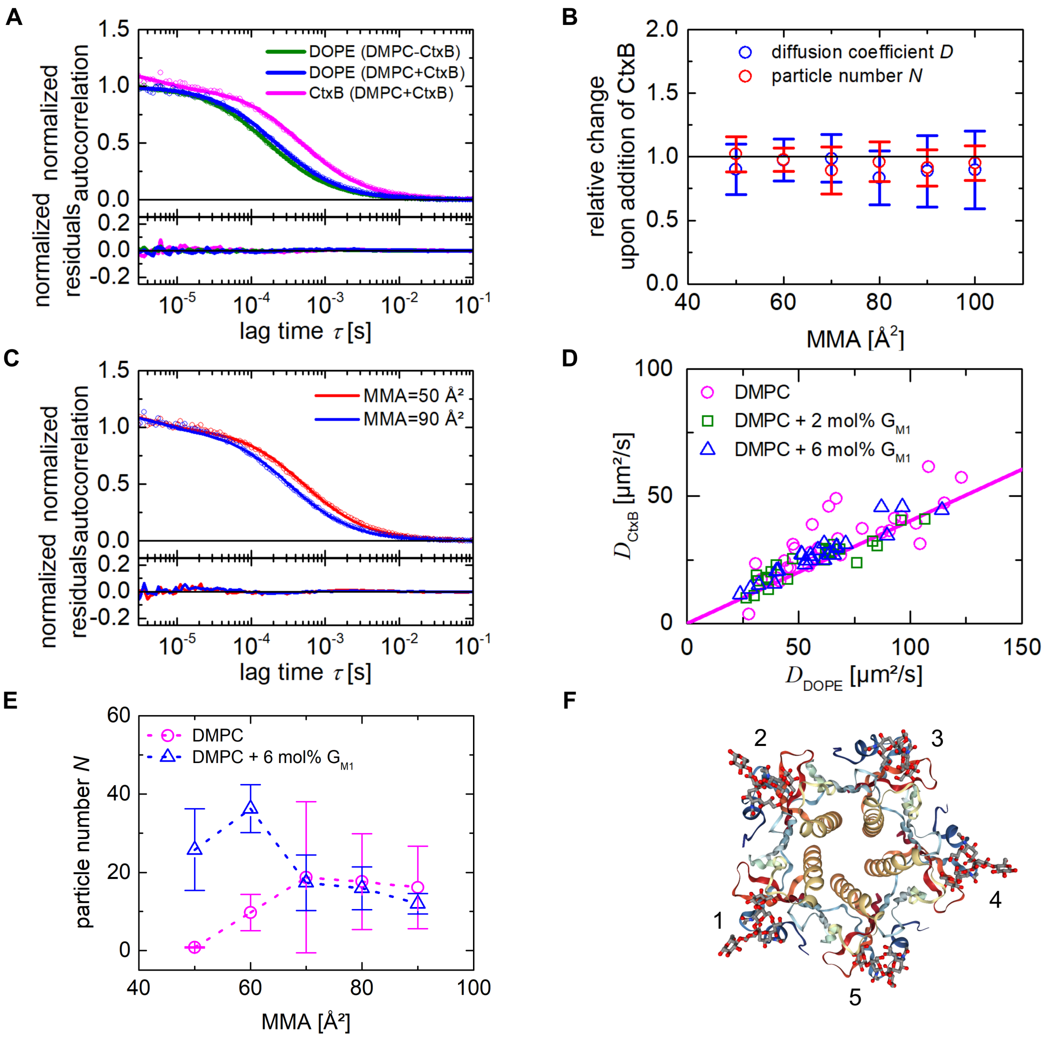

Figure VI.7: Diffusion coefficient of monolayer-bound CtxB depends on the lipid packing. A) The autocorrelation curve of 0.01 mol% ATTO655-DOPE in 70 Å^2 MMA DMPC does not change upon addition of 10 nM Alexa488 labeled CtxB (green to blue). B) For an entire range of MMAs from 50 Å^2 to 100 Å^2 both parameters N and τ_D, which govern the autocorrelation function of ATTO655-DOPE, do not change upon addition of 10 nM Alexa488 labeled CtxB. C) Normalized autocorrelation curves and fits by a 2D diffusion model function of monolayer-bound CtxB labeled with Alexa488. The autocorrelation curve measured in DMPC monolayers of 50 Å^2 MMA (red) decays at larger lag times than the autocorrelation curve measured at 90 Å^2 MMA (blue). D) Diffusion coefficient of CtxB shows a strong correlation with the diffusion coefficient of ATTO655-DOPE measured in a DMPC monolayer doped with different amounts of G_{M1}. The amount of G_{M1} does not appear to alter the diffusion coefficients. The relation between the diffusion coefficients of lipid and CtxB appears to be approximately linear, a corresponding fit for pure DMPC monolayers is depicted (see table VI.4). E) Particle number of CtxB as obtained by FCS is higher in the presence of 6 mol% G_{M1}, but becomes indistinguishable from the case of no G_{M1} at high MMA. All measurements were performed at 30 °C. F) Crystal structure of a CtxB pentamer with five G_{M1} bound [Merritt et al., 1997].

VI.2.3.1 Pentameric β subunit of Cholera Toxin (CtxB)

The model protein CtxB falls into the category of proteins that do not aggregate at the lipid monolayer interface (figure VI.5A) and thus, is suitable for analysis by point FCS. Previously, binding of CtxB to lipid monolayers has been qualitatively assessed in phase-separated lipid mixtures [Chwastek and Schwille, 2013]. However, to date, the diffusion behavior of CtxB at the lipid monolayer has not been studied. As discussed in the context of figure VI.4, the lipid diffusion strongly depends on the MMA of the monolayer. Moreover, it has been proposed that lipid packing also has an effect on the diffusion of monolayer-bound biomolecules [Gudmand et al., 2009], which is reasonable, but to date has not been shown. Therefore, in this section the diffusion of CtxB is accurately measured at different densities of lipids at the air-water interface.

To exclude any influence of protein binding on lipid MMA and diffusion, low protein concentrations ($\leq 10\,\mathrm{nM}$) are used. Indeed, the autocorrelation curves for the lipid diffusion in the monolayer before and after addition of protein are perfectly superimposed and reproducible, as shown in figure VI.7A for ATTO655-DOPE in DMPC upon addition of CtxB. Moreover, both fit parameters N and τ_D, and thus the diffusion coefficient D, do not change upon injection of CtxB (figure VI.7B). This holds for a whole range of MMAs from $50\,\text{Å}^2$ to $100\,\text{Å}^2$. Consequently, protein binding in these conditions does not change the lipid diffusion, which in return corresponds to an unaltered surface pressure Π.

Furthermore, the use of a low protein concentration allows for the use of a simple single-component 2D diffusion model with a triplet component (equation II.33) to fit the experimental autocorrelation curves of CtxB. Here, the triplet term accounts for the photophysics of the fluorescent label Alexa488. The analysis yields small random residuals, and virtually no contribution from protein in solution is detected. In theory, as long as the diffusion in solution is considerably faster than the diffusion in the monolayer, the solution diffusion could be accommodated in the fitting function. However, the molecular brightnesses need to be considered with care. The monolayer-bound particles are always in focus, whereas the solution offers an axial escape direction. Assuming a 3D Gaussian, particles bound to the monolayer appear on average a factor of $\sqrt{2}$ brighter than the particles in solution, which is a direct consequence of the Gaussian integrals solved when deriving the confocal autocorrelation curve (compare chapter II).

Compared to the lipid diffusion, the autocorrelation curve obtained for CtxB is shifted to larger decay times (figure VI.7A), although CtxB is observed in the smaller green-shifted detection volume. This effect is easily attributed to the significantly larger size of CtxB, which in its pentameric form has a radius of around 3.1 nm and a height of 3.2 nm [Zhang et al., 1995]. Regardless of the way CtxB binds to the monolayer, its five binding sites for G_{M1} or its physical insertion will always cause a smaller diffusion coefficient than that of small phospholipids, which have a typical radius of only around 0.3 nm to 0.4 nm [Marsh, 2013].

As hypothesized, the diffusion coefficient of CtxB depends on the MMA of the monolayer, as indicated by the shift between the two representative autocorrelation curves at MMAs of 50 $Å^2$ and 90 $Å^2$ shown in figure VI.7C. The decrease in lipid MMA, and consequent reduction of lipid mobility, results in a shift of the autocorrelation curves of CtxB to larger diffusion times. The diffusion coefficient is extracted for the whole range of MMAs. For example, for MMA = 70 $Å^2$ the measurements yield $D_{\mathrm{CtxB}} = (26.5 \pm 4.6)\,\mu\mathrm{m}^2/\mathrm{s}$. Strikingly, both, the lipids and CtxB can be monitored in two distinct spectral channel, which allows for the measurement of both diffusion coefficients. Remarkably, there is a linear relation between the diffusion coefficients of CtxB and lipids (figure VI.7D). It is reasonable to assume that a tightly packed monolayer, which has no lipid diffusion, will also not allow for the diffusion of associated biomolecules. Consequently, the linear dependence between both diffusion coefficients is fitted by a slope m only $D_{\mathrm{CtxB}} = m \cdot D_{\mathrm{lipid}}$, the results are presented in table VI.4. This linear dependence, together with the discussed lipid diffusion implies that the diffusion coefficient of CtxB is a linear function of the MMA itself. The relation is easily computed from the fit results given in tables VI.2 and VI.4.

CtxB is known to interact specifically with G_{M1}, a ganglioside. Supposedly, the pentameric CtxB binds up to five monolayer-bound G_{M1} as each monomer exhibits a binding site with a reported dissociation constant $K_D = 0.1 - 1\,\mathrm{nM}$ [Fishman et al., 1978, Ludwig et al., 1986, Reed et al., 1987], as can be seen in the crystal structure in figure VI.7F (image from the RCSB PDB (www.rcsb.org) [Rose and Hildebrand, 2015], PDB ID: 2CHB) [Merritt et al., 1997]. Interestingly, the addition of G_{M1} does not significantly influence the diffusion coefficient D_{CtxB} (figure VI.7D). Moreover, the counts per molecule is similar for CtxB in pure DMPC monolayers and in DMPC doped with G_{M1}. On the other hand, at low MMA, the particle number N of CtxB is higher in the presence of 6 mol% G_{M1} than for pure DMPC monolayers (figure VI.7E, for clarity DMPC + 2 mol% is not shown). This is in line with the used concentrations, which are well above K_D. With increasing MMA, 6 mol% G_{M1} correspond to less and less molecules, and at around MMA = 70 $Å^2$, the number of bound CtxB molecules is identical, with and without 6 mol% G_{M1}. The higher numbers of bound CtxB molecules in the presence of G_{M1} indicate a different binding mode, in line with the specific binding of CtxB to G_{M1}. Despite the different binding modes, the diffusion coefficients of CtxB in the monolayer do not depend on the concentration of G_{M1}. One can thus hypothesize that the similar diffusion coefficients obtained in presence and absence of the ligand G_{M1} indicate that the insertion size of the pentameric CtxB non-specifically bound to the lipid monolayer is similar to the effective insertion size of the lipid group co-diffusing upon binding of the pentameric CtxB to five G_{M1} molecules. However, a more detailed study is required to support this hypothesis further, because the diffusion coefficient depends only weakly on the molecule's inclusion in the membrane [Saffman and Delbrück, 1975, Hughes et al., 1981]. Thus, FCS is rather insensitive to differences in the membrane insertion size. However, this argument can be also turned around: even a rough guess of the insertion size may yield reasonably good estimates of the diffusion coefficient or the surface viscosity. A thorough discussion will be performed in section VI.2.3.4 on page 154.

VI.2.3.2 Membrane proximal external region (MPER)

The membrane proximal external region (MPER) studied in this work corresponds to amino acids 662 to 673 of the envelope glycoprotein gp41 of HIV-1, modified with a cysteine, which is targeted for fluorescent labeling by ATTO488 with a maleimide moiety. This peptide forms an α-helix and inserts into the membrane under an angle, due to its distribution of hydrophobic amino acids [Sun et al., 2008]. The MPER is part of the viral envelope complex, which plays a major role in the virus entry into the host [Chan and Kim, 1998, Castagna et al., 2005, Montero et al., 2008]. As such, gp41 as a whole, but also MPER itself, have become important targets for HIV-1 drugs [Gardner and Farzan, 2017, Kelsoe and Haynes, 2017, Montero et al., 2008]. The MPER peptide does not only have a strong medical significance, but is also interesting for establishing FCS as a tool to study the interaction of biomolecules with lipid monolayers. Fluorescence imaging and FCS show no evidence for aggregation of MPER at the lipid monolayer, supposedly because this short peptide does not exhibit a higher order structure which may unfold when it encounters the hydrophobic interface. Moreover, MPER is known to insert its α-helix into the membrane [Sun et al., 2008], which at least in theory makes its interaction conceptually different from the interaction of CtxB with lipid monolayers.

Similarly to the previously shown measurements on CtxB, all experiments on MPER are performed in a low concentration regime (10 nM), which ensures that the monolayer is not altered upon injection of MPER. Indeed, the autocorrelation curves of the lipid

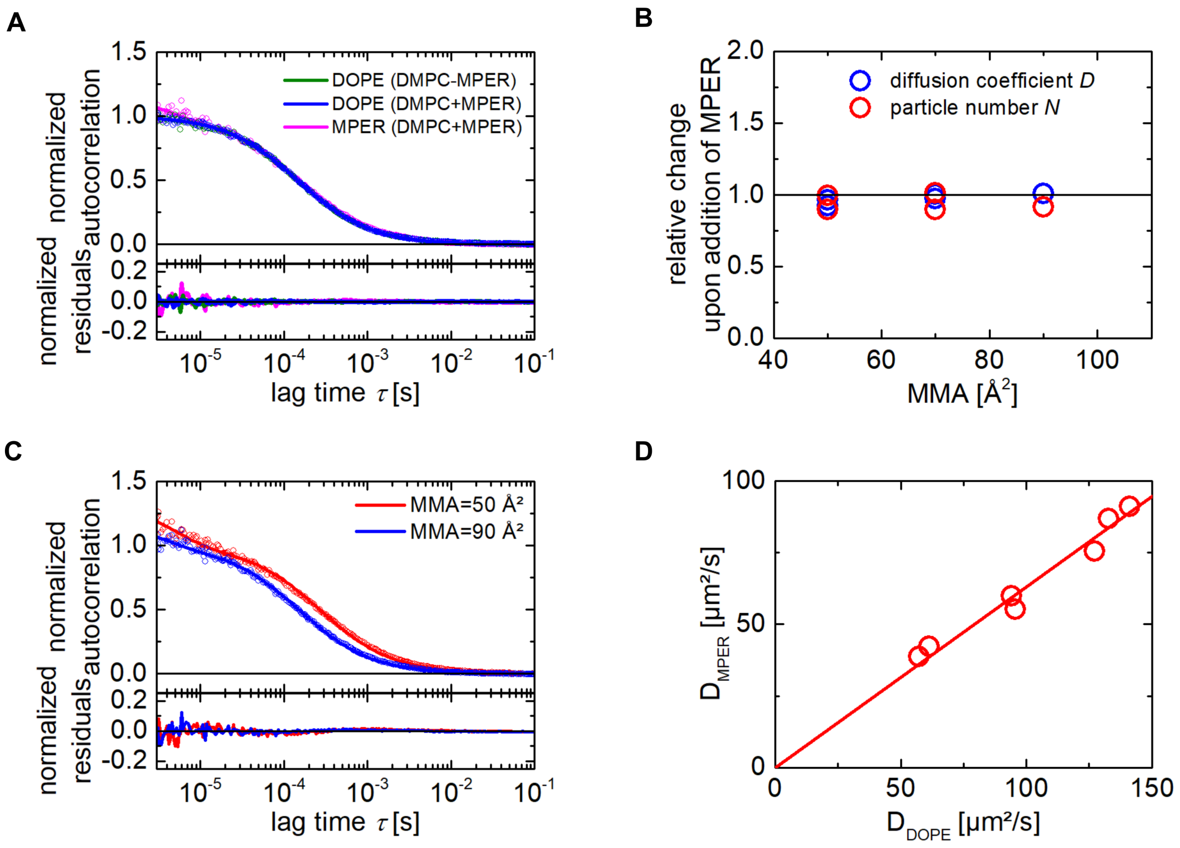

Figure VI.8: Diffusion coefficient of monolayer-bound MPER depends on the lipid packing. A) The autocorrelation curve of 0.01 mol% ATTO655-DOPE in 70 Å^2 MMA DMPC does not change upon addition of 10 nM ATTO488 labeled MPER (green to blue). The superimposed autocorrelation curve of ATTO488-MPER seems to overlap with the autocorrelation curves of the lipid, yet the diffusion is slower, as MPER is measured at 488 nm excitation, which features smaller detection volumes than the more red shifted wavelengths for the lipid measurements. B) The determining parameters N and τ_D do not change for the lipid monolayer upon addition of MPER. C) Normalized autocorrelation curves and fits by a 2D diffusion model function with triplet contribution of monolayer-bound MPER labeled with ATTO488. The autocorrelation curve measured in DMPC monolayers of 50 Å^2 MMA (red) decays at larger lag times than the autocorrelation curve measured at 90 Å^2 MMA (blue). D) As for CtxB, the diffusion coefficients of MPER show a strong correlation with the diffusion coefficient of ATTO655-DOPE measured in a DMPC monolayer. The relation between the diffusion coefficients of lipid and MPER appears to be linear, a corresponding fit is shown (see table VI.4).

before and after addition of MPER are indistinguishable and the fitting parameters do not change, independently of the MMA (figure VI.8A,B).

MPER is labeled with ATTO488, which exhibits triplet blinking. Accordingly, the

Table VI.4: Relation of the diffusion coefficients of CtxB and MPER to the diffusion coefficient of lipids. Conversion factor m between the diffusion coefficient of ATTO655-DOPE and the diffusion coefficients of CtxB and MPER for different monolayer compositions: $D_{\mathrm{CtxB/MPER}} = m \cdot D_{\mathrm{lipid}}$ (see figures VI.7D and VI.8D). The diffusion coefficients can be easily related to the MMA through table VI.2. All measurements were performed at 30 °C.

biomolecule	monolayer composition	m
CtxB	DMPC	0.47 ± 0.02
	DMPC + 2 mol% G_{M1}	0.42 ± 0.01
	DMPC + 6 mol% G_{M1}	0.45 ± 0.01
MPER	DMPC	0.63 ± 0.01

autocorrelation curves are fitted with a 2D diffusion model with a triplet contribution, which describes the experimental data with low and random residuals. As for CtxB, the diffusion of MPER depends on the MMA. A decrease in MMA is accompanied by decrease in diffusion coefficient (figure VI.8C,D). For MMA = 70 Å^2 the measurements yield $D_{\mathrm{MPER}} = (40.7 \pm 1.8)\,\mu\mathrm{m}^2/\mathrm{s}$. Both diffusion coefficient D_{MPER} and D_{lipid} show a linear relation to the MMA. The slope is given in table VI.4 and is larger than the slope obtained for CtxB, which is in line with the overall larger diffusion coefficient of MPER. It is important to note that the studied peptide is fluorescently labeled through a cysteine. Therefore, the measurements presented here correspond to MPER dimers, formed through disulfide bonds. While estimating the effective hydrodynamic radius of the insertion size of MPER into the lipid monolayer is already challenging, but presumably can be done using the geometrical considerations by Sun *et al.* [Sun et al., 2008], the situation is even more error prone for dimeric MPER. Nonetheless, this effect could be tested for instance by breaking the disulfide bonds using mercaptoethanol.

VI.2.3.3 Rod-like DNA origamis

So far, the diffusion of lipids, a small peptide and a pentameric protein have been studied by FCS in this work. To increase the range of covered sizes even further, this chapter describes the diffusion of large rod-like DNA origami, which are membrane targeted through the functionalization with hydrophobic moieties. Since the first demonstration in 2006 [Rothemund, 2006], DNA origamis have attracted the attention of many researchers, as they show promising potential for a variety of applications. The functionalization of DNA origamis for membrane association itself has been subject to a plethora of research articles and reviews, e.g. [Langecker et al., 2012, Langecker et al., 2014, Bell and Keyser, 2014, Czogalla et al., 2016]. Here, a DNA origami approach is chosen, because structures that span tens of nanometers, and are decorated with cholesterol anchors to mediate membrane binding, can be easily produced. In detail, the DNA origami used here has a cuboid shape with the dimensions 110 nm × 16 nm × 8 nm and has been previously described by Khmelinskaia and colleagues [Khmelinskaia et al., 2016]. The persistence length of this 20 helix-bundle DNA origami is much larger than its contour length, which means that the DNA origami behaves like a stiff rod. One of the larger facets exposes 5 × 3 target sites, which can be selectively modified with cholesterol anchors, as shown in figure D.1 (appendix D.1). For this study, the DNA origami is either decorated by five cholesterol anchors (denoted as structure X5, for information on the precise location of the anchors see [Khmelinskaia et al., 2016]), or free of any membrane anchors (denoted as structure N). The opposite top facet carries three ATTO488 labels, which are located close to the center-of-mass to avoid effects of rotational diffusion on the autocorrelation function [Czogalla et al., 2013, Czogalla et al., 2015].

The bare nanostructure N, which has no affinity to GUVs in the used buffer conditions [Khmelinskaia et al., 2016], also shows no enrichment at the DMPC monolayer interface (data not shown). This is reasonable, as DNA origami are typically highly charged hydrophilic objects. Interestingly, no significant structure clustering is observed either. In contrast, the structure X5 binds to the DMPC monolayer, which is in line with the previously shown binding to GUVs [Khmelinskaia et al., 2016]. For the tested concentrations up to 200 pM, structure X5 does not influence the lipid mobility upon binding to the lipid monolayer (data not shown). Nonetheless, a lower concentration was chosen for FCS measurements. Czogalla *et al.* reported that the lateral diffusion coefficient of rods diffusing in 2D is almost not affected by crowding if the product of rod density and squared rod length is smaller than 0.4 [Czogalla et al., 2015]. Theoretically, these results should be transferable to lipid monolayers. Accordingly, the rod density σ in these monolayer experiments should be smaller than 30 particles/µm^2. Using FCS, the particle number in the confocal volume is accessible through the autocorrelation amplitude of diffusing particles, whereas the confocal volume size is known from an initial calibration measurement. Based on a sweep of DNA origami concentrations, a regime $\sigma < 30$ particles/µm^2 is identified for concentrations of less than 40 pM. A representative autocorrelation curve at MMA $= 70\,\text{Å}^2$ is shown with the corresponding fit in figure VI.9A (yellow curve). It should be noted that the residuals for the X5 nanostructure are larger than for all other biomolecules, and partially systematic. The autocorrelation curve obtained for the structure X5 decays at larger diffusion times than CtxB, corresponding to a smaller diffusion coefficient of $D_{\mathrm{X5}} = 10.1\,\mu\mathrm{m}^2/\mathrm{s}$. As for MPER, an estimation of the effective insertion size of X5 into the membrane is challenging and not very precise because of the weak size dependence of SD-model and HPW-model. A respective discussion is presented in section VI.2.3.4.

VI.2.3.4 Estimation of the lipid monolayer surface viscosity through the Hughes-Pailthorpe-White model

Within the previous sections, the diffusion coefficients of DOPE, MPER, CtxB and the DNA nanostructure X5 in DMPC monolayers have been reported, some at several MMAs, but all of them at MMA $= 70\,\text{Å}^2$. These results are, depending on the MMA, around three- to fourfold faster, than the diffusion of the same objects at similar free-standing bilayers, as depicted in figure VI.9B. Clearly, temperature and lipids of the reference bilayer measurements are not identical to the conditions of the lipid monolayer experiments, but the corresponding changes are ought to be small compared to the observed differences between lipid monolayers and bilayers. In conclusion, the surface viscosity η_s of the lipid monolayer is considerably lower than the surface viscosity of a lipid bilayer, in good agreement with previous studies [Sickert and Rondelez, 2003, Wilke et al., 2010, Peters and Cherry, 1982, Petrov et al., 2012]. Accordingly, the characteristic hydrodynamic length of the system, the Saffmann-Delbrück length $l_{\mathrm{SD}} = \frac{\eta_s}{\eta_1+\eta_2}$ ($\eta_{1,2}$ are the bulk viscosities of the adjacent media, see section section II.1.1 in chapter II) [Saffman and Delbrück, 1975, Saffman, 1976], is shorter in lipid monolayers than bilayers. Assuming that the monolayer has half the thickness of a bilayer, and that the viscosity of air is negligible compared to the viscosity of water, the ratio of hydrodynamic length scales of monolayer and bilayer are equivalent to the ratio of their surface viscosities $l_{\mathrm{SD,mono}}/l_{\mathrm{SD,bi}} = \eta_{\mathrm{s,mono}}/\eta_{\mathrm{s,bi}}$. Here, the different thicknesses of both membrane systems are accounted for by a factor of 2. A lower viscosity of the lipid monolayer at MMA $= 70\,\text{Å}^2$ compared to the lipid bilayer is reasonable, as the packing density is lower and no interleaflet coupling occurs. The correspondingly smaller hydrodynamic length scale of the lipid monolayer implies a slightly larger sensitivity of the lipid monolayer system to size variations on relevant length scales, as already discussed in the context of figure II.1.

Ideally, the measured diffusion coefficient should enable to extract an effective insertion size for the considered biomolecules. However, there are two major problems with this

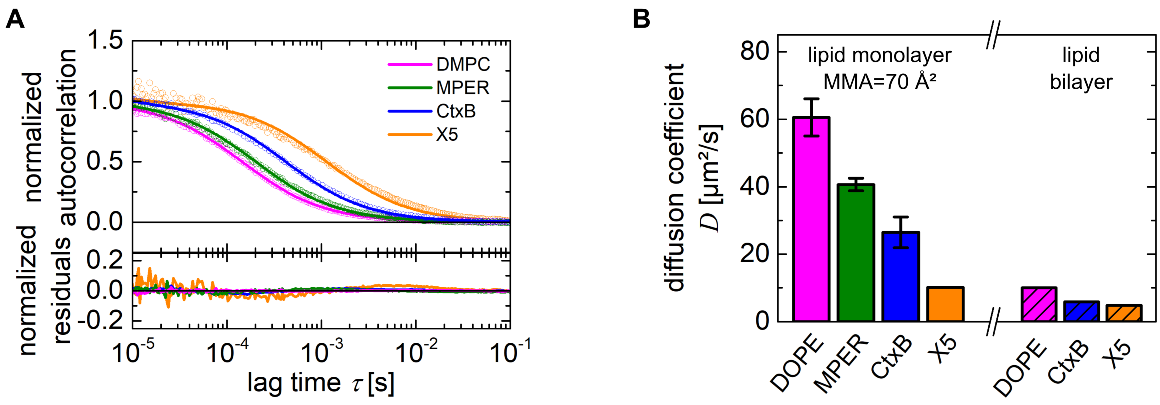

Figure VI.9: Diffusion of several biomolecules in DMPC monolayers. A) Experimental autocorrelation curves and the corresponding fits for several biomolecules diffusing in a DMPC monolayer of 70 Å^2 MMA. The studied biomolecules range from a small lipid to a large, more than 100 nm long DNA origami structure (X5). All correlation curves decay at different lag times, which corresponds to their differences in membrane insertion and physical size. B) The corresponding diffusion coefficients in DMPC lipid monolayers are significantly larger than in free-standing bilayers, which is in line with the significantly smaller surface viscosity of the lipid monolayer compared to the lipid bilayer. The values for lipid bilayers should be considered as rough references as they were measured in DOPC at different temperatures: DOPE and CtxB at 23.5 °C [Heinemann et al., 2012, Heinemann et al., 2013], X5 at 27.5 °C (data not shown).

approach: first, the surface viscosity of the monolayer is required for such a calculation. Unfortunately, the reported values scatter significantly [Brooks et al., 1999, Wurlitzer et al., 2000, Schwartz et al., 1994] and potentially have been overestimated in many studies [Sickert and Rondelez, 2003, Fischer, 2004, Sickert and Rondelez, 2004]. Second, both, SD-model and HPW-model, are in the relevant regime only weakly depending on the insertion size through a logarithmic relation (equations II.7 and II.8). On the other hand, the latter argument can be evaluated from another angle: because of the weak size dependence of both models, a reasonable estimate of the insertion size should yield reasonably good estimates of the surface viscosity. A manifold of measurements of the diffusion coefficient of CtxB at different MMA is presented in figure VI.7. From these values, the surface viscosities are calculated based on the previously reported radius $r = 3.1$ nm of pentameric CtxB [Zhang et al., 1995]. Care needs to be taken to choose the appropriate model, because at high MMA, the Saffmann-Delbrück length appears to become small and the SD-model becomes inapplicable (figure VI.10A). On the other hand, the HPW-model describes all size ranges which are much larger than the lipids, properly. Consequently, the calculations here

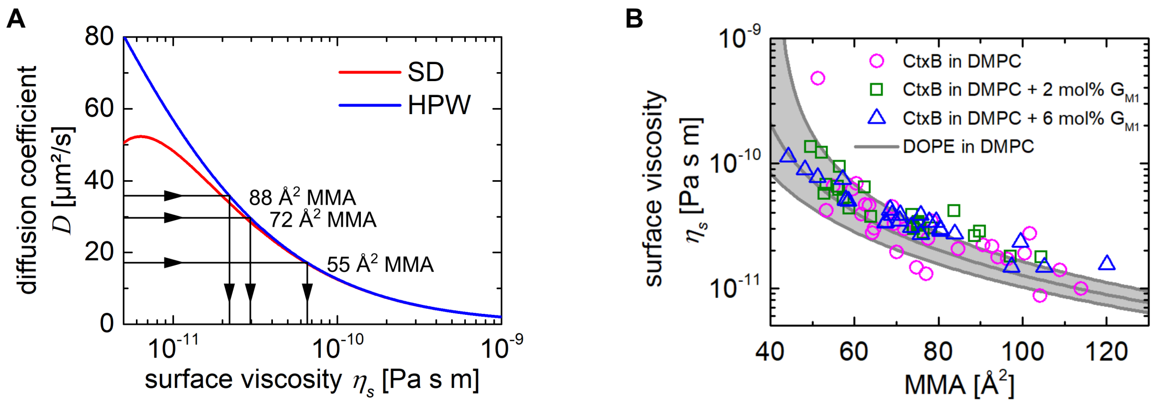

Figure VI.10: Viscosity of the DMPC lipid monolayer determined by FCS. A) Theoretical diffusion coefficient based on SD-model and HPW-model for an insertion of radius 3.1 nm into the monolayer at 30 °C. The surrounding bulk viscosities are set to $\eta_1 = 0.83\,\mathrm{mPa\,s}$ and $\eta_2 = 0$. At low surface viscosities, the Saffmann-Delbrück length is no longer much larger than the insertion diameter and the SD-model fails. For every FCS measurement of CtxB in a monolayer of known MMA (figure VI.7), the corresponding surface viscosity η_s is determined numerically by comparing the measured diffusion coefficient with the prediction from the HPW-model. B) Scatter plots of the surface viscosities obtained from FCS measurements on CtxB. As expected, the surface viscosity increases with increasing lipid packing. The data points are in themselves consistent, but also are in line with the predictions based on the lipid measurements (figure VI.4 and table VI.2), which are shown with their 95% confidence intervals. The dependence of the surface viscosity on the MMA can be empirically described by a bi-exponential (see equation VI.3). All relations are obtained at 30 °C.

are performed using the HPW-model. Finally, one needs to realize that neither SD-model nor HPW-model can be solved for η_s analytically (equations II.6, II.7, II.8). Therefore, in this study the surface viscosities are calculated numerically by estimating the zero of $D_{\mathrm{HPWM}}(\eta_s) - D_{\mathrm{measured}}$ using Newton's method. This computation is performed for all measurements shown in figure VI.7D. The respective MMAs are inferred from the lipid diffusion coefficients using the linear relation presented in table VI.2. The corresponding scatter plot of surface viscosities for a range of MMAs is presented in figure VI.10B. As one would expect, the surface viscosity decreases with increasing MMA. The absolute values of the surface viscosity are relatively low compared to previous studies [Brooks et al., 1999, Wurlitzer et al., 2000, Schwartz et al., 1994, Sickert and Rondelez, 2003, Sickert et al., 2007], which are however still debated, as mentioned above. In detail, the obtained viscosities for DMPC monolayers at the air-water interface range from $\eta_s = 1 \cdot 10^{-10}\,\mathrm{Pa\,s\,m}$ at MMA $= 50\,\text{Å}^2$ to $\eta_s = 2 \cdot 10^{-11}\,\mathrm{Pa\,s\,m}$ at MMA $= 100\,\text{Å}^2$. The presented data set is relatively large and covers the entire liquid-extended phase. To provide a reference for future studies, the points shown in figure VI.10B are fitted by a bi-exponential (fit not shown) with four free parameters $a_{1\ldots4}$, to provide an empirical relation, such that the viscosity can be calculated for any arbitrary MMA:

$$\eta_s(T = 303.15\,\mathrm{K}) = a_1 e^{-a_2 \cdot \mathrm{MMA}} + a_3 e^{-a_4 \cdot \mathrm{MMA}} \qquad \text{(VI.3)}$$

$$a_1 = 1.2 \cdot 10^{-8}\,\mathrm{Pa\,s\,m} \quad a_2 = 0.104\,\text{Å}^{-2} \quad a_3 = 1.7 \cdot 10^{-10}\,\mathrm{Pa\,s\,m} \quad a_4 = 0.025\,\text{Å}^{-2}$$

The choice of a biexponential has no physical justification, but is a pragmatic approach to provide estimates of η_s for future studies.

As for CtxB, the viscosity of the DMPC monolayer is also calculated based on the measured diffusion of ATTO655-DOPE. The empirical linear dependence between D and MMA for ATTO655-DOPE was presented in table VI.2 and we assume radius of $r = 0.36\,\mathrm{nm}$, which is estimated from the physical area of $42\,\text{Å}^2$ [Peters and Beck, 1983, Kim and Yu, 1992, Tanaka et al., 1999, Ke and Naumann, 2001, Gudmand et al., 2009, Boguslavsky et al., 1994]. It needs to be stressed that this approach violates the assumption that the membrane inclusion is much larger than the lipids themselves, a key prerequisite of SD-model and HPW-model. The experimental evidence in this regime is inconclusive, as some studies found the SD-model to hold for small insertions [Weiß et al., 2013, Ramadurai et al., 2009], whereas others found a Stokes-Einstein-Smoluchowski-like behavior [Kriegsmann et al., 2009, Gambin et al., 2006]. The surface viscosities of the DMPC monolayer, calculated based on lipid diffusion, are shown together with the 95% confidence intervals (table VI.2) in gray in figure VI.10B. Remakably, these results not only follow the same trend as the results for CtxB, but also the absolute numbers agree reasonably well.

With a characterized surface viscosity it is straightforward to estimate the effective inclusion sizes for MPER and the nanostructure X5. With $\eta_s = 3.8 \cdot 10^{-11}\,\mathrm{Pa\,s\,m}$ at $\mathrm{MMA} = 70\,\text{Å}^2$ and $\eta_1 = 0.83 \cdot 10^{-3}\,\mathrm{Pa\,s}$, the corresponding Saffmann-Delbrück length is $l_{\mathrm{SD}} = 44.8\,\mathrm{nm}$, which is in good agreement with the rough initial estimate of 100 nm in section II.1.1 in chapter II. Accordingly, for MPER the inclusion size is $a = 0.8\,\mathrm{nm}$. Although difficult to estimate, geometrical considerations based on the alignment of MPER in lipid bilayers [Sun et al., 2008], yield a similar, yet slightly larger radius. The effective inclusion size for X5 is $r = 28.3\,\mathrm{nm}$, which is less than a factor 2 smaller than l_{SD}. Consequently, the SD-model is no longer an appropriate choice. Moreover, this effective inclusion size is much larger than the combined inclusion of its five cholesterol anchors. The space between the anchors is not infinitely large, thus the inclusion sizes do not just add up, but the effective inclusion size is considerably larger. However, this estimate of the effective inclusion size needs to be reconfirmed by further experiments, as it is likely to represents a mixture of viscous drag in solution and in the membrane. Previous experiments on GUVs suggest that such rod-like structures are gliding on the membrane [Czogalla et al., 2015], while being held in the lipid monolayer by its cholesterol anchors. Typically, the viscous drag in aqueous solution is neglected in bilayer experiments, as the diffusion is governed by the viscous drag in the membrane. Here however, because of the large physical size of the DNA origami and the relatively low viscosity of the monolayer, it is not clear whether this assumption still holds.

VI.3 Conclusion

This work establishes conditions for reproducible, long, high-quality point FCS measurements on lipid monolayer systems at the air-water interface. Most importantly, the use of miniaturized microchambers is validated, which is a major step towards the study of protein-monolayer interactions with only minute amounts of protein. Moreover, this study illustrates the necessity to reach an equilibrated system in which the lipid monolayer stays at a constant height to minimize focus drift. To reach this state, it is necessary to heat the closed monolayer chamber to the working temperature of the microscope or above. This study is conducted at 30 °C, almost 3 K above the objective's temperature.

In a set of proof-of-principle experiments, we apply FCS to study the lateral diffusion of selected biomolecules at the lipid monolayer and benchmarked the results against previous FCS studies [Gudmand et al., 2009, Chwastek and Schwille, 2013]. The use of FCS cannot only substitute canonical Π measurements to characterize the monolayer state, but also, due to its high sensitivity, allows for the quantitative characterization of protein-lipid monolayer interactions in a regime where the physical properties of the monolayer are not modified.

To cover a wide range of sizes and membrane insertions of diffusing particles, not only the diffusion of the rather small peptide MPER, but also the model protein CtxB and a large DNA origami are characterized. This study shows that the viscosity and consequently the hydrodynamic length scale in lipid monolayers are smaller than in lipid bilayers. Furthermore, the effect of lipid packing on protein diffusion in the lipid monolayer is demonstrated for the first time. This study finds and quantifies a linear dependence between the diffusion coefficient of bound protein and the diffusion coefficients of the lipids themselves. The direct impact of lipid packing on the mobility of monolayer-associated biomolecules may have implications on intermolecular reaction rates, which are often diffusion-limited.

Finally, the results are discussed in the context of SD-model and HPW-model. Based on the latter model, the viscosity of the DMPC monolayer is quantified for the entire range of MMAs within the liquid-extended phase. Future studies will profit from the provided empirical relation between viscosity and MMA.

VI.4 Outlook

This study demonstrates the first steps towards the routine FCS study of protein-lipid interactions on lipid monolayers. From here, several future directions are conceivable. Reversible binding to the monolayer, ligand induced modulation of membrane-targeted protein behavior, diffusion of a wide range of biomolecules, and the study of other lipids and lipid mixtures on protein binding to the monolayer are accessible by FCS based on this work. Moreover, all these processes may potentially depend not only on the lipid packing, but also on a range of thermodynamic factors like ionic strength, pH and temperature, which adds additional dimensions to all these potential studies.

Moreover, the applicability of the SD-model in the high MMA regime should be addressed. Although assumed here, it is not obvious that the SD-model holds with an increasingly large free area in between molecules. Finally, in the light of the low surface viscosity determined here, it would be interesting to characterize the surface viscosity of lipid monolayers consisting of other lipid molecules than DMPC.

Finally, the study of rod-like DNA nanostructures qualitatively seems to show similar effects regarding crowding on GUVs [Czogalla et al., 2015] and lipid monolayers: an increased surface density increases the decay time of the measured autocorrelation curve (data not shown). It would be interesting to study the effect of lipid packing on such a system. In general, DNA nanostructures appear to be ideally suited for studies on monolayers. Because of their hydrophilic character, they are less prone to aggregation at the air-water interface than proteins. Thus, they could potentially be studied with a wide range of hydrophobic modifications to target them to the lipid monolayer.

Bibliography

[Abuillan et al., 2013] Abuillan, W., Schneck, E., Körner, A., Brandenburg, K., Gutsmann, T., Gill, T., Vorobiev, A., Konovalov, O., and Tanaka, M. (2013). Physical interactions of fish protamine and antisepsis peptide drugs with bacterial membranes revealed by combination of specular x-ray reflectivity and grazing-incidence x-ray fluorescence. *Phys. Rev. E*, 88(1):12705.

[Adams and Errington, 2009] Adams, D. W. and Errington, J. (2009). Bacterial cell division: assembly, maintenance and disassembly of the Z ring. *Nature Reviews Microbiology*, 7:642.

[Ahijado-Guzmán et al., 2013] Ahijado-Guzmán, R., Alfonso, C., Reija, B., Salvarelli, E., Mingorance, J., Zorrilla, S., Monterroso, B., and Rivas, G. (2013). Control by Potassium of the Size Distribution of Escherichia coli FtsZ Polymers Is Independent of GTPase Activity. *Journal of Biological Chemistry*, 288(38):27358–27365.

[Alberts, 2002] Alberts, B. (2002). *Molecular Biology of the cell.* Garland Science, 4 edition.

[Altman et al., 2011] Altman, R. B., Terry, D. S., Zhou, Z., Zheng, Q., Geggier, P., Kolster, R. A., Zhao, Y., Javitch, J. A., Warren, J. D., and Blanchard, S. C. (2011). Cyanine fluorophore derivatives with enhanced photostability. *Nature Methods*, 9:68.

[Amado et al., 2008] Amado, E., Kerth, A., Blume, A., and Kressler, J. (2008). Infrared Reflection Absorption Spectroscopy Coupled with Brewster Angle Microscopy for Studying Interactions of Amphiphilic Triblock Copolymers with Phospholipid Monolayers. *Langmuir*, 24(18):10041–10053.

[Amin et al., 2014] Amin, S., Barnett, G. V., Pathak, J. A., Roberts, C. J., and Sarangapani, P. S. (2014). Protein aggregation, particle formation, characterization rheology. *Current Opinion in Colloid Interface Science*, 19(5):438–449.

[Angelova et al., 1996] Angelova, A., Vollhardt, D., and Ionov, R. (1996). 2D-3D Transformations of Amphiphilic Monolayers Influenced by Intermolecular Interactions: A Brewster Angle Microscopy Study. *The Journal of Physical Chemistry*, 100(25):10710–10720.

[Angelova and Dimitrov, 1986] Angelova, M. I. and Dimitrov, D. S. (1986). Liposome electroformation. *Faraday Discussions of the Chemical Society*, 81(0):303–311.

[Anhut et al., 2005] Anhut, T., Hassler, K., Lasser, T., Koenig, K., and Rigler, R. (2005). Fluorescence correlation spectroscopy on dielectric surfaces in total internal reflection geometries.

[Arnebrant and Wahlgren, 1995] Arnebrant, T. and Wahlgren, M. C. (1995). Protein-Surfactant Interactions at Solid Surfaces. In *Proteins at Interfaces II*, volume 602 of *ACS Symposium Series*, pages 17–239. American Chemical Society.

[Auer et al., 2017] Auer, A., Strauss, M. T., Schlichthaerle, T., and Jungmann, R. (2017). Fast, Background-Free DNA-PAINT Imaging Using FRET-Based Probes. *Nano Letters*, 17(10):6428–6434.

[Axelrod, 1981] Axelrod, D. (1981). Cell-substrate contacts illuminated by total internal reflection fluorescence. *The Journal of Cell Biology*, 89(1):141–145.

[Axelrod, 2001a] Axelrod, D. (2001a). Selective imaging of surface fluorescence with very high aperture microscope objectives. *Journal of Biomedical Optics*, 6(1):6–13.

[Axelrod, 2001b] Axelrod, D. (2001b). Total Internal Reflection Fluorescence Microscopy in Cell Biology. *Traffic*, 2(11):764–774.

[Bacia et al., 2006] Bacia, K., Kim, S. A., and Schwille, P. (2006). Fluorescence cross-correlation spectroscopy in living cells. *Nature Methods*, 3:83.

[Bacia and Schwille, 2003] Bacia, K. and Schwille, P. (2003). A dynamic view of cellular processes by in vivo fluorescence auto- and cross-correlation spectroscopy. *Methods*, 29(1):74–85.

[Bacia and Schwille, 2007] Bacia, K. and Schwille, P. (2007). Practical guidelines for dual-color fluorescence cross-correlation spectroscopy. *Nature Protocols*, 2(11):2842–2856.

[Backer and Moerner, 2014] Backer, A. S. and Moerner, W. E. (2014). Extending Single-Molecule Microscopy Using Optical Fourier Processing. *The Journal of Physical Chemistry B*, 118(28):8313–8329.

[Bag et al., 2012] Bag, N., Sankaran, J., Paul, A., Kraut, R. S., and Wohland, T. (2012). Calibration and Limits of Camera-Based Fluorescence Correlation Spectroscopy: A Supported Lipid Bilayer Study. *ChemPhysChem*, 13(11):2784–2794.

[Bag et al., 2014] Bag, N., Yap, D. H. X., and Wohland, T. (2014). Temperature dependence of diffusion in model and live cell membranes characterized by imaging fluorescence correlation spectroscopy. *Biochimica et Biophysica Acta (BBA) - Biomembranes*, 1838(3):802–813.

[Banachowicz et al., 2014] Banachowicz, E., Patkowski, A., Meier, G., Klamecka, K., and Gapinski, J. (2014). Successful FCS experiment in nonstandard conditions. *Langmuir*, 30(29):8945–8955.

[Barroca et al., 2012] Barroca, T., Balaa, K., Lévêque-Fort, S., and Fort, E. (2012). Full-Field Near-Field Optical Microscope for Cell Imaging. *Physical Review Letters*, 108(21):218101.

[Bayburt et al., 2002] Bayburt, T. H., Grinkova, Y. V., and Sligar, S. G. (2002). Self-Assembly of Discoidal Phospholipid Bilayer Nanoparticles with Membrane Scaffold Proteins. *Nano Letters*, 2(8):853–856.

[Bayburt and Sligar, 2010] Bayburt, T. H. and Sligar, S. G. (2010). Membrane protein assembly into Nanodiscs. *FEBS Letters*, 584(9):1721–1727.

[Bell and Keyser, 2014] Bell, N. A. W. and Keyser, U. F. (2014). Nanopores formed by DNA origami: A review. *FEBS Letters*, 588(19):3564–3570.

[Benda et al., 2003] Benda, A., Beneš, M., Mareček, V., Lhotský, A., Hermens, W. T., and Hof, M. (2003). How To Determine Diffusion Coefficients in Planar Phospholipid Systems by Confocal Fluorescence Correlation Spectroscopy. *Langmuir*, 19(10):4120–4126.

[Benesch and Benesch, 1953] Benesch, R. E. and Benesch, R. (1953). Enzymatic Removal of Oxygen for Polarography and Related Methods. *Science*, 118(3068):447–448.

[Berland et al., 1996] Berland, K. M., So, P. T., Chen, Y., Mantulin, W. W., and Gratton, E. (1996). Scanning two-photon fluctuation correlation spectroscopy: particle counting measurements for detection of molecular aggregation. *Biophysical Journal*, 71(1):410–420.

[Berland et al., 1995] Berland, K. M., So, P. T., and Gratton, E. (1995). Two-photon fluorescence correlation spectroscopy: method and application to the intracellular environment. *Biophysical Journal*, 68(2):694–701.

[Beseničar et al., 2006] Beseničar, M., Maček, P., Lakey, J. H., and Anderluh, G. (2006). Surface plasmon resonance in protein-membrane interactions. *Chemistry and Physics of Lipids*, 141(1-2):169–178.

[Betaneli and Schwille, 2013] Betaneli, V. and Schwille, P. (2013). Fluorescence Correlation Spectroscopy to Examine Protein-Lipid Interactions in Membranes. In Kleinschmidt, J. H., editor, *Lipid-Protein Interactions: Methods and Protocols*, pages 253–278. Humana Press, Totowa, NJ.

[Bi and Lutkenhaus, 1991] Bi, E. and Lutkenhaus, J. (1991). FtsZ ring structure associated with division in Escherichia coli. *Nature*, 354:161.

[Bierbaum and Bastiaens, 2013] Bierbaum, M. and Bastiaens, P. I. (2013). Cell Cycle-Dependent Binding Modes of the Ran Exchange Factor RCC1 to Chromatin. *Biophysical Journal*, 104(8):1642–1651.

[Bigay and Antonny, 2012] Bigay, J. and Antonny, B. (2012). Curvature, Lipid Packing, and Electrostatics of Membrane Organelles: Defining Cellular Territories in Determining Specificity. *Developmental Cell*, 23(5):886–895.

[Bingemann, 2006] Bingemann, D. (2006). Analysis of 'blinking' or 'hopping' single molecule signals with a limited number of transitions. *Chemical Physics Letters*, 433(1):234–238.

[BiolinScientific, 2018] BiolinScientific (2018). http://www.biolinscientific.com/ksvnima/technical-specifications (Accessed: 2018-03-01).

[Bisson-Filho et al., 2017] Bisson-Filho, A. W., Hsu, Y.-P., Squyres, G. R., Kuru, E., Wu, F., Jukes, C., Sun, Y., Dekker, C., Holden, S., VanNieuwenhze, M. S., Brun, Y. V., and Garner, E. C. (2017). Treadmilling by FtsZ filaments drives peptidoglycan synthesis and bacterial cell division. *Science*, 355(6326):739–743.

[Biteen et al., 2012] Biteen, J. S., Goley, E. D., Shapiro, L., and Moerner, W. E. (2012). Three-Dimensional Super-Resolution Imaging of the Midplane Protein FtsZ in Live Caulobacter crescentus Cells Using Astigmatism. *ChemPhysChem*, 13(4):1007–1012.

[Blom et al., 2009] Blom, H., Chmyrov, A., Hassler, K., Davis, L. M., and Widengren, J. (2009). Triplet-State Investigations of Fluorescent Dyes at Dielectric Interfaces Using Total Internal Reflection Fluorescence Correlation Spectroscopy. *The Journal of Physical Chemistry A*, 113(19):5554–5566.

[Bloomfield et al., 1967] Bloomfield, V., Dalton, W. O., and Van Holde, K. E. (1967). Frictional coefficients of multisubunit structures. I. Theory. *Biopolymers*, 5(2):135–148.

[Böckmann et al., 2003] Böckmann, R. A., Hac, A., Heimburg, T., and Grubmüller, H. (2003). Effect of Sodium Chloride on a Lipid Bilayer. *Biophysical Journal*, 85(3):1647–1655.

[Boguslavsky et al., 1994] Boguslavsky, V., Rebecchi, M., Morris, A. J., Jhon, D. Y., Rhee, S. G., and McLaughlin, S. (1994). Effect of Monolayer Surface Pressure on the Activities of Phosphoinositide-Specific Phospholipase C-β1, -gamma1, and -delta1. *Biochemistry*, 33(10):3032–3037.

[Böhmer et al., 2002] Böhmer, M., Wahl, M., Rahn, H.-J., Erdmann, R., and Enderlein, J. (2002). Time-resolved fluorescence correlation spectroscopy. *Chemical Physics Letters*, 353(5):439–445.

[Booth et al., 1998] Booth, M. J., Neil, M. A. A., and Wilson, T. (1998). Aberration correction for confocal imaging in refractive-index-mismatched media. *Journal of Microscopy*, 192(2):90–98.

[Boulanger et al., 2014] Boulanger, J., Gueudry, C., Münch, D., Cinquin, B., Paul-Gilloteaux, P., Bardin, S., Guérin, C., Senger, F., Blanchoin, L., and Salamero, J. (2014). Fast high-resolution 3D total internal reflection fluorescence microscopy by incidence angle scanning and azimuthal averaging. *Proceedings of the National Academy of Sciences*, 111(48):17164–17169.

[Bowen et al., 2005] Bowen, M. E., Weninger, K., Ernst, J., Chu, S., and Brunger, A. T. (2005). Single-Molecule Studies of Synaptotagmin and Complexin Binding to the SNARE Complex. *Biophysical Journal*, 89(1):690–702.

[Brandão et al., 2014] Brandão, H. B., Sangji, H., Pandžić, E., Bechstedt, S., Brouhard, G. J., and Wiseman, P. W. (2014). Measuring ligand-receptor binding kinetics and dynamics using k-space image correlation spectroscopy. *Methods*, 66(2):273–282.

[Bratton and Shaevitz, 2015] Bratton, B. P. and Shaevitz, J. W. (2015). Simple Experimental Methods for Determining the Apparent Focal Shift in a Microscope System. *PLOS ONE*, 10(8):e0134616.

[Brinkmeier et al., 1999] Brinkmeier, M., Dörre, K., Stephan, J., and Eigen, M. (1999). Two-Beam Cross-Correlation: A Method To Characterize Transport Phenomena in Micrometer-Sized Structures. *Analytical Chemistry*, 71(3):609–616.

[Brockman, 1999] Brockman, H. (1999). Lipid monolayers: why use half a membrane to characterize protein-membrane interactions? *Current Opinion in Structural Biology*, 9(4):438–443.

[Brooks et al., 1999] Brooks, C. F., Fuller, G. G., Frank, C. W., and Robertson, C. R. (1999). An Interfacial Stress Rheometer To Study Rheological Transitions in Monolayers at the Air-Water Interface. *Langmuir*, 15(7):2450–2459.

[Brown, 1828] Brown, R. (1828). XXVII. A brief account of microscopical observations made in the months of June, July and August 1827, on the particles contained in the pollen of plants; and on the general existence of active molecules in organic and inorganic bodies. *Philosophical Magazine Series 2*, 4(21):161–173.

[Browne et al., 1973] Browne, M., Cecil, R., and Miller, J. C. (1973). Some Reactions of Insulin at Non-Polar Surfaces. *European Journal of Biochemistry*, 33(2):233–240.

[Brunstein et al., 2014a] Brunstein, M., Hérault, K., and Oheim, M. (2014a). Eliminating Unwanted Far-Field Excitation in Objective-Type TIRF. Part II. Combined Evanescent-Wave Excitation and Supercritical-Angle Fluorescence Detection Improves Optical Sectioning. *Biophysical Journal*, 106(5):1044–1056.

[Brunstein et al., 2017] Brunstein, M., Roy, L., and Oheim, M. (2017). Near-Membrane Refractometry Using Supercritical Angle Fluorescence. *Biophysical Journal*, 112(9):1940–1948.

[Brunstein et al., 2014b] Brunstein, M., Teremetz, M., Hérault, K., Tourain, C., and Oheim, M. (2014b). Eliminating unwanted far-field excitation in objective-type TIRF. Part I. Identifying sources of nonevanescent excitation light. *Biophysical Journal*, 106(5):1020–1032.

[Brutzer et al., 2012] Brutzer, H., Schwarz, F. W., and Seidel, R. (2012). Scanning Evanescent Fields Using a pointlike Light Source and a Nanomechanical DNA Gear. *Nano Letters*, 12(1):473–478.

[Buchholz et al., 2012] Buchholz, J., Krieger, J. W., Mocsár, G., Kreith, B., Charbon, E., Vámosi, G., Kebschull, U., and Langowski, J. (2012). FPGA implementation of a 32x32 autocorrelator array for analysis of fast image series. *Optics Express*, 20(16):17767–17782.

[Burghardt, 2012] Burghardt, T. P. (2012). Measuring incidence angle for through-the-objective total internal reflection fluorescence microscopy. *Journal of Biomedical Optics*, 17(12):126007.

[Burstyn and Sengers, 1983] Burstyn, H. C. and Sengers, J. V. (1983). Time dependence of critical concentration fluctuations in a binary liquid. *Physical Review A*, 27(2):1071–1085.

[Buske and Levin, 2013] Buske, P. J. and Levin, P. A. (2013). A flexible C-terminal linker is required for proper FtsZ assembly in vitro and cytokinetic ring formation in vivo. *Molecular Microbiology*, 89(2):249–263.

[Cabriel et al., 2018] Cabriel, C., Bourg, N., Dupuis, G., and Lévêque-Fort, S. (2018). Aberration-accounting calibration for 3D single-molecule localization microscopy. *Optics Letters*, 43(2):174–177.

[Capoulade et al., 2011] Capoulade, J., Wachsmuth, M., Hufnagel, L., and Knop, M. (2011). Quantitative fluorescence imaging of protein diffusion and interaction in living cells. *Nature Biotechnology*, 29:835.

[Carl Zeiss Microscopy GmbH, 2012] Carl Zeiss Microscopy GmbH (2012). *Operating Manual ZEN 2011 (black edition), LSM 710, LSM 780, LSM 710 NLO, LSM 780 NLO and ConfoCor 3.*

[Carpenter et al., 1999] Carpenter, J. F., Kendrick, B. S., Chang, B. S., Manning, M. C., and Randolph, T. W. (1999). Inhibition of stress-induced aggregation of protein therapeutics. In *Amyloid, Prions, and Other Protein Aggregates*, volume 309 of *Methods in Enzymology*, pages 236–255. Academic Press.

[Castagna et al., 2005] Castagna, A., Biswas, P., Beretta, A., and Lazzarin, A. (2005). The Appealing Story of HIV Entry Inhibitors. *Drugs*, 65(7):879–904.

[Chan and Kim, 1998] Chan, D. C. and Kim, P. S. (1998). HIV Entry and Its Inhibition. *Cell*, 93(5):681–684.

[Chan et al., 2009] Chan, Y.-H. M., van Lengerich, B., and Boxer, S. G. (2009). Effects of linker sequences on vesicle fusion mediated by lipid-anchored DNA oligonucleotides. *Proceedings of the National Academy of Sciences of the United States of America*, 106(4):979–984.

[Chattopadhyay et al., 2005] Chattopadhyay, K., Saffarian, S., Elson, E. L., and Frieden, C. (2005). Measuring Unfolding of Proteins in the Presence of Denaturant Using Fluorescence Correlation Spectroscopy. *Biophysical Journal*, 88(2):1413–1422.

[Chen et al., 2017] Chen, C., Huang, H., and Wu, C. H. (2017). Protein Bioinformatics Databases and Resources. *Methods in molecular biology (Clifton, N.J.)*, 1558:3–39.

[Chen et al., 2007] Chen, Y., Anderson, D. E., Rajagopalan, M., and Erickson, H. P. (2007). Assembly Dynamics of Mycobacterium tuberculosis FtsZ. *Journal of Biological Chemistry*, 282(38):27736–27743.

[Chen and Erickson, 2005] Chen, Y. and Erickson, H. P. (2005). Rapid in Vitro Assembly Dynamics and Subunit Turnover of FtsZ Demonstrated by Fluorescence Resonance Energy Transfer. *Journal of Biological Chemistry*, 280(23):22549–22554.

[Chenouard et al., 2014] Chenouard, N., Smal, I., de Chaumont, F., Maška, M., Sbalzarini, I. F., Gong, Y., Cardinale, J., Carthel, C., Coraluppi, S., Winter, M., Cohen, A. R., Godinez, W. J., Rohr, K., Kalaidzidis, Y., Liang, L., Duncan, J., Shen, H., Xu, Y., Magnusson, K. E. G., Jaldén, J., Blau, H. M., Paul-Gilloteaux, P., Roudot, P., Kervrann, C., Waharte, F., Tinevez, J.-Y., Shorte, S. L., Willemse, J., Celler, K., van Wezel, G. P., Dan, H.-W., Tsai, Y.-S., de Solórzano, C. O., Olivo-Marin, J.-C., and Meijering, E. (2014). Objective comparison of particle tracking methods. *Nature Methods*, 11:281.

[Chiaruttini et al., 2015] Chiaruttini, N., Redondo-Morata, L., Colom, A., Humbert, F., Lenz, M., Scheuring, S., and Roux, A. (2015). Relaxation of Loaded ESCRT-III Spiral Springs Drives Membrane Deformation. *Cell*, 163(4):866–879.

[Cho et al., 2010] Cho, N.-J., Frank, C. W., Kasemo, B., and Höök, F. (2010). Quartz crystal microbalance with dissipation monitoring of supported lipid bilayers on various substrates. *Nature Protocols*, 5:1096.

[Choi et al., 2007] Choi, W., Fang-Yen, C., Badizadegan, K., Oh, S., Lue, N., Dasari, R. R., and Feld, M. S. (2007). Tomographic phase microscopy. *Nature Methods*, 4:717.

[Chwastek, 2013] Chwastek, G. (2013). *Interactions of FCHo2 with lipid membranes*. PhD thesis, Technische Universität Dresden.

[Chwastek and Schwille, 2013] Chwastek, G. and Schwille, P. (2013). A Monolayer Assay Tailored to Investigate Lipid-Protein Systems. *ChemPhysChem*, 14(9):1877–1881.

[Cicuta et al., 2007] Cicuta, P., Keller, S. L., and Veatch, S. L. (2007). Diffusion of Liquid Domains in Lipid Bilayer Membranes. *The Journal of Physical Chemistry B*, 111(13):3328–3331.

[Codling et al., 2008] Codling, E. A., Plank, M. J., and Benhamou, S. (2008). Random walk models in biology. *Journal of The Royal Society Interface*, 5(25):813 LP – 834.

[Cohen and Turnbull, 1959] Cohen, M. H. and Turnbull, D. (1959). Molecular Transport in Liquids and Glasses. *The Journal of Chemical Physics*, 31(5):1164–1169.

[Coltharp and Xiao, 2017] Coltharp, C. and Xiao, J. (2017). Beyond force generation: Why is a dynamic ring of FtsZ polymers essential for bacterial cytokinesis? *BioEssays*, 39(1):1–11.

[Conci, 2016] Conci, F. (2016). *A streamlined setup for lipid-protein interaction manipulation*. Master's thesis, Uppsala University.

[Costantino et al., 2005] Costantino, S., Comeau, J. W. D., Kolin, D. L., and Wiseman, P. W. (2005). Accuracy and Dynamic Range of Spatial Image Correlation and Cross-Correlation Spectroscopy. *Biophysical Journal*, 89(2):1251–1260.

[Czogalla et al., 2016] Czogalla, A., Franquelim, H. G., and Schwille, P. (2016). DNA Nanostructures on Membranes as Tools for Synthetic Biology. *Biophysical Journal*, 110(8):1698–1707.

[Czogalla et al., 2015] Czogalla, A., Kauert, D. J., Seidel, R., Schwille, P., and Petrov, E. P. (2015). DNA Origami Nanoneedles on Freestanding Lipid Membranes as a Tool

To Observe Isotropic-Nematic Transition in Two Dimensions. *Nano Letters*, 15(1):649–655.

[Czogalla et al., 2013] Czogalla, A., Petrov, E. P., Kauert, D. J., Uzunova, V., Zhang, Y., Seidel, R., and Schwille, P. (2013). Switchable domain partitioning and diffusion of DNA origami rods on membranes. *Faraday discussions*, 161:31–43.

[Dave et al., 2009] Dave, R., Terry, D. S., Munro, J. B., and Blanchard, S. C. (2009). Mitigating Unwanted Photophysical Processes for Improved Single-Molecule Fluorescence Imaging. *Biophysical Journal*, 96(6):2371–2381.

[Davidson, 1979] Davidson, R. S. (1979). Mechanisms of photo-oxidation reactions. *Pesticide Science*, 10(2):158–170.

[Day and Davidson, 2009] Day, R. N. and Davidson, M. W. (2009). The fluorescent protein palette: tools for cellular imaging. *Chemical Society Reviews*, 38(10):2887–2921.

[De Maeyer, 1960] De Maeyer, L. (1960). V1. Methoden zur Untersuchung chemischer Relaxation. *Zeitschrift für Elektrochemie, Berichte der Bunsengesellschaft für physikalische Chemie*, 64(1):65–72.

[Deagle et al., 2017] Deagle, R. C., Wee, T.-L. E., and Brown, C. M. (2017). Reproducibility in light microscopy: Maintenance, standards and SOPs. *The International Journal of Biochemistry Cell Biology*, 89:120–124.

[Dempsey, 2013] Dempsey, G. T. (2013). Chapter 24 - A User's Guide to Localization-Based Super-Resolution Fluorescence Imaging. In Sluder, G. and Wolf, D. E. B. T. M. i. C. B., editors, *Digital Microscopy*, volume 114, pages 561–592. Academic Press.

[Dempsey et al., 2009] Dempsey, G. T., Wang, W., and Zhuang, X. (2009). Fluorescence Imaging at Sub-Diffraction-Limit Resolution with Stochastic Optical Reconstruction Microscopy. In Hinterdorfer, P. and Oijen, A., editors, *Handbook of Single-Molecule Biophysics*, pages 95–127. Springer US, New York, NY.

[Demtröder, 2013] Demtröder, W. (2013). *Molekülphysik: theoretische Grundlagen und experimentelle Methoden*. Walter de Gruyter.

[Deng and Shaevitz, 2009] Deng, Y. and Shaevitz, J. W. (2009). Effect of aberration on height calibration in three-dimensional localization-based microscopy and particle tracking. *Applied Optics*, 48(10):1886–1890.

[Dertinger et al., 2007] Dertinger, T., Pacheco, V., von der Hocht, I., Hartmann, R., Gregor, I., and Enderlein, J. (2007). Two-Focus Fluorescence Correlation Spectroscopy: A New Tool for Accurate and Absolute Diffusion Measurements. *ChemPhysChem*, 8(3):433–443.

[Dertinger et al., 2006] Dertinger, T., von der Hocht, I., Benda, A., Hof, M., and Enderlein, J. (2006). Surface Sticking and Lateral Diffusion of Lipids in Supported Bilayers. *Langmuir*, 22(22):9339–9344.

[Deschamps et al., 2014] Deschamps, J., Mund, M., and Ries, J. (2014). 3D superresolution microscopy by supercritical angle detection. *Optics Express*, 22(23):29081–29091.

[Diakowski and Sikorski, 2002] Diakowski, W. and Sikorski, A. F. (2002). Brain spectrin exerts much stronger effect on anionic phospholipid monolayers than erythroid spectrin. *Biochimica et Biophysica Acta (BBA) - Biomembranes*, 1564(2):403–411.

[Diaspro, 2010] Diaspro, A. (2010). *Optical fluorescence microscopy: from the spectral to the nano dimension*. Springer Science Business Media.

[Diaspro et al., 2002] Diaspro, A., Federici, F., and Robello, M. (2002). Influence of refractive-index mismatch in high-resolution three-dimensional confocal microscopy. *Applied Optics*, 41(4):685–690.

[Digman et al., 2005] Digman, M. A., Brown, C. M., Sengupta, P., Wiseman, P. W., Horwitz, A. R., and Gratton, E. (2005). Measuring Fast Dynamics in Solutions and Cells with a Laser Scanning Microscope. *Biophysical Journal*, 89(2):1317–1327.

[Digman et al., 2009] Digman, M. A., Wiseman, P. W., Horwitz, A. R., and Gratton, E. (2009). Detecting Protein Complexes in Living Cells from Laser Scanning Confocal Image Sequences by the Cross Correlation Raster Image Spectroscopy Method. *Biophysical Journal*, 96(2):707–716.

[Dittrich et al., 2011] Dittrich, M., Bottcher, M., Oliveira, J. S. L., Dobner, B., Mohwald, H., and Brezesinski, G. (2011). Physical-chemical characterization of novel cationic transfection lipids and the binding of model DNA at the air-water interface. *Soft Matter*, 7(21):10162–10173.

[Ditzler et al., 2007] Ditzler, M. A., Alemán, E. A., Rueda, D., and Walter, N. G. (2007). Focus on function: Single molecule RNA enzymology. *Biopolymers*, 87(5-6):302–316.

[Dixon, 2008] Dixon, M. C. (2008). Quartz Crystal Microbalance with Dissipation Monitoring: Enabling Real-Time Characterization of Biological Materials and Their Interactions. *Journal of Biomolecular Techniques*, 19(3):151–158.

[Doeven et al., 2005] Doeven, M. K., Folgering, J. H. A., Krasnikov, V., Geertsma, E. R., van den Bogaart, G., and Poolman, B. (2005). Distribution, Lateral Mobility and Function of Membrane Proteins Incorporated into Giant Unilamellar Vesicles. *Biophysical Journal*, 88(2):1134–1142.

[Doolittle, 1951] Doolittle, A. K. (1951). Studies in Newtonian Flow. II. The Dependence of the Viscosity of Liquids on Free-Space. *Journal of Applied Physics*, 22(12):1471–1475.

[Dorn et al., 1998] Dorn, I. T., Neumaier, K. R., and Tampé, R. (1998). Molecular Recognition of Histidine-Tagged Molecules by Metal-Chelating Lipids Monitored by Fluorescence Energy Transfer and Correlation Spectroscopy. *Journal of the American Chemical Society*, 120(12):2753–2763.

[Dupuis et al., 2000] Dupuis, M., Denis-Mize, K., Woo, C., Goldbeck, C., Selby, M. J., Chen, M., Otten, G. R., Ulmer, J. B., Donnelly, J. J., Ott, G., and McDonald, D. M. (2000). Distribution of DNA vaccines determines their immunogenicity after intramuscular injection in mice. *J Immunol*, 165(5):2850–2858.

[Duschl et al., 1998] Duschl, C., Boncheva, M., and Vogel, H. (1998). A miniaturized monolayer trough with variable surface area in the square-millimeter range. *Biochimica et Biophysica Acta (BBA) - Biomembranes*, 1371(2):345–350.

[Edelstein-Keshet and Ermentrout, 1998] Edelstein-Keshet, L. and Ermentrout, G. B. (1998). Models for the length distributions of actin filaments: I. Simple polymerization and fragmentation. *Bulletin of mathematical biology*, 60(3):449–475.

[Eggeling et al., 2008] Eggeling, C., Ringemann, C., Medda, R., Schwarzmann, G., Sandhoff, K., Polyakova, S., Belov, V. N., Hein, B., von Middendorff, C., Schönle, A., and Hell, S. W. (2008). Direct observation of the nanoscale dynamics of membrane lipids in a living cell. *Nature*, 457:1159.

[Eggeling et al., 1998] Eggeling, C., Widengren, J., Rigler, R., and Seidel, C. A. M. (1998). Photobleaching of Fluorescent Dyes under Conditions Used for Single-Molecule Detection: Evidence of Two-Step Photolysis. *Analytical Chemistry*, 70(13):2651–2659.

[Eggeling et al., 1999] Eggeling, C., Widengren, J., Rigler, R., and Seidel, C. A. M. (1999). Photostability of Fluorescent Dyes for Single-Molecule Spectroscopy: Mechanisms and Experimental Methods for Estimating Photobleaching in Aqueous Solution. In Rettig, W., Strehmel, B., Schrader, S., and Seifert, H., editors, *Applied Fluorescence in Chemistry, Biology and Medicine*, pages 193–240. Springer Berlin Heidelberg, Berlin, Heidelberg.

[Egner and Hell, 1999] Egner, A. and Hell, S. W. (1999). Equivalence of the Huygens-Fresnel and Debye approach for the calculation of high aperture point-spread functions in the presence of refractive index mismatch. *Journal of Microscopy*, 193(3):244–249.

[Eigen and Rigler, 1994] Eigen, M. and Rigler, R. (1994). Sorting single molecules: application to diagnostics and evolutionary biotechnology. *Proceedings of the National Academy of Sciences*, 91(13):5740–5747.

[Einstein, 1905] Einstein, A. (1905). Über die von der molekularkinetischen Theorie der Wärme geforderte Bewegung von in ruhenden Flüssigkeiten suspendierten Teilchen. *Annalen der Physik*, 322(8):549–560.

[Elenko et al., 2010] Elenko, M. P., Szostak, J. W., and van Oijen, A. M. (2010). Single-molecule binding experiments on long time scales. *Review of Scientific Instruments*, 81(8):83705.

[Elson, 2011] Elson, E. L. (2011). Fluorescence Correlation Spectroscopy: Past, Present, Future. *Biophysical Journal*, 101(12):2855–2870.

[Elson and Magde, 1974] Elson, E. L. and Magde, D. (1974). Fluorescence correlation spectroscopy. I. Conceptual basis and theory. *Biopolymers*, 13(1):1–27.

[Enderlein, 1999] Enderlein, J. (1999). Single-molecule fluorescence near a metal layer. *Chemical Physics*, 247(1):1–9.

[Enderlein, 2003] Enderlein, J. (2003). Electrodynamics of Fluorescence. Technical report, Georg-August-Universität Göttingen.

[Enderlein and Gregor, 2005] Enderlein, J. and Gregor, I. (2005). Using fluorescence lifetime for discriminating detector afterpulsing in fluorescence-correlation spectroscopy. *Review of Scientific Instruments*, 76(3):33102.

[Enderlein et al., 2005] Enderlein, J., Gregor, I., Patra, D., Dertinger, T., and Kaupp, U. B. (2005). Performance of Fluorescence Correlation Spectroscopy for Measuring Diffusion and Concentration. *ChemPhysChem*, 6(11):2324–2336.

[Enderlein et al., 2004] Enderlein, J., Gregor, I., Patra, D., and Fitter, J. (2004). Art and Artefacts of Fluorescence Correlation Spectroscopy. *Current Pharmaceutical Biotechnology*, 5(2):155–161.

[Enderlein and Ruckstuhl, 2005] Enderlein, J. and Ruckstuhl, T. (2005). The efficiency of surface-plasmon coupled emission for sensitive fluorescence detection. *Optics Express*, 13(22):8855–8865.

[Enderlein et al., 1999] Enderlein, J., Ruckstuhl, T., and Seeger, S. (1999). Highly efficient optical detection of surface-generated fluorescence. *Appl. Opt.*, 38(4):724–732.

[Engelborghs and Visser, 2014] Engelborghs, Y. and Visser, A. J. W. G. (2014). *Fluorescence spectroscopy and microscopy*. Humana Press;.

[Erickson et al., 2010] Erickson, H. P., Anderson, D. E., and Osawa, M. (2010). FtsZ in Bacterial Cytokinesis: Cytoskeleton and Force Generator All in One. *Microbiology and Molecular Biology Reviews*, 74(4):504–528.

[Erikson, 1965] Erikson, T. A. (1965). The Surface Area of Liquids in Circular Tubes. *The Journal of Physical Chemistry*, 69(6):1809–1813.

[Eun et al., 2015] Eun, Y.-J., Kapoor, M., Hussain, S., and Garner, E. C. (2015). Bacterial Filament Systems: Toward Understanding Their Emergent Behavior and Cellular Functions. *Journal of Biological Chemistry*, 290(28):17181–17189.

[Fawcett, 2006] Fawcett, T. (2006). An introduction to ROC analysis. *Pattern Recognition Letters*, 27(8):861–874.

[Felekyan et al., 2012] Felekyan, S., Kalinin, S., Sanabria, H., Valeri, A., and Seidel, C. A. M. (2012). Filtered FCS: Species Auto- and Cross-Correlation Functions Highlight Binding and Dynamics in Biomolecules. *ChemPhysChem*, 13(4):1036–1053.

[Fick, 1855] Fick, A. (1855). Ueber Diffusion. *Annalen der Physik*, 170(1):59–86.

[Fiolka et al., 2008] Fiolka, R., Belyaev, Y., Ewers, H., and Stemmer, A. (2008). Even illumination in total internal reflection fluorescence microscopy using laser light. *Microscopy Research and Technique*, 71(1):45–50.

[Fischer, 2004] Fischer, T. M. (2004). Comment on "Shear Viscosity of Langmuir Monolayers in the Low-Density Limit”. *Phys. Rev. Lett.*, 92(13):139603.

[Fish, 2001] Fish, K. N. (2001). Total Internal Reflection Fluorescence (TIRF) Microscopy. In *Current Protocols in Cytometry*. John Wiley Sons, Inc.

[Fishman et al., 1978] Fishman, P. H., Moss, J., and Osborne Jr, J. C. (1978). Interaction of choleragen with the oligosaccharide of ganglioside GM1: evidence for multiple oligosaccharide binding sites. *Biochemistry*, 17(4):711–716.

[Fleming and Fleming, 2018] Fleming, P. J. and Fleming, K. G. (2018). HullRad: Fast Calculations of Folded and Disordered Protein and Nucleic Acid Hydrodynamic Properties. *Biophysical Journal*, 114(4):856–869.

[Flory, 1936] Flory, P. J. (1936). Molecular size distribution in linear condensation polymers1. *Journal of the American Chemical Society*, 58(10):1877–1885.

[Frenzel and Willbold, 2014] Frenzel, D. and Willbold, D. (2014). Kinetic Titration Series with Biolayer Interferometry. *PLOS ONE*, 9(9):e106882.

[Freyer and Lewis, 2008] Freyer, M. W. and Lewis, E. A. (2008). Isothermal Titration Calorimetry: Experimental Design, Data Analysis, and Probing Macromolecule/Ligand Binding and Kinetic Interactions. In *Biophysical Tools for Biologists, Volume One: In Vitro Techniques*, volume 84 of *Methods in Cell Biology*, pages 79–113. Academic Press.

[Fujita et al., 2017] Fujita, J., Harada, R., Maeda, Y., Saito, Y., Mizohata, E., Inoue, T., Shigeta, Y., and Matsumura, H. (2017). Identification of the key interactions in structural transition pathway of FtsZ from Staphylococcus aureus. *Journal of Structural Biology*, 198(2):65–73.

[Galla et al., 1979] Galla, H. J., Hartmann, W., Theilen, U., and Sackmann, E. (1979). On two-dimensional passive random walk in lipid bilayers and fluid pathways in biomembranes. *The Journal of Membrane Biology*, 48(3):215–236.

[Galush et al., 2008] Galush, W. J., Nye, J. A., and Groves, J. T. (2008). Quantitative Fluorescence Microscopy Using Supported Lipid Bilayer Standards. *Biophysical Journal*, 95(5):2512–2519.

[Gambin et al., 2006] Gambin, Y., Lopez-Esparza, R., Reffay, M., Sierecki, E., Gov, N. S., Genest, M., Hodges, R. S., and Urbach, W. (2006). Lateral mobility of proteins in liquid membranes revisited. *Proceedings of the National Academy of Sciences of the United States of America*, 103(7):2098–2102.

[García-Sáez et al., 2010] García-Sáez, A. J., Carrer, D. C., and Schwille, P. (2010). Fluorescence Correlation Spectroscopy for the Study of Membrane Dynamics and Organization in Giant Unilamellar Vesicles. In Weissig, V., editor, *Liposomes: Methods and Protocols, Volume 2: Biological Membrane Models*, pages 493–508. Humana Press, Totowa, NJ.

[García-Sáez and Schwille, 2008] García-Sáez, A. J. and Schwille, P. (2008). Fluorescence correlation spectroscopy for the study of membrane dynamics and protein/lipid interactions. *Methods*, 46(2):116–122.

[Gardner and Farzan, 2017] Gardner, M. R. and Farzan, M. (2017). Engineering antibody-like inhibitors to prevent and treat HIV-1 infection. *Current Opinion in HIV and AIDS*, 12(3):294–301.

[Gebhardt et al., 2013] Gebhardt, J. C. M., Suter, D. M., Roy, R., Zhao, Z. W., Chapman, A. R., Basu, S., Maniatis, T., and Xie, X. S. (2013). Single-molecule imaging of transcription factor binding to DNA in live mammalian cells. *Nature Methods*, 10:421.

[Gell et al., 2009] Gell, C., Berndt, M., Enderlein, J., and Diez, S. (2009). TIRF microscopy evanescent field calibration using tilted fluorescent microtubules. *Journal of Microscopy*, 234(1):38–46.

[Ghai et al., 2012] Ghai, R., Falconer, R. J., and Collins, B. M. (2012). Applications of isothermal titration calorimetry in pure and applied research - survey of the literature from 2010. *Journal of Molecular Recognition*, 25(1):32–52.

[Gielen et al., 2009a] Gielen, E., Smisdom, N., VandeVen, M., De Clercq, B., Gratton, E., Digman, M., Rigo, J.-M., Hofkens, J., Engelborghs, Y., and Ameloot, M. (2009a). Measuring Diffusion of Lipid-like Probes in Artificial and Natural Membranes by Raster

Image Correlation Spectroscopy (RICS): Use of a Commercial Laser-Scanning Microscope with Analog Detection. *Langmuir*, 25(9):5209–5218.

[Gielen et al., 2009b] Gielen, E., VandeVen, M., Margineanu, A., Dedecker, P., der Auweraer, M. V., Engelborghs, Y., Hofkens, J., and Ameloot, M. (2009b). On the use of Z-scan fluorescence correlation experiments on giant unilamellar vesicles. *Chemical Physics Letters*, 469(1):110–114.

[Gierer and Meinhardt, 1972] Gierer, A. and Meinhardt, H. (1972). A theory of biological pattern formation. *Kybernetik*, 12(1):30–39.

[González et al., 2005] González, J. M., Vélez, M., Jiménez, M., Alfonso, C., Schuck, P., Mingorance, J., Vicente, M., Minton, A. P., and Rivas, G. (2005). Cooperative behavior of Escherichia coli cell-division protein FtsZ assembly involves the preferential cyclization of long single-stranded fibrils. *Proceedings of the National Academy of Sciences of the United States of America*, 102(6):1895–1900.

[Gösch et al., 2000] Gösch, M., Blom, H., Holm, J., Heino, T., and Rigler, R. (2000). Hydrodynamic Flow Profiling in Microchannel Structures by Single Molecule Fluorescence Correlation Spectroscopy. *Analytical Chemistry*, 72(14):3260–3265.

[Gösch and Rigler, 2005] Gösch, M. and Rigler, R. (2005). Fluorescence correlation spectroscopy of molecular motions and kinetics. *Advanced Drug Delivery Reviews*, 57(1):169–190.

[Graves et al., 2015] Graves, E. T., Duboc, C., Fan, J., Stransky, F., Leroux-Coyau, M., and Strick, T. R. (2015). A dynamic DNA-repair complex observed by correlative single-molecule nanomanipulation and fluorescence. *Nature Structural Molecular Biology*, 22:452.

[Gregor et al., 2005] Gregor, I., Patra, D., and Enderlein, J. (2005). Optical Saturation in Fluorescence Correlation Spectroscopy under Continuous-Wave and Pulsed Excitation. *ChemPhysChem*, 6(1):164–170.

[Groves et al., 1997] Groves, J. T., Ulman, N., and Boxer, S. G. (1997). Micropatterning Fluid Lipid Bilayers on Solid Supports. *Science*, 275(5300):651–653.

[Gudmand et al., 2009] Gudmand, M., Fidorra, M., Bjørnholm, T., and Heimburg, T. (2009). Diffusion and Partitioning of Fluorescent Lipid Probes in Phospholipid Monolayers. *Biophysical Journal*, 96(11):4598–4609.

[Guigas and Weiss, 2006] Guigas, G. and Weiss, M. (2006). Size-Dependent Diffusion of Membrane Inclusions. *Biophysical Journal*, 91(7):2393–2398.

[Guigas and Weiss, 2008] Guigas, G. and Weiss, M. (2008). Influence of Hydrophobic Mismatching on Membrane Protein Diffusion. *Biophysical Journal*, 95(3):L25–L27.

[Guo et al., 2008] Guo, L., Har, J. Y., Sankaran, J., Hong, Y., Kannan, B., and Wohland, T. (2008). Molecular Diffusion Measurement in Lipid Bilayers over Wide Concentration Ranges: A Comparative Study. *ChemPhysChem*, 9(5):721–728.

[Haeusser and Margolin, 2016] Haeusser, D. P. and Margolin, W. (2016). Splitsville: structural and functional insights into the dynamic bacterial Z ring. *Nature Reviews Microbiology*, 14:305.

[Haken and Wolf, 2013] Haken, H. and Wolf, H. C. (2013). *Molekülphysik und Quantenchemie: Einführung in die experimentellen und theoretischen Grundlagen.* Springer-Verlag.

[Hamon et al., 2009] Hamon, L., Panda, D., Savarin, P., Joshi, V., Bernhard, J., Mucher, E., Mechulam, A., Curmi, P. A., and Pastré, D. (2009). Mica Surface Promotes the Assembly of Cytoskeletal Proteins. *Langmuir*, 25(6):3331–3335.

[Hänggi and Marchesoni, 2005] Hänggi, P. and Marchesoni, F. (2005). Introduction: 100 years of Brownian motion. *Chaos: An Interdisciplinary Journal of Nonlinear Science*, 15(2):26101.

[Hansen and Harris, 1998a] Hansen, R. L. and Harris, J. M. (1998a). Measuring Reversible Adsorption Kinetics of Small Molecules at Solid/Liquid Interfaces by Total Internal Reflection Fluorescence Correlation Spectroscopy. *Analytical Chemistry*, 70(20):4247–4256.

[Hansen and Harris, 1998b] Hansen, R. L. and Harris, J. M. (1998b). Total Internal Reflection Fluorescence Correlation Spectroscopy for Counting Molecules at Solid/Liquid Interfaces. *Analytical Chemistry*, 70(13):2565–2575.

[Happel and Brenner, 2012] Happel, J. and Brenner, H. (2012). *Low Reynolds number hydrodynamics: with special applications to particulate media*, volume 1. Springer Science Business Media.

[Haranahalli et al., 2016] Haranahalli, K., Tong, S., and Ojima, I. (2016). Recent advances in the discovery and development of antibacterial agents targeting the cell-division protein FtsZ. *Bioorganic Medicinal Chemistry*, 24(24):6354–6369.

[Harlepp et al., 2004] Harlepp, S., Robert, J., Darnton, N. C., and Chatenay, D. (2004). Subnanometric measurements of evanescent wave penetration depth using total internal reflection microscopy combined with fluorescent correlation spectroscopy. *Applied Physics Letters*, 85(17):3917–3919.

[Hassler et al., 2005a] Hassler, K., Anhut, T., Rigler, R., Gösch, M., and Lasser, T. (2005a). High Count Rates with Total Internal Reflection Fluorescence Correlation Spectroscopy. *Biophysical Journal*, 88(1):L01 – L03.

[Hassler et al., 2005b] Hassler, K., Leutenegger, M., Rigler, P., Rao, R., Rigler, R., Gösch, M., and Lasser, T. (2005b). Total internal reflection fluorescence correlation spectroscopy (TIR-FCS) with low background and high count-rate per molecule. *Opt. Express*, 13(19):7415–7423.

[Hassler et al., 2007] Hassler, K., Rigler, P., Blom, H., Rigler, R., Widengren, J., and Lasser, T. (2007). Dynamic disorder in horseradish peroxidase observed with total internal reflection fluorescence correlation spectroscopy. *Opt. Express*, 15(9):5366–5375.

[Haupts et al., 1998] Haupts, U., Maiti, S., Schwille, P., and Webb, W. W. (1998). Dynamics of fluorescence fluctuations in green fluorescent protein observed by fluorescence correlation spectroscopy. *Proceedings of the National Academy of Sciences*, 95(23):13573–13578.

[Haydon et al., 2008] Haydon, D. J., Stokes, N. R., Ure, R., Galbraith, G., Bennett, J. M., Brown, D. R., Baker, P. J., Barynin, V. V., Rice, D. W., Sedelnikova, S. E., Heal, J. R., Sheridan, J. M., Aiwale, S. T., Chauhan, P. K., Srivastava, A., Taneja, A., Collins, I., Errington, J., and Czaplewski, L. G. (2008). An Inhibitor of FtsZ with Potent and Selective Anti-Staphylococcal Activity. *Science*, 321(5896):1673–1675.

[Haynes, 2014] Haynes, W. M. (2014). *CRC handbook of chemistry and physics*. CRC press.

[Hebert et al., 2005] Hebert, B., Costantino, S., and Wiseman, P. W. (2005). Spatiotemporal Image Correlation Spectroscopy (STICS) Theory, Verification, and Application to Protein Velocity Mapping in Living CHO Cells. *Biophysical Journal*, 88(5):3601–3614.

[Heinemann et al., 2012] Heinemann, F., Betaneli, V., Thomas, F. A., and Schwille, P. (2012). Quantifying lipid diffusion by fluorescence correlation spectroscopy: a critical treatise. *Langmuir*, 28(37):13395–13404.

[Heinemann et al., 2013] Heinemann, F., Vogel, S. K., and Schwille, P. (2013). Lateral Membrane Diffusion Modulated by a Minimal Actin Cortex. *Biophysical Journal*, 104(7):1465–1475.

[Heinze et al., 2000] Heinze, K. G., Koltermann, A., and Schwille, P. (2000). Simultaneous two-photon excitation of distinct labels for dual-color fluorescence crosscorrelation analysis. *Proceedings of the National Academy of Sciences*, 97(19):10377–10382.

[Hell et al., 1993] Hell, S., Reiner, G., Cremer, C., and Stelzer, E. H. K. (1993). Aberrations in confocal fluorescence microscopy induced by mismatches in refractive index. *Journal of Microscopy*, 169(3):391–405.

[Hellen and Axelrod, 1987] Hellen, E. H. and Axelrod, D. (1987). Fluorescence emission at dielectric and metal-film interfaces. *Journal of the Optical Society of America B*, 4(3):337–350.

[Herold et al., 2012] Herold, C., Chwastek, G., Schwille, P., and Petrov, E. P. (2012). Efficient Electroformation of Supergiant Unilamellar Vesicles Containing Cationic Lipids on ITO-Coated Electrodes. *Langmuir*, 28(13):5518–5521.

[Herold et al., 2010] Herold, C., Schwille, P., and Petrov, E. P. (2010). DNA Condensation at Freestanding Cationic Lipid Bilayers. *Physical Review Letters*, 104(14):148102.

[Hess et al., 2002] Hess, S. T., Huang, S., Heikal, A. A., and Webb, W. W. (2002). Biological and Chemical Applications of Fluorescence Correlation Spectroscopy: A Review. *Biochemistry*, 41(3):697–705.

[Hlady et al., 1986] Hlady, V., Reinecke, D. R., and Andrade, J. D. (1986). Fluorescence of adsorbed protein layers: I. Quantitation of total internal reflection fluorescence. *Journal of Colloid and Interface Science*, 111(2):555–569.

[Hodnik and Anderluh, 2013] Hodnik, V. and Anderluh, G. (2013). Surface Plasmon Resonance for Measuring Interactions of Proteins with Lipid Membranes. In Kleinschmidt, J. H., editor, *Lipid-Protein Interactions: Methods and Protocols*, pages 23–36. Humana Press, Totowa, NJ.

[Hof et al., 2004] Hof, M., Hutterer, R., and Fidler, V. (2004). *Fluorescence spectroscopy in biology: advanced methods and their applications to membranes, proteins, DNA, and cells*, volume 3. Springer Science Business Media.

[Holden et al., 2014] Holden, S. J., Pengo, T., Meibom, K. L., Fernandez Fernandez, C., Collier, J., and Manley, S. (2014). High throughput 3D super-resolution microscopy reveals Caulobacter crescentus in vivo Z-ring organization. *Proceedings of the National Academy of Sciences*, 111(12):4566–4571.

[Holthuis and Menon, 2014] Holthuis, J. C. M. and Menon, A. K. (2014). Lipid landscapes and pipelines in membrane homeostasis. *Nature*, 510:48.

[Hönig and Moebius, 1991] Hönig, D. and Moebius, D. (1991). Direct visualization of monolayers at the air-water interface by Brewster angle microscopy. *The Journal of Physical Chemistry*, 95(12):4590–4592.

[Hoppe et al., 2012] Hoppe, W., Lohmann, W., Markl, H., and Ziegler, H. (2012). *Biophysics*. Springer Science Business Media.

[Hou et al., 2012] Hou, S., Wieczorek, S. A., Kaminski, T. S., Ziebacz, N., Tabaka, M., Sorto, N. A., Foss, M. H., Shaw, J. T., Thanbichler, M., Weibel, D. B., Nieznanski, K., Holyst, R., and Garstecki, P. (2012). Characterization of Caulobacter crescentus FtsZ Protein Using Dynamic Light Scattering. *Journal of Biological Chemistry*, 287(28):23878–23886.

[Hu and Lutkenhaus, 1999] Hu, Z. and Lutkenhaus, J. (1999). Topological regulation of cell division in Escherichia coli involves rapid pole to pole oscillation of the division inhibitor MinC under the control of MinD and MinE. *Molecular Microbiology*, 34(1):82–90.

[Hu and Lutkenhaus, 2003] Hu, Z. and Lutkenhaus, J. (2003). A conserved sequence at the C-terminus of MinD is required for binding to the membrane and targeting MinC to the septum. *Molecular Microbiology*, 47(2):345–355.

[Huang et al., 2008] Huang, B., Wang, W., Bates, M., and Zhuang, X. (2008). Three-Dimensional Super-Resolution Imaging by Stochastic Optical Reconstruction Microscopy. *Science*, 319(5864):810–813.

[Huang et al., 2015] Huang, H., Simsek, M. F., Jin, W., Pralle, A., Ishibashi, M., and Miwa, Y. (2015). Effect of Receptor Dimerization on Membrane Lipid Raft Structure Continuously Quantified on Single Cells by Camera Based Fluorescence Correlation Spectroscopy. *PLOS ONE*, 10(3):e0121777.

[Huang et al., 1992] Huang, Z., Pearce, K. H., and Thompson, N. L. (1992). Effect of bovine prothrombin fragment 1 on the translational diffusion of phospholipids in Langmuir-Blodgett monolayers. *Biochimica et Biophysica Acta (BBA) - Biomembranes*, 1112(2):259–265.

[Huecas et al., 2008] Huecas, S., Llorca, O., Boskovic, J., Martín-Benito, J., Valpuesta, J. M., and Andreu, J. M. (2008). Energetics and Geometry of FtsZ Polymers: Nucleated Self-Assembly of Single Protofilaments. *Biophysical Journal*, 94(5):1796–1806.

[Hughes et al., 1981] Hughes, B. D., Pailthorpe, B. A., and White, L. R. (1981). The translational and rotational drag on a cylinder moving in a membrane. *Journal of Fluid Mechanics*, 110:349–372.

[Israelachvili et al., 1980] Israelachvili, J. N., Marčelja, S., and Horn, R. G. (1980). Physical principles of membrane organization. *Quarterly Reviews of Biophysics*, 13(2):121–200.

[Izeddin et al., 2012] Izeddin, I., El Beheiry, M., Andilla, J., Ciepielewski, D., Darzacq, X., and Dahan, M. (2012). PSF shaping using adaptive optics for three-dimensional single-molecule super-resolution imaging and tracking. *Optics Express*, 20(5):4957–4967.

[Jerabek-Willemsen et al., 2014] Jerabek-Willemsen, M., André, T., Wanner, R., Roth, H. M., Duhr, S., Baaske, P., and Breitsprecher, D. (2014). MicroScale Thermophoresis: Interaction analysis and beyond. *Journal of Molecular Structure*, 1077:101–113.

[Jerabek-Willemsen et al., 2011] Jerabek-Willemsen, M., Wienken, C. J., Braun, D., Baaske, P., and Duhr, S. (2011). Molecular Interaction Studies Using Microscale Thermophoresis. *ASSAY and Drug Development Technologies*, 9(4):342–353.

[Jiang et al., 2009] Jiang, Y., Nashed-Samuel, Y., Li, C., Liu, W., Pollastrini, J., Mallard, D., Wen, Z.-Q., Fujimori, K., Pallitto, M., Donahue, L., Chu, G., Torraca, G., Vance, A., Mire-Sluis, T., Freund, E., Davis, J., and Narhi, L. (2009). Tungsten-induced protein aggregation: Solution behavior. *Journal of Pharmaceutical Sciences*, 98(12):4695–4710.

[Jones et al., 2012] Jones, E. M., Dubey, M., Camp, P. J., Vernon, B. C., Biernat, J., Mandelkow, E., Majewski, J., and Chi, E. Y. (2012). Interaction of Tau Protein with Model Lipid Membranes Induces Tau Structural Compaction and Membrane Disruption. *Biochemistry*, 51(12):2539–2550.

[Juette et al., 2008] Juette, M. F., Gould, T. J., Lessard, M. D., Mlodzianoski, M. J., Nagpure, B. S., Bennett, B. T., Hess, S. T., and Bewersdorf, J. (2008). Three-dimensional sub-100 nm resolution fluorescence microscopy of thick samples. *Nature Methods*, 5:527.

[Juette et al., 2014] Juette, M. F., Terry, D. S., Wasserman, M. R., Zhou, Z., Altman, R. B., Zheng, Q., and Blanchard, S. C. (2014). The bright future of single-molecule fluorescence imaging. *Current Opinion in Chemical Biology*, 20:103–111.

[Junghans et al., 2016] Junghans, C., Schmitt, F.-J., Vukojević, V., and Friedrich, T. (2016). Diffusion behavior of the fluorescent proteins eGFP and Dreiklang in solvents of different viscosity monitored by fluorescence correlation spectroscopy. *Optofluid. Microfluid. Nanofluid*, 3:27–34.

[Jungmann et al., 2016] Jungmann, R., Avendano, M. S., Dai, M., Woehrstein, J. B., Agasti, S. S., Feiger, Z., Rodal, A., and Yin, P. (2016). Quantitative super-resolution imaging with qPAINT. *Nat Meth*, 13(5):439–442.

[Jungmann et al., 2010] Jungmann, R., Steinhauer, C., Scheible, M., Kuzyk, A., Tinnefeld, P., and Simmel, F. C. (2010). Single-Molecule Kinetics and Super-Resolution Microscopy by Fluorescence Imaging of Transient Binding on DNA Origami. *Nano Letters*, 10(11):4756–4761.

[Kahya et al., 2001] Kahya, N., Pécheur, E.-I., de Boeij, W. P., Wiersma, D. A., and Hoekstra, D. (2001). Reconstitution of Membrane Proteins into Giant Unilamellar Vesicles via Peptide-Induced Fusion. *Biophysical Journal*, 81(3):1464–1474.

[Kahya and Schwille, 2006] Kahya, N. and Schwille, P. (2006). Fluorescence correlation studies of lipid domains in model membranes (Review). *Molecular Membrane Biology*, 23(1):29–39.

[Kannan et al., 2007] Kannan, B., Guo, L., Sudhaharan, T., Ahmed, S., Maruyama, I., and Wohland, T. (2007). Spatially Resolved Total Internal Reflection Fluorescence Correlation Microscopy Using an Electron Multiplying Charge-Coupled Device Camera. *Analytical Chemistry*, 79(12):4463–4470.

[Kapusta et al., 2007] Kapusta, P., Wahl, M., Benda, A., Hof, M., and Enderlein, J. (2007). Fluorescence Lifetime Correlation Spectroscopy. *Journal of Fluorescence*, 17(1):43–48.

[Kapusta et al., 2015] Kapusta, P., Wahl, M., and Erdmann, R. (2015). *Advanced Photon Counting*, volume 15. Springer.

[Karedla et al., 2014] Karedla, N., Chizhik, A. I., Gregor, I., Chizhik, A. M., Schulz, O., and Enderlein, J. (2014). Single-Molecule Metal-Induced Energy Transfer (smMIET): Resolving Nanometer Distances at the Single-Molecule Level. *ChemPhysChem*, 15(4):705–711.

[Kashin et al., 2011] Kashin, V. V., Shakirov, K. M., and Poshevneva, A. I. (2011). The capillary constant in calculating the surface tension of liquids. *Steel in Translation*, 41(10):795–798.

[Kastrup et al., 2005] Kastrup, L., Blom, H., Eggeling, C., and Hell, S. W. (2005). Fluorescence Fluctuation Spectroscopy in Subdiffraction Focal Volumes. *Physical Review Letters*, 94(17):178104.

[Ke and Naumann, 2001] Ke, P. C. and Naumann, C. A. (2001). Single Molecule Fluorescence Imaging of Phospholipid Monolayers at the AirâĹŠWater Interface. *Langmuir*, 17(12):3727–3733.

[Kelsoe and Haynes, 2017] Kelsoe, G. and Haynes, B. F. (2017). Host controls of HIV broadly neutralizing antibody development. *Immunological Reviews*, 275(1):79–88.

[Kestin et al., 1978] Kestin, J., Sokolov, M., and Wakeham, W. A. (1978). Viscosity of liquid water in the range -8 C to 150 C. *Journal of Physical and Chemical Reference Data*, 7(3):941–948.

[Khmelinskaia et al., 2016] Khmelinskaia, A., Franquelim, H. G., Petrov, E. P., and Schwille, P. (2016). Effect of anchor positioning on binding and diffusion of elongated

3D DNA nanostructures on lipid membranes. *Journal of Physics D: Applied Physics*, 49(19):194001.

[Kibron, 2018] Kibron (2018). http://www.kibron.com/media/tuotekuvat/29/broscure.pdf (Accessed: 2018-03-01).

[Kiekebusch et al., 2012] Kiekebusch, D., Michie, K. A., Essen, L.-O., Löwe, J., and Thanbichler, M. (2012). Localized Dimerization and Nucleoid Binding Drive Gradient Formation by the Bacterial Cell Division Inhibitor MipZ. *Molecular Cell*, 46(3):245–259.

[Kiekebusch and Thanbichler, 2014] Kiekebusch, D. and Thanbichler, M. (2014). Spatiotemporal organization of microbial cells by protein concentration gradients. *Trends in Microbiology*, 22(2):65–73.

[Kiese et al., 2008] Kiese, S., Papppenberger, A., Friess, W., and Mahler, H.-C. (2008). Shaken, not stirred: Mechanical stress testing of an IgG1 antibody. *Journal of Pharmaceutical Sciences*, 97(10):4347–4366.

[Kim and Yu, 1992] Kim, S. and Yu, H. (1992). Lateral diffusion of amphiphiles and macromolecules at the air/water interface. *The Journal of Physical Chemistry*, 96(10):4034–4040.

[Kim et al., 2007] Kim, S. A., Heinze, K. G., and Schwille, P. (2007). Fluorescence correlation spectroscopy in living cells. *Nature Methods*, 4:963.

[Kim et al., 2012] Kim, Y.-C., Park, J.-H., and Prausnitz, M. R. (2012). Microneedles for drug and vaccine delivery. *Advanced Drug Delivery Reviews*, 64(14):1547–1568.

[Kinjo and Rigler, 1995] Kinjo, M. and Rigler, R. (1995). Ultrasensitive hybridization analysis using fluorescence correlation spectroscopy. *Nucleic Acids Research*, 23(10):1795–1799.

[Kolin et al., 2006a] Kolin, D. L., Costantino, S., and Wiseman, P. W. (2006a). Sampling Effects, Noise, and Photobleaching in Temporal Image Correlation Spectroscopy. *Biophysical Journal*, 90(2):628–639.

[Kolin et al., 2006b] Kolin, D. L., Ronis, D., and Wiseman, P. W. (2006b). k-Space Image Correlation Spectroscopy: A Method for Accurate Transport Measurements Independent of Fluorophore Photophysics. *Biophysical Journal*, 91(8):3061–3075.

[Kooyman et al., 2008] Kooyman, R. P. H., Corn, R. M., Wark, A., Lee, H. J., Gedig, E., Engbers, G., Walstrom, L., de Mol, N. J., Hall, D. R., Yager, P., Chinowsky, T., Fu, E., Nelson, K., McWhirter, A., Fischer, M. J. E., Lokate, A. M. C., Beusink, J. B., Pruijn, G. J. M., Knoll, W., Kasry, A., Liu, J., Neumann, T., Niu, L., Park, H., Paulsen, H., Robelek, R., Yu, F., Schuck, P., Schasfoort, R. B. M., and Tudos, A. J. (2008). *Handbook of Surface Plasmon Resonance*. The Royal Society of Chemistry.

[Krichevsky and Bonnet, 2002] Krichevsky, O. and Bonnet, G. (2002). Fluorescence correlation spectroscopy: the technique and its applications. *Reports on Progress in Physics*, 65(2):251.

[Kriegsmann et al., 2009] Kriegsmann, J., Gregor, I., von der Hocht, I., Klare, J., Engelhard, M., Enderlein, J., and Fitter, J. (2009). Translational Diffusion and Interaction of a Photoreceptor and Its Cognate Transducer Observed in Giant Unilamellar Vesicles by Using Dual-Focus FCS. *ChemBioChem*, 10(11):1823–1829.

[Kubitscheck, 2017] Kubitscheck, U. (2017). *Fluorescence microscopy: from principles to biological applications*. John Wiley Sons.

[Kubitscheck et al., 2005] Kubitscheck, U., Grünwald, D., Hoekstra, A., Rohleder, D., Kues, T., Siebrasse, J. P., and Peters, R. (2005). Nuclear transport of single molecules. *The Journal of Cell Biology*, 168(2):233– 243.

[Kubo et al., 2001] Kubo, I., Adachi, S., Maeda, H., and Seki, A. (2001). Phosphatidylcholine monolayers observed with Brewster angle microscopy and π-A isotherms. *Thin Solid Films*, 393(1):80–85.

[Kubo, 1966] Kubo, R. (1966). The fluctuation-dissipation theorem. *Reports on Progress in Physics*, 29(1):255.

[Kyoung and Sheets, 2006] Kyoung, M. and Sheets, E. D. (2006). Manipulating and probing the spatio-temporal dynamics of nanoparticles near surfaces.

[Kyoung and Sheets, 2008] Kyoung, M. and Sheets, E. D. (2008). Vesicle Diffusion Close to a Membrane: Intermembrane Interactions Measured with Fluorescence Correlation Spectroscopy. *Biophysical Journal*, 95(12):5789–5797.

[Lagerholm and Thompson, 1998] Lagerholm, B. C. and Thompson, N. L. (1998). Theory for Ligand Rebinding at Cell Membrane Surfaces. *Biophysical Journal*, 74(3):1215–1228.

[Lagerholm and Thompson, 2000] Lagerholm, B. C. and Thompson, N. L. (2000). Temporal Dependence of Ligand Dissociation and Rebinding at Planar Surfaces. *The Journal of Physical Chemistry B*, 104(4):863–868.

[Lagny and Bassereau, 2015] Lagny, T. J. and Bassereau, P. (2015). Bioinspired membrane-based systems for a physical approach of cell organization and dynamics: usefulness and limitations. *Interface Focus*, 5(4).

[Lakowicz, 2006] Lakowicz, J. R. (2006). *Principles of Fluorescence Spectroscopy*. Springer, Boston, MA, 3rd edition.

[Lang and Schwarz, 2007] Lang, B. E. and Schwarz, F. P. (2007). Thermodynamic dependence of DNA/DNA and DNA/RNA hybridization reactions on temperature and ionic strength. *Biophysical Chemistry*, 131(1):96–104.

[Langecker et al., 2014] Langecker, M., Arnaut, V., List, J., and Simmel, F. C. (2014). DNA Nanostructures Interacting with Lipid Bilayer Membranes. *Accounts of Chemical Research*, 47(6):1807–1815.

[Langecker et al., 2012] Langecker, M., Arnaut, V., Martin, T. G., List, J., Renner, S., Mayer, M., Dietz, H., and Simmel, F. C. (2012). Synthetic Lipid Membrane Channels Formed by Designed DNA Nanostructures. *Science*, 338(6109):932–936.

[Langowski and Bryan, 1991] Langowski, J. and Bryan, R. (1991). Maximum entropy analysis of photon correlation spectroscopy data using a Bayesian estimate for the regularization parameter. *Macromolecules*, 24(23):6346–6348.

[Lasker et al., 2016] Lasker, K., Mann, T. H., and Shapiro, L. (2016). An intracellular compass spatially coordinates cell cycle modules in Caulobacter crescentus. *Current Opinion in Microbiology*, 33:131–139.

[Laurence et al., 2007] Laurence, T. A., Kwon, Y., Yin, E., Hollars, C. W., Camarero, J. A., and Barsky, D. (2007). Correlation Spectroscopy of Minor Fluorescent Species: Signal Purification and Distribution Analysis. *Biophysical Journal*, 92(6):2184–2198.

[Lehmann et al., 2015] Lehmann, S., Seiffert, S., and Richtering, W. (2015). Refractive Index Mismatch Can Misindicate Anomalous Diffusion in Single-Focus Fluorescence Correlation Spectroscopy. *Macromolecular Chemistry and Physics*, 216(2):156–163.

[Leipe et al., 2002] Leipe, D. D., Wolf, Y. I., Koonin, E. V., and Aravind, L. (2002). Classification and evolution of P-loop GTPases and related ATPases11Edited by J. Thornton. *Journal of Molecular Biology*, 317(1):41–72.

[Leung et al., 2004] Leung, A. K. W., Lucile White, E., Ross, L. J., Reynolds, R. C., DeVito, J. A., and Borhani, D. W. (2004). Structure of Mycobacterium tuberculosis FtsZ Reveals Unexpected, G Protein-like Conformational Switches. *Journal of Molecular Biology*, 342(3):953–970.

[Leutenegger et al., 2006] Leutenegger, M., Blom, H., Widengren, J., Eggeling, C., Gösch, M., Leitgeb, R. A., Lasser, T., GoÌĹsch, M., Leitgeb, R. A., and Lasser, T. (2006). Dual-color total internal reflection fluorescence cross-correlation spectroscopy. *Journal of Biomedical Optics*, 11(4):40502–40503.

[Leutenegger et al., 2012] Leutenegger, M., Ringemann, C., Lasser, T., Hell, S. W., and Eggeling, C. (2012). Fluorescence correlation spectroscopy with a total internal reflection fluorescence STED microscope (TIRF-STED-FCS). *Opt. Express*, 20(5):5243–5263.

[Li et al., 2017] Li, J., Dong, C., and Ren, J. (2017). Strategies to reduce detection volume of fluorescence correlation spectroscopy (FCS) to realize physiological concentration measurements. *TrAC Trends in Analytical Chemistry*, 89:181–189.

[Li et al., 2010] Li, J. T., Rank, M. A., Squillace, D. L., Kita, H., and James T. Li Diane L. Squillace, and Hirohito Kita, M. A. R. (2010). Ovalbumin content of influenza vaccines. *J Allergy Clin Immunol*, 125(6):1412–1414.

[Li et al., 2015] Li, W., Cowley, A., Uludag, M., Gur, T., McWilliam, H., Squizzato, S., Park, Y. M., Buso, N., and Lopez, R. (2015). The EMBL-EBI bioinformatics web and programmatic tools framework. *Nucleic acids research*, 43(W1):W580–4.

[Lieto et al., 2003] Lieto, A. M., Cush, R. C., and Thompson, N. L. (2003). Ligand-Receptor Kinetics Measured by Total Internal Reflection with Fluorescence Correlation Spectroscopy. *Biophysical Journal*, 85(5):3294–3302.

[Lieto and Thompson, 2004] Lieto, A. M. and Thompson, N. L. (2004). Total Internal Reflection with Fluorescence Correlation Spectroscopy: Nonfluorescent Competitors. *Biophysical Journal*, 87(2):1268–1278.

[Lim et al., 2013] Lim, K. H., Huang, H., Pralle, A., and Park, S. (2013). Stable, high-affinity streptavidin monomer for protein labeling and monovalent biotin detection. *Biotechnology and Bioengineering*, 110(1):57–67.

[Liu and Fletcher, 2009] Liu, A. P. and Fletcher, D. A. (2009). Biology under construction: in vitro reconstitution of cellular function. *Nature Reviews Molecular Cell Biology*, 10:644.

[Liu et al., 2009] Liu, R., Garcia-Manyes, S., Sarkar, A., Badilla, C. L., and Fernández, J. M. (2009). Mechanical Characterization of Protein L in the Low-Force Regime by Electromagnetic Tweezers/Evanescent Nanometry. *Biophysical Journal*, 96(9):3810–3821.

[Livesey and Brochon, 1987] Livesey, A. K. and Brochon, J. C. (1987). Analyzing the Distribution of Decay Constants in Pulse-Fluorimetry Using the Maximum Entropy Method. *Biophysical Journal*, 52(5):693–706.

[Loose et al., 2008] Loose, M., Fischer-Friedrich, E., Ries, J., Kruse, K., and Schwille, P. (2008). Spatial Regulators for Bacterial Cell Division Self-Organize into Surface Waves in Vitro. *Science*, 320(5877):789–792.

[Loose et al., 2011] Loose, M., Kruse, K., and Schwille, P. (2011). Protein Self-Organization: Lessons from the Min System. *Annual Review of Biophysics*, 40(1):315–336.

[Loose and Mitchison, 2013] Loose, M. and Mitchison, T. J. (2013). The bacterial cell division proteins FtsA and FtsZ self-organize into dynamic cytoskeletal patterns. *Nature Cell Biology*, 16:38.

[Lorenz et al., 2016] Lorenz, R., Wolfinger, M. T., Tanzer, A., and Hofacker, I. L. (2016). Predicting RNA secondary structures from sequence and probing data. *Methods*, 103:86–98.

[Loura et al., 2003] Loura, L. M. S., de Almeida, R. F. M., Coutinho, A., and Prieto, M. (2003). Interaction of peptides with binary phospholipid membranes: application of fluorescence methodologies. *Chemistry and Physics of Lipids*, 122(1):77–96.

[Löwe and Amos, 1998] Löwe, J. and Amos, L. A. (1998). Crystal structure of the bacterial cell-division protein FtsZ. *Nature*, 391:203.

[Ludwig et al., 1986] Ludwig, D. S., Ribi, H. O., Schoolnik, G. K., and Kornberg, R. D. (1986). Two-dimensional crystals of cholera toxin B-subunit-receptor complexes: projected structure at 17-A resolution. *Proceedings of the National Academy of Sciences*, 83(22):8585–8588.

[Lukosz and Kunz, 1977a] Lukosz, W. and Kunz, R. E. (1977a). Light emission by magnetic and electric dipoles close to a plane dielectric interface. II. Radiation patterns of perpendicular oriented dipoles. *Journal of the Optical Society of America*, 67(12):1615–1619.

[Lukosz and Kunz, 1977b] Lukosz, W. and Kunz, R. E. (1977b). Light emission by magnetic and electric dipoles close to a plane interface. I. Total radiated power. *Journal of the Optical Society of America*, 67(12):1607–1615.

[Lutkenhaus, 2007] Lutkenhaus, J. (2007). Assembly Dynamics of the Bacterial MinCDE System and Spatial Regulation of the Z Ring. *Annual Review of Biochemistry*, 76(1):539–562.

[Lutkenhaus et al., 2012] Lutkenhaus, J., Pichoff, S., and Du, S. (2012). Bacterial cytokinesis: From Z ring to divisome. *Cytoskeleton*, 69(10):778–790.

[Ma and Margolin, 1999] Ma, X. and Margolin, W. (1999). Genetic and Functional Analyses of the Conserved C-Terminal Core Domain of Escherichia coli FtsZ. *Journal of Bacteriology*, 181(24):7531–7544.

[Maa and Hsu, 1997] Maa, Y.-F. and Hsu, C. C. (1997). Protein denaturation by combined effect of shear and air-liquid interface. *Biotechnology and Bioengineering*, 54(6):503–512.

[Macedo and Litovitz, 1965] Macedo, P. B. and Litovitz, T. A. (1965). On the Relative Roles of Free Volume and Activation Energy in the Viscosity of Liquids. *The Journal of Chemical Physics*, 42(1):245–256.

[Machán and Hof, 2010] Machán, R. and Hof, M. (2010). Lipid diffusion in planar membranes investigated by fluorescence correlation spectroscopy. *Biochimica et Biophysica Acta (BBA) - Biomembranes*, 1798(7):1377–1391.

[Machán and Wohland, 2014] Machán, R. and Wohland, T. (2014). Recent applications of fluorescence correlation spectroscopy in live systems. *FEBS Letters*, 588(19):3571–3584.

[Magde et al., 1972] Magde, D., Elson, E., and Webb, W. W. (1972). Thermodynamic Fluctuations in a Reacting System - Measurement by Fluorescence Correlation Spectroscopy. *Physical Review Letters*, 29(11):705–708.

[Magde et al., 1974] Magde, D., Elson, E. L., and Webb, W. W. (1974). Fluorescence correlation spectroscopy. II. An experimental realization. *Biopolymers*, 13(1):29–61.

[Magde et al., 1978] Magde, D., Webb, W. W., and Elson, E. L. (1978). Fluorescence correlation spectroscopy. III. Uniform translation and laminar flow. *Biopolymers*, 17(2):361–376.

[Majewski and Stec, 2010] Majewski, J. and Stec, B. (2010). X-ray scattering studies of model lipid membrane interacting with purothionin provide support for a previously proposed mechanism of membrane lysis. *European Biophysics Journal*, 39(8):1155–1165.

[Maltseva et al., 2005] Maltseva, E., Kerth, A., Blume, A., Möhwald, H., and Brezesinski, G. (2005). Adsorption of Amyloid β (1-40) Peptide at Phospholipid Monolayers. *ChemBioChem*, 6(10):1817–1824.

[Mandal et al., 2016] Mandal, P., Noutsi, P., and Chaieb, S. (2016). Cholesterol Depletion from a Ceramide/Cholesterol Mixed Monolayer: A Brewster Angle Microscope Study. *Scientific Reports*, 6:26907.

[Margolin, 2012] Margolin, W. (2012). The Price of Tags in Protein Localization Studies. *Journal of Bacteriology*, 194(23):6369–6371.

[Marsh, 2013] Marsh, D. (2013). *Handbook of lipid bilayers*. CRC Press.

[Mathews, 2006] Mathews, D. H. (2006). Revolutions in RNA Secondary Structure Prediction. *Journal of Molecular Biology*, 359(3):526–532.

[Matos et al., 2010] Matos, P. M., Franquelim, H. G., Castanho, M. A. R. B., and Santos, N. C. (2010). Quantitative assessment of peptide-lipid interactions.: Ubiquitous fluorescence methodologies. *Biochimica et Biophysica Acta (BBA) - Biomembranes*, 1798(11):1999–2012.

[Matsui et al., 2012] Matsui, T., Yamane, J., Mogi, N., Yamaguchi, H., Takemoto, H., Yao, M., and Tanaka, I. (2012). Structural reorganization of the bacterial cell-division protein FtsZ from Staphylococcus aureus. *Acta Crystallographica Section D*, 68(9):1175–1188.

[Matsumoto and Nishimura, 1998] Matsumoto, M. and Nishimura, T. (1998). Mersenne Twister: A 623-dimensionally Equidistributed Uniform Pseudo-random Number Generator. *ACM Trans. Model. Comput. Simul.*, 8(1):3–30.

[Mattheyses and Axelrod, 2006] Mattheyses, A. L. and Axelrod, D. (2006). Direct measurement of the evanescent field profile produced by objective-based total internal reflection fluorescence. *Journal of Biomedical Optics*, 11(1):14006–14007.

[May, 1976] May, R. M. (1976). Simple mathematical models with very complicated dynamics. *Nature*, 261:459.

[Mazo, 2002] Mazo, R. M. (2002). *Brownian motion: fluctuations, dynamics, and applications*, volume 112. Oxford University Press on Demand.

[McCain and Harris, 2003] McCain, K. S. and Harris, J. M. (2003). Total Internal Reflection Fluorescence-Correlation Spectroscopy Study of Molecular Transport in Thin Sol-Gel Films. *Analytical Chemistry*, 75(14):3616–3624.

[McCain et al., 2004a] McCain, K. S., Schluesche, P., and Harris, J. M. (2004a). Modifying the Adsorption Behavior of Polyamidoamine Dendrimers at Silica Surfaces Investigated by Total Internal Reflection Fluorescence Correlation Spectroscopy. *Analytical Chemistry*, 76(4):930–938.

[McCain et al., 2004b] McCain, K. S., Schluesche, P., and Harris, J. M. (2004b). Poly(amidoamine) Dendrimers as Nanoscale Diffusion Probes in Sol-Gel Films Investigated by Total Internal Reflection Fluorescence Spectroscopy. *Analytical Chemistry*, 76(4):939–946.

[McGorty et al., 2013] McGorty, R., Kamiyama, D., and Huang, B. (2013). Active microscope stabilization in three dimensions using image correlation. *Optical Nanoscopy*, 2(1):3.

[McWilliam et al., 2013] McWilliam, H., Li, W., Uludag, M., Squizzato, S., Park, Y. M., Buso, N., Cowley, A. P., and Lopez, R. (2013). Analysis Tool Web Services from the EMBL-EBI. *Nucleic acids research*, 41(Web Server issue):W597–600.

[Meister et al., 2006] Meister, A., Nicolini, C., Waldmann, H., Kuhlmann, J., Kerth, A., Winter, R., and Blume, A. (2006). Insertion of Lipidated Ras Proteins into Lipid Monolayers Studied by Infrared Reflection Absorption Spectroscopy (IRRAS). *Biophysical Journal*, 91(4):1388–1401.

[Méléard et al., 2009] Méléard, P., Bagatolli, L. A., and Pott, T. B. T. M. i. E. (2009). Chapter 9 - Giant Unilamellar Vesicle Electroformation: From Lipid Mixtures to Native Membranes Under Physiological Conditions. In *Methods in Enzymology*, volume 465, pages 161–176. Academic Press.

[Melo et al., 2011] Melo, A. M., Prieto, M., and Coutinho, A. (2011). The effect of variable liposome brightness on quantifying lipid-protein interactions using fluorescence correlation spectroscopy. *Biochimica et Biophysica Acta (BBA) - Biomembranes*, 1808(10):2559–2568.

[Melo et al., 2014] Melo, A. M., Prieto, M., and Coutinho, A. (2014). Quantifying Lipid-Protein Interaction by Fluorescence Correlation Spectroscopy (FCS). In Engelborghs, Y. and Visser, A. J. W. G., editors, *Fluorescence Spectroscopy and Microscopy: Methods and Protocols*, pages 575–595. Humana Press, Totowa, NJ.

[Merritt et al., 1997] Merritt, E. A., Sarfaty, S., Hol, W. I. M. G. J., Jobling, M. G., Holmes, R. K., Chang, T., and Hirst, T. R. (1997). Structural studies of receptor binding by cholera toxin mutants. *Protein Science*, 6(7):1516–1528.

[Meseth et al., 1999] Meseth, U., Wohland, T., Rigler, R., and Vogel, H. (1999). Resolution of Fluorescence Correlation Measurements. *Biophysical Journal*, 76(3):1619–1631.

[Michelman-Ribeiro et al., 2009] Michelman-Ribeiro, A., Mazza, D., Rosales, T., Stasevich, T. J., Boukari, H., Rishi, V., Vinson, C., Knutson, J. R., and McNally, J. G. (2009). Direct Measurement of Association and Dissociation Rates of DNA Binding in Live Cells by Fluorescence Correlation Spectroscopy. *Biophysical Journal*, 97(1):337–346.

[Mikuni et al., 2015] Mikuni, S., Kodama, K., Sasaki, A., Kohira, N., Maki, H., Munetomo, M., Maenaka, K., and Kinjo, M. (2015). Screening for FtsZ Dimerization Inhibitors Using Fluorescence Cross-Correlation Spectroscopy and Surface Resonance Plasmon Analysis. *PLOS ONE*, 10(7):e0130933.

[Mingorance et al., 2005] Mingorance, J., Tadros, M., Vicente, M., González, J. M., Rivas, G., and Vélez, M. (2005). Visualization of Single Escherichia coli FtsZ Filament Dynamics with Atomic Force Microscopy. *Journal of Biological Chemistry*, 280(21):20909–20914.

[Minsky, 1957] Minsky, M. (1957). Microscopy apparatus, U.S. Patent no. 3,013,467.

[Mitsuhashi, 1996] Mitsuhashi, M. (1996). Technical report: Part 1. Basic requirements for designing optimal oligonucleotide probe sequences. *Journal of Clinical Laboratory Analysis*, 10(5):277–284.

[Miyagi et al., 2017] Miyagi, A., Ramm, B., Schwille, P., and Scheuring, S. (2017). High-speed AFM reveals the inner workings of the MinDE protein oscillator. *Nano Letters*.

[Mondal and Diaspro, 2013] Mondal, P. P. and Diaspro, A. (2013). *Fundamentals of fluorescence microscopy: exploring life with light*. Springer Science Business Media.

[Montecinos-Franjola et al., 2012] Montecinos-Franjola, F., Ross, J. A., Sánchez, S. A., Brunet, J. E., Lagos, R., Jameson, D. M., and Monasterio, O. (2012). Studies on the Dissociation and Urea-Induced Unfolding of FtsZ Support the Dimer Nucleus Polymerization Mechanism. *Biophysical Journal*, 102(9):2176–2185.

[Montero et al., 2008] Montero, M., van Houten, N. E., Wang, X., and Scott, J. K. (2008). The Membrane-Proximal External Region of the Human Immunodeficiency Virus Type 1 Envelope: Dominant Site of Antibody Neutralization and Target for Vaccine Design. *Microbiology and Molecular Biology Reviews*, 72(1):54–84.

[Monterroso et al., 2012] Monterroso, B., Ahijado-Guzmán, R., Reija, B., Alfonso, C., Zorrilla, S., Minton, A. P., and Rivas, G. (2012). Mg2+-Linked Self-Assembly of FtsZ in the Presence of GTP or a GTP Analogue Involves the Concerted Formation of a Narrow Size Distribution of Oligomeric Species. *Biochemistry*, 51(22):4541–4550.

[Monterroso et al., 2013] Monterroso, B., Alfonso, C., Zorrilla, S., and Rivas, G. (2013). Combined analytical ultracentrifugation, light scattering and fluorescence spectroscopy studies on the functional associations of the bacterial division FtsZ protein. *Methods*, 59(3):349–362.

[Mouritsen and Bagatolli, 2015] Mouritsen, O. G. and Bagatolli, L. A. (2015). *Life-as a matter of fat: lipids in a membrane biophysics perspective*. Springer.

[Mukherjee and Lutkenhaus, 1994] Mukherjee, A. and Lutkenhaus, J. (1994). Guanine nucleotide-dependent assembly of FtsZ into filaments. *Journal of Bacteriology*, 176(9):2754–2758.

[Mukherjee and Lutkenhaus, 1999] Mukherjee, A. and Lutkenhaus, J. (1999). Analysis of FtsZ Assembly by Light Scattering and Determination of the Role of Divalent Metal Cations. *Journal of Bacteriology*, 181(3):823–832.

[Müller et al., 2005] Müller, B. K., Zaychikov, E., Bräuchle, C., and Lamb, D. C. (2005). Pulsed Interleaved Excitation. *Biophysical Journal*, 89(5):3508–3522.

[Müller, 2012] Müller, P. (2012). *Fluoreszenzfluktuationsmikroskopie mit Totalreflexionsanregung zur zeit- und ortsaufgelösten Messung an Biomembranen unter Verwendung einer CMOS Kamera.* Diplomarbeit, Technische Universität Dresden.

[Murray, 2007] Murray, B. S. (2007). Stabilization of bubbles and foams. *Current Opinion in Colloid Interface Science*, 12(4):232–241.

[Mütze et al., 2010a] Mütze, J., Ohrt, T., Petrášek, Z., and Schwille, P. (2010a). In Vivo Fluorescence Correlation and Cross-Correlation Spectroscopy. In Gräslund, A., Rigler, R., and Widengren, J., editors, *Single Molecule Spectroscopy in Chemistry, Physics and Biology: Nobel Symposium*, pages 139–154. Springer Berlin Heidelberg, Berlin, Heidelberg.

[Mütze et al., 2010b] Mütze, J., Ohrt, T., and Schwille, P. (2010b). Fluorescence correlation spectroscopy in vivo. *Laser Photonics Reviews*, 5(1):52–67.

[Nagai et al., 2002] Nagai, T., Ibata, K., Park, E. S., Kubota, M., Mikoshiba, K., and Miyawaki, A. (2002). A variant of yellow fluorescent protein with fast and efficient maturation for cell-biological applications. *Nature Biotechnology*, 20:87.

[Nair et al., 2011] Nair, P. M., Salaita, K., Petit, R. S., and Groves, J. T. (2011). Using patterned supported lipid membranes to investigate the role of receptor organization in intercellular signaling. *Nature Protocols*, 6:523.

[Nath et al., 2007] Nath, A., Atkins, W. M., and Sligar, S. G. (2007). Applications of Phospholipid Bilayer Nanodiscs in the Study of Membranes and Membrane Proteins. *Biochemistry*, 46(8):2059–2069.

[Nguyen et al., 2015] Nguyen, H. H., Park, J., Kang, S., and Kim, M. (2015). Surface Plasmon Resonance: A Versatile Technique for Biosensor Applications.

[Nguyen et al., 2012] Nguyen, T. T., Swift, J. L., and Cramb, D. T. (2012). Fluorescence Correlation Spectroscopy: The Measurement of Molecular Binding. In Geddes, C. D., editor, *Reviews in Fluorescence 2010*, pages 45–66. Springer New York, New York, NY.

[Niederauer, 2018] Niederauer, C. (2018). *Direct Characterization of the Evanescent Field in Objective-Type Total Internal Reflection Microscopy.* Master's thesis, Ludwig-Maximilians-Universität München.

[Nielsen et al., 2007] Nielsen, L. K., Bjørnholm, T., and Mouritsen, O. G. (2007). Thermodynamic and Real-Space Structural Evidence of a 2D Critical Point in Phospholipid Monolayers. *Langmuir*, 23(23):11684–11692.

[Nielsen and Otzen, 2013] Nielsen, S. B. and Otzen, D. E. (2013). Quartz Crystal Microbalances as Tools for Probing Protein–Membrane Interactions. In Kleinschmidt, J. H., editor, *Lipid-Protein Interactions: Methods and Protocols*, pages 1–21. Humana Press, Totowa, NJ.

[Nieto-Suárez et al., 2008] Nieto-Suárez, M., Vila-Romeu, N., and Prieto, I. (2008). Behaviour of insulin Langmuir monolayers at the air-water interface under various conditions. *Thin Solid Films*, 516(24):8873–8879.

[Nyeo and Chu, 1989] Nyeo, S. L. and Chu, B. (1989). Maximum-entropy analysis of photon correlation spectroscopy data. *Macromolecules*, 22(10):3998–4009.

[Oheim and Schapper, 2005] Oheim, M. and Schapper, F. (2005). Non-linear evanescent-field imaging. *Journal of Physics D: Applied Physics*, 38(10):R185.

[Ohsugi et al., 2006] Ohsugi, Y., Saito, K., Tamura, M., and Kinjo, M. (2006). Lateral Mobility of Membrane-Binding Proteins in Living Cells Measured by Total Internal Reflection Fluorescence Correlation Spectroscopy. *Biophysical Journal*, 91(9):3456–3464.

[Oliva et al., 2004] Oliva, M. A., Cordell, S. C., and Löwe, J. (2004). Structural insights into FtsZ protofilament formation. *Nature Structural Molecular Biology*, 11(12):1243.

[Oliva et al., 2007] Oliva, M. A., Trambaiolo, D., and Löwe, J. (2007). Structural Insights into the Conformational Variability of FtsZ. *Journal of Molecular Biology*, 373(5):1229–1242.

[Oliver, 1979] Oliver, C. J. (1979). Spectral analysis with short data batches (photon correlation spectroscopy). *Journal of Physics A: Mathematical and General*, 12(4):591.

[Oreopoulos and Yip, 2008] Oreopoulos, J. and Yip, C. M. (2008). Combined scanning probe and total internal reflection fluorescence microscopy. *Methods*, 46(1):2–10.

[Ortega Arroyo et al., 2014] Ortega Arroyo, J., Andrecka, J., Spillane, K. M., Billington, N., Takagi, Y., Sellers, J. R., and Kukura, P. (2014). Label-Free, All-Optical Detection, Imaging, and Tracking of a Single Protein. *Nano Letters*, 14(4):2065–2070.

[Osawa et al., 2008] Osawa, M., Anderson, D. E., and Erickson, H. P. (2008). Reconstitution of Contractile FtsZ Rings in Liposomes. *Science*, 320(5877):792–794.

[Otosu and Yamaguchi, 2017] Otosu, T. and Yamaguchi, S. (2017). Communication: Development of standing evanescent-wave fluorescence correlation spectroscopy and its application to the lateral diffusion of lipids in a supported lipid bilayer. *The Journal of Chemical Physics*, 147(4):41101.

[Owczarzy et al., 2003] Owczarzy, R., Dunietz, I., Behlke, M. A., Klotz, I. M., and Walder, J. A. (2003). Thermodynamic treatment of oligonucleotide duplex-simplex equilibria. *Proceedings of the National Academy of Sciences*, 100(25):14840–14845.

[Owczarzy et al., 2008] Owczarzy, R., Moreira, B. G., You, Y., Behlke, M. A., and Walder, J. A. (2008). Predicting Stability of DNA Duplexes in Solutions Containing Magnesium and Monovalent Cations. *Biochemistry*, 47(19):5336–5353.

[Paddock, 2014] Paddock, S. W. (2014). *Confocal Microscopy*. Springer.

[Papadakis et al., 2014] Papadakis, C. M., Košovan, P., Richtering, W., and Wöll, D. (2014). Polymers in focus: fluorescence correlation spectroscopy. *Colloid and Polymer Science*, 292(10):2399–2411.

[Pavani et al., 2009] Pavani, S. R. P., Thompson, M. A., Biteen, J. S., Lord, S. J., Liu, N., Twieg, R. J., Piestun, R., and Moerner, W. E. (2009). Three-dimensional, single-molecule fluorescence imaging beyond the diffraction limit by using a double-helix point spread function. *Proceedings of the National Academy of Sciences*, 106(9):2995–2999.

[Pawley, 2006] Pawley, J. B. (2006). *Handbook Of Biological Confocal Microscopy*. Springer, Boston, MA.

[Pecora, 2013] Pecora, R. (2013). *Dynamic light scattering: applications of photon correlation spectroscopy.* Springer Science Business Media.

[Persson et al., 2009] Persson, G., Thyberg, P., Sandén, T., and Widengren, J. (2009). Modulation Filtering Enables Removal of Spikes in Fluorescence Correlation Spectroscopy Measurements without Affecting the Temporal Information. *The Journal of Physical Chemistry B*, 113(25):8752–8757.

[Peters and Beck, 1983] Peters, R. and Beck, K. (1983). Translational diffusion in phospholipid monolayers measured by fluorescence microphotolysis. *Proceedings of the National Academy of Sciences*, 80(23):7183–7187.

[Peters and Cherry, 1982] Peters, R. and Cherry, R. J. (1982). Lateral and rotational diffusion of bacteriorhodopsin in lipid bilayers: experimental test of the Saffman-Delbrück equations. *Proceedings of the National Academy of Sciences*, 79(14):4317–4321.

[Peterson et al., 2016a] Peterson, E. M., Manhart, M. W., and Harris, J. M. (2016a). Competitive Assays of Label-Free DNA Hybridization with Single-Molecule Fluorescence Imaging Detection. *Analytical Chemistry*, 88(12):6410–6417.

[Peterson et al., 2016b] Peterson, E. M., Manhart, M. W., and Harris, J. M. (2016b). Single-Molecule Fluorescence Imaging of Interfacial DNA Hybridization Kinetics at Selective Capture Surfaces. *Analytical Chemistry*, 88(2):1345–1354.

[Petrášek and Schwille, 2008] Petrášek, Z. and Schwille, P. (2008). Precise Measurement of Diffusion Coefficients using Scanning Fluorescence Correlation Spectroscopy. *Biophysical Journal*, 94(4):1437–1448.

[Petrášek and Schwille, 2009] Petrášek, Z. and Schwille, P. (2009). Fluctuations as a source of information in fluorescence microscopy. *Journal of The Royal Society Interface*, 6:S15–S25.

[Petrov et al., 2006] Petrov, E. P., Ohrt, T., Winkler, R. G., and Schwille, P. (2006). Diffusion and Segmental Dynamics of Double-Stranded DNA. *Physical Review Letters*, 97(25):258101.

[Petrov et al., 2012] Petrov, E. P., Petrosyan, R., and Schwille, P. (2012). Translational and rotational diffusion of micrometer-sized solid domains in lipid membranes. *Soft Matter*, 8(29):7552–7555.

[Petrov and Schwille, 2008a] Petrov, E. P. and Schwille, P. (2008a). State of the Art and Novel Trends in Fluorescence Correlation Spectroscopy. In *Standardization and Quality Assurance in Fluorescence Measurements II*, pages 145–197. Springer Berlin Heidelberg, Berlin, Heidelberg.

[Petrov and Schwille, 2008b] Petrov, E. P. and Schwille, P. (2008b). Translational diffusion in lipid membranes beyond the Saffman-Delbrück approximation. *Biophysical journal*, 94(5):L41–L43.

[Pfeiffer and Höök, 2004] Pfeiffer, I. and Höök, F. (2004). Bivalent Cholesterol-Based Coupling of Oligonucletides to Lipid Membrane Assemblies. *Journal of the American Chemical Society*, 126(33):10224–10225.

[Piliarik and Sandoghdar, 2014] Piliarik, M. and Sandoghdar, V. (2014). Direct optical sensing of single unlabelled proteins and super-resolution imaging of their binding sites. *Nature Communications*, 5:4495.

[Połatyńska et al., 2017] Połatyńska, A., Tomczyk, K., Pochylski, M., Meier, G., Gapinski, J., Banachowicz, E., Śliwa, T., and Patkowski, A. (2017). Temperature dependent FCS studies using a long working distance objective: Viscosities of supercooled liquids and particle size. *Journal of Chemical Physics*, 146(8):84506.

[Posokhov et al., 2008] Posokhov, Y. O., Rodnin, M. V., Lu, L., and Ladokhin, A. S. (2008). Membrane Insertion Pathway of Annexin B12: Thermodynamic and Kinetic Characterization by Fluorescence Correlation Spectroscopy and Fluorescence Quenching. *Biochemistry*, 47(18):5078–5087.

[Price and Jerome, 2011] Price, R. L. and Jerome, W. G. J. (2011). *Basic confocal microscopy*. Springer Science Business Media.

[Przybylo et al., 2006] Przybylo, M., Sýkora, J., Humpolíčková, J., Benda, A., Zan, A., and Hof, M. (2006). Lipid Diffusion in Giant Unilamellar Vesicles Is More than 2 Times Faster than in Supported Phospholipid Bilayers under Identical Conditions. *Langmuir*, 22(22):9096–9099.

[Quardokus et al., 1996] Quardokus, E., Din, N., and Brun, Y. V. (1996). Cell cycle regulation and cell type-specific localization of the FtsZ division initiation protein in Caulobacter. *Proceedings of the National Academy of Sciences*, 93(13):6314–6319.

[Ramachandran et al., 2013] Ramachandran, S., Cohen, D. A., Quist, A. P., and Lal, R. (2013). High performance, LED powered, waveguide based total internal reflection microscopy. *Scientific Reports*, 3:2133.

[Ramadurai et al., 2009] Ramadurai, S., Holt, A., Krasnikov, V., van den Bogaart, G., Killian, J. A., and Poolman, B. (2009). Lateral Diffusion of Membrane Proteins. *Journal of the American Chemical Society*, 131(35):12650–12656.

[Rant, 2012] Rant, U. (2012). Sensing with electro-switchable biosurfaces. *Bioanalytical Reviews*, 4(2-4):97–114.

[Rappaz et al., 2005] Rappaz, B., Marquet, P., Cuche, E., Emery, Y., Depeursinge, C., and Magistretti, P. J. (2005). Measurement of the integral refractive index and dynamic cell morphometry of living cells with digital holographic microscopy. *Optics Express*, 13(23):9361–9373.

[Raskin and de Boer, 1999] Raskin, D. M. and de Boer, P. A. J. (1999). Rapid pole-to-pole oscillation of a protein required for directing division to the middle of Escherichia col. *Proceedings of the National Academy of Sciences*, 96(9):4971–4976.

[Rasnik et al., 2006] Rasnik, I., McKinney, S. A., and Ha, T. (2006). Nonblinking and long-lasting single-molecule fluorescence imaging. *Nature Methods*, 3:891.

[Raymond et al., 2009] Raymond, A., Lovell, S., Lorimer, D., Walchli, J., Mixon, M., Wallace, E., Thompkins, K., Archer, K., Burgin, A., and Stewart, L. (2009). Combined protein construct and synthetic gene engineering for heterologous protein expression and crystallization using Gene Composer. *BMC Biotechnology*, 9(1):37.

[Reed et al., 1987] Reed, R. A., Mattai, J., and Shipley, G. G. (1987). Interaction of cholera toxin with ganglioside GM1 receptors in supported lipid monolayers. *Biochemistry*, 26(3):824–832.

[Reija et al., 2011] Reija, B., Monterroso, B., Jiménez, M., Vicente, M., Rivas, G., and Zorrilla, S. (2011). Development of a homogeneous fluorescence anisotropy assay to monitor and measure FtsZ assembly in solution. *Analytical Biochemistry*, 418(1):89–96.

[Richards and Wolf, 1959] Richards, B. and Wolf, E. (1959). Electromagnetic diffraction in optical systems, II. Structure of the image field in an aplanatic system. *Proceedings of the*

Royal Society of London. Series A. Mathematical and Physical Sciences, 253(1274):358–379.

[Ričká and Binkert, 1989] Ričká, J. and Binkert, T. (1989). Direct measurement of a distinct correlation function by fluorescence cross correlation. *Physical Review A*, 39(5):2646–2652.

[Ries, 2008] Ries, J. (2008). *Advanced Fluorescence Correlation Techniques to Study Membrane Dynamics*. PhD thesis, Technische Universität Dresden.

[Ries et al., 2010] Ries, J., Bayer, M., Csúcs, G., Dirkx, R., Solimena, M., Ewers, H., and Schwille, P. (2010). Automated suppression of sample-related artifacts in Fluorescence Correlation Spectroscopy. *Optics Express*, 18(11):11073–11082.

[Ries et al., 2008a] Ries, J., Petrov, E. P., and Schwille, P. (2008a). Total Internal Reflection Fluorescence Correlation Spectroscopy: Effects of Lateral Diffusion and Surface-Generated Fluorescence. *Biophysical Journal*, 95:390–399.

[Ries et al., 2008b] Ries, J., Ruckstuhl, T., Verdes, D., and Schwille, P. (2008b). Supercritical Angle Fluorescence Correlation Spectroscopy. *Biophysical Journal*, 94(1):221–229.

[Ries and Schwille, 2006] Ries, J. and Schwille, P. (2006). Studying Slow Membrane Dynamics with Continuous Wave Scanning Fluorescence Correlation Spectroscopy. *Biophysical Journal*, 91(5):1915–1924.

[Ries and Schwille, 2012] Ries, J. and Schwille, P. (2012). Fluorescence correlation spectroscopy. *BioEssays*, 34(5):361–368.

[Rigler and Elson, 2012] Rigler, R. and Elson, E. S. (2012). *Fluorescence correlation spectroscopy: theory and applications*, volume 65. Springer Science Business Media.

[Rigler et al., 1993] Rigler, R., Mets, Ü., Widengren, J., and Kask, P. (1993). Fluorescence correlation spectroscopy with high count rate and low background: analysis of translational diffusion. *European Biophysics Journal*, 22(3):169–175.

[Rigler and Widengren, 2017] Rigler, R. and Widengren, J. (2017). Fluorescence-based monitoring of electronic state and ion exchange kinetics with FCS and related techniques: from T-jump measurements to fluorescence fluctuations. *European Biophysics Journal*.

[Ringemann et al., 2009] Ringemann, C., Harke, B., von Middendorff, C., Medda, R., Honigmann, A., Wagner, R., Leutenegger, M., Schönle, A., Hell, S. W., and Eggeling, C. (2009). Exploring single-molecule dynamics with fluorescence nanoscopy. *New Journal of Physics*, 11(10):103054.

[Roberts, 2014] Roberts, C. J. (2014). Therapeutic protein aggregation: mechanisms, design, and control. *Trends in Biotechnology*, 32(7):372–380.

[Roberts et al., 2011] Roberts, C. J., Das, T. K., and Sahin, E. (2011). Predicting solution aggregation rates for therapeutic proteins: Approaches and challenges. *International Journal of Pharmaceutics*, 418(2):318–333.

[Rose and Hildebrand, 2015] Rose, A. S. and Hildebrand, P. W. (2015). NGL Viewer: a web application for molecular visualization. *Nucleic Acids Research*, 43(W1):W576–W579.

[Rothemund, 2006] Rothemund, P. W. K. (2006). Folding DNA to create nanoscale shapes and patterns. *Nature*, 440:297.

[Roy et al., 2010] Roy, A., Kucukural, A., and Zhang, Y. (2010). I-TASSER: a unified platform for automated protein structure and function prediction. *Nature Protocols*, 5:725.

[Royon and Converset, 2017] Royon, A. and Converset, N. (2017). Quality Control of Fluorescence Imaging Systems. *Optik Photonik*, 12(2):22–25.

[Ruckstuhl et al., 2003] Ruckstuhl, T., Rankl, M., and Seeger, S. (2003). Highly sensitive biosensing using a supercritical angle fluorescence (SAF) instrument. *Biosensors and Bioelectronics*, 18(9):1193–1199.

[Ruckstuhl and Verdes, 2004] Ruckstuhl, T. and Verdes, D. (2004). Supercritical angle fluorescence (SAF) microscopy. *Optics Express*, 12(18):4246–4254.

[Rusu et al., 2004] Rusu, L., Gambhir, A., McLaughlin, S., and Rädler, J. (2004). Fluorescence Correlation Spectroscopy Studies of Peptide and Protein Binding to Phospholipid Vesicles. *Biophysical Journal*, 87(2):1044–1053.

[Rüttinger et al., 2007] Rüttinger, S., Buschmann, V., Krämer, B., Erdmann, R., Macdonald, R., and Koberling, F. (2007). Determination of the Confocal Volume for Quantitative Fluorescence Correlation Spectroscopy. In *Confocal, Multiphoton, and Nonlinear Microscopic Imaging III*, page $6630_12.OpticalSocietyofAmerica$.

[Rzepecki et al., 2004] Rzepecki, P., Nagel-Steger, L., Feuerstein, S., Linne, U., Molt, O., Zadmard, R., Aschermann, K., Wehner, M., Schrader, T., and Riesner, D. (2004). Prevention of Alzheimer's Disease-associated Aβ Aggregation by Rationally Designed Nonpeptidic β-Sheet Ligands. *Journal of Biological Chemistry*, 279(46):47497–47505.

[Sackmann and Merkel, 2010] Sackmann, E. and Merkel, R. (2010). *Lehrbuch der Biophysik*. Wiley-VCH.

[Saffarian and Elson, 2003] Saffarian, S. and Elson, E. L. (2003). Statistical Analysis of Fluorescence Correlation Spectroscopy: The Standard Deviation and Bias. *Biophysical Journal*, 84(3):2030–2042.

[Saffarian and Kirchhausen, 2008] Saffarian, S. and Kirchhausen, T. (2008). Differential Evanescence Nanometry: Live-Cell Fluorescence Measurements with 10-nm Axial Resolution on the Plasma Membrane. *Biophysical Journal*, 94(6):2333–2342.

[Saffman, 1976] Saffman, P. G. (1976). Brownian motion in thin sheets of viscous fluid. *Journal of Fluid Mechanics*, 73(4):593–602.

[Saffman and Delbrück, 1975] Saffman, P. G. and Delbrück, M. (1975). Brownian motion in biological membranes. *Proceedings of the National Academy of Sciences*, 72(8):3111–3113.

[Sankaran et al., 2009] Sankaran, J., Manna, M., Guo, L., Kraut, R., and Wohland, T. (2009). Diffusion, Transport, and Cell Membrane Organization Investigated by Imaging Fluorescence Cross-Correlation Spectroscopy. *Biophysical Journal*, 97(9):2630–2639.

[SantaLucia, 1998] SantaLucia, J. (1998). A unified view of polymer, dumbbell, and oligonucleotide DNA nearest-neighbor thermodynamics. *Proceedings of the National Academy of Sciences*, 95(4):1460–1465.

[SantaLucia and Hicks, 2004] SantaLucia, J. and Hicks, D. (2004). The Thermodynamics of DNA Structural Motifs. *Annual Review of Biophysics and Biomolecular Structure*, 33(1):415–440.

[Sarkar et al., 2004] Sarkar, A., Robertson, R. B., and Fernandez, J. M. (2004). Simultaneous atomic force microscope and fluorescence measurements of protein unfolding using a calibrated evanescent wave. *Proceedings of the National Academy of Sciences of the United States of America*, 101(35):12882–12886.

[Schäffer et al., 2007] Schäffer, E., Nørrelykke, S. F., and Howard, J. (2007). Surface Forces and Drag Coefficients of Microspheres near a Plane Surface Measured with Optical Tweezers. *Langmuir*, 23(7):3654–3665.

[Schätzel, 1986] Schätzel, K. (1986). Dead time correction of photon correlation functions. *Applied Physics B*, 41(2):95–102.

[Schätzel, 1987] Schätzel, K. (1987). Correlation techniques in dynamic light scattering. *Applied Physics B*, 42(4):193–213.

[Schätzel et al., 1988] Schätzel, K., Drewel, M., and Stimac, S. (1988). Photon Correlation Measurements at Large Lag Times: Improving Statistical Accuracy. *Journal of Modern Optics*, 35(4):711–718.

[Schenk et al., 2004] Schenk, A., Ivanchenko, S., Röcker, C., Wiedenmann, J., and Nienhaus, G. U. (2004). Photodynamics of Red Fluorescent Proteins Studied by Fluorescence Correlation Spectroscopy. *Biophysical Journal*, 86(1):384–394.

[Schindelin et al., 2012] Schindelin, J., Arganda-Carreras, I., Frise, E., Kaynig, V., Longair, M., Pietzsch, T., Preibisch, S., Rueden, C., Saalfeld, S., Schmid, B., Tinevez, J.-Y., White, D. J., Hartenstein, V., Eliceiri, K., Tomancak, P., and Cardona, A. (2012). Fiji: an open-source platform for biological-image analysis. *Nat Meth*, 9(7):676–682.

[Schindelin et al., 2015] Schindelin, J., Rueden, C. T., Hiner, M. C., and Eliceiri, K. W. (2015). The ImageJ ecosystem: An open platform for biomedical image analysis. *Molecular Reproduction and Development*, 82(7-8):518–529.

[Schmitz et al., 2011] Schmitz, R., Yordanov, S., Butt, H. J., Koynov, K., and Dünweg, B. (2011). Studying flow close to an interface by total internal reflection fluorescence cross-correlation spectroscopy: Quantitative data analysis. *Phys. Rev. E*, 84(6):66306.

[Schnitzbauer et al., 2017] Schnitzbauer, J., Strauss, M. T., Schlichthaerle, T., Schueder, F., and Jungmann, R. (2017). Super-resolution microscopy with DNA-PAINT. *Nat. Protocols*, 12(6):1198–1228.

[Schürmann et al., 2016] Schürmann, M., Scholze, J., Müller, P., Guck, J., and Chan, C. J. (2016). Cell nuclei have lower refractive index and mass density than cytoplasm. *Journal of Biophotonics*, 9(10):1068–1076.

[Schwartz et al., 1994] Schwartz, D. K., Knobler, C. M., and Bruinsma, R. (1994). Direct Observation of Langmuir Monolayer Flow through a Channel. *Physical Review Letters*, 73(21):2841–2844.

[Schwarz et al., 2011] Schwarz, J. P., König, I., and Anderson, K. I. (2011). Characterizing System Performance in Total Internal Reflection Fluorescence Microscopy. In Wells, C. M. and Parsons, M., editors, *Cell Migration: Developmental Methods and Protocols*, pages 373–386. Humana Press, Totowa, NJ.

[Schwille, 2001] Schwille, P. (2001). Fluorescence correlation spectroscopy and its potential for intracellular applications. *Cell Biochemistry and Biophysics*, 34(3):383–408.

[Schwille, 2003] Schwille, P. (2003). TIR-FCS: Staying on the Surface Can Sometimes Be Better. *Biophysical Journal*, 85(5):2783–2784.

[Schwille et al., 1999] Schwille, P., Korlach, J., and Webb, W. W. (1999). Fluorescence correlation spectroscopy with single-molecule sensitivity on cell and model membranes. *Cytometry*, 36(3):176–182.

[Schwille et al., 1997] Schwille, P., Meyer-Almes, F. J., and Rigler, R. (1997). Dual-color fluorescence cross-correlation spectroscopy for multicomponent diffusional analysis in solution. *Biophysical Journal*, 72(4):1878–1886.

[Schwille et al., 1996] Schwille, P., Oehlenschläger, F., and Walter, N. G. (1996). Quantitative Hybridization Kinetics of DNA Probes to RNA in Solution Followed by Diffusional Fluorescence Correlation Analysis. *Biochemistry*, 35(31):10182–10193.

[Seils and Pecora, 1995] Seils, J. and Pecora, R. (1995). Dynamics of a 2311 base pair superhelical DNA in dilute and semidilute solutions. *Macromolecules*, 28(3):661–673.

[Sengupta et al., 2003] Sengupta, P., Garai, K., Balaji, J., Periasamy, N., and Maiti, S. (2003). Measuring Size Distribution in Highly Heterogeneous Systems with Fluorescence Correlation Spectroscopy. *Biophysical Journal*, 84(3):1977–1984.

[Seoane et al., 2000] Seoane, R., Miñones, J., Conde, O., Miñones, J., Casas, M., and Iribarnegaray, E. (2000). Thermodynamic and Brewster Angle Microscopy Studies of Fatty Acid/Cholesterol Mixtures at the Air/Water Interface. *The Journal of Physical Chemistry B*, 104(32):7735–7744.

[Seol and Neuman, 2018] Seol, Y. and Neuman, K. C. (2018). Combined Magnetic Tweezers and Micro-mirror Total Internal Reflection Fluorescence Microscope for Single-Molecule Manipulation and Visualization. In Peterman, E. J. G., editor, *Single Molecule Analysis: Methods and Protocols*, pages 297–316. Springer New York, New York, NY.

[Shah and Duncan, 2014] Shah, N. B. and Duncan, T. M. (2014). Bio-layer Interferometry for Measuring Kinetics of Protein-protein Interactions and Allosteric Ligand Effects. *Journal of Visualized Experiments : JoVE*, 84:51383.

[Shaner et al., 2013] Shaner, N. C., Lambert, G. G., Chammas, A., Ni, Y., Cranfill, P. J., Baird, M. A., Sell, B. R., Allen, J. R., Day, R. N., Israelsson, M., Davidson, M. W., and Wang, J. (2013). A bright monomeric green fluorescent protein derived from Branchiostoma lanceolatum. *Nature Methods*, 10:407.

[Shechtman et al., 2015] Shechtman, Y., Weiss, L. E., Backer, A. S., Sahl, S. J., and Moerner, W. E. (2015). Precise Three-Dimensional Scan-Free Multiple-Particle Tracking over Large Axial Ranges with Tetrapod Point Spread Functions. *Nano Letters*, 15(6):4194–4199.

[Sheppard and Török, 1997] Sheppard, R. C. J. and Török, P. (1997). Effects of specimen refractive index on confocal imaging. *Journal of Microscopy*, 185(3):366–374.

[Sherman et al., 2008] Sherman, E., Itkin, A., Kuttner, Y. Y., Rhoades, E., Amir, D., Haas, E., and Haran, G. (2008). Using Fluorescence Correlation Spectroscopy to Study Conformational Changes in Denatured Proteins. *Biophysical Journal*, 94(12):4819–4827.

[Shi et al., 2010] Shi, X., Lim, J., and Ha, T. (2010). Acidification of the Oxygen Scavenging System in Single-Molecule Fluorescence Studies: In Situ Sensing with a Ratiometric Dual-Emission Probe. *Analytical Chemistry*, 82(14):6132–6138.

[Sickert and Rondelez, 2003] Sickert, M. and Rondelez, F. (2003). Shear Viscosity of Langmuir Monolayers in the Low-Density Limit. *Phys. Rev. Lett.*, 90(12):126104.

[Sickert and Rondelez, 2004] Sickert, M. and Rondelez, F. (2004). Sickert and Rondelez Reply:. *Phys. Rev. Lett.*, 92(13):139604.

[Sickert et al., 2007] Sickert, M., Rondelez, F., and Stone, H. A. (2007). Single-particle Brownian dynamics for characterizing the rheology of fluid Langmuir monolayers. *EPL (Europhysics Letters)*, 79(6):66005.

[Sievers et al., 2011] Sievers, F., Wilm, A., Dineen, D., Gibson, T. J., Karplus, K., Li, W., Lopez, R., McWilliam, H., Remmert, M., Söding, J., Thompson, J. D., and Higgins, D. G. (2011). Fast, scalable generation of high-quality protein multiple sequence alignments using Clustal Omega. *Molecular systems biology*, 7:539.

[Singh et al., 2013] Singh, A. P., Krieger, J. W., Buchholz, J., Charbon, E., Langowski, J., and Wohland, T. (2013). The performance of 2D array detectors for light sheet based fluorescence correlation spectroscopy. *Optics Express*, 21(7):8652–8668.

[Singh and Wohland, 2014] Singh, A. P. and Wohland, T. (2014). Applications of imaging fluorescence correlation spectroscopy. *Current Opinion in Chemical Biology*, 20:29–35.

[Singh, 2016] Singh, P. (2016). SPR Biosensors: Historical Perspectives and Current Challenges.

[Sly and Conboy, 2014] Sly, K. L. and Conboy, J. C. (2014). Determination of Multivalent Protein-Ligand Binding Kinetics by Second-Harmonic Correlation Spectroscopy. *Analytical Chemistry*, 86(22):11045–11054.

[Sly et al., 2013] Sly, K. L., Mok, S.-W., and Conboy, J. C. (2013). Second Harmonic Correlation Spectroscopy: A Method for Determining Surface Binding Kinetics and Thermodynamics. *Analytical Chemistry*, 85(17):8429–8435.

[Sonesson et al., 2008] Sonesson, A. W., Blom, H., Hassler, K., Elofsson, U. M., Callisen, T. H., Widengren, J., and Brismar, H. (2008). Protein surfactant interactions at hydrophobic interfaces studied with total internal reflection fluorescence correlation spectroscopy (TIR-FCS). *Journal of Colloid and Interface Science*, 317(2):449–457.

[Speight and Cooper, 2012] Speight, R. E. and Cooper, M. A. (2012). A Survey of the 2010 Quartz Crystal Microbalance Literature. *Journal of Molecular Recognition*, 25(9):451–473.

[Starr and Thompson, 2001] Starr, T. E. and Thompson, N. L. (2001). Total Internal Reflection with Fluorescence Correlation Spectroscopy: Combined Surface Reaction and Solution Diffusion. *Biophysical Journal*, 80(3):1575–1584.

[Starr and Thompson, 2002] Starr, T. E. and Thompson, N. L. (2002). Local Diffusion and Concentration of IgG near Planar Membranes: Measurement by Total Internal Reflection with Fluorescence Correlation Spectroscopy. *The Journal of Physical Chemistry B*, 106(9):2365–2371.

[Stefaniu et al., 2014] Stefaniu, C., Brezesinski, G., and Möhwald, H. (2014). Langmuir monolayers as models to study processes at membrane surfaces. *Advances in Colloid and Interface Science*, 208(Supplement C):197–213.

[Steiert, 2016] Steiert, F. (2016). *Photophysical Characterization of GFP Variants by Single-Molecule Spectroscopy and Microscopy.* Master's thesis, Technische Universität Munich.

[Stellwagen et al., 2003] Stellwagen, E., Lu, Y., and Stellwagen, N. C. (2003). Unified Description of Electrophoresis and Diffusion for DNA and Other Polyions. *Biochemistry*, 42(40):11745–11750.

[Steyer and Almers, 1999] Steyer, J. A. and Almers, W. (1999). Tracking Single Secretory Granules in Live Chromaffin Cells by Evanescent-Field Fluorescence Microscopy. *Biophysical Journal*, 76(4):2262–2271.

[Stout and Axelrod, 1989] Stout, A. L. and Axelrod, D. (1989). Evanescent field excitation of fluorescence by epi-illumination microscopy. *Applied Optics*, 28(24):5237–5242.

[Strehlow, 1972] Strehlow, H. (1972). Relaxation techniques in fast reaction kinetics. *Advances in Molecular Relaxation Processes*, 2(2):235–249.

[Sun et al., 2008] Sun, Z.-Y. J., Oh, K. J., Kim, M., Yu, J., Brusic, V., Song, L., Qiao, Z., Wang, J.-h., Wagner, G., and Reinherz, E. L. (2008). HIV-1 Broadly Neutralizing Antibody Extracts Its Epitope from a Kinked gp41 Ectodomain Region on the Viral Membrane. *Immunity*, 28(1):52–63.

[Sundararajan and Goley, 2017a] Sundararajan, K. and Goley, E. D. (2017a). Cytoskeletal Proteins in Caulobacter crescentus: Spatial Orchestrators of Cell Cycle Progression, Development, and Cell Shape. In Löwe, J. and Amos, L. A., editors, *Prokaryotic Cytoskeletons: Filamentous Protein Polymers Active in the Cytoplasm of Bacterial and Archaeal Cells*, pages 103–137. Springer International Publishing, Cham.

[Sundararajan and Goley, 2017b] Sundararajan, K. and Goley, E. D. (2017b). The intrinsically disordered C-terminal linker of FtsZ regulates protofilament dynamics and superstructure in vitro. *Journal of Biological Chemistry*, 292(50):20509–20527.

[Sundararajan et al., 2015] Sundararajan, K., Miguel, A., Desmarais, S. M., Meier, E. L., Casey Huang, K., and Goley, E. D. (2015). The bacterial tubulin FtsZ requires its intrinsically disordered linker to direct robust cell wall construction. *Nature Communications*, 6:7281.

[Sutherland, 1905] Sutherland, W. (1905). LXXV. A dynamical theory of diffusion for non-electrolytes and the molecular mass of albumin. *The London, Edinburgh, and Dublin Philosophical Magazine and Journal of Science*, 9(54):781–785.

[Swamy and Sankhala, 2013] Swamy, M. J. and Sankhala, R. S. (2013). Probing the Thermodynamics of Protein-Lipid Interactions by Isothermal Titration Calorimetry. In Kleinschmidt, J. H., editor, *Lipid-Protein Interactions: Methods and Protocols*, pages 37–53. Humana Press, Totowa, NJ.

[Swoboda et al., 2012] Swoboda, M., Henig, J., Cheng, H.-M., Brugger, D., Haltrich, D., Plumeré, N., and Schlierf, M. (2012). Enzymatic Oxygen Scavenging for Photostability without pH Drop in Single-Molecule Experiments. *ACS Nano*, 6(7):6364–6369.

[Swulius and Jensen, 2012] Swulius, M. T. and Jensen, G. J. (2012). The Helical MreB Cytoskeleton in Escherichia coli MC1000/pLE7 Is an Artifact of the N-Terminal Yellow Fluorescent Protein Tag. *Journal of Bacteriology*, 194(23):6382–6386.

[Szeto et al., 2003] Szeto, T. H., Rowland, S. L., Habrukowich, C. L., and King, G. F. (2003). The MinD Membrane Targeting Sequence Is a Transplantable Lipid-binding Helix. *Journal of Biological Chemistry*, 278(41):40050–40056.

[Szeto et al., 2002] Szeto, T. H., Rowland, S. L., Rothfield, L. I., and King, G. F. (2002). Membrane localization of MinD is mediated by a C-terminal motif that is conserved across eubacteria, archaea, and chloroplasts. *Proceedings of the National Academy of Sciences*, 99(24):15693–15698.

[Tan et al., 2012] Tan, C. M., Therien, A. G., Lu, J., Lee, S. H., Caron, A., Gill, C. J., Lebeau-Jacob, C., Benton-Perdomo, L., Monteiro, J. M., Pereira, P. M., Elsen, N. L., Wu, J., Deschamps, K., Petcu, M., Wong, S., Daigneault, E., Kramer, S., Liang, L., Maxwell, E., Claveau, D., Vaillancourt, J., Skorey, K., Tam, J., Wang, H., Meredith, T. C., Sillaots, S., Wang-Jarantow, L., Ramtohul, Y., Langlois, E., Landry, F., Reid, J. C., Parthasarathy, G., Sharma, S., Baryshnikova, A., Lumb, K. J., Pinho, M. G., Soisson, S. M., and Roemer, T. (2012). Restoring Methicillin-Resistant Staphylococcus aureus Susceptibility to β-Lactam Antibiotics. *Science Translational Medicine*, 4(126):126ra35–126ra35.

[Tanaka et al., 1999] Tanaka, K., Manning, P. A., Lau, V. K., and Yu, H. (1999). Lipid Lateral Diffusion in Dilauroylphosphatidylcholine/Cholesterol Mixed Monolayers at the Air/Water Interface. *Langmuir*, 15(2):600–606.

[Taylor et al., 2018] Taylor, A., Verhoef, R., Beuwer, M., Wang, Y., and Zijlstra, P. (2018). All-Optical Imaging of Gold Nanoparticle Geometry Using Super-Resolution Microscopy. *The Journal of Physical Chemistry C*, 122(4):2336–2342.

[Tcherniak et al., 2009] Tcherniak, A., Reznik, C., Link, S., and Landes, C. F. (2009). Fluorescence Correlation Spectroscopy: Criteria for Analysis in Complex Systems. *Analytical Chemistry*, 81(2):746–754.

[Thanbichler, 2009] Thanbichler, M. (2009). Spatial regulation in Caulobacter crescentus. *Current Opinion in Microbiology*, 12(6):715–721.

[Thanbichler and Shapiro, 2006] Thanbichler, M. and Shapiro, L. (2006). MipZ, a Spatial Regulator Coordinating Chromosome Segregation with Cell Division in Caulobacter. *Cell*, 126(1):147–162.

[Thanbichler and Shapiro, 2008] Thanbichler, M. and Shapiro, L. (2008). Getting organized-how bacterial cells move proteins and DNA. *Nature Reviews Microbiology*, 6:28.

[Thirumangalathu et al., 2009] Thirumangalathu, R., Krishnan, S., Ricci, M. S., Brems, D. N., Randolph, T. W., and Carpenter, J. F. (2009). Silicone oil- and agitation-induced aggregation of a monoclonal antibody in aqueous solution. *Journal of Pharmaceutical Sciences*, 98(9):3167–3181.

[Thomas et al., 2015] Thomas, F. A., Visco, I., Petrášek, Z., Heinemann, F., and Schwille, P. (2015). Introducing a fluorescence-based standard to quantify protein partitioning into membranes. *Biochimica et Biophysica Acta (BBA) - Biomembranes*, 1848(11, Part A):2932–2941.

[Thompson, 1999] Thompson, N. L. (1999). Fluorescence Correlation Spectroscopy. In Lakowicz, J. R., editor, *Topics in Fluorescence Spectroscopy: Techniques*, pages 337–378. Springer US, Boston, MA.

[Thompson and Axelrod, 1983] Thompson, N. L. and Axelrod, D. (1983). Immunoglobulin surface-binding kinetics studied by total internal reflection with fluorescence correlation spectroscopy. *Biophysical Journal*, 43(1):103–114.

[Thompson et al., 1981] Thompson, N. L., Burghardt, T. P., and Axelrod, D. (1981). Measuring surface dynamics of biomolecules by total internal reflection fluorescence with photobleaching recovery or correlation spectroscopy. *Biophysical Journal*, 33(3):435–454.

[Thompson et al., 2002] Thompson, N. L., Lieto, A. M., and Allen, N. W. (2002). Recent advances in fluorescence correlation spectroscopy. *Current Opinion in Structural Biology*, 12(5):634–641.

[Thompson et al., 2011] Thompson, N. L., Navaratnarajah, P., and Wang, X. (2011). Measuring Surface Binding Thermodynamics and Kinetics by Using Total Internal Reflection with Fluorescence Correlation Spectroscopy: Practical Considerations. *The Journal of Physical Chemistry B*, 115(1):120–131.

[Thompson and Steele, 2007] Thompson, N. L. and Steele, B. L. (2007). Total internal reflection with fluorescence correlation spectroscopy. *Nat. Protocols*, 2(4):878–890.

[Tinnefeld et al., 2015] Tinnefeld, P., Eggeling, C., and Hell, S. W. (2015). *Far-Field Optical Nanoscopy*, volume 14. Springer.

[Toomre and Manstein, 2001] Toomre, D. and Manstein, D. J. (2001). Lighting up the cell surface with evanescent wave microscopy. *Trends in Cell Biology*, 11(7):298–303.

[Török et al., 1997] Török, P., Hewlett, J. S., and Varga, P. (1997). The role of specimen-induced spherical aberration in confocal microscopy. *Journal of Microscopy*, 188(2):158–172.

[Torres and Levitus, 2007] Torres, T. and Levitus, M. (2007). Measuring Conformational Dynamics: A New FCS-FRET Approach. *The Journal of Physical Chemistry B*, 111(25):7392–7400.

[Travkova et al., 2013] Travkova, O. G., Andrä, J., Möhwald, H., and Brezesinski, G. (2013). Influence of Arenicin on Phase Transitions and Ordering of Lipids in 2D Model Membranes. *Langmuir*, 29(39):12203–12211.

[UniProt Consortium., 2017] UniProt Consortium. (2017). UniProt: the universal protein knowledgebase. *Nucleic Acids Research*, 45(D1):D158–D169.

[Unno et al., 2017] Unno, N., Kigami, H., Fujinami, T., Nakata, S., Satake, S.-i., and Taniguchi, J. (2017). Fabrication of calibration plate for total internal reflection fluorescence microscopy using roll-type liquid transfer imprint lithography. *Microelectronic Engineering*, 180:86–92.

[Unno et al., 2015] Unno, N., Maeda, A., Satake, S.-i., Tsuji, T., and Taniguchi, J. (2015). Fabrication of nanostep for total internal reflection fluorescence microscopy to calibrate in water. *Microelectronic Engineering*, 133:98–103.

[Valeur and Berberan-Santos, 2012] Valeur, B. and Berberan-Santos, M. N. (2012). *Molecular fluorescence: principles and applications*. John Wiley Sons.

[Van de Sande and Persoons, 1985] Van de Sande, W. and Persoons, A. (1985). The size and shape of macromolecular structures: determination of the radius, the length and the persistance length of rod-like micelles of dodecyldimethylammonium chloride and bromide. *The Journal of Physical Chemistry*, 89(3):404–406.

[van den Brink-van der Laan et al., 2004] van den Brink-van der Laan, E., Antoinette Killian, J., and de Kruijff, B. (2004). Nonbilayer lipids affect peripheral and integral membrane proteins via changes in the lateral pressure profile. *Biochimica et Biophysica Acta (BBA) - Biomembranes*, 1666(1):275–288.

[van der Velde et al., 2016] van der Velde, J. H. M., Oelerich, J., Huang, J., Smit, J. H., Aminian Jazi, A., Galiani, S., Kolmakov, K., Gouridis, G., Eggeling, C., Herrmann, A., Roelfes, G., and Cordes, T. (2016). A simple and versatile design concept for fluorophore derivatives with intramolecular photostabilization. *Nature Communications*, 7:10144.

[Vaughan et al., 2004] Vaughan, S., Wickstead, B., Gull, K., and Addinall, S. G. (2004). Molecular Evolution of FtsZ Protein Sequences Encoded Within the Genomes of Archaea, Bacteria, and Eukaryota. *Journal of Molecular Evolution*, 58(1):19–29.

[Vauquelin and Packeu, 2009] Vauquelin, G. and Packeu, A. (2009). Ligands, their receptors and . . . plasma membranes. *Molecular and Cellular Endocrinology*, 311(1):1–10.

[Velazquez-Campoy and Freire, 2006] Velazquez-Campoy, A. and Freire, E. (2006). Isothermal titration calorimetry to determine association constants for high-affinity ligands. *Nature Protocols*, 1:186.

[Velazquez-Campoy et al., 2015] Velazquez-Campoy, A., Leavitt, S. A., and Freire, E. (2015). Characterization of Protein-Protein Interactions by Isothermal Titration Calorimetry. In Meyerkord, C. L. and Fu, H., editors, *Protein-Protein Interactions: Methods and Applications*, pages 183–204. Springer New York, New York, NY.

[Verveer, 2015] Verveer, P. J. (2015). *Advanced Fluorescence Microscopy: Methods and Protocols*. Humana Press.

[Vitovič et al., 2008] Vitovič, P., Alakoskela, J.-M., and Kinnunen, P. K. J. (2008). Assessment of Drug-Lipid Complex Formation by a High-Throughput Langmuir-Balance and Correlation to Phospholipidosis. *Journal of Medicinal Chemistry*, 51(6):1842–1848.

[Vogel et al., 2013] Vogel, S. K., Heinemann, F., Chwastek, G., and Schwille, P. (2013). The design of MACs (minimal actin cortices). *Cytoskeleton*, 70(11):706–717.

[Vogelsang et al., 2008] Vogelsang, J., Kasper, R., Steinhauer, C., Person, B., Heilemann, M., Sauer, M., and Tinnefeld, P. (2008). A Reducing and Oxidizing System Minimizes Photobleaching and Blinking of Fluorescent Dyes. *Angewandte Chemie International Edition*, 47(29):5465–5469.

[von Ahsen et al., 2001] von Ahsen, N., Wittwer, C. T., and Schütz, E. (2001). Oligonucleotide Melting Temperatures under PCR Conditions: Nearest-Neighbor Corrections for Mg2+, Deoxynucleotide Triphosphate, and Dimethyl Sulfoxide Concentrations with Comparison to Alternative Empirical Formulas. *Clinical Chemistry*, 47(11):1956–1961.

[von Smoluchowski, 1906] von Smoluchowski, M. (1906). Zur kinetischen Theorie der Brownschen Molekularbewegung und der Suspensionen. *Annalen der Physik*, 326(14):756–780.

[Vukojević et al., 2005] Vukojević, V., Pramanik, A., Yakovleva, T., Rigler, R., Terenius, L., and Bakalkin, G. (2005). Study of molecular events in cells by fluorescence correlation spectroscopy. *Cellular and Molecular Life Sciences*, 62(5):535.

[Wagstaff et al., 2017] Wagstaff, J. M., Tsim, M., Oliva, M. A., García-Sanchez, A., Kureisaite-Ciziene, D., Andreu, J. M., and Löwe, J. (2017). A Polymerization-Associated Structural Switch in FtsZ That Enables Treadmilling of Model Filaments. *mBio*, 8(3).

[Wallner et al., 2013] Wallner, J., Lhota, G., Jeschek, D., Mader, A., and Vorauer-Uhl, K. (2013). Application of Bio-Layer Interferometry for the analysis of protein/liposome interactions. *Journal of Pharmaceutical and Biomedical Analysis*, 72:150–154.

[Walter et al., 2008] Walter, N. G., Huang, C.-Y., Manzo, A. J., and Sobhy, M. A. (2008). Do-it-yourself guide: how to use the modern single-molecule toolkit. *Nature Methods*, 5:475.

[Wang, 2005] Wang, W. (2005). Protein aggregation and its inhibition in biopharmaceutics. *International Journal of Pharmaceutics*, 289(1):1–30.

[Wang et al., 2010] Wang, W., Nema, S., and Teagarden, D. (2010). Protein aggregation - Pathways and influencing factors. *International Journal of Pharmaceutics*, 390(2):89–99.

[Watkins et al., 2011] Watkins, E. B., Miller, C. E., Majewski, J., and Kuhl, T. L. (2011). Membrane texture induced by specific protein binding and receptor clustering: active roles for lipids in cellular function. *Proceedings of the National Academy of Sciences*, 108(17):6975–6980.

[Waugh, 1982] Waugh, R. E. (1982). Surface viscosity measurements from large bilayer vesicle tether formation. II. Experiments. *Biophysical Journal*, 38(1):29–37.

[Webb, 2001] Webb, W. W. (2001). Fluorescence Correlation Spectroscopy: Genesis, Evolution, Maturation and Prognosis. In Rigler, R. and Elson, E. S., editors, *Fluorescence Correlation Spectroscopy: Theory and Applications*, pages 305–330. Springer Berlin Heidelberg, Berlin, Heidelberg.

[Weger and Hoffmann-Jacobsen, 2017] Weger, L. and Hoffmann-Jacobsen, K. (2017). A total internal reflection-fluorescence correlation spectroscopy setup with pulsed diode laser excitation. *Review of Scientific Instruments*, 88(9):93102.

[Weidemann et al., 2014] Weidemann, T., Mücksch, J., and Schwille, P. (2014). Fluorescence fluctuation microscopy: a diversified arsenal of methods to investigate molecular dynamics inside cells. *Current Opinion in Structural Biology*, 28:69–76.

[Weidemann et al., 2003] Weidemann, T., Wachsmuth, M., Knoch, T. A., Müller, G., Waldeck, W., and Langowski, J. (2003). Counting Nucleosomes in Living Cells with a Combination of Fluorescence Correlation Spectroscopy and Confocal Imaging. *Journal of Molecular Biology*, 334(2):229–240.

[Weiß et al., 2013] Weiß, K., Neef, A., Van, Q., Kramer, S., Gregor, I., and Enderlein, J. (2013). Quantifying the Diffusion of Membrane Proteins and Peptides in Black Lipid Membranes with 2-Focus Fluorescence Correlation Spectroscopy. *Biophysical Journal*, 105(2):455–462.

[White et al., 2000] White, E. L., Ross, L. J., Reynolds, R. C., Seitz, L. E., Moore, G. D., and Borhani, D. W. (2000). Slow Polymerization of Mycobacterium tuberculosis FtsZ. *Journal of Bacteriology*, 182(14):4028–4034.

[Widengren and Mets, 2002] Widengren, J. and Mets, Ü. (2002). Conceptual Basis of Fluorescence Correlation Spectroscopy and Related Techniques as Tools in Bioscience. In *Single Molecule Detection in Solution*, pages 69–120. Wiley-VCH.

[Widengren et al., 1995] Widengren, J., Mets, U., and Rigler, R. (1995). Fluorescence correlation spectroscopy of triplet states in solution: a theoretical and experimental study. *The Journal of Physical Chemistry*, 99(36):13368–13379.

[Widengren and Rigler, 1996] Widengren, J. and Rigler, R. (1996). Mechanisms of photobleaching investigated by fluorescence correlation spectroscopy. *Bioimaging*, 4(3):149–157.

[Widengren et al., 1994] Widengren, J., Rigler, R., and Mets, Ü. (1994). Triplet-state monitoring by fluorescence correlation spectroscopy. *Journal of Fluorescence*, 4(3):255–258.

[Widengren and Schwille, 2000] Widengren, J. and Schwille, P. (2000). Characterization of Photoinduced Isomerization and Back-Isomerization of the Cyanine Dye Cy5 by Fluorescence Correlation Spectroscopy. *The Journal of Physical Chemistry A*, 104(27):6416–6428.

[Widengren et al., 1999] Widengren, J., Terry, B., and Rigler, R. (1999). Protonation kinetics of GFP and FITC investigated by FCS - aspects of the use of fluorescent indicators for measuring pH. *Chemical Physics*, 249(2):259–271.

[Wienken et al., 2010] Wienken, C. J., Baaske, P., Rothbauer, U., Braun, D., and Duhr, S. (2010). Protein-binding assays in biological liquids using microscale thermophoresis. *Nature Communications*, 1:100.

[Wilke et al., 2010] Wilke, N., Vega Mercado, F., and Maggio, B. (2010). Rheological Properties of a Two Phase Lipid Monolayer at the Air/Water Interface: Effect of the Composition of the Mixture. *Langmuir*, 26(13):11050–11059.

[Wilkinson et al., 1994] Wilkinson, F., McGarvey, D. J., and Olea, A. F. (1994). Excited Triplet state interactions with molecular oxygen: Influence of charge transfer on the bimolecular quenching rate constants and the yields of singlet oxygen for substituted naphthalenes in various solvents. *The Journal of Physical Chemistry*, 98(14):3762–3769.

[Winterflood and Seeger, 2016] Winterflood, C. M. and Seeger, S. (2016). Simultaneous Surface-Near and Solution Fluorescence Correlation Spectroscopy. *Journal of Fluorescence*, 26(3):753–756.

[Wiseman, 2013] Wiseman, P. W. (2013). Image Correlation Spectroscopy: Mapping Correlations in Space, Time, and Reciprocal Space. In Tetin, S., editor, *Fluorescence Fluctuation Spectroscopy (FFS), Part A*, volume 518, pages 245–267. Academic Press.

[Wiseman, 2015] Wiseman, P. W. (2015). Image Correlation Spectroscopy: Principles and Applications. *Cold Spring Harbor Protocols*, 2015(4):pdb.top086124.

[Wohland et al., 1999] Wohland, T., Friedrich, K., Hovius, R., and Vogel, H. (1999). Study of Ligand-Receptor Interactions by Fluorescence Correlation Spectroscopy with Different Fluorophores: Evidence That the Homopentameric 5-Hydroxytryptamine Type 3As Receptor Binds Only One Ligand. *Biochemistry*, 38(27):8671–8681.

[Woll, 2014] Woll, D. (2014). Fluorescence correlation spectroscopy in polymer science. *RSC Advances*, 4(5):2447–2465.

[Woodson, 2005] Woodson, S. A. (2005). Metal ions and RNA folding: a highly charged topic with a dynamic future. *Current Opinion in Chemical Biology*, 9(2):104–109.

[Wright et al., 2015] Wright, C. S., Banerjee, S., Iyer-Biswas, S., Crosson, S., Dinner, A. R., and Scherer, N. F. (2015). Intergenerational continuity of cell shape dynamics in Caulobacter crescentus. *Scientific reports*, 5:9155.

[Wu et al., 2008] Wu, B., Chen, Y., and Müller, J. D. (2008). Fluorescence Correlation Spectroscopy of Finite-Sized Particles. *Biophysical Journal*, 94(7):2800–2808.

[Wu et al., 1998] Wu, F., Gericke, A., Flach, C. R., Mealy, T. R., Seaton, B. A., and Mendelsohn, R. (1998). Domain Structure and Molecular Conformation in Annexin V/1,2-Dimyristoyl-sn-Glycero-3-Phosphate/Ca2+ Aqueous Monolayers: A Brewster Angle Microscopy/Infrared Reflection-Absorption Spectroscopy Study. *Biophysical Journal*, 74(6):3273–3281.

[Wurlitzer et al., 2000] Wurlitzer, S., Steffen, P., and Fischer, T. M. (2000). Line tension of Langmuir monolayer phase boundaries determined with optical tweezers. *The Journal of Chemical Physics*, 112(13):5915–5918.

[Yang et al., 2014] Yang, J., Yan, R., Roy, A., Xu, D., Poisson, J., and Zhang, Y. (2014). The I-TASSER Suite: protein structure and function prediction. *Nature Methods*, 12:7.

[Yang et al., 2004] Yang, W., Gelles, J., and Musser, S. M. (2004). Imaging of single-molecule translocation through nuclear pore complexes. *Proceedings of the National Academy of Sciences of the United States of America*, 101(35):12887–12892.

[Yang et al., 2017] Yang, X., Lyu, Z., Miguel, A., McQuillen, R., Huang, K. C., and Xiao, J. (2017). GTPase activity-coupled treadmilling of the bacterial tubulin FtsZ organizes septal cell wall synthesis. *Science*, 355(6326):744–747.

[Yordanov et al., 2011] Yordanov, S., Best, A., Weisshart, K., and Koynov, K. (2011). Note: An easy way to enable total internal reflection-fluorescence correlation spectroscopy (TIR-FCS) by combining commercial devices for FCS and TIR microscopy. *Review of Scientific Instruments*, 82(3):36105.

[Young et al., 2017] Young, G., Hundt, N., Cole, D., Fineberg, A., Andrecka, J., Tyler, A., Olerinyova, A., Ansari, A., Marklund, E. G., Collier, M. P., Chandler, S. A., Tkachenko, O., Allen, J., Crispin, M., Billington, N., Takagi, Y., Sellers, J. R., Eichmann, C., Selenko, P., Frey, L., Riek, R., Galpin, M. R., Struwe, W. B., Benesch, J. L. P., and Kukura, P. (2017). Quantitative mass imaging of single molecules in solution. *bioRxiv*.

[Zacharias et al., 2002] Zacharias, D. A., Violin, J. D., Newton, A. C., and Tsien, R. Y. (2002). Partitioning of Lipid-Modified Monomeric GFPs into Membrane Microdomains of Live Cells. *Science*, 296(5569):913–916.

[Zadeh et al., 2011] Zadeh, J. N., Steenberg, C. D., Bois, J. S., Wolfe, B. R., Pierce, M. B., Khan, A. R., Dirks, R. M., and Pierce, N. A. (2011). NUPACK: Analysis and design of nucleic acid systems. *Journal of Computational Chemistry*, 32(1):170–173.

[Zhang et al., 1995] Zhang, R.-G., Westbrook, M. L., Westbrook, E. M., Scott, D. L., Otwinowski, Z., Maulik, P. R., Reed, R. A., and Shipley, G. G. (1995). The 2.4 Å Crystal Structure of Cholera Toxin B Subunit Pentamer: Choleragenoid. *Journal of Molecular Biology*, 251(4):550–562.

[Zhang et al., 2007] Zhang, X., Wang, Y., Wang, J., Wang, Y., and Li, S. (2007). Effect of pore former on the properties of casted film prepared from blends of Eudragit NE 30 D and Eudragit L 30 D-55. *Chem Pharm Bull (Tokyo)*, 55(8):1261–1263.

[Zhang, 2008] Zhang, Y. (2008). I-TASSER server for protein 3D structure prediction. *BMC Bioinformatics*, 9(1):40.

[Zhao et al., 2003] Zhao, M., Jin, L., Chen, B., Ding, Y., Ma, H., and Chen, D. (2003). Afterpulsing and its correction in fluorescence correlation spectroscopy experiments. *Applied Optics*, 42(19):4031–4036.

[Zheng et al., 2014] Zheng, Q., Juette, M. F., Jockusch, S., Wasserman, M. R., Zhou, Z., Altman, R. B., and Blanchard, S. C. (2014). Ultra-stable organic fluorophores for single-molecule research. *Chem. Soc. Rev.*, 43(4):1044–1056.

[Zhuang, 2005] Zhuang, X. (2005). Single-Molecule RNA Science. *Annual Review of Biophysics and Biomolecular Structure*, 34(1):399–414.

[Zieske et al., 2016] Zieske, K., Chwastek, G., and Schwille, P. (2016). Protein Patterns and Oscillations on Lipid Monolayers and in Microdroplets. *Angewandte Chemie*, 128(43):13653–13657.

[Zieske et al., 2014] Zieske, K., Schweizer, J., and Schwille, P. (2014). Surface topology assisted alignment of Min protein waves. *FEBS Letters*, 588(15):2545–2549.

[Zuker, 2000] Zuker, M. (2000). Calculating nucleic acid secondary structure. *Current Opinion in Structural Biology*, 10(3):303–310.

A

APPENDIX TO CHAPTER III

A.1 Custom-built TIRF microscope for SI-FCS

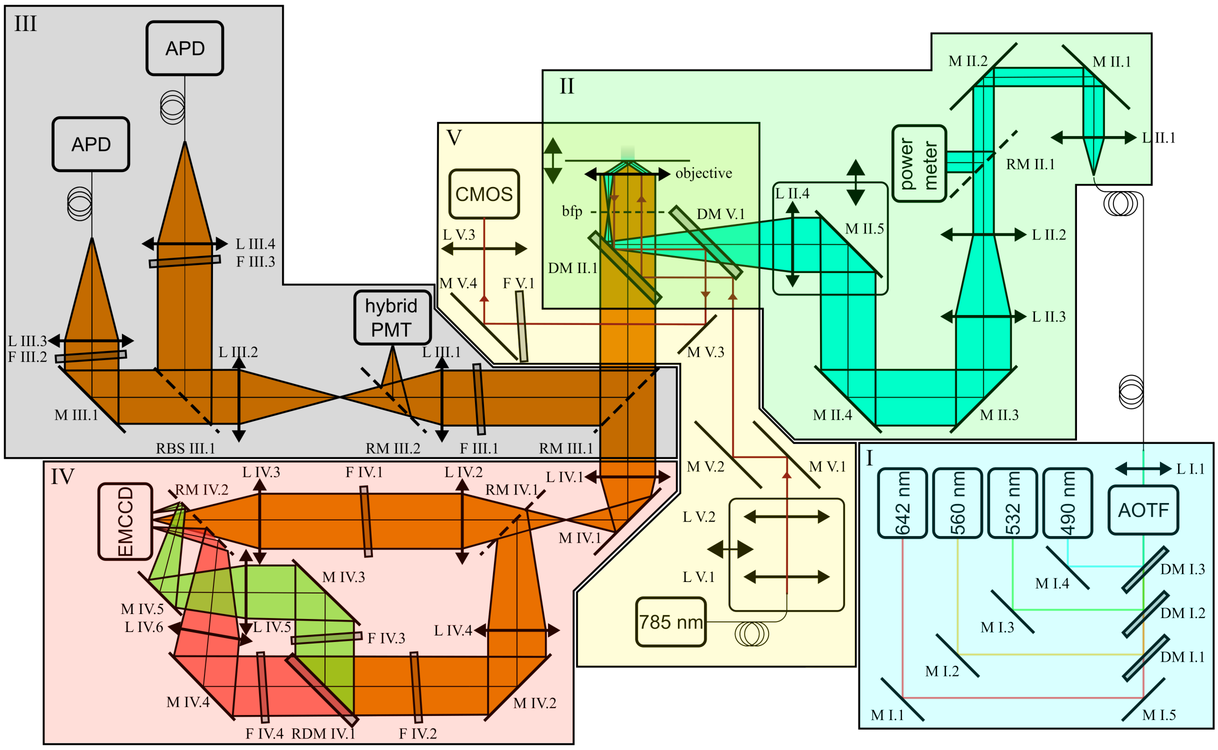

Figure A.1: Custom-built TIRF Microscope. Four Laser lines are selectable for excitation by an AOTF and are coupled into a polarization maintaining single mode fiber (Box I). The fiber output is collimated, passes through a telescope and is finally focused onto the bfp of the objective. The excitation beam is shifted off axis by means of a motorized stage to achieve TIR excitation (Box II). For detection, the fluorescence light is directed towards point detectors (Box III) or an EMCCD camera (Box IV). Both detection pathways offer dual-color detection. The sample is kept in focus by a custom-built feedback mechanism, which adjusts the axial sample position (Box V). A detailed description can be found in the main text.

Although, it was generally desirable to develop a fluorescence-based method to measure binding kinetics without highly specialized and customized equipment, this work was performed on a custom-built TIRF microscope. Compared to commercial TIRF microscopes, this approach ensured maximum freedom in terms of electronics, timing and optical pathway. The microscope was designed with the premise to meet the following requirements: First, as SI-FCS aims at resolving single molecule kinetics, the detection had to feature a high sensitivity. Second, the resolution of subsecond time-scales and the synchronization of excitation and detection required tools to control the timing of measurements. Third, the length of individual measurements was not obvious from the very beginning. Thus, the microscope had to provide a mechanism to stably keep the sample in focus over an arbitrarily long time. Finally, maximum stability of the microscope over months was a major concern. Especially the penetration depth of the evanescent field was sought to be highly reproducible to ensure comparable measurements. Consequently, low drift optics mounts were used. If not mentioned otherwise, 1″ stainless steel posts were used to mount the following components: 1″ and 2″ mirrors: Polaris series, 1″ lenses: CXY1 translation mounts (all Thorlabs GmbH, Dachau, Germany). Furthermore, the penetration depth was controlled by moving the excitation beam off axis by means of a motorized stage with high reproducibility. The TIRF microscope was designed and built around a Nikon Ti-S microscope body (Nikon GmbH, Düsseldorf, Germany), which provided a large degree of freedom, as it comes with two stacked filter turrets. A detailed schematic of the TIRF microscope is shown in figure A.1.

A.1.1 Excitation pathway

Laser combiner For fluorescence excitation purposes, lasers with nominal emission wavelengths of 490 nm (diode laser Calypso), 532 nm (diode-pumped solid state (DPSS) laser Samba), 560 nm (DPSS laser Jive) and 640 nm (Cobolt 06-MLD diode laser, all Cobolt AB, Solna, Sweden) were directed on a shared optical axis by means of mirrors (M I.1-M I.5) and dielectric mirrors (DM I.1-DM I.3), as depicted in figure A.1, Box I. The excitation light passed through an AOTF (Gooch & Housego, TF525-250-6-3-GH18A, Ilminster, UK), which generated an interference pattern, of which the first order was selected by focusing (lens L I.1) it on a polarization-maintaining singlemode fiber (kineFLEX-P-3-S-405.640-0.7-FCS-P0). The fiber was mounted in kinematic holder (kineMATIX, both Qioptiq, Hamble, UK) that provided all required degrees of freedom for alignment. For each of the laser lines, an analog signal was used to control the intensity the AOTF directed towards the first maximum of the interference pattern. The analog signal was generated by a multi-function I/O-device (PCIe-6323) in combination with a BNC output box (BNC-2110) and controlled through a custom-written LabView software[1] (all from National Instruments, Austin, USA). The timing of the AOTF was controlled by transistor transistor logic (TTL) pulses. In general, two different modes were implemented in the custom-written LabView software: continuous wave (cw) excitation, i.e. permanent transmission of the AOTF, and external trigger. For the latter, the EMCCD camera served as a master. In this mode of operation, the AOTF transmitted the selected laser light exclusively when the camera shutter was opened. The described setup also features an alternating excitation option to reduce spectral cross-talk, or to perform sequential multi-color imaging. The laser combiner system depicted in figure A.1 was purchased pre-assembled but without an electronic control and a user interface from Acal BFi (Gröbenzell, Germany).

Total internal Reflection Fluorescence Excitation To achieve TIRF excitation, the laser beam was subject to several alterations, which are shown in figure A.1, Box II. All components shown in Box II were mounted on a customized optical breadboard (MB60120/M), which was supported by a honeycomb breadboard (PBG52522) and mounted on 1″ posts (RS-series, all Thorlabs GmbH, Dachau, Germany). In brief, the top filter turret of the commercial Nikon Ti-S micrsoscope body was removed and replaced by the customized optical breadboard.

The single-mode fiber served as a spatial filter to achieve a Gaussian-shaped TEM_{00} mode output. After the fiber, the laser beam was collimated (L II.1, $f_{\mathrm{II.1}} = 50\,\mathrm{mm}$, Edmund Optics, Barrington, USA). Throughout the excitation pathway, silver mirrors (M II.1-M II.4, PF10-03-P01) in low drift holders (Polaris series, both Thorlabs GmbH, Dachau, Germany) provided the required degrees of freedom for optics alignment. Galilean telescopes of achromatic lenses expanded the beam three-fold (L II.2/II.3, $f_{\mathrm{II.2}} = -25\,\mathrm{mm}$, $f_{\mathrm{II.3}} = 75\,\mathrm{mm}$ both Edmund Optics, Barrington, USA) or ten-fold ($f_{\mathrm{II.2}} = -10\,\mathrm{mm}$, $f_{\mathrm{II.3}} = 100\,\mathrm{mm}$). The respective telescopes were preassembled and aligned, and coupled to a kinematic mount (KB25/M), such that the required telescope could be clicked into the optical pathway in a reproducible manner.

An achromatic lens L II.4 ($f_{\mathrm{II.4}} = 225\,\mathrm{mm}$, #47-646-INK, Edmund Optics, Karlsruhe, Germany) focused the beam on the bfp of the objective (SR APO TIRF, 100x, NA 1.49, Nikon GmbH, Düsseldorf, Germany). The lens was mounted together with a 2″ silver mirror (M II.5) on a common customized baseplate. Therefore, both elements could be moved in a block relative to the optical axis, while maintaining the overlap of the lens' focal

[1] Software development by Dr. Christoph Herold.

point and the bfp of the objective. Consequently, the exit angle of the laser beam from the objective, and thus the penetration depth of the evanescent field, was controlled by moving both elements together. The physical translation was achieved by moving the baseplate using a piezo-electric stage (Q-545 Q-Motion® and E-709 controller, both Physikalische Instrumente, Karlsruhe, Germany) and two cross roller slide tables (GRH20-35m GMT Global Inc., Westerstede, Germany). The stage postion was set through a custom-written LabView 2015 software (National Instrumens, Austin, USA).

A notch beam splitter (zt405/488/561/640rpc flat, AHF Analysentechnik, Tübingen, Germany) was mounted (DFM1/M Thorlabs GmbH, Dachau, Germany) below the objective to reflect the excitation light onto the back pupil of the objective and transmit the collected fluorescence signal. To provide compatibility with the 532 nm laser line, the dichroic mirror could be easily exchanged as it is only held in position by a magnetic mount. For transmission, a hole was drilled into the customized optical breadboard.

If required, the power before the telescope was measured by inserting a mirror, mounted on a magnetic mount, which was temporarily inserted into the optical pathway to direct the laser beam onto a detector (S120C) connected to a powermeter (PM100USB, both Thorlabs GmbH, Dachau, Germany). Moreover, the power behind the objective was measured using a sensor that was positioned on the objective with immersion oil like a regular sample slide (S170C, Thorlabs GmbH, Dachau, Germany). To estimate the irradiance at a known power, we measured the cross-section of the excitation in TIRF and widefield mode by imaging free fluorophore in solution. The images were fitted by a two-dimensional Gaussian $\exp\left(-2\frac{(x-x_0)^2(y-y_0)^2}{w_{\mathrm{ex}}^2}\right)$ with a $1/e^2$-width w_{ex}.

Sample positioning The Nikon Ti-S micrsoscope body is equipped with a conventional focus knob through which the objective is positioned such that the sample is in focus. Moreover, the microscope was equipped with a piezo sample holder (P737.2SL and E-709.SRG, Physikalische Instrumente, Karlsruhe, Germany), which moved the sample in axial direction over a range of 250 µm.

The lateral sample position was controlled through an automated stage (M26821LNJ, Physikalische Instrumente, Karlsruhe, Germany) with a travel range of 135 mmx135 mm. The stage was interfaced by a joystick or a custom-written LabView 2015 software (National Instruments, Austin, USA).

A.1.2 Detection pathway

Point detection The presented TIRF microscope features the option of fluorescence detection with point detectors (figure A.1, Box III), which offer a high temporal resolution. For this purpose, a flat silver mirror (RM III.1, AHF Analysentechnik, Tübingen, Germany) mounted in a filter cube of the lower filter turret of the Nikon Ti-S microscope body was moved into the detection pathway. All further objects in Box III (figure A.1) were placed on a customized aluminum breadboard mounted on 1″ posts (all Thorlabs GmbH, Dachau, Germany). The collected fluorescence passed a bandpass filter (F III.1) and was focused by an achromatic tube lens (L III.1, $f = 200\,\mathrm{mm}$, AC254-200-A-ML, Thorlabs, Dachau, Germany), which was equivalent to the tube lens used in commercial Nikon microscopes. Two different point detectors were set up. For the hybrid PMT (HPM-100-40C, Becker & Hickl GmbH, Berlin, Germany), the collected fluorescence was directed by a removable silver mirror (RM III.2, PF10-03-P01) mounted on a magnetic mount (KB25/M, both Thorlabs, Dachau, Germany). This hybrid PMT has a cathode diameter of 3 mm. The detector generated a pulse for every detected photon; the pulse stream was processed by a TCSPC unit (SPC-150), which sampled events relative to the pulses from a reference source (25 MHz or 12.5 MHz, SYNC Generator, all Becker & Hickl GmbH, Berlin, Germany). From the photon arrival times, the autocorrelation function can be computed.

Alternatively, the collected fluorescence was directed towards APDs. For this purpose, 1:1 telescopes ($f = 200\,\mathrm{mm}$, L III.2 and L III.3/L III.4, AC254-200-A-ML, Thorlabs, Dachau, Germany) were used. At the final focal points, multimode fibers, which guided the light towards the APD (SPCM-AQR, Perkin Elmer (Excelitas Technologies), Waltham, USA), were placed. Acquisition of pseudo-crosscorrelation curves was done in two ways: either by inserting a 50:50 beamsplitter (RBS III.1) or by using a split fiber with two exits (core diameter 50 µm, MMC-A-1x2-600∼700nm-50/50-0-002-FC/PCx3-1.5M, AMS Technologies, Martinsried, Germany). The projected pinhole size in the sample was adjusted by the choice of L III.3 and L III.4, ranging from common achromatic lenses to long distance objectives (here Mitutoyo MY5X-802, MY10X-803, MY20X-804, Thorlabs GmbH, Dachau, Germany). From the detected signal, the autocorrelations were directly calculated using a digital correlator (Flex02-02D, correlator.com, USA).

Camera detection For camera detection (figure A.1, Box IV), the emission light was directed towards the microscope's side-port, thereby passing the internal tube lens ($f = 200\,\mathrm{mm}$) which focused to the exit of this side-port. This TIRF microscope offers single-color and dual-color camera detection schemes. For single-color detection, the intermediate image at the side-port was projected on an EMCCD (iXon Ultra 897, Andor Technologies, Belfast, UK) through a $4f$ telescope ($f = 200\,\mathrm{mm}$, L IV.2 and L IV.3, AC254-200-A-ML, Thorlabs, Dachau, Germany). Bandpass filters, in this chapter 525/50 and 593/46 were used (BrightLine® HC series, Semrock, Rochester, USA), could be inserted in the infinity pathway on demand (F IV.1). The camera acquisition triggered the transmission of the AOTF by TTL pulses. All images were recorded using the Andor Solis software (Version 4.28, Andor Technologies, Belfast, UK) and saved as 16 bit tif files.

For the parallel detection of two spectrally separated channels, the same EMCCD was used and the individual images were clipped in one dimension and projected side-by-side on the camera. To clip the images, a pair of anodized razorblades was mounted on a custom-made holder and placed in the equivalent focal plane at the exit of the microscope's side-port (not shown). The holder incorporated a µm-stage to adjust the spacing between both razor blades. Moreover, the holder was mounted on a translation stage (LTM 45-40-HiSM, controller PS10-32, OWIS GmbH, Staufen i. Br., Germany), such that the holder can be efficiently moved into and out of the optical pathway. Similarly, the mirrors RM IV.1 and RM IV.2 were placed on identical translation stages, which were controlled through a custom-written LabView 2015 software (National Instruments, Austin, USA). Consequently, the operator can reproducibly switch between single-color and dual-color detection within seconds. For space reasons, the $4f$ telescope for dual-color detection was composed of $f = 300\,\mathrm{mm}$ lenses (L IV.4 and L IV.5/L IV.6, AC254-300-A-ML, Thorlabs, Dachau, Germany). Both channels are spectrally separated by a removable dichroic mirror (RDM IV.1), which needs to be chosen depending on the fluorophores in use. Subsequently, both channels were independently projected on the EMCCD-chip. Ideally, each image covers 512 pixels × 256 pixels on the camera, i.e. half the chip. To ensure that both images correspond to the same area in the sample, a calibration with beads, labeled with spectrally different fluorophores (TetraSpeck Microspheres T7280, Thermo Fisher Scientific), needed to be performed prior to each experiment. Again, bandpass filters can be inserted according to experimental demands (F IV.2, F IV.3, F IV.4).

A.1.3 Focus stabilization

All optical systems show drift over time, which may have a plethora of reasons, with temperature changes being among the most important ones. Optical microscopy in general, and long acquisitions and super resolution microscopy in particular, are affected by any drift in the system. Over the last decade, active feedback mechanisms to compensate for axial drifts have become more commonly used. Today, many commercial microscope vendors like Carl Zeiss, Olympus, Nikon offer such feedback mechanisms for their product, especially for TIRF microscopes. Moreover, many companies have developed devices that can upgrade microscopes in this regard. Independent of the commercial device, many reported custom-built implementations, or this study, the working principle is usually the same, but the post-processing may differ [Dempsey et al., 2009]. Typically, the lateral displacement $\Delta x'$ of a beam reflected at the coverslide-sample interface is monitored, as it changes with axial displacements Δz of the glass-sample interface (figure A.2A).

In detail (figure A.1, Box V), the light from a far-red (785 nm) pig-tailed laser diode (LPS-785-FC, mounted in LDM9LP, both Thorlabs, Dachau, Germany) is focused onto the bfp of the objective. The beam can be moved off-axis to control the angle, under which the beam hits the coverslide-sample interface. Upon reflection, the beam is separated from the incoming counterpart by a small pick-up mirror (M V.3, MRA10-P01, Thorlabs, Dachau, Germany). Finally, the beam passes through a longpass filter (F V.1, 785 LP, AHF Analysentechnik, Tübingen, Germany), and is focused on a CMOS camera (UI-3240CP-NIR-GL, Imaging Development Systems, Obersulm, Germany). The current position of the back-reflected beam on the CMOS camera is related to an initial target position, and the deviation is translated into a command to move the sample in axial direction accordingly (z-stage P737.2SL and E-709.SRG, Physikalische Instrumente, Karlsruhe, Germany). It is worth mentioning, that no high-end optical components are required for this approach, as the beam shape is not of particular interest.

So far, this axial focus stabilization is conform with commonly used implementations [Dempsey et al., 2009]. In this work, the lateral displacement of the back-reflected reference beam is analyzed in a novel way. The displacement is an intrinsically one-dimensional problem, and the optical system is aligned, such that $\Delta x'$ is directed along the longer axis of the camera chip. Consequently, the system can be reduced to a one-dimensional profile by integrating along the orthogonal axis (figure A.2C). From here, it would be possible to determine the center of the beam and to relate it to the center of a reference profile, which would be acquired at the beginning of a measurement. The distance between both should be kept at zero by the feedback mechanism. Alternatively, the CMOS chip could be divided into two halves, similar to the use of quadrant photodiodes (QPDs). Problems occur however, when the beam shape is altered upon displacement, e.g. because of imperfections of the coverslide, or if the beam intensity changes. Without a detailed comparison, we

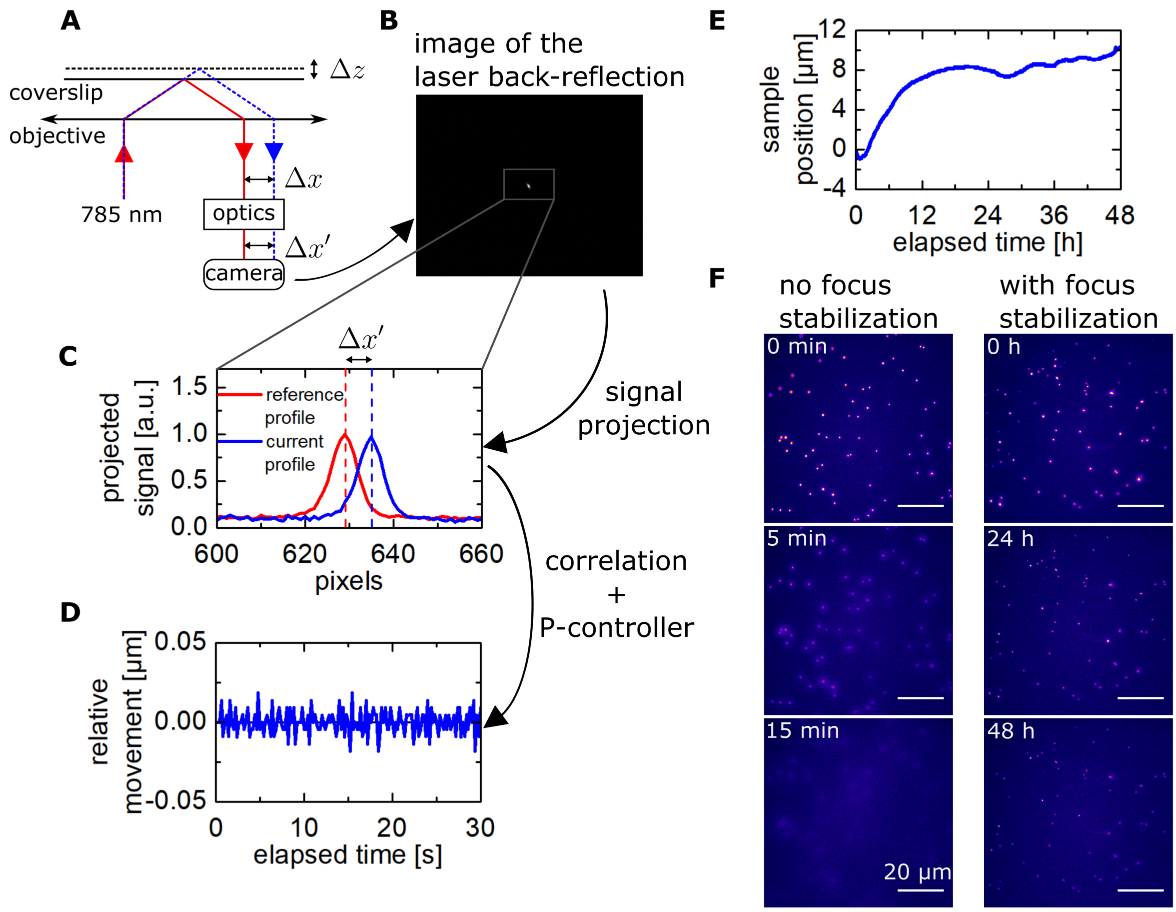

Figure A.2: Working principle of the focus stabilization. A) Schematic of the focus stabilization hardware: A beam that is reflected on a coverslide interface experiences a lateral displacement Δx upon an axial movement Δz of the coverslide. During transition through appropriate optics, the lateral displacement is translated into a different displacement $\Delta x'$. B) Image of a back-reflected beam. C) The image is projected onto one axis yielding a profile which shifts laterally by $\Delta x'$ in response to a shift Δz of the coverslide. The profile is correlated with a reference profile, which corresponds to the target position of the profile. The center of the correlation is the process variable, which is targeted to be at a setpoint 0. D) The sample is moved in z, according to a proportional gain and the deviation of the center of the profile correlation from 0. E) Representative axial drift over 2 days exceeds a total of 8 µm with the strongest drift during the initial 12 h. E) Excerpt from an image series of fluorescent beads with and without focus stabilization. Without stabilization, already after 5 min the beads appear blurry, whereas with focus stabilization, the beads get dimmer because of photobleaching, but stay sharply in focus over the entire duration of this test (48 h). One image was taken every minute, the scale bars correspond to 20 µm.

find that a cross-correlation approach yields a robust feedback mechanism. We correlate the profile at every time instance with the initial target profile and determine the center of the cross-correlation function. The approach is conceptually identical to TICS with flow [Hebert et al., 2005]. Ideally, if there is no displacement, the correlation is centered at zero shift. If both profiles are shifted with respect to each other, their cross-correlation peaks at a lag different than zero. Consequently, the peak position of the cross-correlation becomes the process variable of the feedback and the setpoint is a lag of zero. The error value is multiplied by a fixed proportionality factor (P) to define the step size, by which the sample is moved accordingly. This approach is termed P-controller and P is optimized for the absence of oscillations and a fast conversion to the setpoint. A simple P-controller yielded satisfying performance. Therefore, no advanced PID-controller was implemented. The entire feedback mechanism was implemented in a custom-written software in LabView 2015 (National Instruments, Austin, USA).

The axial drift on a TIRF microscope can be considerable and does not even need to be monotonous, as shown by an example in figure A.2E. Here, the position of the z-stage was tracked over 48 h with a sample of beads constantly held in focus. The overall drift exceeded 8 µm. Figure A.2F illustrates the benefit of a focus stabilization even more: Two identical samples with beads were imaged every 60 s. Without a focus stabilization, the sample drifts out of focus within less than 5 min and the signal is completely lost after 15 min. In stark contrast, with a focus stabilization, the beads stay in focus for the entire time tested, they only get dimmer because of photobleaching.

In the following, some advantages of the implemented focus stabilization shall be briefly highlighted. Time lapse and long time acquisitions are intrinsically possible with a focus stabilization, as the sample is kept in focus for arbitrarily long times. Second, the feedback algorithm can be manipulated such that the sample is moved to a new z-position, which is then held. This can be repeated arbitrarily often, which is not only of direct advantage for the calibration of 3D super resolution measurements using a cylindrical lens [Huang et al., 2008]. In general, a stable focus position is of key relevance for super resolution studies with high axial resolution [McGorty et al., 2013, Dempsey, 2013], but was also exploited in this study to demonstrate that SI-FCS does not require any calibration of the detection volume. In addition, this focus stabilization was successfully tested for flow chambers with manual liquid exchange and for massive in situ pipetting in the sample, on the objective, to change buffer conditions, which was exploited in another study[2]. Finally, objective-

[2] Sonal, Ganzinger, K., Vogel, S., Mücksch, J., Blumhardt, P., Schwille, P., Balancing Assembly and contraction in a reconstituted Minimal Actin Cortex. *(manuscript in preparation)*

type TIRF microscopy is limited to high-NA objectives which feature small effective focal lengths, a large magnification, and can consequently only be used to image a small field of view, typically not larger than 100 µm to 200 µm. To circumvent these limitations, the sample can be raster-scanned and the acquired images can be stitched together. However, the coverslide is typically not perfectly straight and shows inhomogeneities. This focus stabilization compensates to some degree for these effects, which means such raster-scanned image acquisitions can be performed in a fully automated fashion. The functionality has been implemented in this microscope and has been employed for the imaging of SLBs.

A.2 Materials and Methods

Chemicals and buffers Labeled imager strands with the sequence 5′-CTAGATGTAT-3′-Cy3B (denoted P1) were purchased from Eurofins Genomics (Ebersberg, Germany). For simplicity, the buffers used in this study are denoted A, A+, B and B+. Buffer A contains 10 mM Tris-HCl, 100 mM NaCl, and is adjusted to pH 8. Buffer B is used primarily when there are origamis in the sample and has thus Mg^{2+} ions. In detail, it contains 5 mM Tris-HCl, 10 mM $MgCl_2$, 1 mM EDTA and is adjusted to pH 8.. The additional '+' in A+ and B+ buffers indicates that these buffers are identical to A and B buffers respectively, but contain 0.05 vol% Tween20 to minimize unspecific surface binding.

Folding of DNA origamis DNA origami structures were synthesized as previously described [Schnitzbauer et al., 2017]. The structures were folded[3] in a one-pot reaction with a total volume of 40 µL containing 10 nM of scaffold (circular genome from the virus M13mp18, 7,249 nt total length), 10 nM biotinylated staples for surface attachment, 100 nM core staples and 1 µM extended staples in 1xTE buffer supplemented with 12.5 mM $MgCl_2$. The DNA origami structures were folded in a thermocycler, which kept the samples first at 80 °C for 5 min, and subsequently goes from 65 °C to 4 °C over the course of 3 h.

Four different DNA origami structures were designed. All of them exposed 5x4 ssDNA handles at their surface, as shown in figure A.3A. These handles featured TT-spacers, which were followed by the pairing sequence. In detail, the exposed single-stranded sequences were 5′-TT**ATACATC**-3′, 5′-TT**ATACATCT**-3′, 5′-TT**ATACATCTA**-3′, and 5′-TT**ATACATCTAG**-3′, with the 3′-ends pointing away from the structure. These DNA

[3]Folding by Maximilian T. Strauss (Jungmann lab, Max Planck Institute of Biochemistry, Martinsried, and Ludwig-Maximilians-University, Munich, Germany)

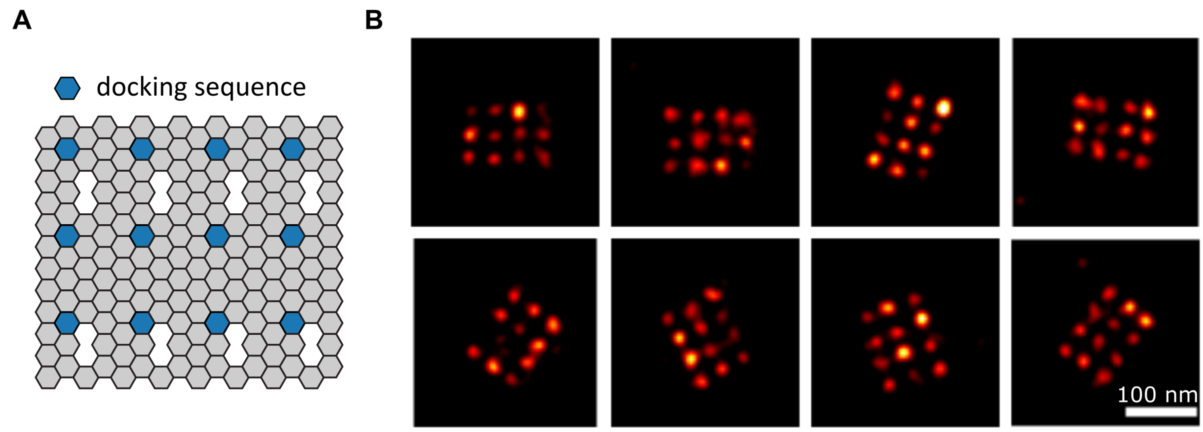

Figure A.3: Rectangular DNA origami exposing 20 single-stranded DNA handles. A) Schematic of the DNA origami used in this work. The image was generated using the Picasso software tool [Schnitzbauer et al., 2017]. B) Representative super-resolved DNA-PAINT images of the DNA origami structure in A).

origamis formed a 7 nt, 8 nt, 9 nt and 10 nt overlap with the labeled imager strand, which was highlighted by bold letters in the sequences. The correct folding was confirmed by DNA-PAINT imaging, which enables to render a localization-based super-resolved image (figure A.3B). The DNA-PAINT images were computed using the Picasso software tool [Schnitzbauer et al., 2017].

Assembly of the sample chambers For SI-FCS measurements, DNA origamis were immobilized on a coverslide inside a flow chamber, following a previously reported protocol [Schnitzbauer et al., 2017]. High precision #1.5 coverslides (Paul Marienfeld GmbH, Lauda-Königshofen, Germany) were sonicated in acetone (chemical grade, Merck KGaA, Darmstadt, Germany) for 10 min, rinsed twice with ethanol (chemical grade, Merck Millipore, Darmstadt, Germany) and water (milli-Q, Merck Millipore, Darmstadt, Germany) and gently dried with pressurized air. The cleaning of the coverslide was completed by loading the coverslides with a drop of 2-propanol (Uvasol, Merck KGaA, Germany), which was wiped with a paper tissue (Kimtech Science, Sigma Aldrich, Germany) while excerting gentle pressure on the coverslide. The same procedure was performed on microscope slides (76x26 mm^2, Menzel Gläser, Thermo Fisher Scientific). The high precision coverslide and the microscope slide together formed a flow chamber with double-sided sticky-tape (Scotch, Conrad Electronic SE, Germany) that served as glue and as a spacer, inbetween. The final chamber measures approximately 5x22x0.08 mm^3. The first two lateral dimensions are controlled by the distance between the sticky tapes and the width of the coverslide. The heigth of the chamber was determined by scanning a confocal volume through a chamber loaded with fluorescent labels in solution. The flow chamber is sufficiently small, such that liquid droplets at the edge of the empty chamber are forced into the chamber by capillary forces. The chamber volume is exchanged by applying the fresh volume at the entrance of the chamber and simultaneous suction with a tissue on the other end of the chamber. The empty and unused chambers were stored for up to a few weeks without any notable effect of the storage on the measurements.

After assembly, the flow chamber was first incubated for two minutes with 20 µL of 1 mg/mL albumin, biotin-labeled bovine (Sigma-Aldrich) in buffer A+, which unspecifically binds to the surface, thereby exposing immobilized biotin. The volume was washed with 40 µL of buffer A+, and incubated with 20 µL of 0.5 mg/mL streptavidin (Thermo Fisher Scientific) in buffer A+ for two minutes. Due to its four binding sites for biotin, streptavidin got immobilized in this step, now exposing biotin binding sites at the surface. Next, to prepare the loading of DNA origamis, the sample was washed with, washed with 40 µL of buffer A+, and then washed with 40 µL of buffer B+. Afterwards, the chamber was incubated for 10 min with 20 µL of 0.5 nM of the desired folded DNA origami structures, which were dissolved in buffer B+. Only for the experiments with varying surface densities of DNA origamis (compare figures III.15 and A.5 in appendix A.3), other concentrations of DNA origami structures were used for incubation. The unbound DNA origamis were washed off with 20 µL of buffer B+ and the chamber was loaded with 20 µL of imager strand in the required target concentration. In a final step, the chamber was sealed using two-component epoxy glue (Toolcraft, Conrad Electronic SE, Germany).The final concentration of imager strand was confirmed using confocal FCS measurements (compare figure A.4 in appendix A.3).

SI-FCS image acquisition Unless stated otherwise, the analysis of SI-FCS data sets was performed on image sequences of 64x64 pixels. To keep the acquired amount of data to a reasonable level, if not mentioned otherwise, the images were acquired with a 4x4 hardware pixel binning. To make all acquisitions comparable with respect to their number of pixels, the acquired images were rendered into 256x256 pixels images, which was the largest native image size used in this work. Typical image stacks were reordered for 1.5 million frames for 7 nt, 8 nt and 9 nt with an exposure time of 10 ms and a frame rate of 85 Hz. For 10 nt hybridizations, the dwell time $\tau_d = k_d^{-1}$ was considerably longer. To reduce any effects of bleaching, 150,000 images were acquired with 10 ms exposure time and a frame rate of 10 Hz. To ensure that the EM gain does not alter the results, the settings of the EM gain were systematically varied but did not have any impact on the measured autocorrelation curves (data not shown). All SI-FCS measurments presented in this work were taken at 23 °C.

SI-FCS data analysis The autocorrelation curves were computed and analyzed using a custom-written MATLAB 2017a (The MathWorks, Natick, USA) software. Each image was subdivided into 7x7 ROIs, each of them covering 31x31 pixels, spaced in a grid around the center of illumination. In each ROI in each frame, all pixel values were summed up, yielding 49 intensity traces. These intensity traces were bleach and drift-corrected by a single exponential, and individually correlated using a multiple-τ algorithm [Schätzel, 1987], in which the binwidth was doubled after every sixteenth point in the autocorrelation curve. The obtained autocorrelation curves were fitted individually by a single exponential decay with offset, from which the amplitude and more importantly, the characteristic decay time were obtained. For samples containing two species, the autocorrelation curves were fitted by a sum of two exponentials with offset. In the titration experiments, the bi-exponential fit accounted for a supposedly non-specific component appearing at high concentrations (10 nM for 10 nt, and 100 nM for 9 nt).

Confocal FCS measurements Confocal FCS measurements were performed on a commercial LSM 780 ConfoCor3 system equipped with a 40X C-Apochromat NA 1.2 water immersion objective (Carl Zeiss AG, Oberkochen Germany) using an inbuilt 561 nm DPSS laser. To avoid detector afterpulsing related artifacts, pseudo-crosscorrelation was performed (for more experimental details, see chapter IV). The confocal volume was positioned 30 µm above the bottom coverslide in the assembled sample chambers. A calibration measurement was performed on a daily basis using Alexa546NHS (ThermoFisher Scientific), which has a reported diffusion coefficient $D = 341\,\mu\mathrm{m}^2/\mathrm{s}$ at 22.5 °C (compare table II.1) [Petrášek and Schwille, 2008]. The confocal measurements were taken at 27 °C and the diffusion coefficient of Alexa546NHS was calculated accordingly based on equation II.5 and the empirical equation for the temperature dependence of the viscosity of water given in [Kestin et al., 1978]. A power series ensured that triplet build-up and photobleaching were negligible at an irradiance $I_0 = 0.5\,\mathrm{kW/cm^2}$ ($w_{xy} \approx 240\,\mathrm{nm}$, $P = 0.42\,\mu\mathrm{W}$), which was chosen for all measurements. As on the TIRF microscope described above, the power was measured using a powermeter (PM100USB) with a microscopy slide-like detector (S170C, both Thorlabs GmbH, Dachau, Germany) that was placed on top of the objective with immersion water in between. The confocal autocorrelation curves were fitted using a single-component diffusion model (equation II.34). The concentrations were calculated based on the autocorrelation amplitude N^{-1} and the calibrated size of the detection volume $c = N\left(\pi^{3/2} w_{xy}^3 S\right)^{-1}$.

Monte Carlo simulations If not mentioned otherwise, Monte Carlo Simulations were performed using a custom-written MATLAB code (R2016a, The MathWorks, Natick, USA). The time step between two iterations was set to $\Delta t = 1\,\text{ms}$ and the signal from 10 iterations was integrated to form one time point in the signal trace. This corresponds to a notional time resolution of the detector of 10 ms. For the majority of simulations presented here, the focus was on signal fluctuations originating from binding and unbinding events. Therefore, N_S immobile binding sites were initialized and a fraction $\beta = \left(1 + \frac{k_d}{k_a \langle A \rangle}\right)^{-1}$ of them was initially bound by a ligand. The two simulated processes are binding and unbinding, for which the probabilities $P_\text{binding} = 1 - e^{-k_a \langle A \rangle \Delta t}$ and $P_\text{unbinding} = 1 - e^{-k_d \Delta t}$ were defined. During each iteration, occupied and unoccupied binding sites were treated differently. For all bound sites, a uniformly distributed random number in the interval (0,1) was generated using the inbuilt Mersenne Twister [Matsumoto and Nishimura, 1998]. If the random number was smaller than a threshold given by $P_\text{unbinding}$, the binding site was converted to an unoccupied state, otherwise it remained unchanged. The transitions from the unbound to bound state were simulated following an equivalent strategy. Each bound receptor contributed with the brightness 1 to the signal per iteration, each unoccupied binding site did not contribute to the signal.

For Monte Carlo simulations of particles diffusing in 2D with confocal detection, $N = 10^4$ point-like non-interacting particles with a diffusion coefficient $D = 1\,\mu\text{m}^2/\text{s}$ were randomly distributed in a box with periodic boundary conditions. The confocal volume was a Gaussian $\Omega(\vec{r}) = \exp(-2\vec{r}^2/w_{xy}^2)$ with an $1/e^2$-width $w_{xy} = 300\,\text{nm}$, positioned in the center of the box. At every iteration, the displacement of each particle was determined by two random numbers, which were drawn from a normal distribution with standard deviation $\sqrt{2D\Delta t}$, with $\Delta t = 0.01 \frac{w_{xy}^2}{4D}$ being the time increment of each iteration step. Thus, the time elapsed after j iterations was $t_j = j\Delta t$. The collected signal F_j after each iteration step was calculated based on the value of Ω at all particle positions $r_i(\vec{t_j})$: $F_j = \sum_{i=1}^{N} \Omega(\vec{r_i})$. In total, 10^7 iterations were performed and the simulation was repeated 10 times.

The Monte Carlo simulations of combined reversible surface binding and 3D ligand diffusion (figure III.8) was performed as previously described [Ries et al., 2008a]. In particular, supercritical emission and its effect on the effective brightness of individual emitters depending on their distance to the surface was taken into account. In detail, the assumed parameters regarding the optical properties were the refractive indices $n_1 = 1.33$, $n_2 = 1.52$, the effective wavelength $\lambda_0 = 580\,\mathrm{nm}$, which was a trade off between excitation wavelength and the red-shifted fluorescence emission, a random dipole orientation, the numerical aperture $\mathrm{NA} = 1.46$, the evanescent penetration depth $d_{\mathrm{eva}} = 100\,\mathrm{nm}$, and the square detection profile of side length $a = 4.8\,\mathrm{\mu m}$, which was convoluted with a Gaussian with an $1/e^2$-width of $0.21\lambda_0/\mathrm{NA}$ [Zhang et al., 2007], resembling the shape of the PSF. In practice, the width of the PSF may be larger than the theoretical ideal width of the PSF as calculated by Zhang *et al.* [Zhang et al., 2007, Bag et al., 2012]. The Monte Carlo simulations of combined reversible surface binding and 3D ligand diffusion are however only used to illustrate the potential contribution of free ligand diffusion to the total autocorrelation curve, and no quantitative information is extracted. Moreover, the following kinetic and system parameters were assumed: receptor density $S = 20.3\,\mathrm{\mu m^{-2}}$, ligand concentration $A = 10\,\mathrm{nM}$, association rate $k_a = 5 \cdot 10^6\,\mathrm{M^{-1}s^{-1}}$, dissociation rate $k_d = 0.1\,\mathrm{s^{-1}}$, diffusion coefficient $D = 50\,\mathrm{\mu m^2/s}$, and time per iteration step $\Delta t = 1\,\mathrm{ms}$.

None of the described codes simulate images, but only the integrated signal over a simulated area. Although it is straightforward to add the functionality of simulating images, all simulations with varying surface density (figure III.14) were performed using the previously published Picasso software tool [Schnitzbauer et al., 2017]. In detail, N_S single binding sites were randomly distributed in a 24x24 pixels large area with square pixels of side length 160 nm (total area $A_{\mathrm{im}} = 14.7\,\mathrm{\mu m^2}$). The PSF was assumed to be Gaussian with a $1/e^2$-value of $w_{xy} = 262.4\,\mathrm{nm}$. One resolution disk was defined as a circle with radius w_{xy}. Moreover, the rate parameters $k_d = (1\,\mathrm{s})^{-1}$ and $k_a \langle A \rangle = (125\,\mathrm{s})^{-1}$ were used. These simulations were conducted with a frame rate of 10 Hz, generating a total of 40000 images, which corresponds to a total measurement time of $t_{\mathrm{meas}} = 4000\,\mathrm{s}$. Based on these settings, the average number of bound sites per resolution disk was calculated as $N_S \beta \pi w_{xy}^2 / A_{\mathrm{im}}$, with beta being the fraction of occupied binding sites (compare section III.2.1). The average number of binding events that contributed to each simulated autocorrelation was calculated as $N_S t_{\mathrm{meas}} \left(k_a^{-1} \langle A \rangle^{-1} + k_d^{-1} \right)^{-1}$.

Fabrication of the calibration slide to measure the TIRF excitation profile The detailed protocol has been described recently [Niederauer, 2018]. In brief, the deposition of polymer coatings onto a #1.5 high precision coverslide (24x50 mm^2, thickness (170±5) µm, Paul Marienfeld GmbH & Co. KG, Lauda Königshofen, Germany) was performed on a custom-built dip coating setup. A motorized linear stage (LTM 45-50-HiSM, controller PS10-32, both OWIS GmbH, Staufen, Germany) holding the sample through a customized clamp was set up vertically, and moved the coverslide into and out of a cuvette (Makro-Küvette 6030-OG, Hellma GmbH, Müllheim, Germany) filled with dip coating solution. In an initial step, the coverslide was coated with the chemical First Contact (Photonic Cleaning Technologies, Wisconsin, USA), which was cured for 5 min and formed a removable layer on both sides of the slide. One of these layers was stripped off before further processing. Next, the coverslides were dip coated with a solution of the polymer MY-133MC (Mypolymers Inc., Ness Ziona, Israel), diluted in the fluorosolvent Novec 7500 (3M, Neuss, Germany). To obtain a multistep slide, the dip coating was repeated several times, at each iteration moving less far into the dip coating solution. The concentration of MY-133MC was adjusted for every iteration, depending on number and height of the steps to be deposited. Finally, the second layer of First Contact was stripped off, leaving only one structured side of the coverslide. The coated coverslides were stored overnight for curing in the dark at ambient temperature and humidity. The height of each step was measured using AFM (Nano Wizard 3, JPK Instruments AG, Berlin, Germany). For TIRF imaging, a rubber spacer (SecureSeal Hybridization Chambers, Grace Bio-Labs, Oregon, USA) was glued on the calibration slide, and 700 µL of 50 µM Alexa Fluor 488 (Alexa488, Thermo Fisher Scientific Messtechnik GmbH, Munich, Germany) were loaded. The imaging was performed using 490 nm excitation wavelength. For background correction, a sample containing only water was imaged.

Lateral displacement method The incident angle θ under which the laser beam meets the glass-water interface was measured based on a method presented by Burghardt [Burghardt, 2012]. In detail, the TIR angle stage (L II.4 and M II.5 in figure A.1) was moved to a fixed position, and a sample of free Alexa488 (Thermo Fisher Scientific Messtechnik GmbH, Munich, Germany) was mounted on the objective. The imaging was performed without any magnification telescope (L II.2 and L II.3 in figure A.1) in the excitation pathway, ensuring that the full excitation profile fitted within the FOV. Next, a series of images was taken with the sample in different axial positions. As the excitation beam leaves the objective under a large angle, a small displacement of the sample Δz results in a measurable lateral displacement Δy of the detected fluorescence distribution in the acquired image. A linear fit of the dependence of Δy on Δz yields a slope that is equivalent to $\tan\theta$, from which the penetration depth was calculated using equation II.17.

A.3 Supporting figures

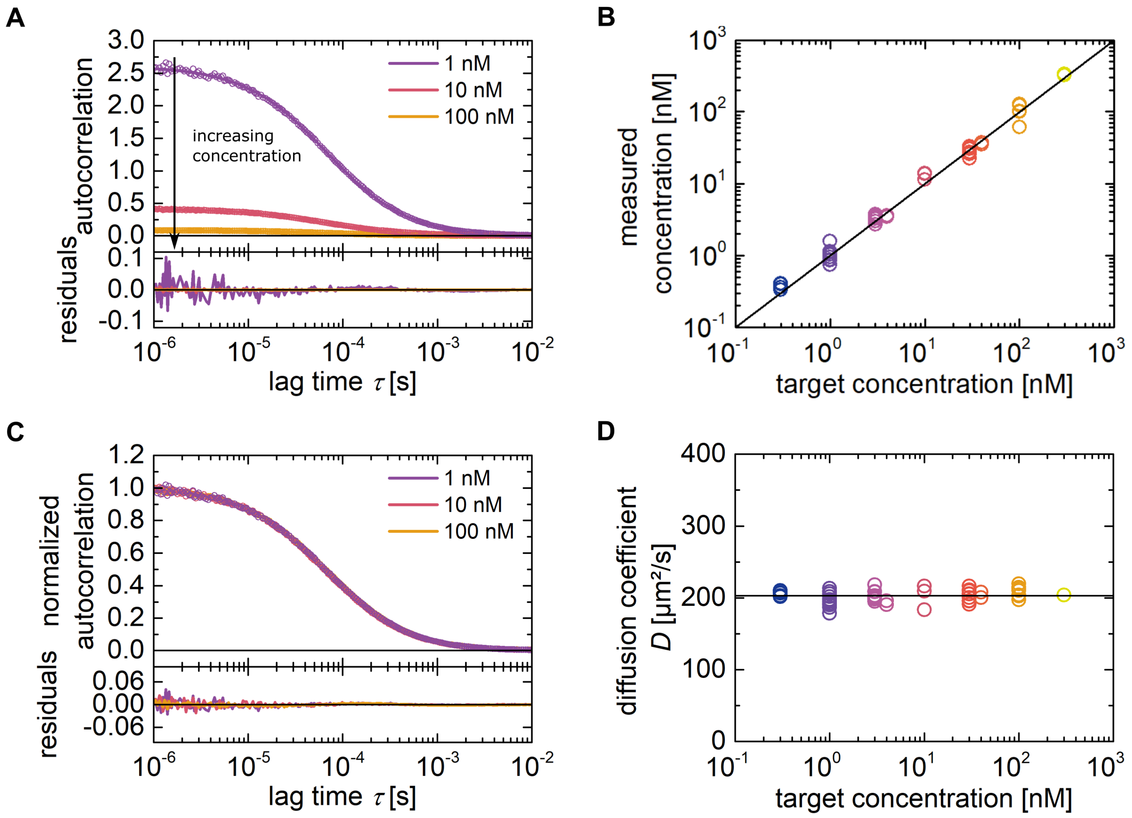

Figure A.4: Confocal FCS measurements on imager strands diffusing in 3D. A) Representative autocorrelation curve of different concentrations of imager strand in solution and the corresponding fits by a single-component diffusion model (equation II.34). B) Imager strand concentrations measured by FCS reproduce the target concentrations that were loaded into the sample. Only at very low concentrations below 1 nM, the measurements are slightly but systematically off, which can be attributed to the relevant contribution of afterpulsing photons at low count rates [Enderlein and Gregor, 2005, Kapusta et al., 2007], which are not accounted for by correcting for the background from scattered and ambient light. C) Correlation curves from A) are indistinguishable upon normalization by the particle number, indicating that the diffusion times are the same, independent of the concentrations of imager strands. D) Diffusion coefficients of the imager strand is reproducible across the range of measured concentrations. The mean and standard deviations of 51 measurements of the 10 nt ssDNA labeled with Cy3B are $D = (203 \pm 9)$ µm^2/s at 27 °C, in good agreement with a previously reported value [Stellwagen et al., 2003]. The sample chambers were prepared as usual with DNA origamis exposing hybridization sites on the surface. Measurements were taken 30 µm above the surface.

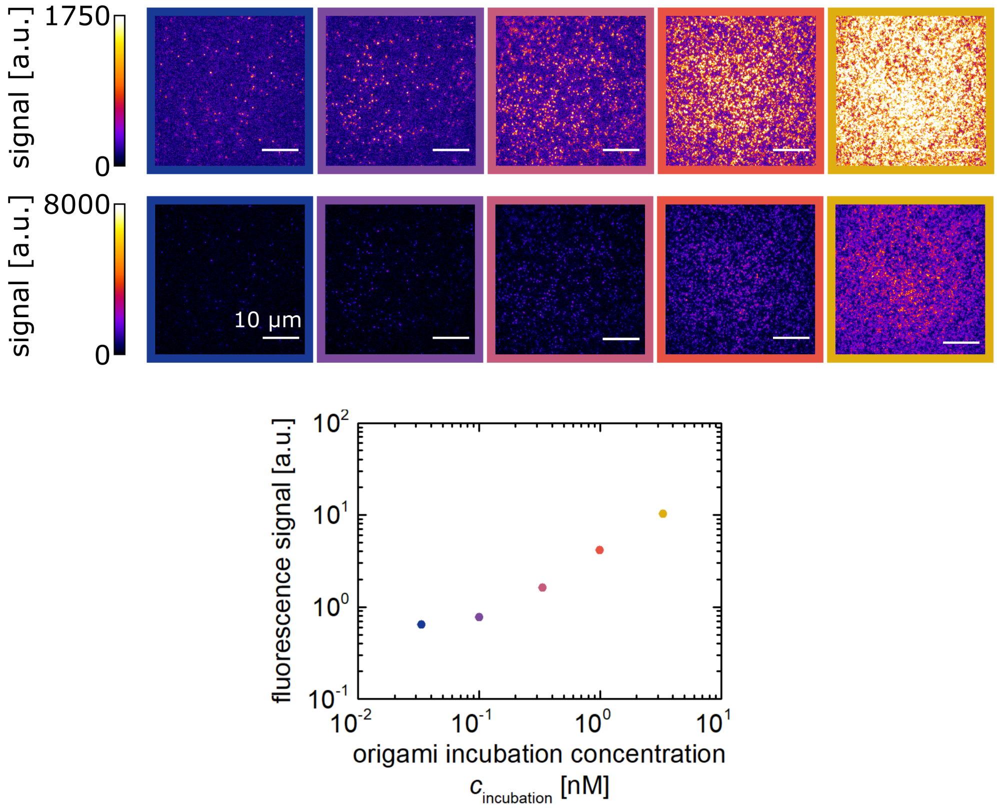

Figure A.5: Fluorescence signal scales with the DNA origami concentration during incubation. Representative fluorescence images and the integrated signal, for different concentrations $c_{\mathrm{incubation}}$ of DNA origami during incubation. The fluorescence images are displayed in different color scales to highlight the single particles at low concentrations without saturating the images at high concentrations. As usual, coverslides were incubated with Biotin-BSA and streptavidin. For the surface immobilization of biotinylated DNA origamis with exposed 9 nt single strands, the incubation solution was prepared with different $c_{\mathrm{incubation}}$ ranging from 30 pM to 3 nM. Upon addition of the P1 imager strand, the integrated signal scales approximately linear with $c_{\mathrm{incubation}}$, indicating that not all streptavidin binding sites are saturated.

B

APPENDIX TO CHAPTER IV

B.1 Materials and Methods

Solution preparations Solutions were prepared[1] from the following reagents: Deionized water (18.2 MΩ cm, model Milli-Q Integral), ethanol (Uvasol, purity ≥99.9% gas chromatography (GC)), methanol for fluorescence microscopy (purity ≥99.5% GC), and glycerol for fluorescence microscopy (purity ≥99.5% GC) were purchased from Merck Millipore (Darmstadt, Germany). Sucrose and urea (both purity ≥99.5% GC) were purchased from Sigma-Aldrich. All volumes of liquids were measured by calibrated volumetric flasks at 21 °C. Weights were measured on a high-precision balance (model XA205, Mettler-Toledo, Gießen, Germany). As fluorescent probes, ATTO 488 carboxylic acid (Atto488), ATTO 655 carboxylic acid (Atto655, both from ATTO-TEC, Siegen, Germany), Alexa Fluor 488 carboxylic acid (Alexa488, ThermoFisher) and crimson beads (ThermoFisher) with a radius of 13 nm, as reported by the manufacturer, were used.

Giant unilamellar vesicle formation GUVs were prepared by means of the electroformation method based on the use of ITO-coated coverslides [Angelova and Dimitrov, 1986, Méléard et al., 2009], closely following the protocol presented by Herold *et al.* [Herold et al., 2012]. Glass coverslides of 25 mm diameter and #1.5 thickness (Menzel-Gläser, Braunschweig, Germany) were coated with ITO by reactive magnetron sputtering (GeSim, Grosserkmannsdorf, Germany). The obtained coating had a thickness of (100 ± 5) nm. The ITO-coated coverslides were cleaned by wiping with tissues (KimWipe, Sigma-Aldrich) soaked in acetone (analytical reagent grade, Fisher Scientific, Pittsburgh, US), followed by 80 vol% ethanol (EMSURE, Merck Millipore) water mixtures. This procedure was repeated twice before the coverslides were rinsed with deionized water and dried with pressurized air. Afterwards, the coverslides were annealed on a hotplate (MR Hei-Standard, Heidolph, Schwabach, Germany) at 150 °C for two hours with the ITO-coated side facing the air. Next, a solution of lipids in chloroform (Uvasol, purity ≥99.0% GC, FisherScientific) with a total lipid concentration of 10 mg/mL was prepared. Experiments were performed on

[1] Aqueous solutions were partially prepared by Sigrid Bauer (Schwille lab, Max Planck Institute of Biochemistry Martinsried, Germany)

GUVs formed from DOPC (Avanti Polar Lipids, Alabaster, AL) with 0.001 mol% FAST DiO (DiO, ThermoFisher) or DOPE headgroup-labeled with ATTO 655 (ATTO-TEC, Siegen, Germany).

We refer to FAST DiO (3,3'-Dilinoleyloxacarbocyanine Perchlorate as DiO). Some other studies use the abbreviation DiO for 3,3'-dioctadecyloxacarbocyanine perchlorate (ThermoFisher). We prepared GUVs with both labels and found no difference in diffusion coefficient by FCS (data not shown).

A volume of 0.7 µL of the lipid solution was deposited on the ITO-coating in a snake-like, non-overlapping pattern on a roughly 1.5x1.5 cm^2 area using a 5 µL Hamilton syringe (model 7105 KH SYR, Hamilton Company, Reno, USA). Subsequently, the coverslides were dried in vacuum for 30 min. As in previous publications, the GUVs were grown by electro-formation in a custom-built chamber [Kahya et al., 2001,Herold et al., 2012,Betaneli and Schwille, 2013]. First, adhesive copper tape (SPI, West Chester, Pennsylvania) was attached to the ITO-coated side of the coverslides to establish a flat conductive contact, which later sticks out of the chamber. Next, two coverslides were brought into proximity with a customized 3 mm teflon spacer in between and the ITO-coatings facing each other. This assembly was sealed with grease (glisseal N, VWR). Note that only one of the coverslides carried lipids. The teflon spacer had holes by design, into which tubes (PE-160/10, Warner Instruments) were inserted. The chamber had a total volume of 300 µL and was loaded with liquid at a flowrate of 1 µL/s using a neMESYS pump (Cetoni, Korbussen, Germany). After loading, the tubes were sealed using hose clamps (Roth, Karlsruhe, Germany). The ITO-coated surfaces were connected to an alternating voltage generator (model HMF2525, Hameg, Mainhausen, Germany or model TG330, AIM & Thurlby Thanday Instruments, UK) through the copper contacts. Finally, vesicles were electroformed for 2 h under a sinusoidal electric field of 10 Hz and 1.2 V (rms).

Bulk viscosity measurements The viscosities of solvents were measured using a rolling ball viscometer (model AMVn, Anton Paar, Graz, Austria). In brief, the fall time t_{fall} of a ball in a capillary mounted at an angle of $\alpha = 70°$ to the horizontal and filled with the solvent of interest was measured. From the fall time, the solvent viscosity can be calculated as $\eta = K t_{\mathrm{fall}}(\rho_{\mathrm{ball}} - \rho_{\mathrm{solvent}})$, where ρ_{ball} is the density of the ball, ρ_{solvent} is the density of the solvent, which was measured by a density meter (model DMA 5000, Anton Paar, Graz, Austria), and K is a system constant. K was determined by reference measurements on deionized water at several temperatures from 20 °C to 40 °C with 2.5 K increments, as recommended by the vendor. The obtained fall times were used to find a second order polynomial $K(T) = a_0 + a_1T + a_2T^2$, such that the empirical formula describing the temperature dependence of the viscosity of pure water found by Kestin *et al.* [Kestin et al., 1978] is matched. The relative error in the investigated temperature range was smaller than 10^{-3}.

Confocal FCS measurements All FCS measurements were carried out on a confocal fluorescence LSM (LSM780) equipped with a ConfoCor3 unit and a 40X C-Apochromat NA 1.2 water immersion objective (Carl Zeiss AG, Oberkochen Germany). Depending on the fluorescent probe, the 488 nm line of an Argon-ion laser or the 633 nm line of a Helium-Neon laser were used for excitation. The square pinhole size was set to one Airy unit accordingly. To avoid afterpulsing-related artifacts, the detected light was split by a 50:50 beam splitter in order to employ pseudo-crosscorrelation. The temperature of the objective and the sample chamber were monitored using a thermocouple-based thermometer (model K202 Voltcraft, Conrad, Germany) and found to be constant at (28 ± 1) °C for all measurements.

For measurements in solution, the position of the upper surface of the coverslide was located by an axial z-scan. The upper coverslide surface was the reference plane for all NFPs reported in this work. From there, the objective was moved upwards by a defined distance. Similarly, the surface was found in the ITO-chambers, making use of the fact that usually there is a residual layer of lipids at the surface (compare figure IV.5A). The exact position of the confocal volume relative to the coverslide surface was not tracked directly. Instead, we tracked the absolute objective position, which is a more practical measure. However, a change of the objective position by a certain distance does not necessarily correspond to a confocal volume moved by the same distance [Hell et al., 1993]. The actual focus position of course depends on the NFP, i.e. the axial position the objective relative to when the top surface of the coverslide was in focus. In addition, it also depends on the refractive index of the solvent and the ratio of optical path length through the immersion water and the path length through the solvent.

The optical system was calibrated on a daily basis using Atto488, or Atto655 freely diffusing in aqueous solution: the confocal volume was positioned 50 µm above the bottom coverslide; the lateral pinhole position was optimized for maximum fluorescence signal and the objectives correction collar was positioned for maximal cpp. Finally, the size of the confocal volume was determined by measuring the diffusion time of fluorescent dyes with known diffusion coefficients. The diffusion coefficient of Atto488 was determined relative to

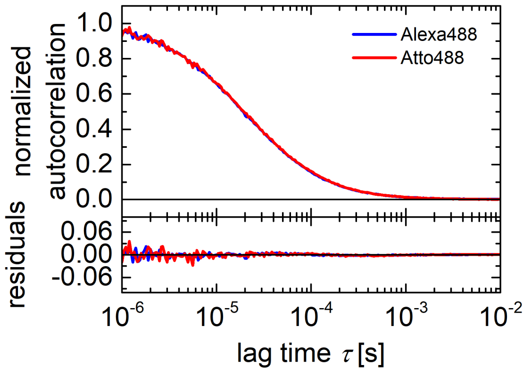

Figure B.1: Measurement of the diffusion coefficient of Atto488 relative to Alexa488. Experimental autocorrelation curves of Atto488 with a carboxyl moiety (Atto488COOH) and Alexa488. For clarity, only the experimental curves are shown without a fit. Both data sets were fit by a 3D diffusion model (equation II.34). Measurements were taken for 4 h at 28 °C and a low excitation irradiance of $I_0/2 = 0.05\,\mathrm{kW/cm^2}$ at 488 nm to exclude photo-artifacts. The fits yield diffusion times of $\tau_D = 19.55\,\mu s$ and $\tau_D = 19.97\,\mu s$ for Alexa488 and Atto488 respectively. The diffusion coefficient of Alexa488 at 25 °C was reported to be $D = 414\,\mu m^2/s$ [Petrov et al., 2006]. Accounting for the temperature dependence of D and η [Kestin et al., 1978], the measurements presented here yield $D = 405\,\mu m^2/s$ at 25 °C for Atto488COOH. In comparison to Alexa488, Atto488 yields a similar cpp but a smaller triplet fraction at the same irradiance. Thus, Atto488 can be excited at higher irradiances without noteworthy triplet saturation effects on the FCS measurements.

Alexa488 (figure B.1). The diffusion coefficients of Alexa488 and Atto655 are given in table II.1. Based on these values, measured at 25 °C, the diffusion coefficient of these fluorophores at any temperature T was calculated based on the well-known relation $D \propto \frac{T}{\eta(T)}$ (equation II.5). The viscosity of water at any temperature was calculated based on the empirical equation provided in [Kestin et al., 1978].

The acquired correlation curves were fitted using a home-written software programmed in MATLAB R2012b (MathWorks, Natick, Massachusetts). Assuming quasi-ergodicity, sufficiently long measurements, i.e. much longer than τ_D [Oliver, 1979, Schätzel et al., 1988, Tcherniak et al., 2009], a 3D Gaussian as detection function, and the absence of optical saturation, equation II.34 was used to analyze the experimental autocorrelation curves. Alternatively, when experimental data showed clear triplet contributions, equation II.35 was used. Similarly, equations II.32 and II.33 were applied to fit autocorrelation curves measured on GUVs. In the case of DiO, the blinking term accounted for cis-trans isomerizations, rather than triplet transitions.

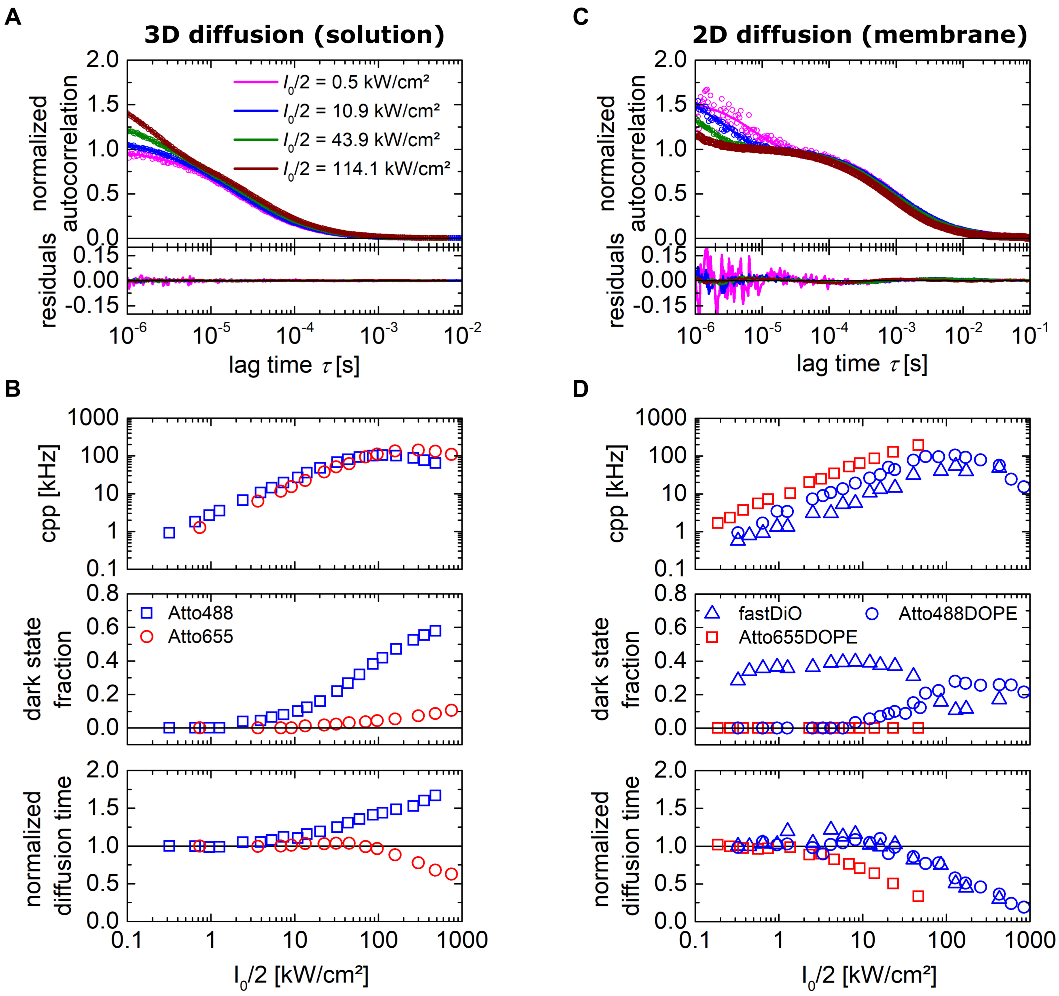

Figure B.2: FCS power series of fluorophores diffusing in 3D and 2D. A) Autocorrelation curves (circles) and fits (lines) with 3D diffusion and triplet blinking model of Atto488 at different excitation irradiances. B) cpp, triplet fraction and apparent diffusion time, normalized to the diffusion time at irradiances below $1\,\mathrm{kW/cm^2}$ are affected by the excitation irradiance. The cpp scales linearly until it reaches a saturation, and the triplet build-up increases only for Atto488 to a noteworthy extent with increasing irradiance. The triplet saturation for Atto488 reflects in the increasing diffusion time, whereas Atto655 shows a reduced diffusion time at large irradiances. C) Autocorrelation curves of DiO in DOPC GUVs at different irradiances. The legend from A) applies. The characteristic time of the isomerization kinetics shifts to shorter lag times with increasing irradiance. D) cpp, triplet fraction and apparent diffusion time for DiO, Atto488DOPE, and Atto655DOPE in DOPC GUVs. For all three fluorophores, the cpp scales linearly with the excitation irradiance until it reaches a saturation. Atto655DOPE reaches the highest cpp. Similarly, all three fluorophores show a notable shortening of the diffusion time above a threshold irradiance because of photobleaching. Atto655DOPE shows in contrast to Atto488DOPE no triplet build-up, whereas DiO shows a dark cis-state population across all irradiances.

To identify a regime free of photo-induced artifacts like triplet saturation and photobleaching [Widengren et al., 1995, Widengren and Rigler, 1996, Eggeling et al., 1998, Petrov and Schwille, 2008a] and yet maximum signal-to-noise, i.e. a high number of detected fluorescence photons, a power series was performed. In detail, autocorrelation curves of several fluorophores diffusing freely in a 3D solution and in a 2D lipid membrane were measured at different excitation powers (figure B.2). The power P behind the objective was measured by placing a specialized sensor (S170C, together with PM100USB hardware powermeter, Thorlabs GmbH, Dachau, Germany) with immersion water directly on the objective. The peak excitation irradiance I_0 was calculated assuming Gaussian beams.

$$I_0/2 = \frac{P}{\pi w_{xy}^2} \tag{B.1}$$

Figures B.2A,B show the results of a power series conducted on Atto488 and Atto655 diffusing freely in deionized water. With increasing irradiance, the autocorrelation curves not only show an increased triplet build-up, but also the apparent diffusion time shifts to larger lag times, which is in line with the previously discussed triplet saturation (compare section II.3.4.3) [Widengren et al., 1995, Gregor et al., 2005, Petrov and Schwille, 2008a]. The cpp increases with increasing irradiance up to more than 200 Hz (around 100 Hz per detector in pseudo-crosscorrelation mode) and decreases afterwards because of photobleaching effects. Interestingly, Atto655 behaves fundamentally different, as it has almost no triplet build-up, which may originate from an effective decay route of the triplet state. One may speculate that the flexible carboxyl chain of Atto655 facilitates such an efficient energy dissipation. At irradiances above $50\,\mathrm{kW/cm^2}$, Atto655 shows effects of bleaching and the apparent diffusion time shortens. Consequently, a higher cpp can be achieved for Atto655 compared to Atto488 without the introduction of photo-induced artifacts. Based on these results, measurements performed in water were conducted at irradiances lower than $I_0/2 < 2.6\,\mathrm{kW/cm^2}$ for Atto488 and $I_0/2 < 20\,\mathrm{kW/cm^2}$ for Atto655. As the photo-physics depends on the local environment, similar controls need to be performed for every solvent separately.

When bound to DOPE and diffusing on GUVs, Atto488 and Atto655 had diffusion times unaffected by photobleaching below $I_0/2 = 10\,\mathrm{kW/cm^2}$ and $I_0/2 = 2\,\mathrm{kW/cm^2}$, respectively (figure B.2D). The lipid analog DiO shows a similar dependence of the apparent diffusion time on the excitation irradiance as DOPE-Atto488. The blinking fraction behaves, however, differently, because DiO is derived from Cy5, which shows pronounced photo-induced cis-trans isomerizations, of which the cis-state is only weakly fluorescent [Widengren and

Schwille, 2000]. All subsequent FCS measurements performed on GUVs in this chapter were thus performed at irradiances $I_0/2 < 1\,\mathrm{kW/cm^2}$.

All fluorescent tracers used in this chapter are considered to be point-like emitters. For crimson beads, which are by far the largest probes used in this study, one may employ a correction for their physical extent [Wu et al., 2008]. The effect is, however, negligible. The autocorrelation curves of crimson beads and Atto655 in deionized water and aqueous solution of 100 mM NaCl were found to be independent of the ion concentration, which allowed us to conclude that electrostatic interactions do not have an impact on the diffusion times of these probes.

B.2 Supporting figures

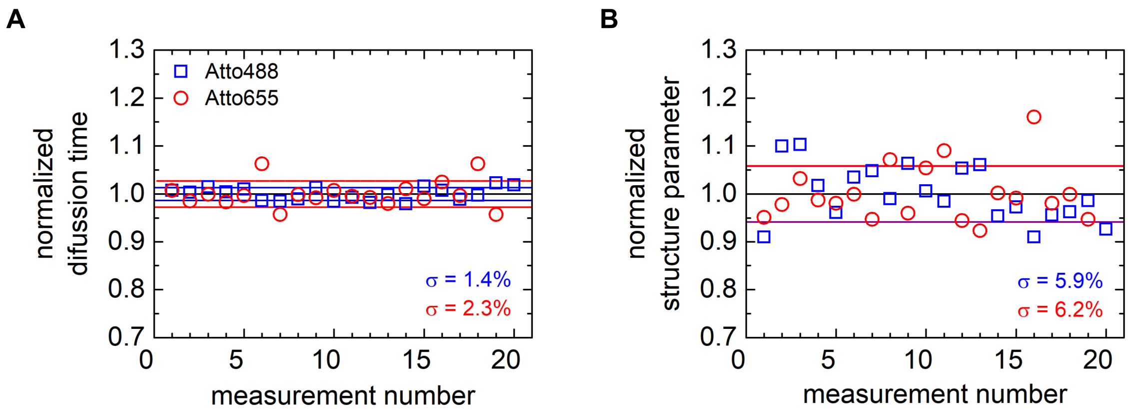

Figure B.3: Reproducibility of individual confocal FCS measurements in water. A) Diffusion times obtained for several FCS measurements on Atto488 and Atto655 in water 100 µm above the coverslide surface. The diffusion times were normalized to their means, lines indicate the standard deviations. B) Structure parameters obtained from the same FCS measurements as in panel A). The relative standard deviations are larger for the structure parameter than for the diffusion time, because the autocorrelation curves for 3D diffusing particles depend only weakly on the structure parameter.

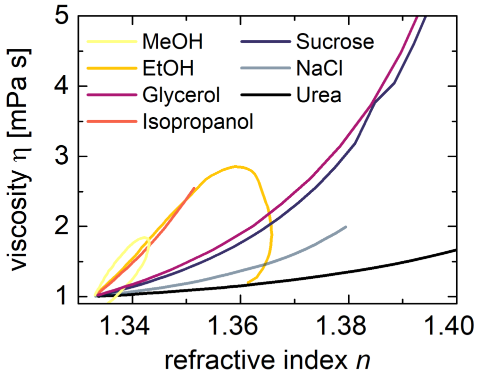

Figure B.4: Relation between viscosity and refractive index for a range of aqueous solutions. All curves share the common point of pure water (bottom left), from which the relation between η and n evolves differently with increasing concentration of a particular substance. The respective concentrations increase along each curve. For methanol (MeOH) and ethanol (EtOH), the viscosity does not show a monotonous dependence on the concentration, but has a local extreme. On the one hand, for MeOH and EtOH the viscosity changes quite drastically with rather small corresponding changes of the refractive index. At the other end of the spectrum, aqueous solutions of urea shows only moderate increase in viscosity, while at the same time the refractive index changes significantly. Data taken from [Haynes, 2014].

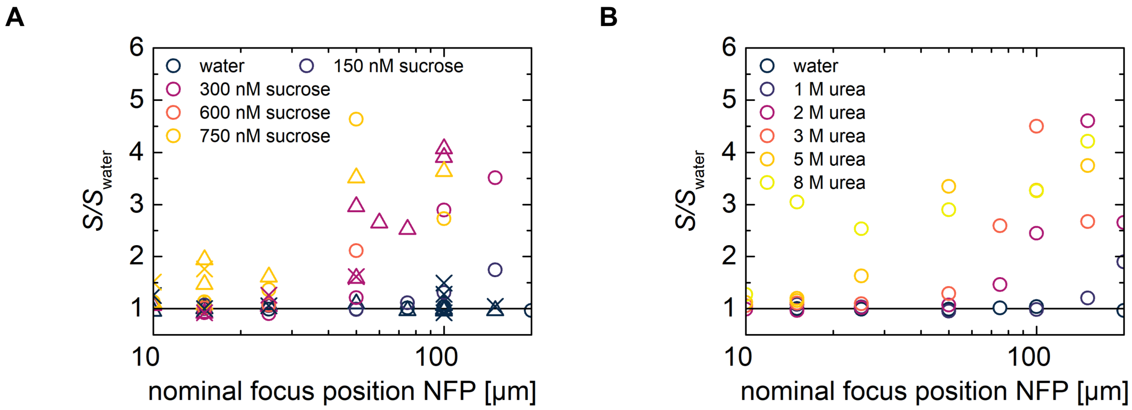

Figure B.5: Structure parameter depends on the NFP in media with a refractive index mismatch. A) Structure parameter S of Atto655 (circles), Atto488(triangles), and crimson beads (crosses) in different sucrose concentrations measured at different NFPs, relative to the structure parameter in water S_{water}. The apparent structure parameter shows a large scatter and differ massively from measurements in pure water. B) As in A), but measurements were performed on Atto655 in aqueous solutions with different concentrations of urea. The results presented in this figure correspond to the same set of measurements as figure IV.3, which shows the corresponding diffusion times. In a regular confocal FCS experiment on Atto655 diffusing in water, performed on the commercial LSM780 ConfoCor3 system used in this work, the structure parameter is around 6 to 7. Consequently, ratios $S/S_{\text{water}} > 2$ cannot be determined reliably as the autocorrelation curves become insensitive to S. Ratios $S/S_{\text{water}} > 6$ were obtained for some fits, but are not displayed here.

B.3 Supporting tables

Table B.1: Refractive indices and viscosities of analyzed aqueous solutions. Refractive indices were taken from [Haynes, 2014]. The viscosities were measured using a rolling ball viscometer (compare Materials and Methods in appendix B.1). The ratio $\eta/\eta_{\mathrm{water}}$ is the quantity accessible via FCS measurements.

aqueous solution	refractive index n	viscosity η at 28 °C [mPa s]	viscosity relative to water $\eta/\eta_{\mathrm{water}}$ at 28 °C
water	1.333	0.833	1
150 mM sucrose	1.340	0.954	1.145
300 mM sucrose	1.347	1.087	1.305
600 mM sucrose	1.362	1.519	1.824
750 mM sucrose	1.370	1.835	2.204
1000 mM sucrose	1.382	2.506	3.009
1200 mM sucrose	1.391	3.488	4.187
1 M urea	1.341	0.865	1.039
2 M urea	1.350	0.905	1.087
3 M urea	1.359	0.955	1.147
5 M urea	1.375	1.087	1.305
8 M urea	1.400	1.380	1.657
10 vol% glycerol	1.348	1.136	1.364
20 vol% glycerol	1.363	1.620	1.945
30 vol% glycerol	1.378	2.352	2.824
10 wt% ethanol	1.340	1.203	1.444
20 wt% ethanol	1.347	1.617	1.941
40 wt% ethanol	1.358	2.121	2.546

C

APPENDIX TO CHAPTER V

C.1 Materials and Methods

Buffers BZ3 buffer contained 50 mM Tris-HCl, together with 300 mM KCl, 20 mM imidazole, and 10 vol% glycerol. BZ4 buffer with 50 mM Tris-HCl, 300 mM KCl, 250 mM imidazole, and 10 vol% glycerol was used for eluting protein from a His-column. P buffer contained 50 mM HEPES/NaOH pH 7.2, 50 mM KCl, 5 mM $MgCl_2$. PG buffer was identical to P buffer, but also contained 10 vol% glycerol.

Protein purification For the purification of WT FtsZ, FtsZN211A[1] and FtsZΔCtl[2], the *E. coli* strain Rosetta was transformed with the respective plasmid and grown to reach an optical density of $OD = 0.6$ at 600 nm. To induce protein expression, Isopropyl β-D-1-thiogalactopyranoside (IPTG) was added to a final concentration of 0.5 mM and the cells were grown for three hours. Subsequently, the transformed cells were harvested by centrifugation. The pellet was weighted and frozen at −80 °C until further use. After thawing, the protein was resuspended in buffer BZ3. The added volume of BZ3 was adjusted such that a ratio of 2 mL/g between added volume and mass of cells was achieved. Here, BZ3 contained 100 µg/mL phenylmethylsulfonyl fluoride (PMSF), which inhibits serine proteases to prevent protein digestion, and 10 units/mL DNase I to digest DNA, which may potentially adhere in the purification column. The suspended cells were lysed in three passages in a french press at 16 000 psi. After centrifugation of the suspension for 60 min at $38400 \cdot g$ and passage through a membrane filter (pore size 0.22 µm), the supernatant was transferred to a HisTrap HP 5 mL column (GE Healthcare, Freiburg, Germany) and equilibrated with BZ3 buffer. Upon equilibration, the protein was eluted with BZ4 buffer. Pooled fractions containing the protein of interest were dialyzed against PG buffer in two steps for 18 and 4 hours. The His-SUMO tag was cleaved by incubation of the protein with Ubiquitin-like-specific-His protease 1 in the presence of 1 mM Dithiothreitol (DTT), to prevent the formation of intermolecular disulfide bonds. The cleaving was performed

[1] Purification by Laura Corrales Guerrero, PhD (Thanbichler lab, Philipps University Marburg, Germany)

[2] Purification by Jaspara Knopp (Thanbichler lab, Philipps University Marburg, Germany)

at 4 °C for 2 hours. In a last purification step, His-SUMO and Ubiquitin-like-specific-His protease 1 were separated from FtsZ through another HisTrap HP 5 mL column and an elution with PG buffer. The fractions containing only FtsZ were pooled together, aliquoted and stored at −80 °C. The protein concentration was determined in a Bradford assay using Roti®-Nanoquant (Carl Roth GmbH + Co. KG, Karlsruhe, Germany), with BSA samples of known concentrations as a standard.

FtsZ-YFP-mts[3] was expressed and purified similar to a previously described protocol [Osawa et al., 2008]. This chimeric protein consists of the first 366 amino acids from *E. coli*, followed by YFP-Venus, and the mts of MinD from *E. coli* (FIEEEKKGFLKRLFGG) [Szeto et al., 2003, Osawa et al., 2008]. The protein was expressed from a pET-447 expression vector in the *E. coli* strain BL21. The cells were grown at 20 °C, and lysed by sonication. The protein was precipitated by 30% ammonium sulphate, incubating the mixture for 20 min on ice (slow shaking). After centrifugation, the pellet was resuspended and the protein was purified by anion exchange chromatography on a 5x 5 mL HiTrap Q-Sepharose column (General Electric Healthcare, 17515601). Finally, the purity of the protein was confirmed by SDS-PAGE and mass spectrometry.

Size exclusion chromatography Size exclusion experiments were performed on a Superdex 200 10/300 GL column on an Äkta® system (General Electrics Healthcare), using Dextran Blue, Thyroglobulin, Ferritin, Aldolase, Conalbumin, Ovoalbumin, Ribonuclease A and Aprotinin as reference standards.

Fluorescent labeling of FtsZ FtsZ from *C. crescentus* contains only one cysteine (residue 123, compare figure V.1 and appendix C.2), which is surface exposed, but does not appear to form disulfide bonds with other FtsZ proteins. Thus, the fluorescent labeling was performed through a fluorescent dye with a maleimide moiety, which binds to thiol groups. In brief, FtsZ was prepared at a concentration of around 75 µM (4 mg/mL). 1 mg Alexa Fluor 488 C5-maleimide (Alexa488, Life Technologies/ Thermo Fisher Scientific) was diluted in 100 µL dimethylsulfoxid (DMSO). 32 µL of this dye solution was added to 500 µL of the FtsZ solution and incubated overnight at 4 °C. Unbound fluorophores were

[3]Expression and Purification by Diego Ramirez, Daniela A. García-Soriano, Michaela Schaper, Kerstin Andersson (all Schwille lab, Max Planck Institute of Biochemistry Martinsried, Germany), and Ana Raso (Rivas lab, Centro de Investigaciones Biológicas, Consejo Superior de Investigaciones Científicas (CSIC), Madrid, Spain, and Schwille lab, Max Planck Institute of Biochemistry Martinsried, Germany), who used the plasmid kindly provided by Masaki Osawa and Harold P. Erickson.

removed in a two step dialysis at 4 °C against 1000 mL and 600 mL of P buffer with PMSF additive. Finally, the procedure was validated via SDS-PAGE with a fluorescence option.

It should be noted, that only 10% of labeled FtsZ was used in FCS experiments. The other 90% were unmodified WT FtsZ proteins, because labeled FtsZ appears not to be fully functional. Thus, it is not entirely clear how Alexa488-labeled FtsZ incorporates into wildtype filaments, and whether it alters the average filament length

Sample chamber preparation All measurements were performed in a simple homemade chamber, previously described for SLB experiments, e.g. [Betaneli and Schwille, 2013, Vogel et al., 2013]. For this, #1.5 coverslides (Menzel Gläser, Braunschweig, Germany) were thoroughly rinsed with acetone, ethanol and milliQ water, with intermediate rubbing with tissue. 500 µL tubes (Eppendorf, Hamburg, Germany) were cut in halves, the lid removed, and glued to the cleaned coverslide with a ultraviolet (UV)-curable glue (Norland Adhesive 65, Norland Products Inc., Cranbury, USA). The whole chamber was plasma-cleaned (MiniFlecto-PC-MFC, plasma technology, Herrenberg-Gültstein, Germany) for 10 minutes at 0.3 mbar (vacuum pump DUO 5M, Pfeiffer Vacuum GmbH, Asslar, Germany). The chambers were incubated with 100 µL of 2 mg/mL BSA for around 20 min and washed 10 times with 200 µL each of P buffer. Finally, all liquid was taken off and a controlled amount of 200 µL P buffer was added quickly after. All experiments were performed with a labeling ratio of 1:10.

FCS experiments The confocal FCS experiments were performed on the same LSM780 equipped with a ConfoCor3 unit (Carl Zeiss AG, Germany) described in appendix B.1 to chapter IV (page 241f). All measurements were perfomred in pseude-crosscorrelation mode. The calibration measurements were performed on a daily basis using ATTO488 carboxylic acid (Atto488) diffusing in water. The diffusion coefficient of Atto488 is $D = 405\,\mu m^2/s$ at 25 °C, as determined in the context of the previous chapter (figure B.1 in appendix B.2). For all experiments, the upper side of the coverslide was located based on the steep increase of signal, once the confocal detection volume enters the sample volume from below. From there, the detection volume was moved 50 µm into the sample to avoid surface effects. The composition of P buffer has no indication for a refractive index significantly different from that of water. Hence, no effects of refractive index mismatch on the FCS experiments was expected.

The experimental autocorrelation curves typically showed at least two distinct decays. Thus, if not mentioned otherwise, the autocorrelation curves were fitted by a model func-

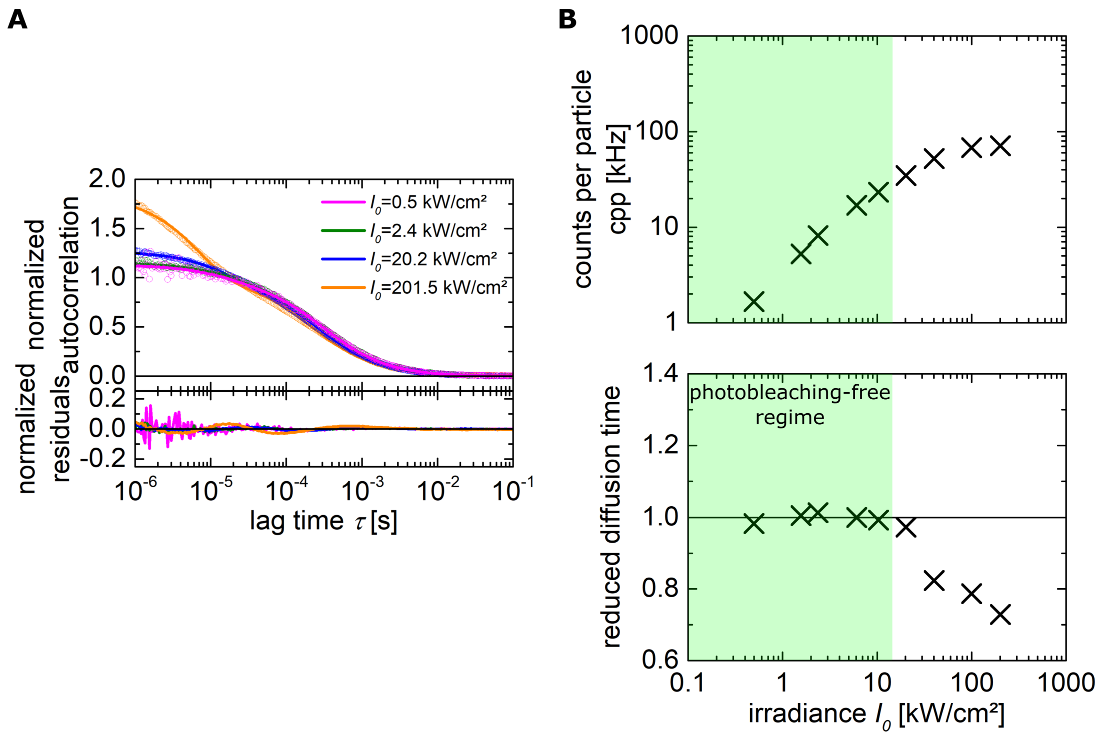

Figure C.1: FCS power series on WT FtsZ. A) Representative autocorrelation curves of WT FtsZ in the absence of GTP at different irradiances. For low irradiances, a two component diffusion model with one fixed diffusion time for free dye describes the measurements with small residuals, whereas for larger irradiances, the correlation curves shift to shorter times and the model function shows systematic residuals. B) cpp and reduced diffusion time for different irradiances. With increasing irradiances, the triplet state is higher populated and the probability of photobleaching increases, both resulting in a deviation from a linear response of the system. Above $I_0 = 10\,\mathrm{kW/cm^2}$, the diffusion time becomes shorter because of photobleaching. All further experiments are therefore conducted at around $I_0 = 2\,\mathrm{kW/cm^2}$. The diffusion time was normalized to the mean of the diffusion times at the lowest four irradiances, yielding the reduced diffusion time.

tion, which accounts for two freely diffusing components of identical brightness $Q_1 = Q_2$. This special case of multicomponent diffusion (equation II.37) is described by the autocorrelation function:

$$G(\tau) = \frac{1}{N_1 + N_2} \sum_{i=1}^{2} f_i \left(1 + \frac{\tau}{\tau_{D,i}}\right)^{-1} \left(1 + \frac{\tau}{S^2 \tau_{D,i}}\right)^{-1/2} \tag{C.1}$$

Here, the relative abundances $f_1 = N_1/(N_1 + N_2)$ and $f_2 = N_2/(N_1 + N_2)$ of both species were introduced. One of the two components is attributed to freely diffusing Alexa488 which is not attached to any protein. To minimize the amount of free parameters, the diffusion coefficient of free Alexa488 was measured once accurately and found to be in line with previously reported values [Petrov et al., 2006]. After each daily calibration measurement, the diffusion time of Alexa488 was calculated for the measured detection volume size. This diffusion time was kept fixed for the first component for all fits.

To ensure that the FCS experiments were taken at irradiances with little to no photo-induced artifacts, a power series was performed, as shown in figure C.1. The irradiance was estimated based on the power P after the objective, as measured with a powermeter (PM100USB) and a slide-mimicking detector (S170C, both Thorlabs GmbH, Dachau, Germany) that is directly positioned on the objective, including immersion fluid. Moreover, the lateral beam diameter w_{xy} is known from the daily calibration measurements on freely diffusing fluorescent dye of known diffusion coefficient. Consequently, the peak irradiance in the focus reads $I_0 = 2P/(\pi w_{xy}^2)$. As expected, at low irradiances, the obtained autocorrelation curves decay at the same lag times, whereas at high irradiances the triplet contribution becomes bigger and the autocorrelation curve shifts to shorter lag times. Moreover, the 3D+3D model does not hold any longer at large irradiances, which can be inferred from the systematic residuals (orange line, figure C.1A). This effect directly reflects on the outcome of the FCS analyses, as shown for cpp and diffusion time in figure C.1B. For low irradiances, the cpp increases linearly with the irradiance and the diffusion time is invariant to the irradiance. On the other hand, at sufficiently high irradiances, triplet build up and photobleaching lead to fluorescence saturation effects. Moreover, the diffusion time shortens, because of photobleaching (compare section II.3.4.3 and figure B.2 in appendix B.1). The diffusion times also show a slight increase from $1\,\mathrm{kW/cm^2}$ to $10\,\mathrm{kW/cm^2}$. This effect is however below 5% and is thus neglected. Based on these findings, all experiments in this chapter were performed at $I_0 \approx 2\,\mathrm{kW/cm^2}$.

C.2 Supporting figures

```
E. coli          ....MFEPMELTNDAVIKVIGVGGGGNAVEHMVRERIEGVEFFAVNT     44
C. crescentus    MAISLSAPRTTELKPRIVVFGVGGAGGNAVNNMIEAGLEGVEFVVANT     48
B. subtilis      ...MLEFETNIDGLASIKVIGVGGGGNNAVNRMIENEVQGVEYIAVNT     45
S. aureus        ...MLEFEQGFNHLATLKVIGVGGGGNNAVNRMIDHGMNNVEFIAINT     45

E. coli          DAQALRKTAVGQTIQIGSGITKGLGAGANPEVGRNAADEDRDALRAAL     92
C. crescentus    DAQQLQFAKTDRRIQLGVQITQGLGAGAHPEVGMSAAEESFPEIGEHL     96
B. subtilis      DAQALNLSKAEVKMQIGAKLTRGLGAGANPEVGKKAAEESKEQIEEAL     93
S. aureus        DGQALNLSKAESKIQIGEKLTRGLGAGANPEIGKKAAEESREQIEDAI     93

                                         fluorescent label
                                                 ↓
E. coli          EGADMVFIAAGMGGGTGTGAAPVVAEVAKDLGILTVAVVTKPFNFEGK    140
C. crescentus    DGAHMVFITAGMGGGTGTGAAPIIAKCARERGILTVGVVTKPFHFEGR    144
B. subtilis      KGADMVFVTAGMGGGTGTGAAPVIAQIAKDLGALTVGVVTRPFTFEGR    141
S. aureus        QGADMVFVTSGMGGGTGTGAAPVVAKIAKEMGALTVGVVTRPFSFEGR    141

E. coli          KRMAFAEQGITELSKHVDSLITIPNDKLLKVLGRGISLLDAFGAANDV    188
C. crescentus    HRMRLADSGIQELQRYVDTLIVIPNQNLFRVANERTTFAEAFGMADQV    192
B. subtilis      KRQLQAAGGISAMKEAVDTLIVIPNDRILEIVDKNTPMLEAFREADNV    189
S. aureus        KRQTQAAAGVEAMKAAVDTLIVIPNDRLLDIVDKSTPMMEAFKEADNV    189

E. coli          LKGAVQGIAELITRPGLMNVDFADVRTVMSEMGYAMMGSGVASGEDRA    236
C. crescentus    LHSGVRSITDLMVLPGLINLDFADVRTVMTEMGKAMMGTGEGTGEDRA    240
B. subtilis      LRQGVQGISDLIATPGLINLDFADVKTIMSNKGSALMGIGIATGENRA    237
S. aureus        LRQGVQGISDLIAVSGEVNLDFADVKTIMSNQGSALMGIGVSSGENRA    237

E. coli          EEAAEMAISSPLLEDIDLSGARGVLVNITAGFDLRLDEFETVGNTIRA    284
C. crescentus    LMAAQNAIANPLLDEVSLKGAKAVLVNVTGGMDMTLLEVDEAANAISD    288
B. subtilis      AEAAKKAISSPLLE.AAIDGAQGVLMNITGGTNLSLYEVQEAADIVAS    284
S. aureus        VEAAKKAISSPLLE.TSIVGAQGVLMNITGGESLSLFEAQEAADIVQD    284

                                                             deleted Ctl
E. coli          FASDNATVVIGTSLDPDMNDELRVTVVATGIGMDKRPEITLVTN....    328
C. crescentus    QVDPEANIIFGAAFDPSLEGVIRVSVVATGMDGASIAQIEPKPVSRNI    336
B. subtilis      ASDQDVNMIFGSVINENLKDEIVVTVIATGFIEQEKDVTKPQ.RP...    328
S. aureus        AADEDVNMIFGTVINPELQDEIVVTVIATGFDDKPTSHGRKSGST...    329
```

```
                                  deleted Ctl
E. coli          ..........KQVQQPVM....DRYQQHGMA..PLTQ..EQKPVAKVV    358
C. crescentus    SAAPLIAETSRPAPQPEPARPTARYEAARPAERPVAFAPEPAPEPEIV    384
B. subtilis      SLNQSIKTHNQSVPKREPKR...E....EPQ...........QQN...    355
S. aureus        GFGTSVNTSSNATSKDESFTSNSS....NAQ...........ATD...    359

                                  deleted Ctl
E. coli          ND............NAP...................QTAKEPDYLDIP    375
C. crescentus    MSAPQPEPEAELYYDEPTVAEEPRVSAAPARSVNRIVDPLVDDVAEEP    432
B. subtilis      ...............................TVSRHTSQPADDTLDIP    372
S. aureus        ...............................SVSE..RTHTTKEDDIP    374

                                  deleted Ctl
E. coli          AFLRKQAD........................................    383
C. crescentus    LFPENNYYEERRPQKQGGFFSMFGGGRQRYEQQASAPQAQARSAQSAR    480
B. subtilis      TFLRNRNKRG......................................    382
S. aureus        SFIRNREERRSRRTRR................................    390

E. coli          ............................    383
C. crescentus    PQLQPIETPQADDAEDLEIPSFLRRLAN    508
B. subtilis      ............................    382
S. aureus        ............................    390
```

X non conserved
X similar
X $\geq$ 50% conserved

Figure C.2: Sequence alignment of FtsZ proteins from different organisms. FtsZ is highly conserved across many bacteria, as shown in a sequence alignment. Sequences for alignment were taken from Uniprot [UniProt Consortium., 2017, Chen et al., 2017]. In detail, the FtsZ proteins from *E. coli* (accession number P0A9A6) , *C. crescentus* (B8H080), *B. subtilis* (P17865), and *S. aureus* (P0A031) were compared. The alignment was performed using Clustal Omega [Sievers et al., 2011, Li et al., 2015, McWilliam et al., 2013]. The annotations refer to *C. crescentus*. At amino acid (aa) 123, a cysteine is used for chemical labeling. The FtsZ mutant (*C. crescentus*) with deleted Ctl ((FtsZΔCtl) was generated with aa 336-480 deleted. The Ctl is slightly longer than the deleted sequence. Accoring to Sundararajan *et al.*, the Ctl of FtsZ spans aa 317–367 in *E. coli*, aa 321–492 in *C. crescentus*, aa 317–364 in *B. subtilis* [Sundararajan et al., 2015].

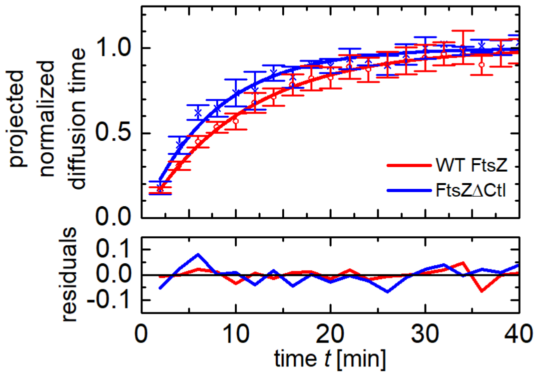

Figure C.3: Time-resolved filament formation of FtsZ. Evolution of the diffusion time for WT FtsZ (blue) and FtsZΔCtl (green) after injection of 2 mM GTP. The diffusion times are obtained from FCS measurements, normalized to the diffusion time prior to the addition of GTP and are projected onto the interval $[0, 1]$ by calculating the quantity $(\tau_D(t) - \tau_D(0)) / (\tau_D(t) - \tau_D(\infty))$. Each point corresponds to mean and standard deviation of 14 (WT FtsZ) and 4 (FtsZΔCtl) polymerization experiments. The points were fitted by a logistic function with an offset. The obtained characteristic rates are $(0.09 \pm 0.01)\ \mathrm{min}^{-1}$ and $(0.13 \pm 0.01)\ \mathrm{min}^{-1}$ for WT FtsZ and FtsZΔCtl respectively.

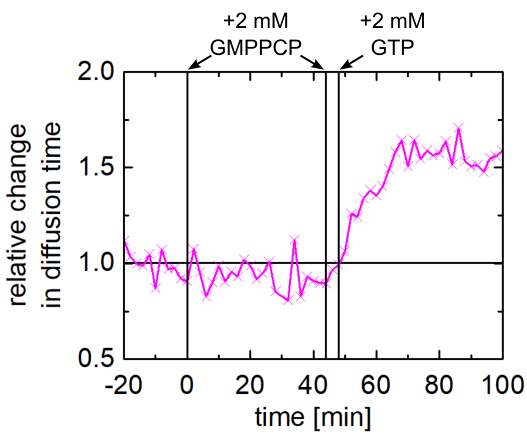

Figure C.4: WT FtsZ does not form filaments with non-hydrolysable GTP. diffusion time as obtained by FCS for WT FtsZ. Upon addition of GMPPCP, which is a non-hydrolysable analogue of GTP, the diffusion time does not change. The same holds, when the concentration of GMPPCP is doubled $t = 42$ min to a total of 4 mM. Upon addition of GTP, filaments start forming, as indicated by an increase in diffusion time. The overall increase in diffusion time is however smaller than after a direct initial addition of GTP (compare figure V.2C).

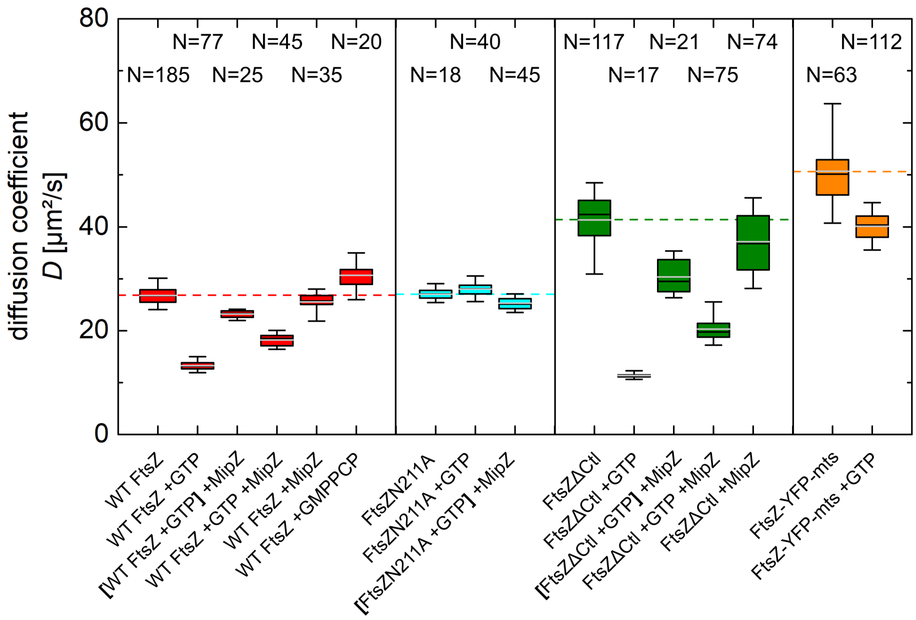

Figure C.5: Diffusion coefficients of several FtsZ mixtures. WT FtsZ diffusion (red) slows down upon addition of 2 mM GTP, and speeds up again upon later addition of 1 µM MipZ (rectangular brackets indicate a preincubation). If all components (1 µM WT FtsZ, 2 mM GTP, 1 µM MipZ) are incubated together from the start, the average diffusion coefficient is larger than after preincubation of WT FtsZ and GTP. All mixtures without GTP, including the mixture of WT FtsZ with non-hydrolizable GMPPCP, yield diffusion coefficients on the level of WT FtsZ only (dashed line), although the mixture of WT FtsZ with MipZ appears to have a slightly lower diffusion coefficient (see text). The diffusion coefficient of the mutant FtsZN211A (cyan) is not affected by the addition of GTP, but is slightly altered by MipZ. The effect of GTP and MipZ on FtsZΔCtl (green) are qualitatively identical to WT FtsZ, although the absolute numbers are different. In contrast to the other FtsZ proteins, which are derived from *C. crescentus*, the construct FtsZ-YFP-mts (orange) is derived from *E. coli*, fused to a fluorescent protein, and terminated by an mts from *E. coli* MinD. Here, the increase in diffusion coefficient upon addition of GTP is less pronounced than for WT FtsZ and FtsZΔCtl. The means (gray lines) and medians (black lines) are shown.

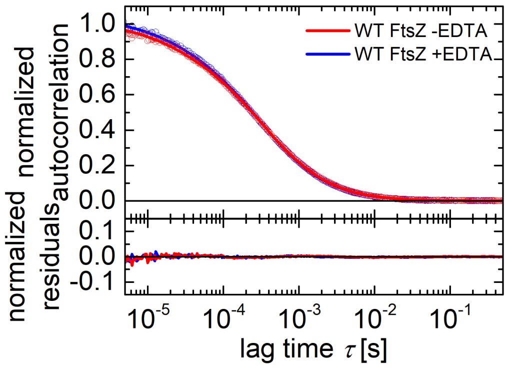

Figure C.6: Effect of EDTA on WT FtsZ. Representative normalized autocorrelation curves of WT FtsZ in the absence of GTP with and without EDTA are indistinguishable. To exclude that any differences between WT FtsZ and FtsZΔCtl are induced by residual nucleotides from the purification protocol, a similar experiment to the previous without GTP was conducted on WT FtsZ. This time, 25 mM EDTA was added to scavenge the cofactor Mg^{2+}. The depletion of Mg^{2+} did not alter the diffusion of WT FtsZ (figure C.6), further supporting the idea that in the absence of GTP the interaction between WT FtsZ proteins is of different nature than the regular filament formation, which requires Mg^{2+} as a cofactor. However, it should be noted, that to further exclude trace amounts of Mg^{2+}, the protein should be dialysed in EDTA containing buffer and remeasured by FCS.

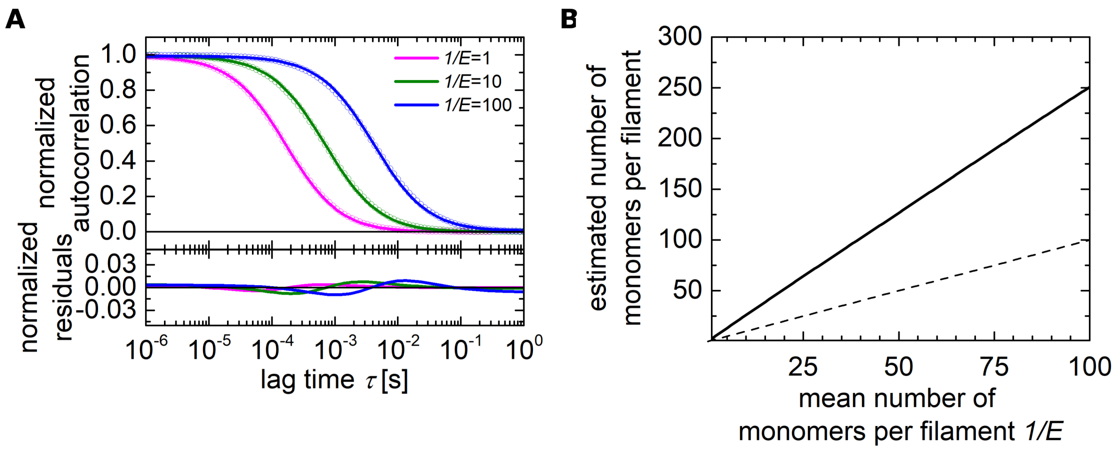

Figure C.7: Brightness-induced bias of the estimated filament length. A) Autocorrelation curves for a length distribution of filaments calculated based on equation V.15 for $E = 0.1, 0.01, 0.001$. The following parameters were used: $r_0 = 2.5\,\text{nm}$, $w_{xy} = 200\,\text{nm}$, $S = 6$, $\eta = 0.857\,\text{mPa s}$, $T = 300\,\text{K}$. The brightness of each j-mer was assumed to be proportional to j. The computed autocorrelation curves were fitted by a single-component diffusion model (equation II.34). B) As in chapter V.2.3, the diffusion times from the single-component fit were translated into a mean filament length using equation V.7. The estimated filament length was plotted versus the assumed mean filament length $1/E$. The dashed line corresponds to the assumed mean filament length, i.e. slope 1.)

D

APPENDIX TO CHAPTER VI

D.1 Materials and Methods

Lipids The lipids1,2-dimyristoyl-sn-glycero-3-phosphocholine (DMPC), ovine brain ganglioside (G_{M1}), 1,2-dioleoyl-sn-glycero-3-[(N-(5-amino-1-carboxypentyl)iminodiacetic-acid)-succinyl] (nickel salt) (DOGS-NTA(Ni)), and *Escherichia coli* polar lipid extract were purchased from Avanti Polar Lipids (Alabaster, Al, USA). 1,2-dioleoyl-sn-glycero-3-phosphoethanolamine (DOPE) with an ATTO655 or ATTO488 headgroup label were purchased from ATTO-TEC (Siegen, Germany). All lipids were stored in their lyophilized form. The lipid mixtures were prepared using high purity chloroform (Merck KGaA, Darmstadt, Germany) and their respective concentration was determined by gravimetry. In brief, a known volume of lipids dissolved in chloroform was deposited in an aluminum crucible (1/3 ME-51119870, Thermal Support Inc., USA) of known mass, heated to 40 °C (Dri-Block DB-3A, Cole-Parmer, Staffordshire, UK) to enforce chloroform evaporation and finally measured on a scale (UMX2, Mettler Toledo GmbH, Gießen, Germany) to determine the residual lipid mass. The lipid mixtures were prepared with a target concentration of 0.1 mg/mL, containing 0.01 mol% of ATTO655-DOPE or ATTO488-DOPE for imaging and FCS purposes.

Proteins and Peptides bovine serum albumin (BSA) was purchased from Sigma-Aldrich (Taufkirchen, Germany); pentameric β subunit of cholera toxin (CtxB) fluorescently labeled with Alexa Fluor 488 was purchased from Invitrogen (Carlsbad, CA, USA). The membrane proximal external region (MPER) of the envelope glycoprotein gp41 of HIV-1 was purified by the Biochemistry Core Facility of the Max Planck Institute of Biochemistry with degree of purity > 90%. In detail, the peptide ATTO488-C<u>ELDKWASLWNWF</u> (underlined sequence corresponds to amino acids 662-673 by HXBc2 numbering) was used. Moreover, following established protocols, MinD, MinE [Loose et al., 2008] and enhanced green fluorescent protein (eGFP)-MinD [Zieske et al., 2014] were purified by the Biochemistry Core Facility of the Max Planck Institute of Biochemistry. For chemical labeling of MinD, LD650-MAL was purchased from Lumidyne Technologies (New York, USA). The mts of the protein MinD from Bacillus subtilis was expressed and purified together with

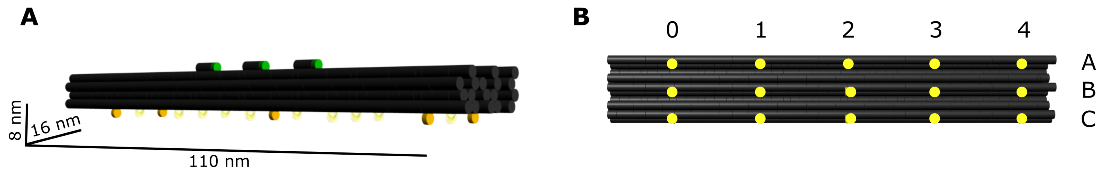

Figure D.1: Schematic of the rod-like DNA origami. A) The DNA origami under investigation has a large aspect ratio and is decorated with five cholesteryl anchors at the bottom facet. The top facet carries three fluorescent dyes (ATTO488). Bottom view of the DNA origami show 15 potential attachment points for cholesteryl anchors. Here, no positions (nanostructure N), or positions A0, A4, B2, C0 and C4 were modified (nanostructure X5). Figure adapted from [Khmelinskaia et al., 2016].

the fluorescent protein mCherry (mCherry-mts) by Philipp Glock and Beatrice Ramm[1]. The fluorescent protein mNeonGreen [Shaner et al., 2013] was purified by Katharina Nakel, Kerstin Andersson and Magnus-Carsten Huppertz following a reported protocol (Master's thesis Frederik Steiert [Steiert, 2016])[2].

DNA origamis The elongated DNA origami structure described in [Khmelinskaia et al., 2016] was designed, folded and purified by Alena Khmelinskaia. The DNA origami is decorated with 15 binding sites, which can be addressed individually by specific DNA hybridization. Two variations of elongated DNA origamis were produced: an unmodified (N) and a cholesterol (Chol)-modified (X5) DNA nanostructure (figure D.1). For X5, the oligonucleotides in the bottom positions A0, A4, B2, C0 and C4 were extended with a 18 nucleotide sequence complementary to the 5′-TEG-Chol modified oligonucleotide AACCAGACCACCCATAGC (Sigma-Aldrich, Taufkirchen, Germany). For detection by fluorescence microscopy and spectroscopy, both N and X5 were functionalized with three 5′-ATTO488-modified oligonucleotides GGGTTTGGTGTTTTTT (Eurofins, Planegg, Germany), positioned on the top facet close to the center of the structure. Folding, purification and quantification of DNA nanostructures was performed as previously reported [Khmelinskaia et al., 2016].

Buffers SLB buffer (10 mM 4-(2-hydroxyethyl)-1-piperazineethanesulfonic acid (HEPES), 150 mM NaCl, pH 7.4) was used for most described measurement. M buffer (25 mM Tris-

[1] Ramm, B., Glock, P., Mücksch, J., Blumhardt, P., Heymann, M., Schwille, P., The MinDE system is a generic spatial cue for membrane protein distribution *in vitro*. *(manuscript submitted)*

[2] Steiert, F., Petrov, E. P., Schultz, P., Schwille, P., Weidemann, T. *(manuscript submitted)*

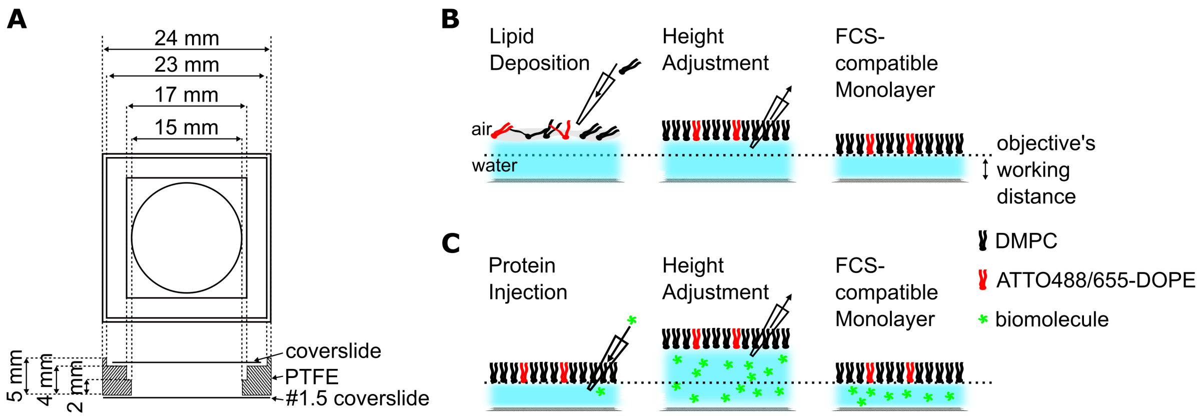

Figure D.2: Monolayer deposition in miniaturized chambers. A) Schematic of the miniaturized chamber. B) A known amount of lipids dissolved in chloroform is deposited on an air-water interface. A lipid monolayer forms upon evaporation of the chloroform. The lipid packing is controlled by the amount of lipid loaded on the interface. To ensure that the monolayer is within the working distance of the imaging objective (from below, not shown), the axial position of the monolayer is adjusted by removing subphase volume. C) For the injection of a biomolecule of interest, a pipette tip pierces the monolayer to inject biomolecules directly into the subphase. This step requires another adjustment of the axial position of the monolayer. For imaging purposes, the monolayer is doped with a small fraction of fluorescently labeled lipids.

HCl, 150 mM KCl, 5 mM $MgCl_2$, pH 7.5) was used for experiments involving Min proteins or mCherry-mts. For DNA nanostructures, FOB buffer (5 mM Tris-HCl, 1 mM EDTA, 5 mM $MgCl_2$, 300 mM NaCl, pH 8.0) was used.

Monolayer preparation in miniaturized chambers The miniaturized chambers were custom-made, inspired by the design by Chwastek and Schwille [Chwastek and Schwille, 2013], but with higher walls to make the system more robust to shaking-induced surface waves, which unavoidably occur during transfer of the chamber to the microscope. The chambers were assembled using spacers, which were laser cut from a 5 mm thick PTFE sheet. Before every experiment, the PTFE spacers were cleaned in a series of 30 min sonication steps in acetone, chloroform, isopropanol and ethanol (all Merck KGaA, Darmstadt, Germany). A #1.5 coverslide (Menzel Gläser, Braunschweig, Germany) was glued to the bottom of the PTFE spacer using picodent twinsil 22 two component glue (picodent, Wipperfürth, Germany). The coverslide size matched the chamber size (24 mm × 24 mm) to ensure that the coverslide would lie flat on the microscopy stage during subsequent FCS and fluorescent imaging experiments, ensuring a perpendicular position of the coverslide with respect to the optical axis. Directly before lipid deposition, the miniaturized chambers were thoroughly rinsed with distilled milliQ water and 99% ethanol, dried under air-flow and plasma-cleaned (MiniFlecto-PC-MFC, plasma technology, Herrenberg-Gültstein, Germany) for 10 minutes at 0.3 mbar (vacuum pump DUO 5M, Pfeiffer Vacuum GmbH, Asslar, Germany) to make the glass hydrophilic. The cleaned chambers were loaded with 200 µL of aqueous buffer. The prepared mixture of lipids in chloroform was deposited drop-by-drop on the buffer-air interface to reach the desired lipid density [Chwastek and Schwille, 2013] (see figure D.2B). To ensure that the monolayer was accessible to experiments using the long working distance objective LD C-Apochromat (40X, NA 1.1, water immersion, Carl Zeiss AG, Oberkochen, Germany), 20 µL to 40 µL of the aqueous phase were pipetted out after complete evaporation of chloroform. The miniaturized chamber was covered with a coverslide and sealed with grease (glisseal N, Borer Chemie AG, Zuchwil, Switzerland). The quality of the lipid monolayer was assessed by fluorescent imaging, especially with respect to the existence of optically resolvable gas phases or the presence of dust particles. Finally, for monolayers which showed defects, the biomolecule of choice was added to the system by temporarily taking off the top coverslide, injecting biomolecule solution into the aqueous phase and subsequent re-sealing of the chamber (figure D.2C).

Langmuir compression isotherms The compression isotherms were measured using a Langmuir-Blodgett trough (Microtrough XL, Kibron Inc. Helsinki, Finland) equipped with a dyne probe. The compression isotherms were acquired using the analytical software FilmWareX 4.0. Three cleaning steps with Kimtech paper tissues soaked with chloroform and ethanol ensured a thorough cleaning of the Langmuir-Blodgett through prior to every measurement. Powder-free gloves were used to minimize contaminations. The dyne probe was cleaned by flaming with a butane torch. The pressure measurements were based on a calibration measurement of the surface pressure Π in aqueous buffer. This calibration provided the baseline, relative to which the pressure with lipids was recorded. To verify the subphase purity, an isotherm was recorded in the absence of lipids with a compression rate of $5\,\mathrm{cm}^2/\,\mathrm{min}$. Provided the system passed this test, lipids were deposited on the air-water interface from a 1 mg/mL stock solution in high purity chloroform. For practical matters, the here stock concentration was higher than described above for the miniaturized chambers. As the interface area is much larger in Langmuir-Blodgett troughs, more lipids are needed. Moreover, the amount of chloroform deposited should not be too high to avoid long evaporation times. After complete solvent evaporation, the isotherm was recorded with a compression rate of $5\,\mathrm{cm^2/\,min}$ until the monolayer collapsed. Generally, all isotherms were measured at least in duplicate at room temperature (21 °C).

Surface pressure measurements in miniaturized chambers For Π measurement in the miniaturized chambers, we used the same dyne probe system as for the Langmuir-Blodgett troughs described above. The pressure on 200 µL of SLB buffer sample was taken as the initial reference. Lipids were deposited on the interface as described above. After full solvent evaporation (about 5 min), the resulting surface pressure Π was recorded at room temperature (21 °C) and at (30 °C). For the latter temperature, the miniaturized chamber was placed on a hot plate together with tissue soaked in water and was covered by a petri dish, in order to achieve a humidity-saturated environment. A small hole had been drilled into the petri dish to ensure accessibility for the dyne probe. With these settings, evaporation was negligible.

FCS and confocal imaging The confocal imaging and the FCS experiments were performed using the same equipment described in appendix B.1 to chapter IV (page 241f). This includes the employment of the pseudo-crosscorrelation setting and the calibration procedure of the system. Here, Alexa Fluor 488 (Alexa488, Thermo Fischer Scientific) or ATTO655 carboxylic acid (Atto655, ATTO-TEC, Siegen, Germany) freely diffusing in aqueous solution were used for calibration measurements. The only difference to chapter IV was the objective, which in this case was a long working distance objective LD C-Apochromat (40X, NA 1.1, water immersion, Carl Zeiss AG, Oberkochen, Germany) with a working distance of 620 µm.

The monolayer interface was easily located by imaging the back-reflection of the excitation laser, a convenient effect of the different refractive indices of water and air. For presentation purposes, the brightness and contrast of images were adjusted using the Fiji software package [Schindelin et al., 2012, Schindelin et al., 2015].

For FCS measurements on lipid monolayers, the optimal axial focus position was first roughly found by manual adjustment of the focus knob until the maximum count rate in the lipid channel was achieved. To precisely tune its axial position, the focus volume was scanned over a range of 2 µm to 3 µm in steps of 0.1 µm. The detected count rate was measured for every position and the detection volume was finally moved to the axial position of maximum count rate. This feature is conveniently implemented in the used commercial control software ZEN (black) 2011 SP6 (Carl Zeiss AG, Oberkochen, Germany) of the LSM780. This procedure needed to be repeated in between FCS measurements, due to sample drift. For all FCS measurements, care was taken to measure at sufficiently low irradiances to minimize artifacts due to photobleaching and fluorescence saturation [Widengren et al., 1995, Petrov and Schwille, 2008a, Gregor et al., 2005]. The buffers used in this study are expected to have a viscosities and refractive indices very close to water [Haynes, 2014], such that no artifacts because of refractive index mismatches are expected.

To control the temperature of the sample, the miniaturized chambers were placed in a heating system (ibidi GmbH, Martinsried, Germany) compatible with mounting on the commercial microscopy stage. To maximize the throughput and the thermal stability and homogeneity of the sample, the temperature control inset was always loaded with two miniaturized chambers.

Measurement of the interface area in miniaturized chambers A monolayer of defined packing was deposited in a miniaturized chamber and imaged with a Zeiss Plan Apo 10X/0.45 objective (Carl Zeiss AG, Oberkochen, Germany). Several adjacent tile images of the interface were acquired to image the entire cross-section of the miniaturized chamber ($R = 7.5\,\mathrm{mm}$). Exploiting the axial sectioning capability of the confocal LSM, this procedure was repeated in 19 different axial z-planes, each of them 100 µm apart. Due to the azimuthal symmetry of the interface and the optical sectioning of the LSM, a circle was imaged in each z-plane above the lowest point of the meniscus, corresponding to the section of the meniscus with the confocal plane (figure VI.1A). The center of mass of each circle was determined and the intensity values were plotted versus their distance to this center. To reduce the noise, the radial distance was binned with a bin width of 5 pixels. The resulting radial intensity distribution was baseline corrected and fitted by a Gaussian to find the peak, which corresponds to the radius of the circle. The image analysis was performed using a home-written MATLAB software (R2016a, The Mathworks, Natick, USA), but previously reported software tools (e.g. [Thomas et al., 2015]) could have been used equally well. Based on the known nominal focus position and the determined radii, I determined the radial meniscus profile $h(r)$ (figure VI.1C), which was extrapolated up to the physical size of the chamber $R = 7.5\,\mathrm{mm}$.

PUBLICATIONS AND MANUSCRIPTS

Manuscripts 5) and 8) include results presented in chapter III. Manuscript 12) is based on chapter IV. Parts of chapter V are described in manuscript 13). The results presented in chapter VI are communicated in publication 4). * denotes equal contributions.

1) Weidemann, T., **Mücksch, J.**, Schwille, P. (2014), Fluorescence fluctuation microscopy: a diversified arsenal of methods to investigate molecular dynamics inside cells. *Curr Opin Struct Biol*, 28: 69-76. doi: 10.1016/j.sbi.2014.07.008

2) **Mücksch, J.***, Spielmann, T.*, Sisamakis, E., Widengren, J. (2015), Transient state imaging of live cells using single plane illumination and arbitrary duty cycle excitation pulse trains. *J. Biophoton*, 8: 392-400. doi: 10.1002/jbio.201400015

3) Glock, P., Broichhagen, J., Kretschmer, S., Blumhardt, P., **Mücksch, J.**, Trauner, D., Schwille, P. (2018), Optical control of a biological reaction-diffusion system. *Angew. Chem. Int. Ed.*, 57(9): 2362-2366. doi: 10.1002/ange.201712002

4) Khmelinskaia, A.*, **Mücksch, J.***, Conci, F., Chwastek, G., Schwille, P. (2018), FCS analysis of protein mobility on lipid monolayers. *Biophys. J.*, 114: 2444-2454. doi: 10.1016/j.bpj.2018.02.031

5) **Mücksch, J.***, Blumhardt, P.*, Strauss, M. T., Petrov., E. P., Jungmann, R., Schwille, P. (2018), Quantifying reversible surface binding via surface-integrated FCS. *Nano Lett.*, 18(5): 3185-3192, doi: 10.1021/acs.nanolett.8b00875

6) Ramirez, D.*, García-Soriano, D.*, Raso, A.*, **Mücksch, J.**, Feingold, M., Rivas, G., Schwille, P. (2018), Treadmilling analysis reveals new insights into dynamic FtsZ ring architecture. *PLoS Biol.*, 16(5): e2004845. doi: 10.1371/journal.pbio.2004845

7) Ramm, B., Glock, P., **Mücksch, J.**, Blumhardt, P., Heymann, M., Schwille, P., The MinDE system is a generic spatial cue for membrane protein distribution in vitro. *(in revision)*

8) Niederauer, C., Blumhardt, P., **Mücksch, J.**, Heymann, M., Lambacher, A., Schwille, P., Direct characterization of the evanescent field in objective-type total internal reflection fluorescence microscopy. *(in revision)*

9) Sonal, Ganzinger, K., Vogel, S., **Mücksch, J.**, Blumhardt, P., Schwille, P., Myosin-II activity generates a dynamic steady state with continuous actin turnover in a minimal actin cortex. *(in revision)*

10) Khmelinskaia, A., **Mücksch, J.**, Petrov., E. P., Franquelim, H. G., Schwille, P., Control of membrane binding and diffusion of cholesteryl-modified DNA origami nanostructures by DNA spacers. *(in revision)*

11) Betaneli, V., **Mücksch, J.**, Schwille, P., Fluorescence Correlation Spectroscopy to examine protein-lipid interactions in membranes. *(in revision)*

12) **Mücksch, J.**, Schwille, P., Petrov, E.P., Disentangling the effects of viscosity and refractive index mismatch in single-focus FCS. *(in preparation)*

13) Corrales-Guerrero, L., Refes, Y., He, B., **Mücksch, J.**, Ramm, B., Heimerl, T., Knopp, J., Steinchen, W., Bange, G., Schwille, P., Thanbichler, M., Regulation of cell division protein FtsZ by MipZ in *Caulobacter crescentus*. *(in preparation)*

14) Blumhardt, P., **Mücksch, J.**, Stein, J., Stehr, F., Bauer, J., Schwille, P., Photo-induced Loss of Binding Sites in DNA-PAINT Microscopy. *(in preparation)*

15) Stein, J.*, Stehr, F.*, Blumhardt, P., **Mücksch, J.**, Auer, A., Schüder, F., Jungmann, R., Schwille, P., Analyzing DNA hybridization on DNA Origami under super-resolution conditions. *(in preparation)*

ACKNOWLEDGMENTS

Not only this thesis and the research presented therein, but also my professional development would not be the same without the support I received, for which I am truly grateful. I cannot stress enough how valuable and important some people were for this work, not only on a professional, but also on an emotional level.

Prof. Petra Schwille: Petra, without you, I certainly would not be the scientist I am today. Thank you for taking me as a PhD student and for all the freedom you granted over the years. I appreciate all the different directions and fields I could explore over the past years, including the supervision of students and the construction of several optical setups.

Prof. Don Lamb and *Dr. Thomas Wollert*: Thank you for being part of my TAC and for the scientific advices.

Philipp Blumhardt: Philipp, it took us a little bit of time, but once we found each other, we were a fantastic team. I could always rely on your help, regardless of whether you would benefit yourself. I believe what we did for the infrastructure of the optics labs was remarkable and will persist in one way or another. Just remember how all these rooms were empty, there were no power sockets and the temperature was oscillating! I am very glad we teamed up and produced some very solid scientific results together (chapter III).

Eugene P. Petrov: You were a great teacher and there is no doubt that you made a significant contribution to how I developed as a scientist. Our collaboration produced some valuable insights for FCS (chapter IV). Thank you not only for sharing all the knowledge on FCS and Monte Carlo simulations, but also for the critical discussions of ideas and experiments.

Alena Khmelinskaia: We shared an office for almost five and a half years by now! It has been a long journey during which I could always count on you, regardless of whether I needed lab help or wanted to go for a drink after work.

Sonal: Doing science together was already an absolute pleasure. Even more did I enjoy our endless discussions, which covered almost every topic one could possibly imagine. Thank you for all your witty and sharp repartee. It made my day more than once.

Beatrice Ramm: Working with you on the "Min pushing" and MipZ projects (chapter V) was a lot of fun and I am very glad we did them. Thank you for all your enthusiasm, inspiration, the knowledge you shared, and the cheerfulness you were spreading.

Prof. Ralf Jungmann and *Maximilian Strauß*: Thank you for the very successful collaboration to validate SI-FCS using DNA origamis. I appreciate your spirit of sharing knowledge and I learned a lot about DNA-PAINT from you.

Dr. Laura Corrales Guerrero and *Prof. Martin Thanbichler*: Thank you for proposing to look at the FtsZ-MipZ interaction by FCS (chapter V). I really enjoyed working with you and I believe we turned this project into quite a success.

Diego Ramirez and *Daniela García-Soriano*: Looking at the FtsZ-YFP-mts mutant by FCS was a short but intense and interesting project, which supplemented my previous experiments nicely (chapter V). Thank you for approaching and running the measurements with me.

Philipp Glock: Thank you for being so nice, helpful and cheerful every day. I actually cannot remember a single day when this was not the case.

Henri Franquelim: Henri, I benefited from all your countless explanations. I am impressed by your excessive knowledge of literally everything, and I admire you helpfulness.

Christopher Jockisch, Wilhelm Frisch, Laura Kacenauskaite: You were the first students I was responsible for, and you were very good catches. I learned a lot on guidance, leading and reflection during your stays.

Araceli Sebastián Sánchez de Castro and *Christian Niederauer*: You were great students, and the quality of your Master's theses clearly demonstrates this. I am happy you joined us and I wish you all the best for the future.

Franco Conci: Thank you for your contributions to the monolayer project (chapter VI) and the hard work you put into it.

Florian Stehr und *Johannes Stein*: I am wishing you all the best for you PhDs and I really hope that you can push SI-FCS together with Philipp to the next level.

Sigrid Bauer: Thank you for all the technical assistance, the preparation of solutions and maintaining the amazingly well organized membrane lab.

Susanne von Gronau: Thank you for introducing me to the densiometer and the rolling ball viscosimeter.

There are many other people with whom I did not collaborate in scientific projects. Nonetheless, their advices and support, the discussions and the good times we had are highly appreciated. I express my gratitude to *Gosia Poczopko*, *Caterina Rini Macrini*, *Tamara Heermann*, *Hiro Eto*, *Dr. Grzegorz Chwastek*, *Dr. Ilaria Visco*, *Dr. Thomas Weidemann*, and *Dr. Kristina Ganzinger*. I also need to thank all other members of the Schwille lab.

Abschließend eine große Umarmung für die Personen, die mir am nächsten stehen und mich schon seit lang vor der Promotion begleiten:

Meine Eltern: Ohne euch würde diese Arbeit nicht existieren. Ihr habt den Weg für alles was ich erreicht habe geebnet. Danke für eure Unterstützung über all die Jahre, das geduldige Zuhören, die Gewissheit immer zu euch kommen zu können. Danke für eure bedingungslose Liebe.

Meine Geschwister Judith und Janek: Wir wohnen seit 16 Jahren nicht mehr alle zusammen unter einem Dach, und doch weiß ich, dass ich mich jederzeit auf euch verlassen kann und bin mir immer eurer Unterstützung bewusst.

Laura: Du freust dich mit mir wenn es Anlass gibt, du baust mich auf wenn ich am Boden liege, du motivierst mich wenn ich träge bin, du bremst mich wenn ich überdrehe, du korrigierst mich wenn ich daneben liege, du hilfst mir wenn ich nicht mehr weiter weiß. Danke dafür, für deine Liebe, und für dein Lächeln, das die beste Medizin gegen Kummer und schlechte Laune ist.